ISSN 0021-3438 (Print)
ISSN 2412-8783 (Online)

IZVESTIYA
NON-FERROUS METALLURGY

Vol. 30, No. 1, 2024

Scientific and Technical Journal
Founded in 1958
4 Issues per year

ИЗВЕСТИЯ ВУЗОВ
ЦВЕТНАЯ МЕТАЛЛУРГИЯ

Том 30, № 1, 2024

Научно-технический журнал
Основан в 1958 г.
Выходит 4 раза в год

ISSN 0021-3438 (Print)
ISSN 2412-8783 (Online)

IZVESTIYA NON-FERROUS METALLURGY

Vol. 30, No. 1
2024

Scientific and Technical Journal
Founded in 1958
4 Issues per year
http://cvmet.misis.ru

Journal is included into the List of the peer-reviewed scientific publications recommended by the Highest Attestation Commission of the Ministry of Education and Science of the Russian Federation for publishing the results of doctoral and candidate dissertations

Abstracting/Indexing: Russian Science Citation Index (RSCI), Chemical Abstracts (Online), INIS, OCLC ArticleFirst, Ulrich's Periodicals Directory, VINITI Database (Abstract Journal)

Founder

National University of Science and Technology "MISIS"
Address: 4 build. 1 Leninskiy Prosp., Moscow 119049, Russia
http://www.misis.ru

Editor-in-Chief

Evgeny A. Levashov
Prof., Dr. Sci. (Eng.), Acad. of the RANS, NUST MISIS, Moscow, Russia

Deputy Editor

Vladislava A. Ignatkina
Prof., Dr. Sci., NUST MISIS, Moscow, Russia

Editorial Board

Abhilash – Dr., Ph.D., CSIR – National Metallurgical Laboratory, Jamshedpur, India
E.V. Ageev – Prof., Dr. Sci. (Eng.), SouthWest State University, Kursk, Russia
M.V. Ananyev – Prof., Dr. Sci. (Chem.), Federal State Research and Development Institute of Rare Metal Industry (JSC "Giredmet"), Moscow, Russia
N.A. Belov – Prof., Dr. Sci. (Eng.), NUST MISIS, Moscow, Russia
E.V. Bogatyreva – Prof., Dr. Sci. (Eng.), NUST MISIS, Moscow, Russia
V.B. Deev – Prof., Dr. Sci. (Eng.), NUST MISIS, Moscow, Russia
V.M. Denisov – Prof., Dr. Sci. (Chem.), Siberian Federal University, Krasnoyarsk, Russia
D.V. Drobot – Prof., Dr. Sci. (Chem.), Russian Technological University (MITHT), Moscow, Russia
F.V. Grechnikov – Prof., Dr. Sci. (Eng.), Acad. of RAS, Samara National Research University n.a. S.P. Korolev (Samara University), Samara, Russia
D.V. Gunderov – Dr. Sci. (Phys.-Math.), Institute of Molecule and Crystal Physics Ufa Research Center of the RAS, Ufa, Russia
B.B. Khina – Dr. Sci. (Phys.-Math.), The Physical-Techical Institute of NAS of Belarus, Minsk, Belarus
D.V. Louzguine – Prof., Dr. Sci., Tohoku University, Sendai, Japan
S.V. Mamyachenkov – Prof., Dr. Sci. (Eng.), Ural Federal University, Yekaterinburg, Russia
Z.A. Mansurov – Dr. Sci. (Chem.), Prof., Institute of Combustion Problems, Almaty, Kazakhstan
N.V. Nemchinova – Prof., Dr. Sci. (Eng.), Irkutsk National Research Technical University, Irkutsk, Russia
K.V. Nikitin – Prof., Dr. Sci. (Eng.), Samara State Technical University, Samara, Russia
H.A. Oye – Prof., Dr., Norwegian University of Science and Technology, Trondheim, Norway
P.V. Polyakov – Prof., Dr. Sci. (Chem.), Siberian Federal University, Krasnoyarsk, Russia
E.S. Prusov – Cand. Sci. (Eng.), Vladimir State University, Vladimir, Russia
V.N. Richkov – Prof., Dr. Sci. (Chem.), Ural Federal University, Ekaterinburg, Russia
D. Sadoway – Prof., Dr., Massachusetts Institute of Technology, Boston, USA
G.A. Salishchev – Prof., Dr. Sci. (Eng.), Belgorod National Research University, Belgorod, Russia
D.V. Shtansky – Prof., Dr. Sci. (Phys.-Math.), NUST MISIS, Moscow, Russia
V.M. Sizyakov – Prof., Dr. Sci. (Eng.), Saint-Petersburg Mining University, St. Petersburg, Russia
Stopic Srecko – Dr.-Ing. habil., RWTH Aachen University, Aachen, Germany
B.B. Straumal – Prof., Dr. Sci. (Phys.-Math.), Institute of Solid State Physics of the RAS, Chernogolovka, Moscow region
O.Yu. Tkacheva – Dr. Sci. (Chem.), Institute of High Temperature Electrochemistry of the Ural Branch of the RAS, Yekaterinburg, Russia
M. Verhaege – Prof., Dr., University of Gent, Belgium
G.M. Vol'dman – Prof., Dr. Sci. (Chem.), Russian Technological University (MITHT), Moscow, Russia
G. Xanthopoulou – Dr., National Center for Scientific Research "Demokritos", Agia Paraskevi, Attica, Greece
A.L. Yerokhin – Prof., Dr., University of Manchester, United Kingdom
Onuralp Yücel – Prof., Dr., Istanbul Technical University, Maslak, Istanbul, Turkey
Yu.P. Zaikov – Prof., Dr. Sci. (Chem.), Institute of High Temperature Electrochemistry of the Ural Branch of the RAS, Yekaterinburg, Russia
R.Kh. Zalavutdinov – Cand. Sci. (Phys.-Math.), A.N. Frumkin Institute of Physical Chemistry and Electrochemistry of the RAS, Moscow, Russia
M. Zinigrad – Prof., Dr., Ariel University, Ariel, Israel
A.I. Zouboulis – Prof., Dr., Aristotle University of Thessaloniki, Greece

Editorial Staff

Address: NUST MISIS, 4 build. 1 Leninskiy Prosp.,
Moscow 119049, Russia

Phone: +7 (495) 638-45-35

E-mail: izv.vuz@misis.ru

Certificate of registration No. 015842 (13.03.1997)
Re-registration PI No. ФС77-79229 (25.09.2020)

Subscription: Ural-Press Agency

Leading Editor – O.V. Sosnina
Executive Editor – A.A. Kudinova
Layout Designer – E.A. Legkaya

Signed print 25.03.2024. Format 60×90 1/8.
Offset paper No. 1. Digital printing. Quires 11,5
Order 19451. Free price

Printed in the printing house of the MISIS Publish House
4 build. 1 Leninskiy Prosp., Moscow 119049, Russia. Phone/fax: +7 (499) 236-76-17

© NUST MISIS, Moscow, 2024
© Izvestiya. Non-Ferrous Metallurgy, 2024

Articles are available under Creative Commons Attribution Non-Commercial No Derivatives

ИЗВЕСТИЯ ВУЗОВ
ЦВЕТНАЯ МЕТАЛЛУРГИЯ

ISSN 0021-3438 (Print)
ISSN 2412-8783 (Online)

Том 30, № 1
2024

Научно-технический журнал   Основан в 1958 г.   Выходит 4 раза в год   http://cvmet.misis.ru

Журнал включен в Перечень рецензируемых научных изданий, рекомендованных ВАК Минобрнауки РФ для публикации результатов диссертаций на соискание ученых степеней

Журнал включен в базы данных: Russian Science Citation Index (RSCI), Chemical Abstracts (Online), INIS, OCLC ArticleFirst, Ulrich's Periodicals Directory, РИНЦ, БД/РЖ ВИНИТИ

Учредитель

ФГАОУ ВО Национальный исследовательский технологический университет «МИСИС»
Адрес: 119049, г. Москва, Ленинский пр-т, 4, стр. 1
http://www.misis.ru

Главный редактор

Евгений Александрович Левашов
д.т.н., академик РАЕН, профессор, НИТУ МИСИС, г. Москва

Заместитель главного редактора

Владислава Анатольевна Игнаткина
д.т.н., профессор, НИТУ МИСИС, г. Москва

Редакционная коллегия

Е.В. Агеев – д.т.н., ЮЗГУ, г. Курск
М.В. Ананьев – д.х.н., АО «Гиредмет», г. Москва
Н.А. Белов – д.т.н., проф., НИТУ МИСИС, г. Москва
Е.В. Богатырева – д.т.н., НИТУ МИСИС, г. Москва
Г.М. Вольдман – д.х.н., проф., РТУ (МИТХТ), г. Москва
Ф.В. Гречников – д.т.н., акад. РАН, проф., СНИУ, г. Самара
Д.В. Гундеров – д.ф.-м.н., ИФМК УНЦ РАН, г. Уфа
В.Б. Деев – д.т.н., проф., НИТУ МИСИС, г. Москва
В.М. Денисов – д.х.н., проф., СФУ, г. Красноярск
Д.В. Дробот – д.х.н., проф., РТУ (МИТХТ), г. Москва
Ю.П. Зайков – д.х.н., проф., ИВТЭ УрО РАН, г. Екатеринбург
Р.Х. Залавутдинов – к.ф.-м.н., ИФХЭ РАН, г. Москва
С.В. Мамяченков – д.т.н., проф., УрФУ, г. Екатеринбург
З.А. Мансуров – д.х.н., проф., Институт проблем горения, г. Алматы, Казахстан
Н.В. Немчинова – д.т.н., проф., ИРНИТУ, г. Иркутск
К.В. Никитин – д.т.н., проф., СамГТУ, г. Самара
П.В. Поляков – д.х.н., проф., СФУ, г. Красноярск
Е.С. Прусов – к.т.н., доцент, ВлГУ, г. Владимир
В.Н. Рычков – д.х.н., проф., УрФУ, г. Екатеринбург
Г.А. Салищев – д.т.н., проф., НИУ «БелГУ», г. Белгород
В.М. Сизяков – д.т.н., проф., СПГУ, г. Санкт-Петербург
Б.Б. Страумал – д.ф.-м.н., проф., ИФТТ РАН, г. Черноголовка
О.Ю. Ткачева – д.х.н., ИВТЭ УрО РАН, г. Екатеринбург
Б.Б. Хина – д.ф.-м.н., доц., ФТИ НАН Беларуси, г. Минск, Беларусь
Д.В. Штанский – д.ф.-м.н., проф., НИТУ МИСИС, г. Москва
Abhilash – Dr., Ph.D., CSIR – National Metallurgical Laboratory, Jamshedpur, India
D.V. Louzguine – Prof., Dr., Tohoku University, Sendai, Japan
H.A. Oye – Prof., Dr., Norwegian University of Science and Technology, Trondheim, Norway
D. Sadoway – Prof., Dr., Massachusetts Institute of Technology, Boston, USA
Stopic Srecko – Dr.-Ing. habil., RWTH Aachen University, Aachen, Germany
M. Verhaege – Prof., Dr., University of Gent, Belgium
G. Xanthopoulou – Dr., National Center for Scientific Research «Demokritos», Agia Paraskevi, Attica, Greece
A.L. Yerokhin – Prof., Dr., University of Manchester, United Kingdom
Yücel Onuralp – Prof., Dr., Istanbul Technical University, Maslak, Istanbul, Turkey
M. Zinigrad – Prof., Dr., Ariel University, Ariel, Israel
A.I. Zouboulis – Prof., Dr., Aristotle University of Thessaloniki, Greece

Редакция журнала

Адрес: 119049, г. Москва, Ленинский пр-т, 4, стр. 1,
НИТУ МИСИС
Тел.: +7 (495) 638-45-35
E-mail: izv.vuz@misis.ru

Свидетельство о регистрации № 015842 от 13.03.1997 г.
Перерегистрация ПИ № ФС77-79229 от 25.09.2020 г.

Подписка: Агентство «Урал-пресс»

Ведущий редактор – О.В. Соснина
Выпускающий редактор – А.А. Кудинова
Дизайн и верстка – Е.А. Легкая

Подписано в печать 25.03.2024. Формат 60×90 1/8.
Бум. офсетная № 1. Печать цифровая. Усл. печ. л. 11,5
Заказ 19451. Цена свободная

Отпечатано в типографии Издательского Дома МИСИС
119049, г. Москва, Ленинский пр-т, 4, стр. 1. Тел./факс: +7 (499) 236-76-17

© НИТУ МИСИС, Москва, 2024
© «Известия вузов. Цветная металлургия», 2024

Статьи доступны под лицензией Creative Commons Attribution Non-Commercial No Derivatives

CONTENTS

Metallurgy of Non-Ferrous Metals

5 **Zelyakh Ya.D., Timofeev K.L., Voinkov R.S., Maltsev G.I., Shunin V.A.**

Purification of process solutions from mercury by sorption

Metallurgy of Rare and Precious Metals

14 **Nikishina E.E., Grechishnikov N.V., Drobot D.V.**

Heterophase synthesis of rare-earth zirconates

Foundry

24 **Sanin V.V., Aheiev M.I., Loginov P.A., Bychkova M.Ya., Shukman E.S., Mezhevaia L.Yu., Sanin V.N., Lobova T.A.**

Structural characteristics and properties of heat-resistant nickel β-alloys produced via the centrifugal SHS-casting method

Physical Metallurgy and Heat Treatment

42 **Slavinskaya N.A., Ri H., Ri E.H., Zhivetev A.S.**

Effects of quenching temperature on the structure, segregation, and properties of the AM4.5Kd+ 0.2 wt.% La alloy after artificial aging

55 **Fedotov A.D., Mukanov S.K., Romanenko B.Yu., Loginov P.A., Bychkova M.Ya., Rupasov S.I.**

Mechanical and tribological characteristics of nickel-rich CoCrCu$_x$FeNi$_2$ high entropy-alloys

70 **Kayasova A.O., Baskov F.A., Lobova T.A., Levashov E.A.**

Structure and mechanical properties of PR-03N18K9M5TYu steel grade fabricated by selective laser melting and post-processing

81 **Gunderov D.V., Stotskiy A.G., Gunderova S.D., Aubakirova V.R., Demin A.Yu.**

Impact of ECAP at 300 °C on the microstructure and mechanical properties of the quenched Zr–2.5%Nb alloy

СОДЕРЖАНИЕ

Металлургия цветных металлов

5 **Зелях Я.Д., Тимофеев К.Л., Воинков Р.С., Мальцев Г.И., Шунин В.А.**

Очистка технологических растворов от ртути сорбцией

Металлургия редких и благородных металлов

14 **Никишина Е.Е., Гречишников Н.В., Дробот Д.В.**

Гетерофазный синтез цирконатов редкоземельных элементов

Литейное производство

24 **Санин В.В., Агеев М.И., Логинов П.А., Бычкова М.Я., Шукман Е.С., Межевая Л.Ю., Санин В.Н., Лобова Т.А.**

Особенности структуры и свойства жаропрочных никелевых β-сплавов, полученных методом центробежного СВС-литья

Металловедение и термическая обработка

42 **Славинская Н.А., Ри Х., Ри Э.Х., Живетьев А.С.**

Влияние температурных режимов закалки на формирование структуры, ликвационные процессы и свойства сплава АМ4,5Кд + 0,2 мас.% La после искусственного старения

55 **Федотов А.Д., Муканов С.К., Романенко Б.Ю., Логинов П.А., Бычкова М.Я. , Рупасов С.И.**

Механические и трибологические свойства высокоэнтропийных сплавов CoCrCu$_x$FeNi$_2$ с высоким содержанием никеля

70 **Каясова А.О., Басков Ф.А., Лобова Т.А., Левашов Е.А.**

Особенности структуры и механические свойства стали ПР-03Н18К9М5ТЮ, полученной методом селективного лазерного сплавления в сочетании с постобработкой

81 **Гундеров Д.В., Стоцкий А.Г., Гундерова С.Д., Аубакирова В.Р., Демин А.Ю.**

Влияние РКУП при температуре 300 °C на структуру и свойства закаленного сплава Zr–2,5%Nb

METALLURGY OF NON-FERROUS METALS / МЕТАЛЛУРГИЯ ЦВЕТНЫХ МЕТАЛЛОВ

UDC 66.081.4 : 546.492 : 661.691.32
https://doi.org/10.17073/0021-3438-2024-1-5-13

Research article
Научная статья

Purification of process solutions from mercury by sorption

Ya.D. Zelyakh[1], **K.L. Timofeev**[1,2], **R.S. Voinkov**[1,2], **G.I. Maltsev**[1], **V.A. Shunin**[1]

[1] **JSC "Uralelectromed"**
1 Uspenskiy Prosp., Verkhnyaya Pyshma, Sverdlovsk region 624091, Russia

[2] **UMMC Technical University**
3 Uspenskiy Prosp., Verkhnyaya Pyshma, Sverdlovsk region 624091, Russia

✉ Yakov D. Zelyakh (zyad@uralcopper.com)

Abstract: At JSC "Uralelectromed", selenium-containing raw materials and industrial products are processed, resulting in solutions containing a mixture of mercury with concentrations as follows (g/dm^3): 157–210 Se; 0.004–0.02 Hg; 0.15–0.20 Te; 2–3 As; 0.15–0.20 Sb; and 45–50 S. To produce branded selenium, the mercury concentration in the solution must be kept below 0.001 g/dm^3. Various methods, such as hydrometallurgical and electrochemical processes, are known for mercury purification from solutions. JSC "Uralelectromed" has selected sorption technology for mercury removal using the weak-base macroporous anionite Lewatit MP-68 (Germany), which allows for control over the degree of solution purification. In pursuit of import substitution for the Western European sorbent Lewatit MP-68, we investigated several pre-selected industrial sorbents for extracting mercury anionic complexes produced in Russia (AM-2B, AN-31, AV 17-8, VP-3Ap), China (Seplite MA 940 and LSC 710), and India (Tulsion CH-95 and CH-97). Initially, in static mode, we determined the distribution coefficient (C_d), the degree of element extraction (ε), the static exchange capacity of the resins (SEC, g/dm^3), and the mercury/selenium separation coefficient ($D_{Hg/Se}$) which led to the selection of the best samples: AV 17-8, Seplite MA 940, AM-2B, and CH-97, with SEC values of 0.95–0.97 g/dm^3 (SEC = 0.98 g/dm^3 of resin Lewatit MP-68). Subsequently, in dynamic mode, we ranked the ionites by decreasing dynamic exchange capacity (DEC / TDEC): AV 17-8 ≥ Lewatit MP-68 > AM-2B > Seplite MA 940 > Tulsion CH-97. Resins AV 17-8, Seplite MA 940, and AM-2B demonstrated similar dynamic sorption characteristics; under comparable conditions, mercury breakthrough occurred after processing at least 950 specific volumes of the initial solution. In contrast, with Lewatit MP-68 ionite, mercury breakthrough occurred after no more than 750 specific volumes, indicating the need to increase the number of sorption steps in the solution purification cascade. Considering the totality of ion-exchange properties, for further industrial testing, it is recommended to use the domestically produced resin AV 17-8 instead of the foreign sorbent Lewatit MP-68 in the sorption purification process of selenic acid to remove mercury, thereby ensuring the production of branded selenium.

Keywords: mercury, selenium, resin, sorption, static exchange capacity, dynamic exchange capacity, hydrometallurgical purification.

For citation: Zelyakh Ya.D., Timofeev K.L., Voinkov R.S., Maltsev G.I., Shunin V.A. Purification of process solutions from mercury by sorption. *Izvestiya. Non-Ferrous Metallurgy*. 2024;30(1):5–13. https://doi.org/10.17073/0021-3438-2024-1-5-13

Очистка технологических растворов от ртути сорбцией

Я.Д. Зелях[1], **К.Л. Тимофеев**[1,2], **Р.С. Воинков**[1,2], **Г.И. Мальцев**[1], **В.А. Шунин**[1]

[1] **АО «Уралэлектромедь»**
Россия, 624091, Свердловская обл., г. Верхняя Пышма, пр-т Успенский, 1

[2] **Технический университете УГМК**
Россия, 624091, Свердловская обл., г. Верхняя Пышма, пр-т Успенский, 3

✉ Яков Дмитриевич Зелях (zyad@uralcopper.com)

Аннотация: При переработке в АО «Уралэлектромедь» селенсодержащего сырья и промпродуктов образуются растворы, содержащие примесь ртути, г/дм^3: 157–210 Se; 0,004–0,02 Hg; 0,15–0,20 Te; 2–3 As; 0,15–0,20 Sb; 45–50 S. Для получения марочного селена концентрация ртути в растворе не должна превышать 0,001 г/дм^3. Известны различные методы очистки растворов от ртути: гидрометаллургические, электрохимические и др. В АО «Уралэлектромедь» выбор сделан в пользу сорбционной технологии удаления ртути на слабоосновном макропористом анионите Lewatit MP-68 (Германия), позволяющей управлять степенью очистки растворов. Для обеспечения замещения западноевропейского сорбента (Lewatit MP-68) проведено исследование ряда предварительно отобранных промышленных сорбентов анионных комплексов ртути производства РФ (АМ-2Б, АН-31, АВ 17-8, ВП-3Ап), Китая (Seplite MA 940 и LSC 710), Индии (Tulsion CH-95 и CH-97). На первой стадии в статическом режиме определены коэффициент распределения (K_p), степень извлечения элементов (ε), значения статической обменной емкости смол (СОЕ, г/дм^3), коэффициент разделения ($D_{Hg/Se}$), на основании которых отобраны лучшие образцы: АВ 17-8, Seplite MA 940, АМ-2Б, CH-97 с величинами СОЕ = 0,95÷0,97 г/дм^3 (у смолы Lewatit MP-68 СОЕ = 0,98 г/дм^3). На второй стадии в динамическом режиме установлено следующее: по величине ДОЕ/ПДОЕ иониты расположены в убывающий ряд: АВ 17-8 ≥ Lewatit MP-68 > > АМ-2Б > Seplite MA 940 >> Tulsion CH-97. Смолы АВ 17-8, Seplite MA 940, АМ-2Б близки по своим динамическим сорбционным характеристикам: в сопоставимых условиях проскок по ртути наступает после пропускания не менее 950 уд. объемов исходного раствора. Для сравнения: на ионите Lewatit MP-68 проскок по ртути наступает после пропускания не более 750 уд. объемов, что требует увеличения числа ступеней сорбции в каскаде очистки растворов. По совокупности ионообменных свойств для дальнейшего исследования в режиме промышленных испытаний рекомендуется использовать смолу АВ 17-8 отечественного производства вместо зарубежного сорбента Lewatit MP-68 в технологической схеме сорбционной очистки селенистой кислоты от ртути с целью обеспечения получения марочного селена.

Ключевые слова: ртуть, селен, смола, сорбция, статическая обменная емкость, динамическая обменная емкость, гидрометаллургическая очистка.

Для цитирования: Зелях Я.Д., Тимофеев К.Л., Воинков Р.С., Мальцев Г.И., Шунин В.А. Очистка технологических растворов от ртути сорбцией. *Известия вузов. Цветная металлургия*. 2024;30(1):5–13. https://doi.org/10.17073/0021-3438-2024-1-5-13

Introduction

At JSC "Uralelectromed", raw materials and industrial products containing selenium are processed, resulting in solutions with varying concentrations of impurities, g/dm^3: 157—210 selenium (Se); 0.004—0.02 mercury (Hg); 0.15—0.20 tellurium (Te); 2—3 arsenic (As); 0.15—0.20 antimony (Sb); and 45—50 sulfur (S). For production of branded selenium, the concentration of mercury in the solution should not exceed 0.001 g/dm^3 [1].

Various methods have been developed to purify solutions of mercury. These include the electrochemical reduction, which removes over 92 % of mercury as an Hg—Cu alloy, followed by the thermal desorption of mercury from the spent cathode [2]. Sorption techniques, utilizing microporous niobium (AM-11) and vanadium (AM-14) silicates, can adsorb approximately 160 mg/g of mercury [3]. Combined electron-beam and adsorption treatments on cellulose, carboxymethylcellulose, and starch remove 98 % of Hg(II) [4]. Activated carbon, alloyed with sulfur, has shown the ability to absorb up to 187 mg/g of mercury [5]. Induction adsorption of HgO on an alkaline sorbent with active chalcogen-based centers [6]; sorption removal of over 80 % of elemental mercury Hg^0 on H_2S modified magnetospheres (S—MS) [7; 8], and mercury desorption techniques via thermal treatment and plasma method [9] have been reported. Photocatalytic oxidation of Hg^0 enables up to 87 % removal of mercury [10]. The photothermal aerogel method enables the potential for achieving complete purification from heavy metal ions [11]. Cementation of mercury ($HgCl_4^{2-}$) from chloride medium using metallic zinc, iron, and aluminum results in a final solution with $8\cdot10^{-2}$ g/dm^3 of mercury [12]. In acidic solutions, mercury complexes such as $[Hg(SO_3)_2]^{2-}$, $[Hg(SO_3)_3]^{4-}$, $[Hg(SO_3)_4]^{6-}$ [13], form and are adsorbed on carbon-containing materials [14]. Sulfur copolymers with micro- and macroporous structures actively interact with mercury compounds in solution [15], forming multinuclear Hg—S sulfide complexes [16—18]. The presence of chloride ions also leads to the formation of mercury complex compounds: $HgCl^+$, $HgCl_3^-$, $HgCl_4^{2-}$ [19—26].

JSC "Uralelectromed" selected the sorption technology using the weak-base macroporous anionite Lewatit MP-68 from Germany for mercury removal. This technology allows for a high degree of solution purification using compact equipment. It is highly reliable, easy to operate, and remains effective regardless of fluctuations in concentration and hydraulic pressure. To facilitate the import substitution of the Western European reagent Lewatit MP-68, we explored several pre-selected industrial sorbents designed for extracting mercury anionic complexes. These sorbents are produced in Russia (AM-2B, AN-31, AV 17-8, VP-3Ap), China (Seplite MA 940 and LSC 710), and India (Tulsion CH-95 and CH-97). The characteristics of these sorbents are detailed in Table 1.

The objective of this study was to identify a sorbent that could serve as an alternative to Lewatit MP-68 and to determine the optimal parameters for purifying selenic acid solutions from mercury to achieve a residual concentration not exceeding 0.001 g/dm^3 Hg.

Methods

The resins tested were pre-treated prior to their use, following these steps: they were soaked in dis-

Tabl. 1. **Characteristics of the studied resins**

Таблица 1. Характеристики исследуемых смол

Description	Type	Purpose according to the data sheet
Lewatit MP-68	Weak-base macroporous anionite based on a styrene-divinylbenzene copolymer with monodisperse granule distribution	Desalinization Treatment of rinse water in galvanic processes Demineralization of water with a high content of humic acids
Seplite MA 940	Macroporous polystyrene weak-base anionic resin Weak-base anionite (tertiary amine functional groups)	Removal of heavy non-ferrous metals from industrial solutions High resistance to osmotic shock Removal of natural organic matter
Seplite LSC 710	Ion-exchange chelating resin with iminodiacite functional groups	Removal of heavy metals from solutions
Tulsion CH-95 Tulsion CH-97	Chelate resin (Cl^-) With functional groups (iminodiacetic acid, phosphoric acid, thiuronium, thiol)	Selective sorption of metals from aqueous and organic solutions at different pH Removal of heavy (Fe, Cu, Ni, Zn, Cr, Co, Mn, Mo, Cd, Hg) and precious (Pt, Pd, Au, Ag, Rh) metals
AV 17-8	Strong-base sorbent with a gel structure Functional group – quaternary trimethylammonium groups of basic nature Matrix – styrene-divinylbenzene	Water softening and desalination at thermal and nuclear power plants and in boiler houses Purification of process solutions and wastewater Separation and sorting of non-ferrous metals
AM-2B	Benzyldimethylammonium and dibenzyldimethylammonium functional groups	Selective extraction of cyanide anionic gold complexes
AN-31	Weak-base resin with functional groups including quaternary trimethylammonium, secondary and tertiary aliphatic amino groups	Applications in water treatment, wastewater treatment, chemical and hydrometallurgical industries Separation and sorting of non-ferrous metals
VP-3Ap	Strong-base macroporous anionite based on a copolymer 4-vinylpyridine and divinylbenzene	Extraction of heavy non-ferrous metals from various media, in particular, thorium and plutonium from nitric acid systems

tilled water for 24 h, then washed with a 5 % NaOH solution to pH = 10÷12. Afterward, they were rinsed with water until a neutral pH was achieved. This was followed by treatment with a 5—15 g/dm^3 solution of H_2SO_4, and finally, they were washed with water to pH = 2÷5.

To determine the static exchange capacity of the resins (SEC, g/dm^3), an initial solution of 0.1 dm^3 with the following composition, g/dm^3: 208.3 Se; 0.02 Hg; 0.15 Te; 2.9 As; 0.16 Sb; 49 S) was brought into contact with 0.002, 0.005, and 0.010 dm^3 of sorbents. The mixture was stirred for 72—96 h. The filtrates after sorption were analyzed, and the following values were calculated: SEC, distribution coefficient (C_d), elements extraction degree (ε), and the mercury/selenium separation coefficient ($D_{Hg/Se}$), as seen in Table 2:

$$\text{SEC} = (C_\text{init} - C_\text{equil})V_\text{solut}/V_\text{sorb}, \quad (1)$$

where C_init and C_equil are the initial and equilibrium concentrations of Hg in the solution, respectively, g/dm^3; V_solut and V_sorb are the volumes of the sorbent and solution, respectively, dm^3;

$$C_d = \text{SEC}/C_\text{equil}, \quad (2)$$

$$\varepsilon = (C_\text{init} - C_\text{equil})/C_\text{init}, \quad (3)$$

$$D_{Hg/Se} = C_d(\text{Hg})/C_d(\text{Se}). \quad (4)$$

To determine the dynamic exchange capacity (DEC, mg/cm^3) and total dynamic exchange capacity (TDEC, mg/cm^3) of the resins, the initial solution (with a composition of 160—170 g/dm^3 Se and 0.004—0.029 g/dm^3 Hg) was passed through 0.020 dm^3 of the test resin loaded into a column at a rate of ~0.020 dm^3/h (1 specific volume). The value of TDEC (mg$_{elem}$/cm$^3{}_{sorb}$) was calculated by summing the amount of the element absorbed from each portion of the solution that had passed through the test resin, relative to the volume of the sorbent:

$$\mathrm{TDEC} = \Sigma V_{\mathrm{solut}}(C_0 - C_{\mathrm{outl}})/V_{\mathrm{sorb}}, \qquad (5)$$

where V_{sorb} represents the volume of the sorbent, dm^3, C_0 is the initial concentration of the element, g/dm^3, C_{outl} is the concentration of the element at the column outlet, respectively, g/dm^3, and V_{solut} is the volume of the solution that has passed through the column, dm^3.

Results and discussion

Table 2 presents experimental data on mercury sorption in static mode.

The criteria for selecting the resin were based on achieving the maximum values of SEC and the degree of impurity extraction for mercury (Hg), while minimizing the extraction of the macrocomponent (Se), as indicated by the highest separation coefficient ($D_{\mathrm{Hg/Se}}$).

Tabl. 2. **Values of SEC, ε, C_d and $D_{\mathrm{Hg/Se}}$ for ion exchange resins**

Таблица 2. Значения СОЕ, ε, K_p и $D_{\mathrm{Hg/Se}}$ для ионообменных смол

Name of resin	L : S	SEC, g/dm^3		C_d		Extraction ε, %		Separation coefficient $D_{\mathrm{Hg/Se}}$
		Hg	Se	Hg	Se	Hg	Se	
AM-2B made in Russia	50	0.97	1210.0	1616.7	6.6	97.00	11.62	246
	20	0.40	218.0	1980.0	1.1	99.00	5.23	1793
	10	0.20	168.0	1990.0	0.9	99.50	8.07	2268
AN-31 made in Russia	50	0.00	790.0	0.0	4.1	0.00	7.59	0
	20	0.08	416.0	5.0	2.2	20.00	9.99	2
	10	0.09	138.0	8.2	0.7	45.00	6.63	12
AV 17-8 made in Russia	50	0.96	1285.0	1086.4	7.0	95.60	12.34	154
	20	0.40	544.0	1719.1	3.0	98.85	13.06	572
	10	0.20	292.0	1990.0	1.6	99.50	14.02	1221
Lewatit MP-68	50	0.98	815.0	2077.7	4.2	97.65	7.83	489
	20	0.40	484.0	3980.0	2.6	99.50	11.62	1514
	10	0.20	316.0	1990.0	1.8	99.50	15.17	1113
Seplite MA 940	50	0.95	1085.0	859.1	5.8	94.50	10.42	148
	20	0.39	336.0	1313.3	1.8	98.50	8.07	749
	10	0.20	99.0	1808.2	0.5	99.45	4.75	3624
Seplite LSC 710	50	0.25	790.0	16.7	4.1	25.00	7.59	4
	20	0.23	366.0	27.1	1.9	57.50	8.79	14
	10	0.15	292.0	31.7	1.6	76.00	14.02	19
Tulsion CH-95	50	0.94	790.0	783.3	4.1	94.00	7.59	191
	20	0.40	276.0	2646.7	1.4	99.25	6.63	1865
	10	0.20	390.0	1990.0	2.3	99.50	18.72	864
Tulsion CH-97	50	0.95	1135.0	859.1	6.1	94.50	10.90	140
	20	0.40	504.0	3980.0	2.8	99.50	12.10	1446
	10	0.20	257.0	1990.0	1.4	99.50	12.34	1414
VP-3Ap made in Russia	50	0.78	1260.0	172.2	6.9	77.50	12.10	25
	20	0.36	474.0	190.5	2.6	90.50	11.38	74
	10	0.19	257.0	275.7	1.4	96.50	12.34	196

The anions in the solution that compete for the binding sites on the functional groups of the sorbents are mercury complexes, namely sulfomercurates ($[Hg(SO_3)_2]^{2-}$, $[Hg(SO_3)_3]^{4-}$, $[Hg(SO_3)_4]^{6-}$) and selenic acid anions (H_2SeO_3 with pK = 2.46 and H_2SeO_4 with pK = –3.0). In acidic solutions (pH < 1), only the strong selenic acid anions SeO_4^{2-} are present, with a molecular volume calculated as $V_m = M/\rho = 144.9/2.95 = 49.1$ cm^3/mol. For sulfomercurates of the specifed composition, the molecular volumes are $V_m = 68.4 \div 98.6$ cm^3/mol. Despite their large molecular volumes in comparison to selenic acid anions, the preferential sorption of sulfomercurates was observed. This can be attributed to their higher negative charge, which ensures a stronger interaction with the functional groups of the ion-exchange resins.

Based on the studies conducted and the calculated separation coefficients, domestic samples AV 17-8 and AM-2B, as well as the foreign samples Seplite MA 940 and Tulsion CH-97, were selected for further investigation of sorption under dynamic conditions. These will be compared with the currently used Lewatit MP-68 resin.

Based on the studies conducted and the calculated separation coefficients, domestic samples AV 17-8 and AM-2B, as well as the foreign samples Seplite MA 940 and Tulsion CH-97, were selected for further investigation of sorption under dynamic conditions. These will be compared with the currently used Lewatit MP-68 resin.

During the saturation of the resin, the concentrations of mercury and selenium in the solutions post-sorption varied. The solutions were analyzed using inductively coupled plasma (ICP) methods on a Shimadzu AA-7000 spectrophotometer (Japan). Figure 1 illustrates the graphical relationship between the mercury concentration in the solution after sorption and the volume of the solution that passed through the resin. The results of the DEC and TDEC calculations are presented in Table 3.

The following conclusions can be drawn from the results of mercury sorption from process solutions in dynamic mode:

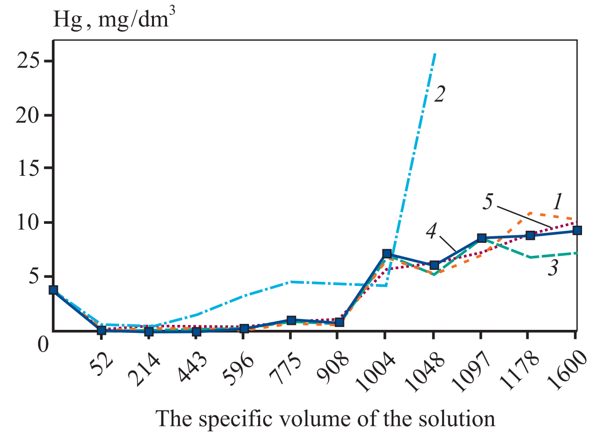

Fig. 1. Mercury concentration in solutions after sorption as a function of the specific volume of the solution passed through the resin

1 – AM-2B; ***2*** – Tulsion CH-97; ***3*** – AV 17-8; ***4*** – Seplite MA 940; ***5*** – Lewatit MP-68

Рис. 1. Концентрация ртути в растворах после сорбции в зависимости от пропущенного удельного объема раствора

1 – АМ-2Б; ***2*** – Tulsion CH-97; ***3*** – АВ 17-8; ***4*** – Seplite MA 940; ***5*** – Lewatit MP-68

1. In terms of the DEC/TDEC values, the resins are ranked in descending order as follows: AV 17-8 ≥ Lewatit MP-68 > AM-2B > Seplite MA 940 >> Tulsion CH-97.

The significant discrepancy between the performance in static mode and the DEC/TDEC for Tulsion CH-97 can likely be attributed to its different functional groups and type of sorbent. It is presumed that in the dynamic mode, the Se macrocomponent displaces the previously sorbed mercury compounds from the resin phase.

2. The resins AV 17-8, Seplite MA 940, and AM-2B display similar dynamic sorption characteristics. Under comparable conditions, a breakthrough in mercury occurs after at least 950 specific volumes of the initial solution have passed through. For comparison, with Lewatit MP-68 resin, mercury breakthrough occurs after

Tabl. 3. **Calculations of DEC/TDEC for mercury**

Таблица 3. Данные расчетов ДОЕ/ПДОЕ по ртути

Name of resin	Sorbed Hg, g	DEC at a breakthrough, mg/cm^3	TDEC, mg/cm^3
AM-2B	0.223	3.4	11.1
Tulsion CH-97	0.029	1.3	1.4
AV 17-8	**0.256**	**3.4**	**12.9**
Lewatit MP-68	0.259	2.6	12.8
Seplite MA 940	0.226	3.2	11.3

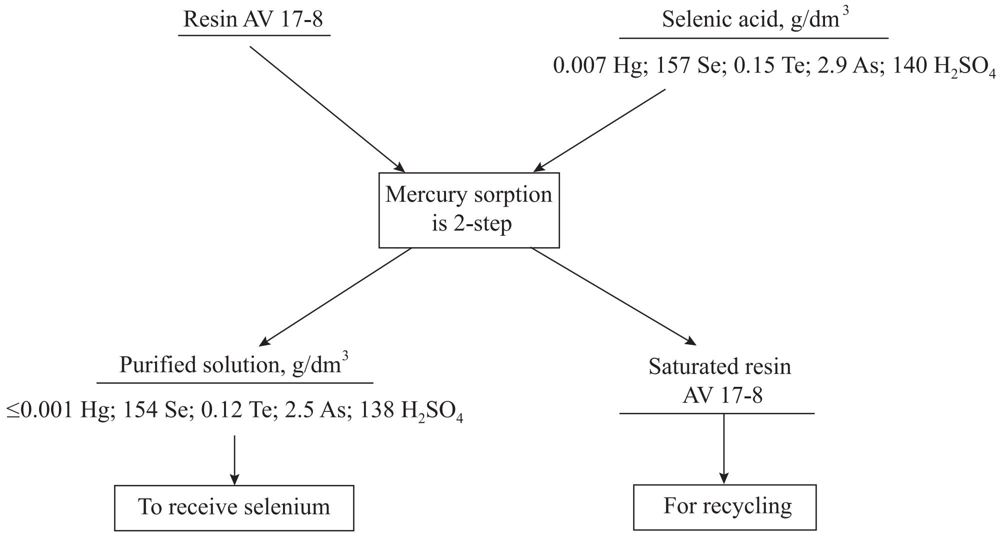

Fig. 2. The basic technological scheme of sorption purification of selenic acid from mercury with resin AV 17-8

Рис. 2. Принципиальная технологическая схема сорбционной очистки смолой АВ 17-8 селенистой кислоты от ртути

no more than 750 specific volumes, indicating that the number of sorption steps in the cascade for solution purification should be increased.

3. Considering the overall ion-exchange properties, it is recommended to use the domestically produced AV 17-8 resin for further tests in an industrial setting to replace Lewatit MP-68 (Germany) in the sorption purification process of selenic acid from mercury. To produce branded selenium, a two-stage sorption process is advisable, as illustrated in Fig. 2. This involves using two columns filled with ionite. If a breakthrough occurs, the first stage is removed for desorption or disposal, the second stage takes its place, and a new column is added to the sequence.

Conclusions

1. To find a replacement for the Lewatit MP-68 ionite currently used for purifying selenic acid solutions from mercury, we reviewed technical literature and selected ionites manufactured in Russia (AM-2B, AN-31, AV 17-8, VP-3Ap), China (Seplite MA 940 and LSC 710), and India (Tulsion CH-95 and CH-97). In the initial static phase, we determined the distribution coefficient (C_d), the degree of elements' extraction (ε), and the static exchange capacity of the resins (SEC, g/dm^3), which led to the selection of the most effective samples: AV 17-8, Seplite MA 940, AM-2B, and Tulsion CH-97, with SEC values of 0.95—0.97 g/dm^3 and a mercury/selenium separation coefficient ($D_{Hg/Se}$) of 1,220—3,620 (for Lewatit MP-68 resin, SEC = 0.98 g/dm^3, $D_{Hg/Se}$ = =1,520).

2. For the resins under study, the following process parameters were established: the volume before a mercury breakthrough, with an initial solution concentration of 4—30 mg/dm^3, was $V_{breakthrough}$ = 750÷950 specific volumes; DEC / TDEC = 2.6÷3.4/11.1÷12.8 mg/cm^3.

Based on the conducted studies, the ionites were ranged according to their mercury sorption performance: AV 17-8 ≥ Lewatit MP-68 > AM-2B >> Seplite MA 940 >> Tulsion CH-97.

3. Considering the comprehensive sorption characteristics determined, the AV 17-8 resin can be recommended as a substitute for the Lewatit MP-68 resin for industrial testing to identify the optimal parameters for purifying selenic acid solutions of mercury.

4. A process flow scheme for purifying industrial selenium solutions of mercury has been developed and implemented into production. It includes two-stage sorption using AV 17-8 ionite with a specific volumetric flow rate of 0.9—1.1 h^{-1}, processing of the saturated resin, and extraction of selenium from the mercury-purified solution.

References

1. Lebed A.B., Naboichenko S.S., Shunin V.A. Production of selenium and tellurium at "Uralelectromed" OJSC. Ekaterinburg: UrFU, 2015. 112 p. (In Russ.).
   Лебедь А.Б., Набойченко С.С., Шунин В.А. Производство селена и теллура на ОАО «Уралэлектромедь». Екатеринбург: УрФУ, 2015. 112 с.
2. Yang S., Li Z., Yan K., Zhang X., Xu Z., Liu W., Liu Z., Liu H. Removing and recycling mercury from scrubbing

solution produced in wet nonferrous metal smelting flue gas purification process. *Journal of Environmental Sciences*. 2021;(103):59—68. https://doi.org/10.1016/j.jes.2020.10.013

3. Fabre E., Rocha A., Cardoso S.P., Brandão P., Vale C. Lopes C.B., Pereira E., Silva C.M. Purification of mercury-contaminated water using new AM-11 and AM-14 microporous silicates. *Separation and Purification Technology*. 2020;(239):116438. https://doi.org/10.1016/j.seppur.2019.116438
4. Ponomarev A.V., Bludenko A.V., Makarov I.E., Pikaev A.K., Kim D.K., Kim Y., Han B. Combined electron-beam and adsorption purification of water from mercury and chromium using materials of vegetable origin as sorbents. *Radiation Physics and Chemistry*. 1997;49(4):473—476. http://dx.doi.org/10.1016/S0969-806X(96)00148-X
5. Zhang B., Petcher S., Gao H., Yan P., Cai D., Fleming G., Parker D.J., Chong S.Y., Hasell T. Magnetic sulfur-doped carbons for mercury adsorption. *Journal of Colloid and Interface Science*. 2021;(603):728—737. https://doi.org/10.1016/j.jcis.2021.06.129
6. Pang X., Liu W., Xu H., Hong Q., Cui P., Huang W., Qu Z., Yan N. Selective uptake of gaseous sulfur trioxide and mercury in ZnO—CuS composite at elevated temperatures from SO_2-rich flue gas. *Chemical Engineering Journal*. 2022;(427):132035. https://doi.org/10.1016/j.cej.2021.132035
7. Xin F., Xiao R., Zhao Y., Zhang J. Surface sulfidation modification of magnetospheres from fly ash for elemental mercury removal from coal combustion flue gas. *Chemical Engineering Journal*. 2022;(436):135212. http://dx.doi.org/10.1016/j.cej.2022.135212
8. Teng H., Altaf A.R. Elemental mercury (Hg^0) emission, hazards, and control: A brief review. *Journal of Hazardous Materials Advances*. 2022;(5):100049. https://doi.org/10.1016/j.hazadv.2022.100049
9. Ji Z., Huang B., Gan M., Fan X., Wang Y., Chen X., Sun Z., Huang X., Zhang D., Fan Y. Recent progress on the clean and sustainable technologies for removing mercury from typical industrial flue gases: A review. *Process Safety and Environmental Protection*. 2021;(150):578—593. https://doi.org/10.1016/j.psep.2021.04.017
10. Jia T., Luo F., Wu J., Chu F., Xiao Y., Liu Q., Pan W., Li F. Nanosized Zn—In spinel-type sulfides loaded on facet-oriented CeO_2 nanorods heterostructures as Z-scheme photocatalysts for efficient elemental mercury removal. *Science of the Total Environment*. 2022;(813):151865. https://doi.org/10.1016/j.scitotenv.2021.151865
11. Meng F., Umair M.M., Iqbal K., Jin X., Zhang S., Tang B. Rapid fabrication of noniridescent structural color coatings with high color visibility, good structural stability, and self-healing properties. *ACS Applied Materials Interfaces*. 2019;11(13):13022—13028. https://doi.org/10.1021/acsami.9b01522
12. Anacleto A.L., Carvalho J.R. Mercury cementation from chloride solutions using iron, zinc and aluminium. *Minerals Engineering*. 1996;9(4):385—397. https://doi.org/10.1016/0892-6875(96)00025-8
13. Gladyshev V.P., Levitskaya S.A., Filippova L.M. Analytical chemistry of mercury. Moscow: Nauka, 1974. 231 p. (In Russ.).
Гладышев В.П., Левицкая С.А., Филиппова Л.М. Аналитическая химия ртути. М.: Наука, 1974. 231 с.
14. Shen F., He S., Li J., Liu C., Xiang K., Liu H. Formation of sulfur oxide groups by SO_2 and their roles in mercury adsorption on carbon-based materials. *Journal of Environmental Sciences*. 2022;(119):44—49. https://doi.org/10.1016/j.jes.2021.11.011
15. Wadi V.S., Mittal H., Fosso-Kankeu E., Jena K.K., Alhassan S.M. Mercury removal by porous sulfur copolymers: Adsorption isotherm and kinetics studies. *Colloids and Surfaces A: Physicochemical and Engineering Aspects*. 2020;(606):125333. http://dx.doi.org/10.1016/j.colsurfa.2020.125333
16. Lennie A.R., Charnock J.M., Pattrick R.A.D. Structure of mercury (II)—sulfur complexes by EXAFS spectroscopic measurements. *Chemical Geology*. 2003;199(3-4):199—207. https://doi:10.1016/S0009-2541(03)00118-9
17. Bell A.M.T., Charnock J.M., Helz G.R., Lennie A.R., Livens F.R., Mosselmas J.F.W., Pattrick R.A.D., Vaughan D.J. Evidence for dissolved polymeric mercury (II)—sulfur complexes. *Chemical Geology*. 2007;243(1-2):122—127. https://doi.org/10.1016/J.CHEMGEO.2007.05.013
18. Al-Jibori S.A., Al-Doori L.A., Al-Janabi A.S.M., Alheety M.A., Wagner C., Karadag A. Mercury (II) mixed ligand complexes of phosphines or amines with 2-cyanoamino thiophenolate ligands formed via monodeprotonation and carbon—sulfur bond cleavage of 2-aminobenzothiazole. *X*-ray crystal structures of $[Hg(SC_6H_4NCN)(PPh_3)]_2$ and $[Hg(SC_6H_4NCN)(Ph_2PCH_2PPh_2)]_2$. *Polyhedron*. 2021;(206):115349. http://dx.doi.org/10.1016/j.poly.2021.115349
19. Shunin V.A., Sokolova I.S., Lebed A.B. Sorption purification of productive selenium solutions from heavy metal impurities. In: *New technologies for the enrichment and complex processing of difficult-to-enrich natural and manmade mineral raw materials (Plaksin readings 2011)*: Abstracts of the reports of the International Meeting (Verkhnyaya Pyshma, 19–24 September 2011). Ekaterinburg: Fort Dialog-Iset, 2011. P. 428–429. (In Russ.).

Шунин В.А., Соколова И.С., Лебедь А.Б. Сорбционная очистка продуктивных селеновых растворов от примесей тяжелых металлов. В сб.: *Новые технологии обогащения и комплексной переработки труднообогатимого природного и техногенного минерального сырья (Плаксинские чтения 2011):* Тезисы докладов международного совещания (Верхняя Пышма, 19—24 сент. 2011 г.). Екатеринбург: Форт Диалог-Исеть, 2011. С. 428—429.

20. Habashi F. Metallurgical plants: How mercury pollution is abated. *Environmental Science and Technology*. 1978; 23(13):1372—1376. https://doi.org/10.1021/ES60148A011
21. Hylander I.D., Herbert R.B. Global emission and production of mercury during the pyrometallurgical extraction of nonferrous sulfide ores. *Environmental Science and Technology*. 2008;42(16):5971—5977. https://doi.org/10.1021/es800495g
22. Yu M-H., Yang H-H., Gu Y-C., Wang B-H., Liu F-C., Lin I.J.B., Lee G-H. Formation of anionic NHC complexes through the reaction of benzimidazoles with mercury chloride. Subsequent protonation and transmetallation reactions. *Journal of Organometallic Chemistry*. 2019;(887):12—17. https://doi.org/10.1016/J.JORGANCHEM.2019.02.015
23. Tugashov K.I., Gribanyov D.A., Dolgushin F.M., Smol'yakov A.F., Peregudov A.S., Klemenkova Z.S., Matvienko O.V., Tikhonova I.A., Shur V.B. Coordination chemistry of anticrowns. Isolation of the chloride complex of the four-mercury anticrown $\{[(o,o'\text{-}C_6F_4C_6F_4Hg)_4]Cl\}^-$ from the reaction of o,o′-dilithiooctafluorobiphenyl with $HgCl_2$ and its transformations to the free anticrown and the complexes with o-xylene, acetonitrile, and acetone. *Organometallics*. 2017;36(13):2437—2445. https://doi.org/10.1021/ACS.ORGANOMET.7B00315
24. Al-Amri A-H.D., Fettouhi M., Wazeer M.I.M., Isab A.A. Synthesis, *X*-ray structure and ^{199}Hg, ^{77}Se CP MAS NMR studies on the first tris(imidazolidine-2-selone) mercury complex: {chloro-tris[N-methyl-2(3H)-imidazolidine-2-selone]mercury(II)}chloride. *Inorganic Chemistry Communications*. 2005;8(12):1109—1112. https://doi.org/10.1016/J.INOCHE.2005.09.010
25. Hadjikakou S.K., Kubicki M. Synthesis, characterisation and study of mercury (II) chloride complexes with triphenylphosphine and heterocyclic thiones. The crystal structures of [(benzothiazole-2-thionato)(benzothiazole-2-thione)(bis-triphenylphosphine) chloro mercury (II)] and [(μ_2-dichloro){(bis-pyrimidine-2-thionato)mercury (II)}{(bis-triphenylphosphine) mercury (II)}] at 100 K. *Polyhedron*. 2000;19(20-21):2231—2236. https://doi.org/10.1016/S0277-5387(00)00533-7
26. Pazderski L., Szlyk E., Wojtczak A., Kozerski L., Sitkowski J., Kamieński B. The crystal and molecular structures of catena[bis(μ_2-chloro)-(μ_2-pyridazine-N,N′)] cadmium (II) and catena[bis(μ_2-chloro)-(μ_2-pyridazine-N,N′)]mercury (II) and the solid-phase ^{13}C, ^{15}N NMR studies of Zn(II), Cd(II), Hg(II) chloride complexes with pyridazine. *Journal of Molecular Structure*. 2004;697(1-3): 143—149. https://doi.org/10.1016/j.molstruc.2004.03.048
27. Korolev A.A., Shunin V.A., Timofeev K.L., Maltsev G.I., Voinkov R.S. Sorption purification of selenic acid solutions from mercury. *Chemistry for Sustainable Development*. 2022;(4):372—382. (In Russ.). http://doi.org/10.15372/CSD2022393
Королев А.А., Шунин В.А., Тимофеев К.Л., Мальцев Г.И., Воинков Р.С. Сорбционная очистка от ртути растворов селенистой кислоты. *Химия в интересах устойчивого развития*. 2022;(30):372—382.

Information about the authors

Yakov D. Zelyakh – Head of the Precious Metals Laboratory of the Research Center of JSC "Uralelectromed".
https://orcid.org/0000-0003-0486-9363
E-mail: zyad@uralcopper.com

Konstantin L. Timofeev – Dr. Sci. (Eng.), Head of the Department of JSC "Uralelectromed"; Associate Professor of the Department of metallurgy of the Technical University of Ural Mining and Metallurgical Conpany.
https://orcid.org/0000-0002-9525-6476
E-mail: K.Timofeev@uralcopper.com

Информация об авторах

Яков Дмитриевич Зелях – начальник лаборатории по драгоценным металлам Исследовательского центра (ИЦ) АО «Уралэлектромедь».
https://orcid.org/0000-0003-0486-9363
E-mail: zyad@uralcopper.com

Константин Леонидович Тимофеев – д.т.н., начальник отдела инженерно-производственного управления (ИПУ) АО «Уралэлектромедь»; научный руководитель кафедры металлургии Технического университета Уральской горно-металлургической компании.
https://orcid.org/0000-0002-9525-6476
E-mail: K.Timofeev@uralcopper.com

Roman S. Voinkov – Cand. (Sci.) Eng., Head of the Research Center of JSC "Uralelectromed".
https://orcid.org/0000-0001-6697-1596
E-mail: R.Voinkov@uralcopper.com

Gennady I. Maltsev – Dr. Sci. (Eng.), Senior Researcher, Chief Specialist of the Research Center of JSC "Uralelectromed".
https://orcid.org/0000-0002-0750-0070
E-mail: mgi@uralcopper.com

Vladimir A. Shunin – Chief Specialist of the Engineering and Production Department of JSC "Uralelectromed".
https://orcid.org/0000-0001-5265-1006
E-mail: V.Shunin@uralcopper.com

Роман Сергеевич Воинков – к.т.н., начальник ИЦ АО «Уралэлектромедь».
https://orcid.org/0000-0001-6697-1596
E-mail: R.Voinkov@uralcopper.com

Геннадий Иванович Мальцев – д.т.н., ст. науч. сотрудник, гл. специалист ИЦ АО «Уралэлектромедь».
https://orcid.org/0000-0002-0750-0070
E-mail: mgi@uralcopper.com

Владимир Александрович Шунин – главный специалист ИПУ АО «Уралэлектромедь».
https://orcid.org/0000-0001-5265-1006
E-mail: V.Shunin@uralcopper.com

Contribution of the authors

Ya.D. Zelyakh – formulated the main concept, prepared and conducted the experiments, performed calculations, analyzed research results, wrote the manuscript, and drew conclusions.

K.L. Timofeev – provided scientific supervision, revised the manuscript, and refined the conclusions.

R.S. Voinkov – supplied resources, formulated the main concept, defined the goals and objectives of the study, wrote the manuscript, and drew conclusions.

G.I. Maltsev – offered scientific supervision, performed calculations, and contributed to manuscript writing.

V.A. Shunin – provided scientific supervision, performed calculations, and contributed to manuscript writing.

Вклад авторов

Я.Д. Зелях – формирование основной концепции, подготовка экспериментов, проведение экспериментов, проведение расчетов, анализ результатов исследований, подготовка текста статьи, формулировка выводов.

К.Л. Тимофеев – научное руководство, корректировка текста статьи, корректировка выводов.

Р.С. Воинков – обеспечение ресурсами, формирование основной концепции, постановка цели и задачи исследования, подготовка текста статьи, формулировка выводов.

Г.И. Мальцев – научное руководство, проведение расчетов, подготовка текста статьи.

В.А. Шунин – научное руководство, проведение расчетов, подготовка текста статьи.

The article was submitted 1.12.2023, revised 26.01.2024, accepted for publication 02.02.2024

Статья поступила в редакцию 11.12.2023, доработана 26.01.2024, подписана в печать 02.02.2024

METALLURGY OF RARE AND PRECIOUS METALS / МЕТАЛЛУРГИЯ РЕДКИХ И БЛАГОРОДНЫХ МЕТАЛЛОВ

UDC 546.66.546.831.4 : 54.31
https://doi.org/10.17073/0021-3438-2024-1-14-23

Research article
Научная статья

Heterophase synthesis of rare-earth zirconates

E.E. Nikishina, N.V. Grechishnikov, D.V. Drobot

M.V. Lomonosov Institute of Fine Chemical Technologies of MIREA – Russian Technological University
86 Vernadskiy Prosp., Moscow 119571, Russia

✉ Elena E. Nikishina (nikishina@mirea.ru)

Abstract: This study focuses on developing a heterophase process for synthesizing rare-earth zirconates, specifically $R_2Zr_2O_7/R_2O_3{\cdot}2ZrO_2$ (R = La, Sm, Gd, Dy). We investigated the sorption properties of low-hydrated zirconium hydroxide, a precursor for complex-oxide phases, towards rare-earth elements' ions (La, Sm, Gd, Dy). The results indicate that sorption by low-hydrated zirconium hydroxide is a multifaceted process, involving the incorporation of rare-earth cations into the pores of low-hydrated hydroxide and ion exchange. The paper details the synthesis of $R_2Zr_2O_7/R_2O_3{\cdot}2ZrO_2$ (R = La, Sm, Gd, Dy), considering both “light” and “heavy” elements. The process involves the interaction between $Zr(OH)_{3\div1}O_{0.5\div1.5}{\cdot}(1.6\div2.6)H_2O$, low-hydrated zirconium hydroxide, and an aqueous solution of rare-earth acetate ($C(La^{3+}) = 0.155$ mol/L, $C(Sm^{3+}) = 0.136$ mol/L, $C(Gd^{3+}) = 0.141$ mol/L, $C(Dy^{3+}) =$ $= 0.120$ mol/L) followed by heat treatment. The resulting phases and their thermolysis products were analyzed using differential thermal analysis and *X*-ray phase analysis. Single-phase rare-earth zirconates $R_2Zr_2O_7$ (R = La, Sm, Gd) and the $Dy_2O_3{\cdot}2ZrO_2$ solid solution were only obtained at 800 °C. The lattice parameters are calculated for each phase. Lanthanum, samarium, and gadolinium zirconates exibited a cubic pyrochlore structure ($Fd\bar{3}m$), while dysprosium displayed a fluorite structure ($Fm\bar{3}m$). The average particle size of all zirconates was 1.14 ± 0.02 μm.

Key words: zirconium, lanthanum, samarium, gadolinium, dysprosium, zirconate, oxide, low-hydrated hydroxide, sorption properties, heterophase synthesis.

Acknowledgments: This work was performed using the equipment of the Center for Collective Use RTU MIREA and supported by the Ministry of Science and Higher Education of the Russian Federation within the framework of agreement No. 075-15-2021-689 dated 01.09.2021

The authors express their gratitude to E.N. Lebedeva and A.I. Lvovsky for assistance during research.

For citation: Nikishina E.E., Grechishnikov N.V., Drobot D.V. Heterophase synthesis of rare-earth zirconates. *Izvestiya. Non-Ferrous Metallurgy*. 2024;30(1):14–23. https://doi.org/10.17073/0021-3438-2024-1-14-23

Гетерофазный синтез цирконатов редкоземельных элементов

Е.Е. Никишина, Н.В. Гречишников, Д.В. Дробот

Институт тонких химических технологий им. М.В. Ломоносова
МИРЭА – Российского технологического университета
Россия, 119571, г. Москва, пр-т Вернадского, 86

✉ Елена Евгеньевна Никишина (nikishina@mirea.ru)

Аннотация: Представлены результаты разработки гетерофазного метода синтеза цирконатов редкоземельных элементов (РЗЭ) состава $R_2Zr_2O_7/R_2O_3{\cdot}2ZrO_2$ (R = La, Sm, Gd, Dy). Предварительно изучены сорбционные свойства маловодного гидроксида циркония (предшественника для получения сложнооксидных фаз) по отношению к ионам редкоземельных элементов (La, Sm, Gd, Dy). Результаты исследований показали, что сорбция маловодным гидроксидом циркония является сложным процессом, включающим вхождение катионов РЗЭ в поры маловодного гидроксида и ионный обмен. Проведен синтез цирконатов РЗЭ состава $R_2Zr_2O_7$ /$R_2O_3 \cdot 2ZrO_2$ (R = La, Sm, Gd, Dy; выбор РЗЭ определялся вовлечением в рассмотрение «легких» и «тяжелых» элементов). Он заключался во взаимодействии маловодного гидроксида циркония $Zr(OH)_{3÷1}O_{0,5÷1,5} \cdot (1,6÷2,6)H_2O$ с водным раствором ацетата РЗЭ ($C(La^{3+})$ = 0,155 моль/л, $C(Sm^{3+})$ = 0,136 моль/л, $C(Gd^{3+})$ = 0,141 моль/л, $C(Dy^{3+})$ = 0,120 моль/л) и последующей термической обработке. Методами дифференциально-термического и рентгенофазового анализов охарактеризованы синтезированные фазы и продукты их термолиза. Только при температуре 800 °С удалось получить однофазные цирконаты РЗЭ состава $R_2Zr_2O_7$ (R = La, Sm, Gd) и твердый раствор $Dy_2O_3 \cdot 2ZrO_2$. Для каждой фазы рассчитаны параметры решетки. Цирконаты лантана, самария и гадолиния имеют кубическую структуру пирохлора ($Fd\overline{3}m$), а диспрозия – структуру флюорита ($Fm\overline{3}m$). Средний размер частиц у всех цирконатов составляет 1,14 ± 0,02 мкм.

Ключевые слова: цирконий, лантан, самарий, гадолиний, диспрозий, цирконат, оксид, маловодный гидроксид, сорбционные свойства, гетерофазный синтез.

Благодарности: Работа выполнена с использованием оборудования Центра коллективного пользования РТУ МИРЭА при поддержке Минобрнауки Российской Федерации в рамках соглашения № 075-15-2021-689 от 01.09.2021 г.

Авторы выражают благодарность Е.Н. Лебедевой и А.И. Львовскому за оказанную помощь при проведении исследований.

Для цитирования: Никишина Е.Е., Гречишников Н.В., Дробот Д.В. Гетерофазный синтез цирконатов редкоземельных элементов. *Известия вузов. Цветная металлургия.* 2024;30(1):14–23.
https://doi.org/10.17073/0021-3438-2024-1-14-23

Introduction

$R_2Zr_2O_7$ rare-earth zirconates find extensive applications as thermal barrier coatings, catalysts, sensors, oxygen-ion conducting solid electrolytes, and matrices for the immobilization of radioactive waste [1—10]. These compositions possess unique physical and chemical properties, including a high melting point, absence of phase transitions over a wide temperature range, high coefficient of thermal expansion, and low thermal conductivity. Additionally, they demonstrate dielectric, piezo- or ferroelectric, fluorescent, and phosphorescent properties, along with chemical and radiation resistance, and a high capacity for radionuclide absorption [1; 4; 10—12].

The primary space groups for $R_2Zr_2O_7$ rare-earth zirconates are cubic pyrochlore ($Fd\overline{3}m$) and defective fluorite ($Fm\overline{3}m$) (Fig. 1) [2].

If the ratio of cation radii $r(R^{3+})/r(Zr^{4+})$ is less than 1.46, the resulting substance is classified under a defective fluorite space group; otherwise, it falls into a pyrochlore space group [9]. Based on the cation radii, La—Gd zirconates exhibit a pyrochlore space group, whereas Tb—Lu zirconates belong to a defective fluorite space group. The coordination number of zirconium ranges from 4 to 6. Additionally, a decrease in the cation radius ratio corresponds to an increase in disorder. To achieve a more ordered structure, one could replace the rare-earth element cation with a larger-radius cation or replace the zirconium cation with a smaller-radius cation. [9; 13—15].

The phase diagrams reveal that within the La_2O_3—ZrO_2 systems, $La_2Zr_2O_7$ present, maintaining a pyrochlore space group up to the melting point. In the case of Sm_2O_3—ZrO_2, $Sm_2Zr_2O_7$ exhibits a pyrochlore space group up to 2080 °C, transitioning to a defective fluorite space group above this temperature. Within the Gd_2O_3—ZrO_2 system, $Gd_2Zr_2O_7$ solidifies with a pyrochlore structure below 1550 °C, subsequently transforming into a disordered fluorite structure (F-$Gd_2Zr_2O_7$). Notavly, the Gd_2O_3—ZrO_2 system encompasses a broad region featuring the $R_2O_3 \cdot 2ZrO_2$ homogeneous solid solution with a fluorite crystal structure [15—19].

Other researchers have outlined various processes for the preparation of $R_2Zr_2O_7$ rare-earth zirconates [1; 4; 12; 14; 15; 20—26]. Notably, papers [4; 20; 21] detail the solid-phase reparation of rare-earth zirconates through the mechanical mixing of zirconium and rare-earth element oxides, followed by calcination at high temperatures (exceeding 1100 °C). However, this process is notably time-consuming. To expedite solid-phase reactions, mechanochemical synthesis offers two approaches:

1. Mechanochemical synthesis involves the direct formation of the compound through the mechanical processing of reactants in an activator mill.
2. A two-stage process incorporates mechanical activation of the initial mixture, followed by subsequent heat treatment [14; 19].

In the co-precipitation method, hydroxides are simultaneously precipitated from precursor solutions, and the resulting sediments are subsequently calcinated to obtain $R_2Zr_2O_7$ [4; 23; 24]. A known process for producing $R_2Zr_2O_7$ rare-earth zirconates (R = Gd, Tb,

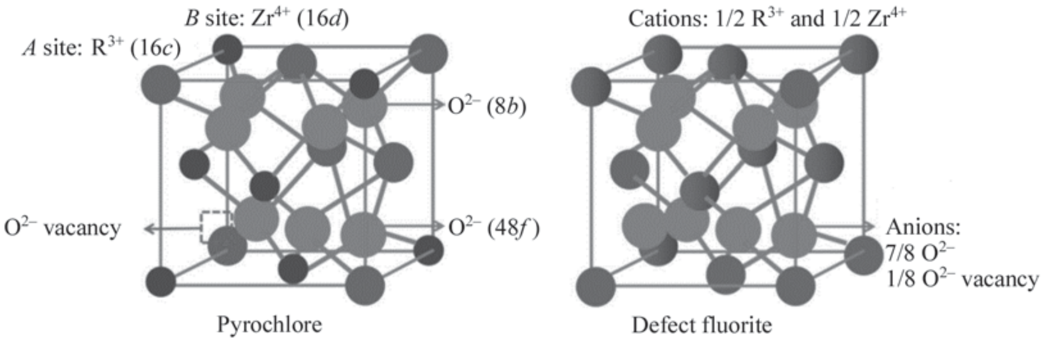

Fig. 1. Crystal structures of $R_2Zr_2O_7$ rare-earth zirconates [2]

Рис. 1. Структуры цирконатов редкоземельных элементов $R_2Zr_2O_7$ [2]

Dy) through co-precipitation involves using rare-earth nitrate and zirconium oxychloride as starting materials. These are mixed and treated with an aqueous ammonia solution. The zirconate powders are obtained by calcination of the washed and dried sediment at temperatures ranging from 1000 to 1500 °C for 3 to 6 h in the presence of air [24].

However, a disadvantage of this method is that the co-precipitation product forms a gel, making it challenging to remove impurities through washing. Consequently, the resulting gel contains a significant amount of wash water.

In the hydrothermal process, the complex oxide phase precipitates from solutions in an autoclave, forming through nucleation and growth at specific temperatures and pressures. This method is convenient, straightforward, and easily controllable. Water serves as the solvent, offering affordability and wide availability [4; 12].

The sol-gel method involves thermally treating gels derived from the hydrolysis and subsequent polycondensation of initial metal alcoholates [4; 12; 22; 25; 26].

It's worth noting that in all the mentioned processes, the initial reagents consist of oxides, salts, or complex compounds of zirconium.

The objective of this study is to establish a heterophase method for synthesizing $R_2Zr_2O_7/R_2O_3{\cdot}2ZrO_2$ (R = La, Sm, Gd, Dy) rare-earth zirconates using low-hydrated zirconium hydroxide (referred to as "low-hydrated hydroxide" or LHH) as the precursor. This approach aims to lower the synthesis temperature while achieving the production of single-phase complex oxides.

Materials and methods

We used zirconium oxochloride (reagent-grade, TU 6-09-3677-74 Spec., Reakhim, Moscow) and an aqueous ammonia solution (ASC, GOST 24147-80, Khimmed, Moscow) in this study. Acetates of rare-earth elements (lanthanum, dysprosium, samarium, gadolinium) were obtained by dissolving the oxide precursors (La_2O_3 — reagent-grade, TU 48-4-523-90 Spec.; Dy_2O_3 (reagent-grade) — TU 48-4-524-90 Spec.; Sm_2O_3 (reagent-grade) — TU 48-4-523-89 Spec.; Gd_2O_3 (reagent-grade), TU 48-4-200-72 Spec.) from Lankhit, Moscow, in glacial acetic acid (ASC grade, GOST 61-75, Khimmed). The resulting solution was solidified, filtered, and air-dried to obtain crystallohydrates, such as $La(CH_3COO)_3{\cdot}1.6H_2O$, $Gd(CH_3COO)_3{\cdot}4.2H_2O$, $La(CH_3COO)_3{\cdot}1.8H_2O$, $Dy(CH_3COO)_3{\cdot}4.1H_2O$. Acetate salts were chosen for their water solubility and the ease with which volatile products (CO and CO_2) could be removed from the substance.

The zirconium dioxide content in the low-hydrated hydroxide was determined by calcination at 800 to 900 °C to form ZrO_2.

The chloride ion content in LHH was assessed using argentometry (the Folgard method).

To evaluate the sorption capacity of low-hydrated zirconium hydroxide under static conditions at room temperature, we employed aqueous solutions of rare-earth acetates.

The procedure involved adding 8.0 mL of aqueous solutions of rare-earth element acetates with varying concentrations (ranging from 0.044 to 0.155 mol/L) to 0.4 g of LHH samples. The filled tubes underwent shaking on an AVU-6S shaker for durations spanning from 20 to 160 min, with 10-minute pauses. Following settling, samples were extracted from the solutions to determine the concentrations of rare-earth elements.

For assessing the concentrations of rare-earth elements in the initial acetous solutions, determining the residual concentrations of rare-earth elements in the mother solutions, and investigating the sorption capacity of low-hydrated zirconium hydroxide, we employed direct titration with Trilon B solution (0.05 mol/L). Xylenol orange indicator (0.1 % solution) was utilized, and titration proceeded until the wine-red color of the solution transitioned to yellow.

The absorption degree (α, %) of rare-earth element cations by the solid phase of low-hydrated zirconium hydroxide was calculated using the following formulas:

$$\alpha = \Delta / C_{\text{init}}, \tag{1}$$

$$\Delta = C_{\text{init}} - C_{\text{aft//sorp.}}, \tag{2}$$

where C_{init} is the initial concentration of the rare-earth element solution before sorption, mol/L; $C_{\text{aft//sorp.}}$ is the concentration of the rare-earth element solution after sorption, mol/L.

The sorption capacity (G, mmol/g) for low-hydrated zirconium hydroxide is determined by:

$$G = \Delta \cdot V / m, \tag{3}$$

where V is the volume of the solution, mL; m is the sorbent weight, g.

We conducted differential thermal analysis (DTA) in the 20—1000 °C temperature range with a heating rate of 10 °C/min (±5 °C error) using a Q-1500 D derivatograph (F. Paulik, J. Paulik, L. Erdey; MOM, Hungary) and a platinum-rhodium (type S) thermocouple.

X-ray diffraction (XRD) was employed to identify final and intermediate products with a Rigaku D/max-C X-ray diffractometer (CuK_α radiation, Ni filter, Si monochromator) in the $10° \le 2\theta \le 80°$ angle range, with a 0.02° scanning step.

Powder granulometry was determined using the DelsaNano laser particle analyzer (Beckman Coulter Inc., USA) applying dynamic light scattering to estimate particle size distribution in the 0.6 nm to 10 μm range.

Results and discussion

The low-hydrated $Zr(OH)_{3÷1}O_{0,5÷1.5} \cdot (1.6÷2.6)H_2O$ was synthesized through heterophase interaction between zirconium oxychloride and a 6.0 mol/L aqueous solution of ammonia hydrate. Detailed information on the method, as well as the physical and chemical properties of zirconium LHH and its thermolysis products, can be found in [27; 28].

Upon filtration and air drying, we obtained a well-filtered, crumbly white powder with a low content of chloride ion impurities (less than 0.05 %). The zirconium dioxide content in the low-hydrated hydroxide is 68.8 ± 0.1 wt.%, and the average particle size of zirconium LHH is 2.2 μm.

Our DTA and XRD studies of the low-hydrated zirconium hydroxide thermolysis indicated that the LLH is an X-ray amorphous phase. The dehydration process halts at $t = 400 \pm 5$ °C, resulting in the formation of monoclinic zirconium dioxide ($a = 0.514 \pm 0.001$ nm, $b = 0.521 \pm 0.002$ nm, $c = 0.531 \pm 0.001$ nm, $\beta = 99.10 \pm$ $\pm\, 0.01°$). Most particles have a size of 2.0—4.0 μm, with an average particle size of 2.8 μm.

We proposed a thermal decomposition process for low-hydrated zirconium hydroxide as follows:

$$Zr(OH)_{3÷1}O_{0.5÷1.5}(1.6 ÷ 2.6)H_2O \xrightarrow[-H_2O]{200\pm5\ °C} \xrightarrow[-H_2O]{200\pm5\ °C} ZrO_2(0.1 ÷ 0.2)H_2O \xrightarrow{400\pm5\ °C} ZrO_2. \tag{4}$$

The low-hydrated zirconium hydroxide, classified as oxyhydrates, exhibits the presence of hydroxo- and aqua groups alongside oxo groups, all of which can serve as sorption sites. Our investigations have identified macro-, nano-, and ultra nanopores in the zirconium LHH samples, rendering this class of compounds suitable for application as a sorbent in the synthesis of complex oxide phases [27; 28].

In an effort to exploit the sorption properties of low-hydrated zirconium hydroxide for intensifying the formation of rare-earth element zirconates, we aimed to obtain a suitable intermediate product during the sorption stage. This approach ultimately lowers the synthesis temperature and facilitates the creation of a single-phase product. To achieve this, we studied the sorption of rare-earth cations by low-hydrated zirconium hydroxide under static conditions at room temperature. Adopting a volume ratio of the aqueous solution of rare-earth element acetate to the zirconium LHH sample as S : L = = 1 : 20, the latter demonstrated robust sorption of R^{3+} cations (R = La, Sm, Gd, Dy) from acetate solutions. Saturation was observed within 30—40 min. Consequently, 40 min of phase contact during the rare-earth zirconate synthesis was considered sufficient to achieve equilibrium in this specific system at the defined S : L ratio. The table below outlines the properties of rare-earth element sorption by low-hydrated zirconium hydroxide.

The rare-earth cations in the aqueous solution exist in the form of hydrates: $R(H_2O)_n]^{3+}$ ($n = 9.0$ for La^{3+}, 8.94 for Sm^{3+}, 8.27 for Gd^{3+}, 8.01 for Dy^{3+}) [29; 30]. We observed no correlation between the size of the rare-earth cation and its sorption capacity. The interaction between rare-earth element hydrates and low-hydrated zirconium hydroxide occurs primarily through cation exchange. The rare-earth cations are bound to the hydroxo- and aqua groups in the LHH, leading to the release of H_3O^+ hydroxonium ions into the solution. This interaction is further confirmed by the acidification of the initial solution, resulting in a change in pH from 6 to 5. Sorption by oxyhydrates represents a complex process involving both ion exchange and the entry of cations into the pores.

The heterophase synthesis of rare-earth zirconates was conducted using amorphous low-hydrated zirconium hydroxide containing 68.8 ± 0.1 wt.% of ZrO_2 zirconium dioxide and aqueous solutions of acetates of lanthanum, samarium, gadolinium, and dysprosium ($C(La^{3+}) = 0.155$ mol/L, $C(Sm^{3+}) = 0.136$ mol/L, $C(Gd^{3+}) = 0.141$ mol/L, $C(Dy^{3+}) = 0.120$ mol/L). The S : L ratio was maintained at 1 : (36÷46). Adequate amounts of acetate solutions were used to achieve the required $R_2O_3 : ZrO_2$ molar ratio. The synthesis procedure for rare-earth element zirconates involved adding an acetate solution of the respective rare-earth element to zirconium LHH and stirring the mixture on a shaker at room temperature for 1—2 h. The resulting suspension was then evaporated to dryness for 24 h at $t = 120$ °C.

Subsequently, a stepwise heat treatment was carried out in the 600—900 °C temperature range with a 100 °C increment. Each step lasted for 2 h. The choice of 600 °C as the initial temperature was based on the differential thermal analysis results, where at this temperature and higher, no observable effects were noted, and the sample weight remained constant. Fig. 2 illustrates the results of the thermal analysis of the intermediate product obtained through the interaction of low-hydrated zirconi-

Sorption of R^{3+} (R = La, Sm, Gd, Dy) by low-hydrated zirconium hydroxide, 68.8 ± 0.1 wt.% ZrO_2 content, 40 min phase contact period

Сорбция R^{3+} (R = La, Sm, Gd, Dy) маловодным гидроксидом циркония при содержании ZrO_2 68,8 ± 0,1 мас.% и продолжительности контактирования фаз 40 мин

Concentration of the $R(CH_3COO)_2$ solution, mol/L		Concentration change after sorption Δ, mol/L	Efficiency of Zr sorption by LHH, %	Sorption capacity *G*, mmol/g
Initial C_{init}	After sorption $C_{aft/sorp}$			
		R = La^{3+}		
0.053	0.045	0.008	15.1	0.16
0.102	0.072	0.030	29.4	0.60
0.155	0.110	0.045	29.0	0.90
		R = Sm^{3+}		
0.044	0.038	0.006	13.6	0.12
0.100	0.073	0.027	27.0	0.54
0.136	0.100	0.036	26.5	0.72
		R = Gd^{3+}		
0.060	0.049	0.011	18.3	0.22
0.103	0.071	0.032	31.1	0.64
0.141	0.096	0.045	31.9	0.90
		R = Dy^{3+}		
0.055	0.045	0.010	18.2	0.20
0.105	0.075	0.030	28.6	0.60
0.120	0.086	0.034	28.3	0.68

um hydroxide with an aqueous solution of dysprosium acetate, followed by the evaporation of the resulting mixture.

The DTA curve reveals two endothermic and two exothermic effects. The first endothermic effect (80—260 °C) corresponds to dehydration. The thermal effects observed in the 310—405 °C range are attributed to the decomposition of the organic component, accompanied by the release of CO and CO_2. The exothermic effect at 500—550 °C can be associated with the formation of the final substance. This is substantiated by the absence of an exothermic effect on the DTA curve at $t = 400 \pm 5$ °C, indicating the solidification of zirconium dioxide.

The stepwise heat treatment produced finely dispersed powders, which were subjected to XRD analysis. It was observed that the formation of $R_2Zr_2O_7$ / $R_2O_3{\cdot}2ZrO_2$ (R = La, Sm, Gd, Dy) commenced at $t = 600$ °C. However, the samples were not single-phase at this stage; they contained not only zirconate but also unreacted oxides of zirconium and the rare-earth element. In Fig. 3, the XRD pattern of lanthanum zirconate obtained at 600 °C for 2 h is presented. Apart from the $La_2Zr_2O_7$ peaks, the XRD pattern exhibits peaks corresponding to zirconium dioxide and lanthanum hydroxide.

Single-phase products were successfully obtained at 800 °C. Using this method, $R_2Zr_2O_7$ (R = La, Sm, Gd) rare-earth zirconates and the $Dy_2O_3{\cdot}2ZrO_2$ solid solution were synthesized. Lanthanum, samarium, and gadolinium zirconates belong to the cubic pyrochlore ($Fd\bar{3}m$) space group:

$$La_2Zr_2O_7\text{:}\quad a = 10.85 \pm 0.01\ \text{Å},$$

$$Sm_2Zr_2O_7\text{:}\quad a = 10.59 \pm 0.02\ \text{Å},$$

$$Gd_2Zr_2O_7\text{:}\quad a = 10.50 \pm 0.01\ \text{Å},$$

while dysprosium zirconate belongs to the fluorite space group ($Fm\bar{3}m$), with a = 5.212 ± 0.002 Å.

Figure 4 displays the XRD patterns of $Sm_2Zr_2O_7$ and the $Dy_2O_3{\cdot}2ZrO_2$ solid solution.

Figure 5 illustrates the particle size distribution of the synthesized zirconates. In all samples, a distinct peak is evident on the curves, indicating the maximum content of powder particles in the range of 0.8—1.8 μm. The average particle size for all zirconates is approximately the same, with differences in hundredths of microns, μm: $La_2Zr_2O_7$ — 1.12, $Sm_2Zr_2O_7$ — 1.10, $Gd_2Zr_2O_7$ — 1.18, $Dy_2O_3{\cdot}2ZrO_2$ — 1.12.

The disparity in particle sizes observed between the synthesized zirconates and low-hydrated zirconium hydroxide can be attributed to the agglomeration of zirconium LHH particles..

Through these investigations, we successfully deve-

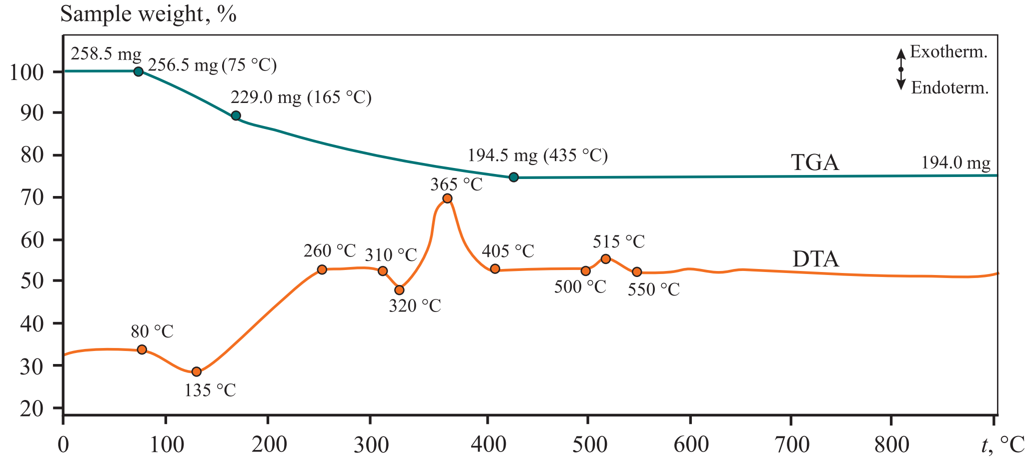

Fig. 2. Thermal analysis curves for the sample obtained by interacting low-hydrated zirconium hydroxide (68.8 ± 0.1 wt.% ZrO_2) with an aqueous solution of dysprosium acetate ($C(Dy^{3+}) = 0.120$ mol/L) followed by evaporation at $t = 120$ °C

TGA – weight change curve; DTA – differential thermal analysis curve

Рис. 2. Кривые термического анализа образца, полученного при взаимодействии маловодного гидроксида циркония (68,8±0,1 мас.% ZrO_2) с водным раствором ацетата диспрозия ($C(Dy^{3+}) = 0{,}120$ моль/л) и последующем выпаривании полученной смеси при $t = 120$ °C

ТГ – кривая изменения массы; ДТА – дифференциальная кривая нагревания

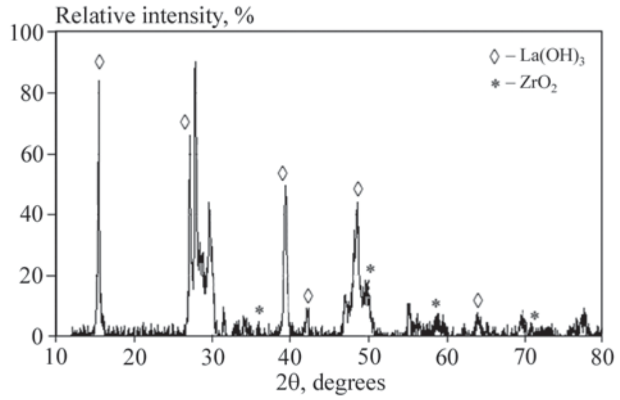

Fig. 3. XRD pattern of $La_2Zr_2O_7$ obtained at $t = 600$ °C, $\tau = 2$ h

Рис. 3. Дифрактограмма цирконата лантана $La_2Zr_2O_7$, полученного при $t = 600$ °C, $\tau = 2$ ч

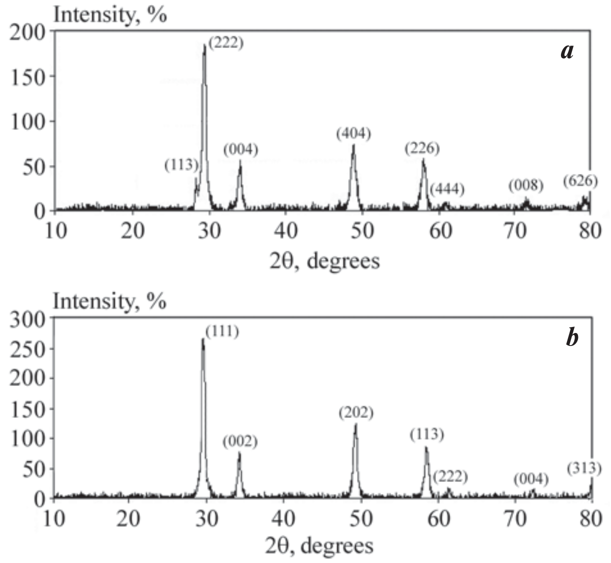

Fig. 4. XRD patterns of $Sm_2Zr_2O_7$ (***a***) and $Dy_2O_3 \cdot 2ZrO_2$ (***b***) obtained at $t = 800$ °C, $\tau = 6$ h

Рис. 4. Дифрактограммы цирконатов $Sm_2Zr_2O_7$ (***a***) и $Dy_2O_3 \cdot 2ZrO_2$ (***b***), полученных при $t = 800$ °C, $\tau = 6$ ч

loped a heterophase process for synthesizing the $R_2Zr_2O_7$ (R = La, Sm, Gd) and $Dy_2O_3 \cdot 2ZrO_2$ complex oxide phases. The use of low-hydrated zirconium hydroxide as a precursor proved effective in lowering the synthesis temperature and achieving single-phase products.

Conclusions

1. The low-hydrated zirconium hydroxide with a composition of $Zr(OH)_{3 \div 1}O_{0,5 \div 1.5} \cdot (1.6 \div 2.6)H_2O$ was produced through a heterophase process, yielding a dioxide content of 68.8 ± 0.1 wt.%.

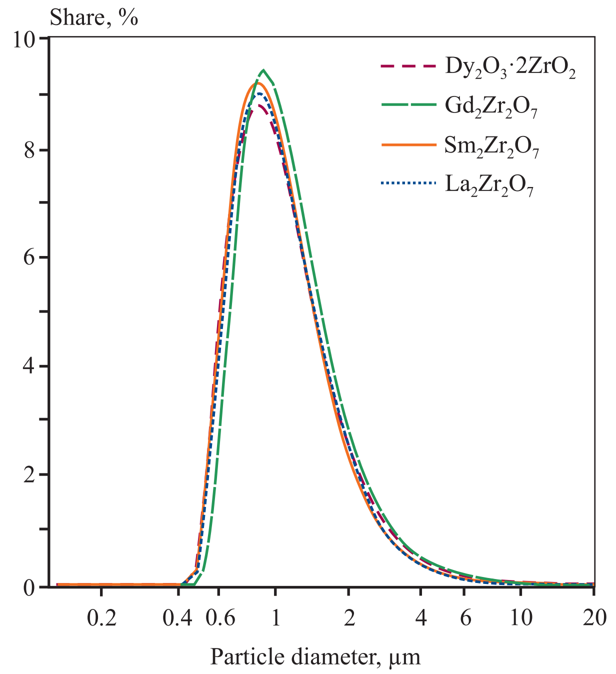

Fig. 5. Particle size distribution in $R_2Zr_2O_7$ (R = La, Sm, Gd) and $Dy_2O_3 \cdot 2ZrO_2$

Рис. 5. Распределение частиц синтезированных цирконатов состава $R_2Zr_2O_7$ (R = La, Sm, Gd) и $Dy_2O_3 \cdot 2ZrO_2$ по размеру

2. The sorption capacity of zirconium LHHs for rare-earth element cations (La, Sm, Gd, Dy) was investigated. The results revealed that sorption by low-hydrated zirconium hydroxide is a multifaceted process, involving the incorporation of rare-earth cations into the pores of low-hydrated hydroxide and ion exchange.

3. Heterophase synthesis experiments were conducted to obtain $R_2Zr_2O_7$ (R = La, Sm, Gd) and $Dy_2O_3 \cdot 2ZrO_2$ rare-earth zirconates, employing low-hydrated zirconium hydroxide and aqueous solutions of rare-earth element acetates as precursors.

4. XRD analysis demonstrated that the $R_2Zr_2O_7$ (R = La, Sm, Gd) single-phase rare-earth zirconates and the $Dy_2O_3 \cdot 2ZrO_2$ solid solution form at 800 °C. Their lattice parameters were estimated through this analysis.

References

1. Jing Zhang, Xingye Guo, Yeon-Gil Jung, Li Li, James Knapp. Lanthanum zirconate based thermal barrier coatings: A review. *Surface and Coatings Technology*. 2017;323:18—29. https://doi.org/10.1016/j.surfcoat.2016.10.019

2. Debao Liu, Baolu Shi, Liyan Geng, Yiguang Wang, Baosheng Xu, Yanfei Chen. High-entropy rare-earth zirconate ceramics with low thermal conductivity for advanced thermal-barrier coatings. *Journal of Advanced Ceramics.* 2022;11(6):961—973. https://doi.org/10.1007/s40145-022-0589-z
3. He-juan Song, Li-qun Zhou, Ying Huang, Ling Li, Ting Wang, Lan Yang. Synthesis, characterization and luminescent properties of $La_2Zr_2O_7 : Eu^{3+}$ nanorods. *Chinese Journal of Chemical Physics.* 2013;26:83—87. https://doi.org/10.1063/1674-0068/26/01/83-87
4. Zinatloo-Ajabshir S., Salavati-Niasari M., Sobhani A., Zinatloo-Ajabshir Z. Rare earth zirconate nanostructures: Recent development on preparation and photocatalytic applications. *Journal of Alloys and Compounds.* 2018;767:1164—1185. https://doi.org/10.1016/j.jallcom.2018.07.198
5. Solomon S., George A., Thomas J.K., John A. Preparation, characterization, and ionic transport properties of nanoscale $Ln_2Zr_2O_7$ (Ln = Ce, Pr, Nd, Sm, Gd, Dy, Er, and Yb) energy materials. *Journal of Electronic Materials.* 2015;44:28—37. https://doi.org/10.1007/s11664-014-3473-y
6. Koho Yang, Jung-Hsiung Shen, Kai-Yun Yang, I.-Ming Hung, Kuan-Zong Fung, Moo-Chin Wang. Formation of $La_2Zr_2O_7$ or $SrZrO_3$ on cathode-supported solid oxide fuel cells. *Journal of Power Sources.* 2006;159:63—67. https://doi.org/10.1016/j.jpowsour.2006.04.049
7. Chunjie Wang, Yue Wang, Xizhi Fan, Wenzhi Huang, Binglin Zou, Xueqiang Cao. Preparation and thermophysical properties of $La_2(Zr_{0.7}Ce_{0.3})_2O_7$ ceramic via sol-gel process. *Surface and Coatings Technology.* 2012;212:88—93. https://doi.org/10.1016/j.surfcoat.2012.09.026
8. Stefanovsky S.V., Yudintsev S.V. Titanates, zirconates, aluminates and ferrites as waste forms for actinide immobilization. *Russian Chemical Reviews.* 2016;85(9): 962—994. (In Russ). https://doi.org/10.1070/rcr4606
Стефановский С.В., Юдинцев С.В. Титанаты, цирконаты, алюминаты и ферриты как матрицы для иммобилизации актинидов. *Успехи химии.* 2016;85(9):962—994.
9. Rejith R.S., Thomas J.K., Solomon S. Structural, optical and impedance spectroscopic characterizations of $RE_2Zr_2O_7$ (RE = La, Y) ceramics. *Solid State Ionics.* 2018;323:112—122. https://doi.org/10.1016/j.ssi.2018.05.025
10. Rejith R.S., Thomas J.K., Solomon S. Order-disorder transformation and its effect on the properties of $(\text{Lanthanide})_2Zr_{1.5}Hf_{0.5}O_7$ functional nanoceramics. *Materials Research Bulletin.* 2019;115:1—11. https://doi.org/10.1016/j.materresbull.2019.03.010
11. Fergus J.W. Zirconia and pyrochlore oxides for thermal barrier coatings in gas turbine engines. *Metallurgical and Materials Transactions E.* 2014;1:118—131. https://doi.org/10.1007/s40553-014-0012-y
12. Sankar J., Kumar S.S. Synthesis of rare earth based pyrochlore structured ($A_2B_2O_7$) materials for thermal barrier coatings (TBCs) — A review. *Current Applied Science and Technology.* 2021;21(3):601—617. https://doi.org/10.14456/cast.2021.47
13. Yamamura H., Nishino H., Kakinuma K. Relationship between oxide-ion conductivity and dielectric relaxation in the $Ln_2Zr_2O_7$ system having pyrochore-type compositions (Ln = Yb, Y, Gd, Eu, Sm, Nd, La). *Journal of Physics and Chemistry of Solids.* 2008;69:1711—1717. https://doi.org/10.1016/j.jpcs.2007.12.015
14. Fuentes A.F., Montemayor S.M., Maczka M., Lang M., Ewing R.C., Amador U. A critical review of existing criteria for the prediction of pyrochlore formation and stability. *Inorganic Chemistry.* 2018;57:12093—12105. https://doi.org/10.1021/acs.inorgchem.8b01665
15. Norby T. Fast oxygen ion conductors — from doped to ordered systems. *Journal of Materials Chemistry.* 2001;11: 11—18. https://doi.org/10.1039/B003463K
16. Rouanet A. Contribution a l'etude des systemes zirconia — oxydes des lanthanides au voisinage de la fusion. *Revue Internationale des Hautes Temperatures et des Refractaires.* 1971;8(2):161—180.
17. Andrievskaya E.R. Phase equilibria in the refractory oxide systems of zirconia, hafnia and yttria with rare-earth oxides. *Journal of the European Ceramic Society.* 2008;28:2363—2388. https://doi.org/10.1016/j.jeurceramsoc.2008.01.009
18. Shugurov S.M., Kurapova O.Y., Lopatin S.I., Konakov V.G., Vasil'eva E.A. Thermodynamic properties of the La_2O_3—ZrO_2 system by Knudsen effusion mass spectrometry at high temperature. *Rapid Communications in Mass Spectrometry.* 2017;31(23):2021—2029. https://doi.org/10.1002/rcm.7997
19. Kalinkin A.M., Vinogradov V.Y., Kalinkina E.V. Solid-state synthesis of nanocrystalline gadolinium zirconate using mechanical activation. *Inorganic Materials.* 2021;57(2):178—185.

Калинкин А.М., Виноградов В.Ю., Калинкина Е.В. Твердофазный синтез нанокристаллического цирконата гадолиния с применением механоактивации. *Неорганические материалы*. 2021;57(2):189—196. https://doi.org/10.1134/S0020168521020072

20. Hagiwara T., Nomura K., Kageyama H. Crystal structure analysis of $Ln_2Zr_2O_7$ (Ln = Eu and La) with a pyrochlore composition by high-temperature powder *X*-ray diffraction. *Journal of the Ceramic Society of Japan*. 2017; 125:65—70. https://doi.org/10.2109/jcersj2.16248
21. Duarte W., Meguekam A., Colas M., Vardelle M., Rossignol S. Effects of the counter-cation nature and preparation method on the structure of $La_2Zr_2O_7$. *Journal of Materials Science*. 2015;50:463—475. https://doi.org/10.1007/s10853-014-8606-4
22. Simonenko N.P., Sakharov K.A., Simonenko E.P., Sevastyanov V.G., Kuznetsov N.T. Glycol—citrate synthesis of ultrafine lanthanum zirconate. *Russian Journal of Inorganic Chemistry*. 2015;60(12):1452—1548. https://doi.org/10.1134/S0036023615120232
Симоненко Н.П., Сахаров К.А., Симоненко Е.П., Севастьянов В.Г., Кузнецов Н.Т. Гликоль-цитратный синтез высокодисперсного цирконата лантана *Журнал неорганической химии*. 2015;60(12):1588—1595.
23. Torres-Rodriguez J., Gutierrez-Cano V., Menelaou M., Kastyl J., Cihlar J., Tkachenko S., Gonzalez J.A., Kalmar J., Fabian I., Lazar I., Celko L., Kaiser J. Rare-earth zirconate $Ln_2Zr_2O_7$ (Ln: La, Nd, Gd, and Dy) powders, xerogels, and aerogels: Preparation, structure, and properties. *Inorganic Chemistry*. 2019;58(21):14467—14477. https://doi.org/10.1021/acs.inorgchem.9b01965
24. Popov V.V., Menushenkov A.P., Ivanov A.A., Gaynanov B.R., Yastrebtsev A.A., d'Acapito F., Puri A., Castro G.R., Shchetinin I.V., Zheleznyi M.V., Zubavichus Ya.V., Ponkratov K.V. Comparative analysis of long- and short-range structures features in titanates $Ln_2Ti_2O_7$ and zirconates $Ln_2Zr_2O_7$ (Ln = Gd, Tb, Dy) upon the crystallization process. *Journal of Physics and Chemistry of Solids*. 2019;130:144—153. https://doi.org/10.1016/j.jpcs.2019.02.019
25. Kong L., Karatchevtseva I., Aughterson R.D., Davis J., Zhang Y., Lumpkin G.R., Triani G. New pathway for the preparation of pyrochlore $Nd_2Zr_2O_7$ nanoparticles. *Ceramics International*. 2015;41(6):7618—7625. https://doi.org/10.1016/j.ceramint.2015.02.087
26. Joulia A., Vardelle M., Rossignol S. Synthesis and thermal stability of $Re_2Zr_2O_7$ (Re = La, Gd) and $La_2(Zr_{1-x}Ce_x)_2O_{7-\delta}$ compounds under reducing and oxidant atmospheres for thermal barrier coatings. *Journal of the European Ceramic Society*. 2013;33(13-14): 2633—2644. https://doi.org/10.1016/j.jeurceramsoc.2013.03.030
27. Nikishina E.E., Lebedeva E.N., Drobot D.V. Individual and bimetallic low-hydrated zirconium and hafnium hydroxides: Synthesis and properties. *Russian Journal of Inorganic Chemistry*. 2015;60(8):921—929. https://doi.org/10.1134/S0036023615080148
Никишина Е.Е., Лебедева Е.Н., Дробот Д.В. Индивидуальные и биметаллические маловодные гидроксиды циркония и гафния: синтез и свойства. *Журнал неорганической химии*. 2015;60(8):1018—1027.
28. Nikishina E.E., Lebedeva E.N., Prokudina N.A., Drobot D.V. Physicochemical properties of low-hydrated zirconium and hafnium hydroxides and their thermolysis products. *Inorganic Materials*. 2015;51(12):1190—1198. https://doi.org/10.1134/S0020168515110072
Никишина Е.Е., Лебедева Е.Н., Прокудина Н.А., Дробот Д.В. Физико-химические свойства маловодных гидроксидов циркония и гафния и продуктов их термолиза. *Неорганические материалы*. 2015;51(12):1284—1292.
29. David F., Vokhminz V., Ionova G. Water characteristics depend on the ionic environment. Thermodynamics and modelisation of the aquo ions. *Journal of Molecular Liquids*. 2001;90:45—62. https://doi.org/10.1016/S0167-7322(01)00106-4
30. Rudolph W.W., Irmer G. On the hydration of the rare earth ions in aqueous solution. *Journal of Solution Chemistry*. 2020;49:316—331. https://doi.org/10.1007/s10953-020-00960-w

Information about the authors

Elena E. Nikishina – Cand. Sci. (Chem.), Assistant Professor of the Department of Chemistry and Technology of Rare Elements, M.V. Lomonosov Institute of Fine Chemical Technologies of MIREA – Russian Technological University.
http://orcid.org/0000-0003-3579-2194
E-mail: nikishina@mirea.ru

Nikolai V. Grechishnikov – Postgraduate Student of the Department of Chemistry and Technology of Rare Elements, M.V. Lomonosov Institute of Fine Chemical Technologies of MIREA – Russian Technological University.
https://orcid.org/0009-0003-9591-391X
E-mail: nklgrchshnkv@yandex.ru

Dmitry V. Drobot – Dr. Sci. (Chem.), Professor of the Department of Chemistry and Technology of Rare Elements, M.V. Lomonosov Institute of Fine Chemical Technologies of MIREA – Russian Technological University.
https://orcid.org/0000-0002-0379-2926
E-mail: dvdrobot@mail.ru

Информация об авторах

Елена Евгеньевна Никишина – к.х.н., доцент кафедры химии и технологии редких элементов Института тонких химических технологий им. М.В. Ломоносова ФГБОУ ВО «МИРЭА – Российский технологический университет».
http://orcid.org/0000-0003-3579-2194
E-mail: nikishina@mirea.ru

Николай Владимирович Гречишников – аспирант кафедры химии и технологии редких элементов Института тонких химических технологий им. М.В. Ломоносова ФГБОУ ВО «МИРЭА – Российский технологический университет».
https://orcid.org/0009-0003-9591-391X
E-mail: nklgrchshnkv@yandex.ru

Дмитрий Васильевич Дробот – д.х.н., профессор кафедры химии и технологии редких элементов Института тонких химических технологий им. М.В. Ломоносова ФГБОУ ВО «МИРЭА – Российский технологический университет».
https://orcid.org/0000-0002-0379-2926
E-mail: dvdrobot@mail.ru

Contribution of the authors

E.E. Nikishina – conducting experiments, discussions, and paper authoring.

N.V. Grechishnikov – preparing and examining the samples, and discussions.

D.V. Drobot – problem statement, discussions.

Вклад авторов

Е.Е. Никишина – проведение экспериментов, участие в обсуждении результатов, написание статьи.

Н.В. Гречишников – подготовка образцов, проведение исследований образцов, участие в обсуждении результатов.

Д.В. Дробот – определение цели работы, участие в обсуждении результатов.

The article was submitted 09.10.2023, revised 21.12.2023, accepted for publication 09.01.2024

Статья поступила в редакцию 09.10.2023, доработана 21.12.2023, подписана в печать 09.01.2024

FOUNDRY / ЛИТЕЙНОЕ ПРОИЗВОДСТВО

UDC 669.245.018.44 : 66.091.3-977
https://doi.org/10.17073/0021-3438-2024-1-24-41

Research article
Научная статья

Structural characteristics and properties of heat-resistant nickel β-alloys produced via the centrifugal SHS-casting method

V.V. Sanin[1,2], M.I. Aheiev[1], P.A. Loginov[1], M.Ya. Bychkova[1], E.S. Shukman[2], L.Yu. Mezhevaia[1,2], V.N. Sanin[3], T.A. Lobova[1]

[1] **National University of Science and Technology "MISIS"**
4 Bld. 1 Leninskiy Prosp., Moscow 119049, Russia

[2] **JSC "Giredmet" n.a. N.P. Sazhin**
1 Bld. 2 Elektrodnaya Str., Moscow 111524, Russia

[3] **Merzhanov Institute of Structural Macrokinetics and Materials Science of the Russian Academy of Sciences**
8 Akademican Osip'yan Str., Chernogolovka, Moscow Region 142432, Russia

✉ Maksym I. Aheiev (aheievmi@gmail.com)

Abstract: Employing centrifugal self-propagating high-temperature synthesis (SHS) metallurgy, complemented by advanced metallurgical processes such as vacuum induction melting (VIM) and vacuum arc remelting (VAR), yielded the alloy formulation denoted as base–2.5Mo–1.5Re–1.5Ta–0.2Ti. This study investigates the effects of various technological modes and additional metallurgical treatments on the alloy's impurity and non-metallic inclusion content, structural characteristics, mechanical behavior under compression, and its oxidation mechanisms and kinetics when exposed to temperatures of 1150 °C for 30 h. With increasing centrifugal acceleration, the proportion of non-metallic inclusions (number of points) drops from 5 to 1–2 points. The best combination mechanical properties, including $\sigma_{ucs} = 1640 \pm 20$ MPa, $\sigma_{ys} = 1518 \pm 10$ MPa, and residual deformation were observed in alloys processed under conditions of increased gravitational force ($g = 50$). Within a centrifugal force range of $g = 20 \div 300$, the composition of the synthesis products aligned with the theoretical expectations. The total content of impurities is 0.15 ± 0.02 %, with a decrease in gas impurities—oxygen and nitrogen levels reduced to 0.018 % and 0.0011 %, respectively. The structural analysis of the alloys revealed the presence of globular and streaked inclusions of a chromium-based solid solution embedded within the matrix. Inclusions with thickness of 2–8 μm are present in the intergranular space: $(Cr)_{Ni,Mo,Co}$, $(Cr)_{Mo,Re}$ and $(Cr)_{Re,Mo}$. The formation of the Ni(Al,Ti) phase at grain boundaries was identified, contributing to an enhancement in plastic resistance and overall strength of the alloy. Oxidation mechanisms varied across different processing modes, with the size of structural components significantly influencing oxidation kinetics. The weight gain observed in SHS samples was 70 ± 10 g/m^2 with oxidation predominantly occurring along the NiAl interphase boundaries and penetrating into the depth of the sample. TEM facilitated the identification of phases enriched with Ti microadditions, reducing the levels of dissolved nitrogen and oxygen within the intermetallic phase to a combined weight percentage ($\Sigma_{O,N}$) of 0.0223 wt.%.

Keywords: heat-resistant nickel alloys, centrifugal SHS-casting, centrifugal acceleration, SHS, vacuum induction melting (VIM), vacuum arc remelting (VAR), nonmetallic inclusions, gas impurity content, heat resistance, oxidation kinetics.

Acknowledgments: This research was supported by the Russian Science Foundation, grant No. 19-79-10226, https://rscf.ru/project/19-79-10226/

For citation: Sanin V.V., Aheiev M.I., Loginov P.A., Bychkova M.Ya., Shukman E.S., Mezhevaia L.Yu., Sanin V.N., Lobova T.A. Structural characteristics and properties of heat-resistant nickel β-alloys produced via the centrifugal SHS-casting method. *Izvestiya. Non-Ferrous Metallurgy*. 2024;30(1):24–41. https://doi.org/10.17073/0021-3438-2024-1-24-41

Особенности структуры и свойства жаропрочных никелевых β-сплавов, полученных методом центробежного СВС-литья

В.В. Санин[1,2], М.И. Агеев[1], П.А. Логинов[1], М.Я. Бычкова[1], Е.С. Шукман[2], Л.Ю. Межевая[1,2], В.Н. Санин[3], Т.А. Лобова[1]

[1] **Национальный исследовательский технологический университет «МИСИС»**
Россия, 119049, г. Москва, Ленинский пр-т, 4, стр. 1

[2] **АО «Гиредмет» им. Н.П. Сажина**
Россия, 111524, г. Москва, ул. Электродная, 2, стр. 1

[3] **Институт структурной макрокинетики и проблем материаловедения им. А.Г. Мержанова РАН**
Россия, 142432, Московская обл., г. Черноголовка, ул. Академика Осипьяна, 8

✉ Максим Игоревич Агеев (aheievmi@gmail.com)

Аннотация: По технологии центробежной СВС-металлургии при разных технологических режимах и дополнительных металлургических переделах (вакуумный индукционный переплав и вакуумный дуговой переплав) получен сплав: base–2,5Mo–1,5Re–1,5Ta–0,2Ti. Исследовано влияние режимов на содержание неметаллический включений и примесей, особенности структуры, механические свойства при сжатии, кинетику и механизм окисления при температуре 1150 °C в течение 30 ч. С ростом центробежного ускорения доля неметаллических включений (балльность) снижается с 5 до 1–2 ед. Наилучшее сочетание свойств по соотношению прочности, предела текучести и остаточной деформации имеет сплав, полученный в условиях перегрузки $g = 50$: $\sigma_в = 1640 \pm 20$ МПа, $\sigma_{0,2} = 1518 \pm 10$ МПа. При значениях перегрузки $g = 20 \div 300$ состав продуктов синтеза соответствует расчетным значениям. Суммарное содержание примесей составляет 0,15 ± 0,02 %, что находится в области допустимых значений. С увеличением центробежной силы уменьшается содержание газовых примесей: кислорода – до 0,018 %, азота – до 0,0011 %. Структура сплавов характеризуется образованием в матрице глобулярных и строчечных включений твердого раствора на основе Cr. В межзеренном пространстве присутствуют включения $(Cr)_{Ni,Mo,Co}$, $(Cr)_{Mo,Re}$ и $(Cr)_{Re,Mo}$ толщиной 2–8 мкм. На границах зерен образуется фаза Ni(Al,Ti), обеспечивающая рост сопротивления пластической деформации и повышение прочности сплава. Механизм окисления сплавов, полученных по разным режимам, отличается. Существенное влияние на кинетику окисления оказывает размерный фактор структурных составляющих. Прирост массы СВС-образцов составляет 70 ± 10 г/м^2. Процесс окисления происходит по межфазным границам NiAl в глубь образца. С помощью просвечивающей электронной микроскопии идентифицированы фазы, содержащие микродобавки Ti, которые снижают содержание в интерметаллидной фазе растворенных азота и кислорода до значения $\Sigma_{O,N} = 0{,}0223$ мас.%.

Ключевые слова: жаропрочные никелевые сплавы, центробежное СВС-литье, центробежное ускорение, вакуумный индукционный переплав (ВИП), вакуумный дуговой переплав (ВДП), неметаллические включения, содержание газовых примесей, жаростойкость, кинетика окисления.

Благодарности: Исследование выполнено за счет гранта Российского научного фонда № 19-79-10226, https://rscf.ru/project/19-79-10226/

Для цитирования: Санин В.В., Агеев М.И., Логинов П.А., Бычкова М.Я., Шукман Е.С., Межевая Л.Ю., Санин В.Н., Лобова Т.А. Особенности структуры и свойства жаропрочных никелевых β-сплавов, полученных методом центробежного СВС-литья. *Известия вузов. Цветная металлургия.* 2024;30(1):24–41.

https://doi.org/10.17073/0021-3438-2024-1-24-41

Introduction

Heat-resistant intermetallic nickel alloys are extensively employed in the construction of engines. However, these alloys exhibit certain limitations, notably their relatively inferior mechanical strength and plasticity at ambient temperatures. Such properties not only hinder mechanical processing but also elevate the risk of material fracture [1—9]. To improve fracture toughness, the addition of various plasticizing additives, including Cr, Co, Mo, Ta, Re, Zr has been investigated [3—12]. Additionally, materials utilized in high-temperature sections of engines must meet stringent requirements regarding the oxidation resistance of their surfaces when exposed to elevated temperatures and to the effects of thermal cycling [3—6; 13—15].

Self-propagating high-temperature synthesis (SHS) and its variants, including elemental synthesis [8—10] and centrifugal SHS-casting [12; 16; 17], represent recognized methods for fabricating cast and powder materials based on β-alloys. Within this domain, efforts are concentrated on refining the compositional makeup and production methodologies of CompoNiAl alloys, particularly those derived from a NiAl—Cr—Co base, here and after referred to as ‘the base’ [12].

Research aimed at augmenting crack resistance at reduced temperatures has led to the exploration of microalloying techniques using diverse elements within these alloys. Studies have identified [11; 12; 16; 18; 19] that in cast SHS alloys formulated from the base + X (where X includes La, Mo, Ta, Re, Zr), the inclusion of Mo and Re is instrumental in promoting the development of a cellular eutectic structure. The introduction of 15 % Mo has been found to significantly bolster mechanical attributes, yielding σ_{ucs} = 1,604 ± 80 MPa, σ_{ys} = 1,520 ± 80 MPa, and ε = 0.79 %. Subsequent annealing at 1,250 °C for 180 min further enhances these properties increasing σ_{ucs} by 12 %, σ_{ys} by 10 %, and ε by 100 %. The addition of 1.5 % rhenium to the base + + 15Mo1.5Re alloy modifies its structural composition, thereby elevating mechanical properties to σ_{ucs} = = 1,682 ± 60 MPa, σ_{ys} = 1,538 ± 60 MPa, and ε = 0.87 %, with further improvements observed following additional annealing: σ_{ucs} by 20 %, σ_{ys} by 7 %, and ε by 640 %. A hierarchical three-level structure characterizes the base + 15%Mo alloy: the first level consists of β-NiAl dendritic grains interlaced with molybdenum-enriched phases $(Ni,Co,Cr)_3Mo_3C$ and $(Mo_{0.8}Cr_{0.2})_xB_y$ with cell size up to 50 μm; the second level includes strengthening submicron Cr(Mo) particles along grain boundaries; and the third level encompasses coherent Cr(Mo) nanodeposits (10—40 nm) within β-NiAl dendrites. The incorporation of alloying interstitial elements enhances the oxidation resistance of β-alloys by fostering the formation of additional phases [11]. The alloy that incorporates zirconium demonstrates superior heat resistance, with an oxidation rate of 21 g/m^2 over 30 h. The formation of a zirconium-rich continuous top layer comprising $Al_2O_3 + Zr_5Al_3O_{0.5}$ obstructs external oxygen and nitrogen diffusion, thereby significantly improving heat resistance [18].

Currently, the alloy base—2.5Mo—1.5Re—1.5Ta—0.2Ti alloy represents the optimal composition, exhibiting strength characteristics with a tensile strength (σ_{ucs}) of 1644 ± 30 MPa, a yield strength (σ_{ys}) of 1518 ± ± 25 MPa, and a total weight gain during of oxidation 52 g/m^2 [19].

Maintaining a low concentration of impurities is crucial for the performance of heat-resistant alloys. The presence of residual metallic and gaseous elements, along with non-metallic inclusions, adversely affects the mechanical, technological, and thermal resistance characteristics of these alloys [20]. A technological approach to mitigate these effects involves the application of conventional metallurgical techniques to refine the alloy’s properties. Prior research on the base alloy [16] has demonstrated the beneficial influence of vacuum induction melting (VIM) and subsequent heat treatment (HT) processes on enhancing its properties. However, the application of VIM technology may introduce non-metallic inclusions into the alloy due to interactions between the metal and lining materials. Thus, it becomes essential to investigate the structural and property changes in alloys subjected to vacuum arc remelting (VAR) within a copper-cooled crystallizer.

This study aims to examine the influence of synthesis parameters (SHS-M) and additional treatment (VIM, VAR, HT) on the structural parameters, mechanical properties and resistance to high-temperature oxidation (heat resistance) of the base—2.5Mo—1.5Re—1.5Ta—0.2Ti alloy.

Research materials and methods

The synthesis was performed using a radial centrifugal apparatus, subject to high gravitational forces of up to 300 g. Reference [12] outlines the centrifugal apparatus’s overall configuration. The design of this apparatus allows for the precise adjustment of the centrifugal rotor’s speed, thus achieving the desired overload conditions. This technology is characterized by its use of readily available oxide raw materials and its capability to reach high combustion temperatures between 2100—3500 °C. Such temperatures facilitate the segre-

Table 1. **Characteristics of initial components and modifying additions**

Таблица 1. Характеристики исходных веществ и модифицирующих добавок

Substance	Brand	GOST / TS	Particle size, μm	Purity, %
Main components				
NiO	OSCh	TS 6-09-02439-87	<40	99.00
Cr_2O_3	Ch	TS 6-09-4272-84	<20	99.00
Co_3O_4	OSCh	GOST 18671-73	<30	99.00
Al	PA-4	GOST 6058-73	<140	98.00
Al	ASD-1	TS 48-5-226-87	<50	99.70
Modifying additions				
MoO_3	ChDA	TS 6-09-4471-77	<50	99.00
Ta	TaPM	TS 48-19-72-92	<20	98.00
Re	Pe-0	TS 48-4-195-87	<150	99.99
Ti	PTOM-1	TS 14-22-57-92	≤30	99.80

gation of the target product phase from the slag phase. The chemical process involved can be summarized by the equation:

$$NiO + Cr_2O_3 + Co_3O_4 + MoO_3 + Al + (AA) + (FA) \rightarrow$$
$$\rightarrow [NiAl–Cr–Co–Mo–(X)] + Al_2O_3,$$

where AA (alloying addition) includes Mo, Re, Ta, and Ti; FA (functional addition) comprises CaF_2, $Na_3[AlF_6]$, etc.; X is a metal (Ta, Re, Ti).

Table 1 presents the classifications and characteristics of the initial powders used in the synthesis. Alloying additions were incorporated into the reaction mixture to achieve the specific desired composition of the alloy.

The preparing exothermic mixtures commenced with the drying of components within SNOL-type ovens (t = 90 °C, τ = 1 h). Subsequent steps included the precise measurement of reagents, their mixing, and the placement of the resulting mixture into graphite molds. The mixing process utilized an MP4/0.5 planetary ball mill for a period of 15—20 min, with a jar capacity of 1 L and a ball-to-powder weight ratio set at 1 : 5. Due to the processing temperature of the mixtures surpassing the melting points of the end synthesis products, phase segregation was facilitated by the gravitational separation of the molten metal from the slag. Within the reaction mixture, tantalum (Ta), rhenium (Re), and titanium (Ti) were incorporated as pure elements, whereas molybdenum (Mo) was added in the form of MoO_3 oxide. The utilization of aluminum powder in varying grades served to regulate the self-propagating high-temperature synthesis (SHS) process [11; 12].

To evaluate the impact of impurity elements and non-metallic inclusions on the alloy's properties, additional processes were employed: vacuum induction melting (VIM) with subsequent ingot casting (slow crystallization; $V_{\text{cooled 1}}$ = 50 °C/min) and rod extrusion directly from the molten state (rapid crystallization, $V_{\text{cooled 2}}$ = = 250 °C/min) for the base—2.5Mo—1.5Re—1.5Ta—0.2Ti alloy sample under an overload condition of $g = 50$, following by vacuum arc remelting (VAR) in the copper cooled crystallizer.

SHS ingots undergo melting within a vacuum induction melting furnace VIP-010. This furnace facilitates the melting of ingots within an corundum crucible, accommodating weights ranging from 0.5 to 10 kg, for subsequent pouring into a steel mold-crystallizer. The vacuum induction melting of the SHS ingot is executed within the vacuum arc remelting furnace, capable of producing ingots up to 500 g. An advantage of VAR lies in the absence of interaction between the liquid metal and the furnace lining materials at elevated temperatures, as the melting occurs within a cooled copper crystallizer. This process significantly diminishes the presence of non-metallic inclusions within the alloy.

Given the lack of standard regulatory documents for the metallographic assessment of intermetallic nickel-aluminum system alloys, we adopted the metallographic method designated for evaluating non-metallic inclusions in steel (GOST 1778-70). This approach was simplified by amalgamating all categories of non-metallic inclusions, aiming to demonstrate the feasibility of enhancing alloy quality through modifications in centrifugal acceleration values and supplementary furnace treatment. The comparative analysis of the produced ingots focused on qualitative improvements without delving into the precise quantitative presence of each non-metallic inclusion type. Sample sections for this evaluation were selected and prepared in strict adherence to GOST 1778-70 standards.

For the quantitative analysis of major elements and impurities, a suite of sophisticated analytical instruments was employed, including the Finnigan Element GD (glow discharge) mass spectrometer (Thermo Fisher Scientific, Germany), the iCAP 6300 inductively coupled plasma-atomic emission spectrometer (Thermo Fisher Scientific), and a Nier—Johnson double-focusing mass spectrometer. The analysis of carbon and sulfur content in metals was carried out using the SC844 analyzer (LECO, USA), while the determination of oxygen, nitrogen, and hydrogen concentrations utilized the ONH836 analyzer (LECO).

The phase composition of the materials was determined through *X*-ray diffraction phase analysis (XRD) employing a D2 PHASER diffractometer (Bruker AXS GmbH, Germany) with CuK_α-radiation within an angle range of $2\theta = 10 \div 140°$.

Microstructural analyses were conducted using the S-3400N scanning electron microscope (SEM) (Hitachi, Japan) equipped with the "NORAN System 7 *X*-ray Microanalysis System" (Thermo Scientific, USA) for energy-dispersive spectrometry. Further investigation was facilitated by the JEM-2100 transmission electron microscope (TEM) (Jeol, Japan) with a double-tilt beryllium holder, utilizing lamellae prepared from pre-manufactured foil through the focused ion beam (FIB) method on the "Quanta 200 3D FIB" microscope (FEI Company, USA). The foils for TEM analysis were prepared via ion etching using the "PIPS II System" (Gatan, Inc., USA).

Mechanical compression testing at ambient temperature was executed on the LF-100KNa universal machine (Walter + Bai AG, Switzerland) according to GOST 25.503-97 standard.

Oxidative annealing experiments were performed in an open atmosphere at a temperature of 1150 °C for 30 h, with sample weights measured periodically in the SShOL 1.1.6/12-M3 laboratory electric pit-type heating furnace. The mass change of samples over specified durations was calculated relative to the unit surface area. Oxidation curves and corresponding approximation equations were formulated based on the collected data. The parabolic oxidation rate constant (k_p) for the studied alloys was calculated using the equation:

$$(\Delta m/S)^2 = k_p\tau, \qquad (1)$$

where Δm is the change in mass, S is the surface area, and τ is the time.

Results and discussion

As the base—2.5Mo—1.5Re—1.5Ta—0.2Ti alloy was synthesized using the centrifugal installation, several key parameters were quantitatively assessed: the burning rate (U) of the mixture, the scattering of the mixture (η_1), and the completeness of the metal phase yield in the ingot (η_2). The burning rate of the mixture during synthesis, under conditions of up to $g = 20$ overload, was $U = 13 \pm 1$ mm/s. An increase in overload to $g = 300$ resulted in a heightened burning rate, recorded at $U = 23 \pm 2$ mm/s. The parameter designated as the scattering of the mixture (η_1) demonstrated a significant reduction only upon reaching the maximum overload value ($g = 300$). Moreover, an incremental overload was associated with a uniform rise in the "yield ratio", or the completeness of the metal phase yield (η_2) (Table 2).

In this investigation, four ingots were synthesized under varying conditions (refer to the entries of *1—4* Table 2).

Additionally, to explore the impact of metallurgical processing on the alloy's properties, three samples (*5—7*) received supplementary treatments: $g = 50$ + VIM into the ingot (*5*); $g = 50$ + VIM into the rod (*6*) and $g = 50$ + VAR (*7*).

Figure 1 presents a comparative analysis of the ratings assigned to the content of non-metallic inclusions, derived from the microstructural examination of the alloys utilizing an optical microscope.

The analysis of the alloy samples' structures revealed several distinctive characteristics. The SHS alloy sample *1* ($g = 1$) exhibited a dendritic structure accompanied by a considerable presence of heterogeneous inclusions and pores, a result of the absence of centrifugal acceleration during the alloy's synthesis. This sample was assigned the maximum score (4—5 points) among the ones studied. SHS alloy sample *2* ($g = 20$) displayed a structure predominantly composed of the metallic phase, albeit with inclusions averaging a score of 3 points.

Table 2. **Synthesis parameters of the base–2.5Mo–1.5Re–1.5Ta–0.2Ti alloy**

Таблица 2. Параметры синтеза сплава base–2,5Mo–1,5Re–1,5Ta–0,2Ti

Sample No.	Overload g	Burning rate U, mm/s	Scattering of the mixture η_1, %	Completeness of the metal phase yield in the ingot η_2, %
1	1	12.8	4.2	79
2	20	13.3	3.8	84
3	50	22.6	3.8	92
4	300	25.8	1.8	98.7

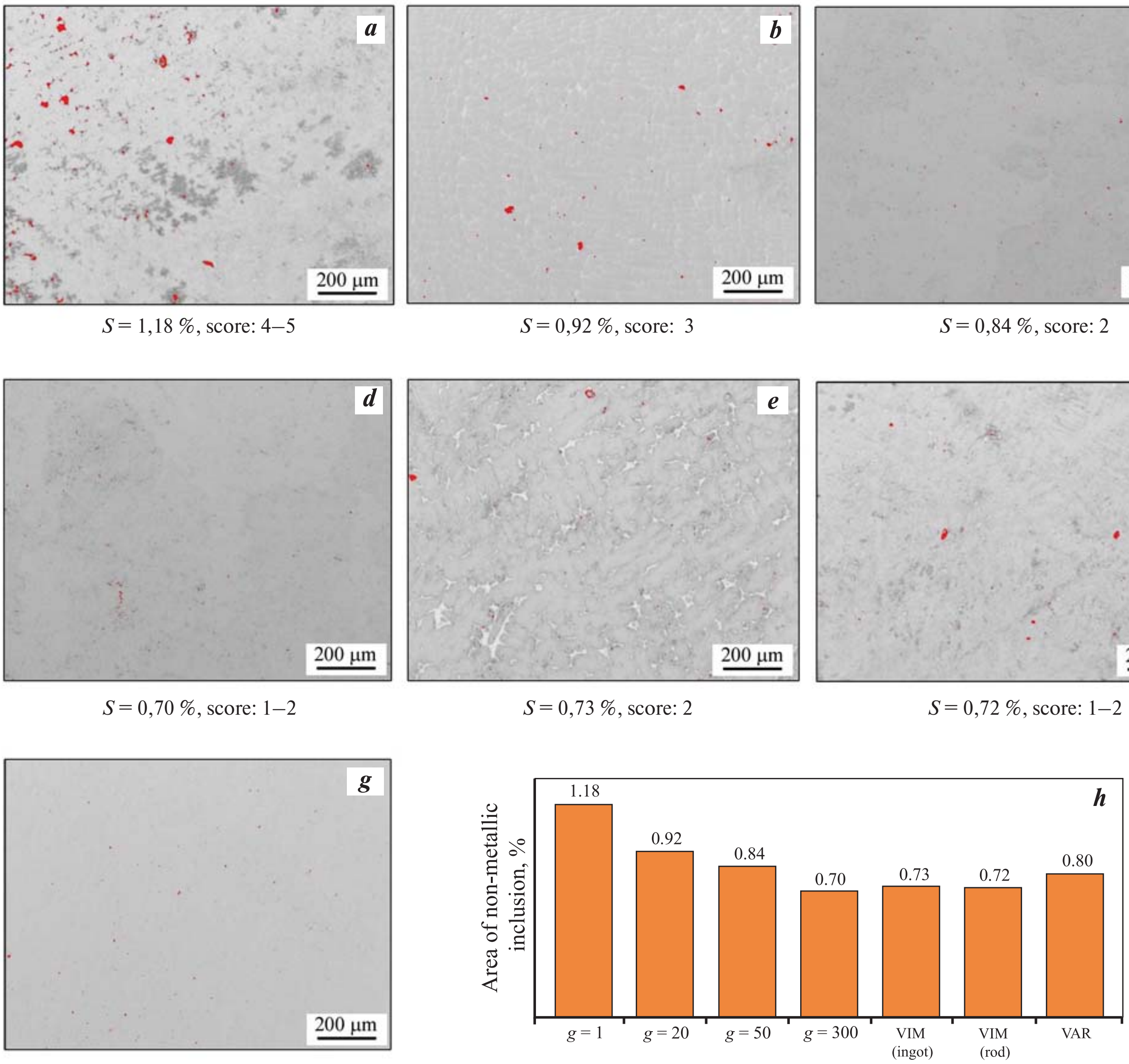

$S = 1{,}18$ %, score: 4–5

$S = 0{,}92$ %, score: 3

$S = 0{,}84$ %, score: 2

$S = 0{,}70$ %, score: 1–2

$S = 0{,}73$ %, score: 2

$S = 0{,}72$ %, score: 1–2

$S = 0{,}80$ %, score: 1–2

Fig. 1. Photographs and analysis of sections for non-metallic inclusion content in the base–2.5Mo–1.5Re–1.5Ta–0.2Ti alloy under various conditions and technologies

a – SHS, $g = 1$; ***b*** – SHS, $g = 20$; ***c*** – SHS, $g = 50$; ***d*** – SHS, $g = 300$; ***e*** – SHS ($g = 50$) + VIM (ingot); ***f*** – SHS ($g = 50$) + VIM (rod); ***g*** – SHS ($g = 50$) + VAR; ***h*** – the content of non-metallic inclusion

Рис. 1. Фотографии и анализ шлифов на содержание неметаллических включений сплава base–2,5Mo–1,5Re–1,5Ta–0,2Ti при различных режимах и технологиях получения

a – СВС, $g = 1$; ***b*** – СВС, $g = 20$; ***c*** – СВС, $g = 50$; ***d*** – СВС, $g = 300$; ***e*** – СВС ($g = 50$) + ВИП (в слиток); ***f*** – СВС ($g = 50$) + ВИП (в стержень); ***g*** – СВС ($g = 50$) + ВДП; ***h*** – содержание неметаллических включений

Exposure of the melt to an overload of $g = 50$ resulted in the production of ingot 3, which exhibited a reduction in impurities and non-metallic inclusions, leading to an average score of 2 points. Further increases in overload did not significantly alter the inclusion rating, with sample *4* achieving an average score of 1—2 points. It is noteworthy that additional metallurgical processes (VIM, VAR) did not substantially decrease the inclusion scores (remaining within 1—2 points); however, these treatments notably affected the sizes of the structural components.

A comprehensive examination of the alloys' microstructures through SEM is depicted in Fig. 2. This analysis revealed that at a centrifugal force of $g = 20$, the average size of the NiAl structural cells is 90 ± 10 µm, whereas at $g = 300$, the cell size significantly reduces to 15 ± 5 µm. The dimension of these structural constituents plays a crucial role in influencing the mechanical

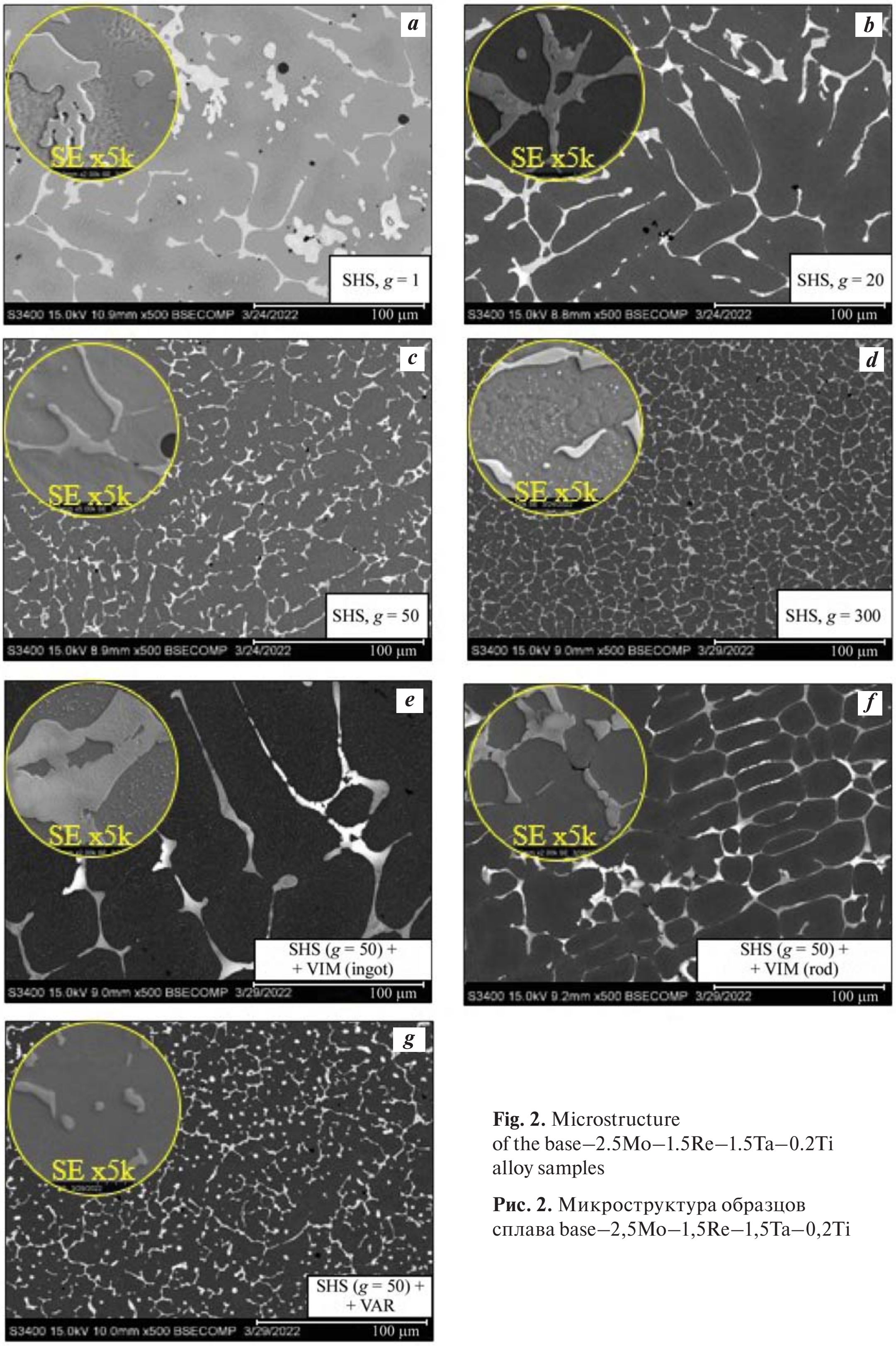

Fig. 2. Microstructure of the base–2.5Mo–1.5Re–1.5Ta–0.2Ti alloy samples

Рис. 2. Микроструктура образцов сплава base–2,5Mo–1,5Re–1,5Ta–0,2Ti

properties and oxidation resistance of the alloys [11; 20—22]. Studies [11; 19] emphasize the transformative effect of adding minute amounts of rhenium to the alloy's structure. At elevated overload values, the synthesized molten products undergo intensive mixing, facilitating the uniform dispersion of refractory rhenium throughout the melt. Consequently, rhenium grains serve as crystallization nuclei during the cooling process. This phe-

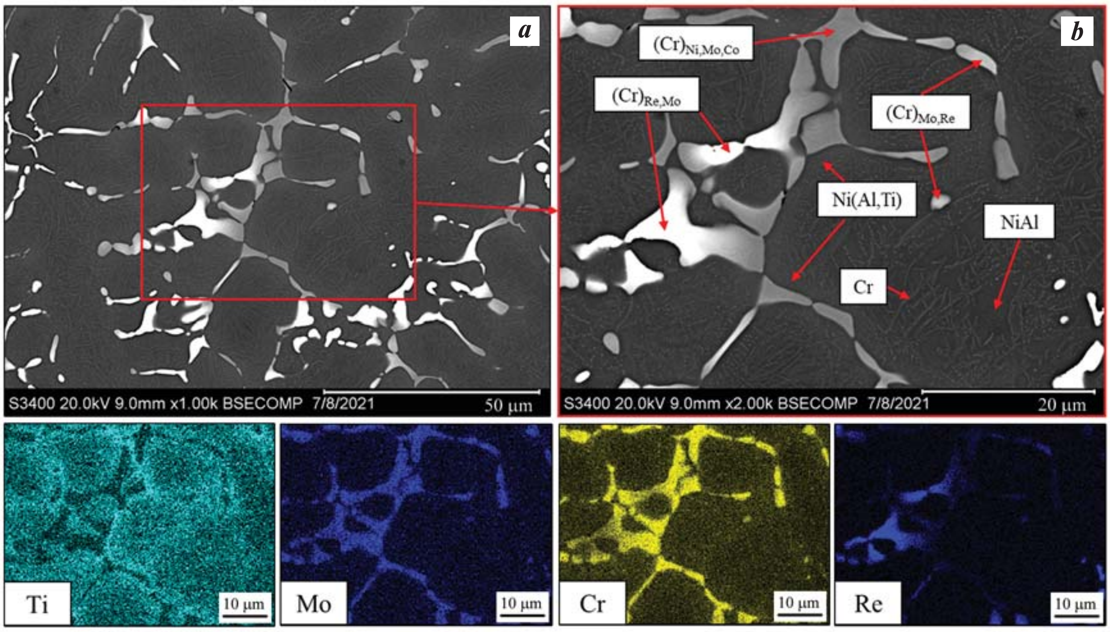

Fig. 3. Microstructure of the base–2.5Mo–1.5Re–1.5Ta–0.2Ti alloy ($g = 50$) (***a***), focused area of analysis (***b***), and the distribution map of the main alloying elements

Рис. 3. Микроструктура сплава base–2,5Mo–1,5Re–1,5Ta–0,2Ti ($g = 50$) (***a***), выделенная область анализа (***b***) и карта распределения основных легирующих элементов

Table 3. **Mechanical properties of the base–2.5Mo–1.5Re–1.5Ta–0.2Ti alloys**

Таблица 3. Механические свойства сплавов base–2,5Mo–1,5Re–1,5Ta–0,2Ti

Sample No.	Production technique	σ_{ucs}, MPa	σ_{ys}, MPa	ε, %
1	SHS, $g = 1$	730	–	<1*
2	SHS, $g = 20$	813	–	<1
3	SHS, $g = 50$	1650	1522	1.95
4	SHS, $g = 300$	1634	1513	1.24
5	SHS ($g = 50$) + + VIM (ingot)	1304	1126	0.51
6	SHS ($g = 50$) + + VIM (rod)	1680	1555	1.34
	CBC ($g = 50$) + VAR	1260	–	<1

* The samples exhibited brittle fracture.

nomenon is corroborated by the chemical analysis of the alloy synthesized at $g = 20$, which indicates an increase in rhenium content corresponding with higher overload levels, from 1.37 % up to the anticipated concentration of 1.5 ± 0.2. Regarding the completeness of the metal phase yield in the ingot (η_2 in Table 2), it is observed that in the absence of centrifugal forces or at minimal overloads (below 20 g), rhenium partially transitions into the oxide (slag) phase. This transition is not economically viable, especially considering the high cost of rhenium.

Figure 3 shows the analysis of the structural components in alloy *3* ($g = 50$). Within the β-NiAl matrix, the formation of globular and string-like micron and submicron inclusions of a chromium-based solid solution is noted. These inclusions, ranging from 2 to 8 μm in thickness, are located within the intergranular spaces, comprising $(\mathrm{Cr})_{\mathrm{Ni,Mo,Co}}$, $(\mathrm{Cr})_{\mathrm{Mo,Re}}$ and $(\mathrm{Cr})_{\mathrm{Re,Mo}}$. The formation of the Ni(Al,Ti) phase at the grain boundaries is observed, contributing to an enhanced plastic resistance and overall strength of the alloy.

The mechanical properties of the base—2.5Mo—1.5Re—1.5Ta—0.2Ti alloy samples, synthesized under varying centrifugal accelerations (1—300 g) and subjected to additional metallurgical processes, are detailed in Table 3. Alloys produced under conditions of elevated centrifugal acceleration ($g = 50 \div 300$) exhibited optimal mechanical properties, with a tensile strength (σ_{ucs}) of 1640 ± 20 MPa and a yield strength (σ_{ys}) of 1518 ± 10 MPa. In contrast, samples subjected to vacuum induction melting (VIM) in ingot form showed deteriorated mechanical properties, with σ_{ucs} and σ_{ys} values of 1304 ± 10 MPa and 1126 ± 10 MPa, respectively. This reduction in mechanical strength is attributed

Table 4. **Content (wt.%) of alloying elements and impurities in base–2.5Mo–1.5Re–1.5Ta–0.2Ti alloys**

Таблица 4. Содержание (мас.%) легирующих элементов и примесей
в сплавах base–2,5Mo–1,5Re–1,5Ta–0,2Ti

Element	Ordered composition	$g = 1$	$g = 20$	$g = 50$	$g = 300$	$g = 50$ + VIM (ingot)	$g = 50$ + VIM (rod)	$g = 50$ + VAR
Ti	0.15–0.25	0.13	0.15	0.21	0.20	0.17	0.19	0.12
Mo	2.0–3.0	1.83	2.11	2.46	2.48	2.44	2.46	2.56
Re	1.4–1.7	1.26	1.37	1.49	1.52	1.47	1.46	1.53
Ta	1.4–1.7	1.86	1.64	1.46	1.46	1.24	1.29	1.38
W	–	0.033	0.032	0.031	0.037	0.031	0.031	0.11
O	–	0.13	0.037	0.021	0.018	0.0016	0.0026	0.0018
N	–	0.0074	0.0068	0.0013	0.0011	0.0001	0.0001	0.0001
C	–	0.013	0.014	0.017	0.017	0.011	0.011	0.011
S	–	0.0046	0.0041	0.0033	0.0032	<0.0005	<0.0005	<0.0005
Σ_1	–	0.1627	0.1533	0.1716	0.1543	0.1498	0.1502	0.2236
Σ_2	–	0.1410	0.1374	0.0223	0.0191	0.0017	0.0027	0.0019

Примечание. Σ_1 – impurity content; Σ_2 – sum of gas impurities.

to the growth in grain size resulting from slow cooling rates ($V_{\text{cooled 1}}$ = 50 °C/min). An indirect confirmation of the influence of cooling rates on mechanical properties is observed in the SHS + VIM (rod) samples. Unlike the ingot samples, these 8-mm diameter rods were extruded from the melt under identical processing conditions but cooled at a rate akin to that of the SHS process ($V_{\text{cooled 2}}$ = 250 °C/min), resulting in superior mechanical properties: σ_{ucs} = 1680 ± 10 MPa and σ_{ys} = 1555 ± ± 10 MPa. This suggests that by leveraging additional thermal post-treatment, it is possible to enhance the mechanical properties of the alloy, as corroborated by previous research [11; 12; 16].

Managing the chemical composition of alloys and minimizing the presence of undesirable impurities is a crucial aspect of the alloy synthesis process. Table 4 outlines the concentrations of principal alloying elements and impurities in the synthesized multicomponent base—2.5Mo—1.5Re—1.5Ta—0.2Ti alloys under various overload conditions and subsequent metallurgical treatments.

Chemical analyses of samples processed through differing technological protocols indicated alignment with the anticipated compositions at overloads g = 20÷300. The chemical composition showcased optimal characteristics at overloads between g = 50 and 300. Impurities such as Mg, Na, Si, Ca, K, Mn, and Cu are incidental, originating from the initial reagents and incorporated into the synthesis products. The aggregate impurity content remained within an acceptable limit of 0.15 ± ± 0.02 %. The tungsten (W) content increased across all samples to a maximum of 0.04 %, likely introduced from the grinding balls during material mixing. After VAR, tungsten concentration further escalated to 0.11 wt.%, attributable to process-specific dynamics and interactions between the melt and the material of the non-consumable electrode (W).

Regarding gas impurities (O, N) — critical for alloy workability — a decreasing trend in their concentrations was observed with increasing centrifugal force. Oxygen content diminished from 0.13 % at g = 1 to 0.018 % at g = 300, while nitrogen content decreased from 0.0074 to 0.0011 %. These gas impurities influence not only mechanical properties but also the oxidation mechanism. VIM and VAR significantly alter the impurity profile; post-VIM processing reduced oxygen content in the ingot from 0.018 to 0.0016 % and nitrogen content from 0.0011 to 0.0001 %. However, this also affected the ratios of fusible elements (Cr, Ta, Al, Ti), thereby impacting the alloy's composition and properties.

The subsequent phase of the study focused on evaluating the effects of impurities and non-metallic inclusions on the properties of the base—2.5Mo—1.5Re—1.5Ta—

Table 5. **Impact of alloying additions on the oxidation kinetics of base–2.5Mo–1.5Re–1.5Ta–0.2Ti cast alloys**

Таблица 5. Влияние легирующих добавок на кинетику окисления литых сплавов base–2,5Mo–1,5Re–1,5Ta–0,2Ti

Sample No.	Production technique	Approximation equation	Weight gain, g/m^2
2	SHS, $g = 20$	$y = 0.0021x^2 + 2.1508x + 4.091$	70.5
3	SHS, $g = 50$	$y = -0.0006x^3 + 0.0038x^2 + 3.0137x + 1.5265$	78.8
4	SHS, $g = 300$	$y = -0.0315x^2 + 2.9026x + 3.3651$	62.7
5	SHS ($g = 50$) + VIM (ingot)	$y = -0.0022x^4 + 0.1539x^3 - 3.7188x^2 + 45.51x + 22.95$	421.5
6	SHS ($g = 50$) + VIM (rod)	$y = -0.0009x^3 + 0.0466x^2 + 0.8678x + 1.6188$	45.1
7	SHS ($g = 50$) + VAR	$y = 8.6204x^{0,9}$	183.58

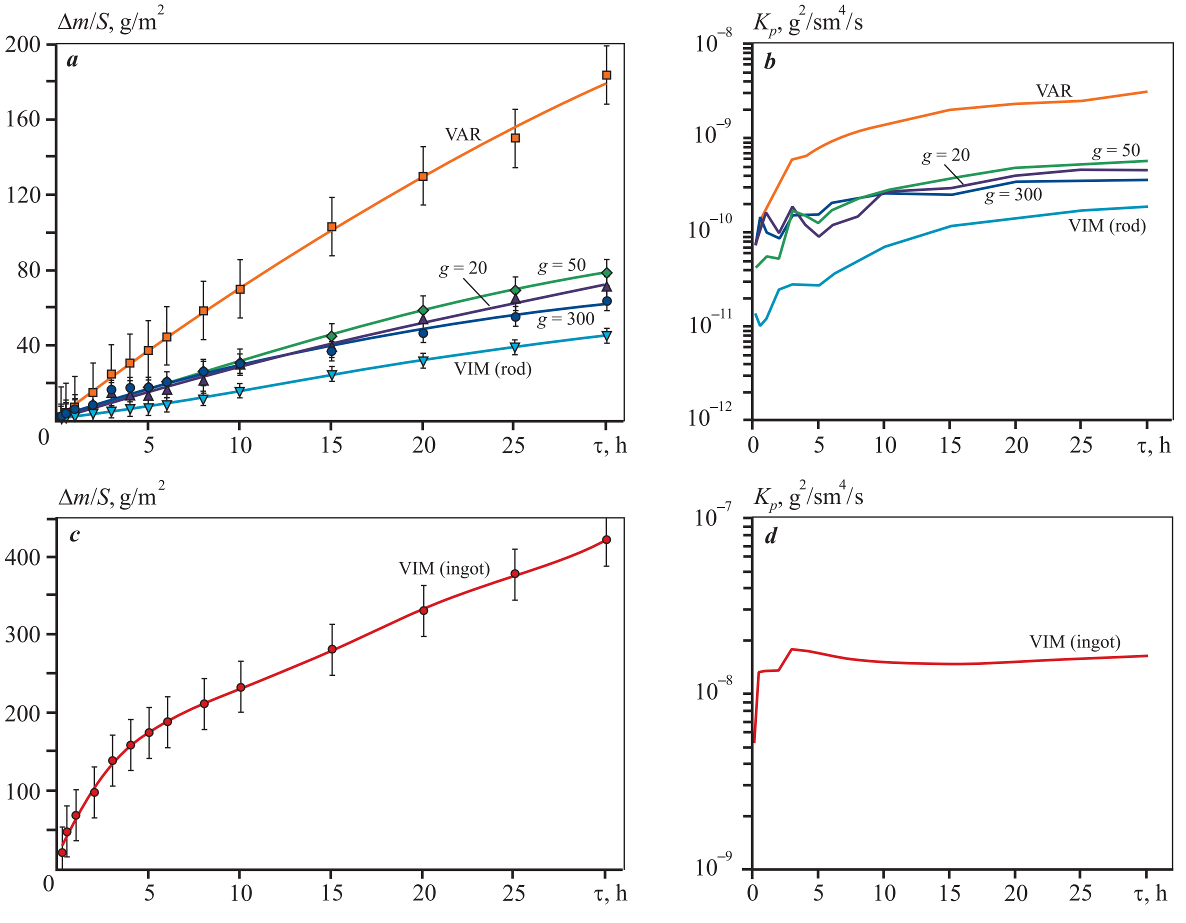

Fig. 4. Oxidation kinetic curves (***а***, ***в***) and rate constant (k_p) (***б***, ***г***) for base–2.5Mo–1.5Re–1.5Ta–0.2%Ti alloys at 1150 °C for 30 h

Рис. 4. Кинетические кривые (***а***, ***в***) и константа скорости (k_p) окисления (***б***, ***г***) сплавов base–2,5Mo–1,5Re–1,5Ta–0,2%Ti при температуре 1150 °C в течение 30 ч

0.2Ti alloy through oxidative annealing conducted in an open environment at 1150 °C for 30 h, with periodic sample weighing.

The ingot synthesized at $g = 1$ was omitted from the experimental series due to non-compliance with chemical composition standards and inadequate mechanical performance. Table 5 details the mass gains of samples following oxidative annealing and the derived approximation equations corresponding to the oxidation curves depicted in Fig. 4. Additionally, Fig. 4 illustrates the parabolic oxidation rate constant curves for the examined alloys.

SHS, $g = 20$ SHS, $g = 50$ SHS, $g = 300$

SHS + VIM (ingot) SHS + VIM (rod) SHS + VAR

Fig. 5. Appearance of base–2.5Mo–1.5Re–1.5Ta–0.2Ti alloy samples after annealing at a 1150 °C for 30 h

Рис. 5. Внешний вид образцов сплавов base–2,5Mo–1,5Re–1,5Ta–0,2Ti после отжига при температуре 1150 °C в течение 30 ч

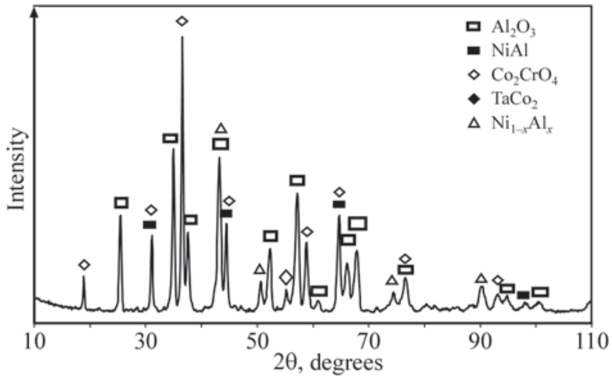

Fig. 6. Diffraction spectra of oxidized surface of the base–2.5Mo–1.5Re–1.5Ta–0.2Ti alloy

Рис. 6. Дифракционные спектры окисленной поверхности сплава base–2,5Mo–1,5Re–1,5Ta–0,2Ti

For all samples, except for the one subjected to VAR, the oxidation behavior aligns with the parabolic law, indicative of a typical oxidation process. Initially, during oxidation, a dense protective oxide layer forms across the surface of all alloys, significantly inhibiting further oxidation. The oxidation pattern for the VAR-treated sample adheres to an exponential law, demonstrating an atypical oxidation course. This anomaly is evidenced by the initial destruction of the oxide layer, followed by the development of a crack within the sample itself (at $\tau = 11 \div 12$ h), a phenomenon substantiated by photographic documentation post 30 h of oxidative annealing (Fig. 5).

The diffraction spectra of the surfaces of β-alloys, oxidized at a $t = 1150$ °C ($\tau = 30$ h), are depicted in Fig. 6. Predominant peaks correspond to the phases of γ-Al_2O_3 aluminum oxide and Co_2CrO_4 spinel, constituting the primary oxidation products and forming the protective upper layer. Alongside these oxides, phases based on nickel aluminide are detected, with alloying additions transitioning into a solid solution.

The oxidation mechanism across all samples under investigation is uniform, where oxygen and nitrogen infiltrate the alloy through the destructible Al_2O_3 oxide surface film and a porous layer of Co_2CrO_4 spinel. The presence of non-metallic inclusions or impurities within the alloy exhibits negligible influence on the high-temperature oxidation process. As indicated by the oxidation kinetic curves (refer to Fig. 4) and microstructural images of the oxidized layer (Fig. 7), all SHS samples ($g = 20 \div 300$) similar oxidation dynamics, featuring the formation of top oxide and nitride layers adjacent to the alloy. The observed weight gain is 70 ± 10 g/m^2. The

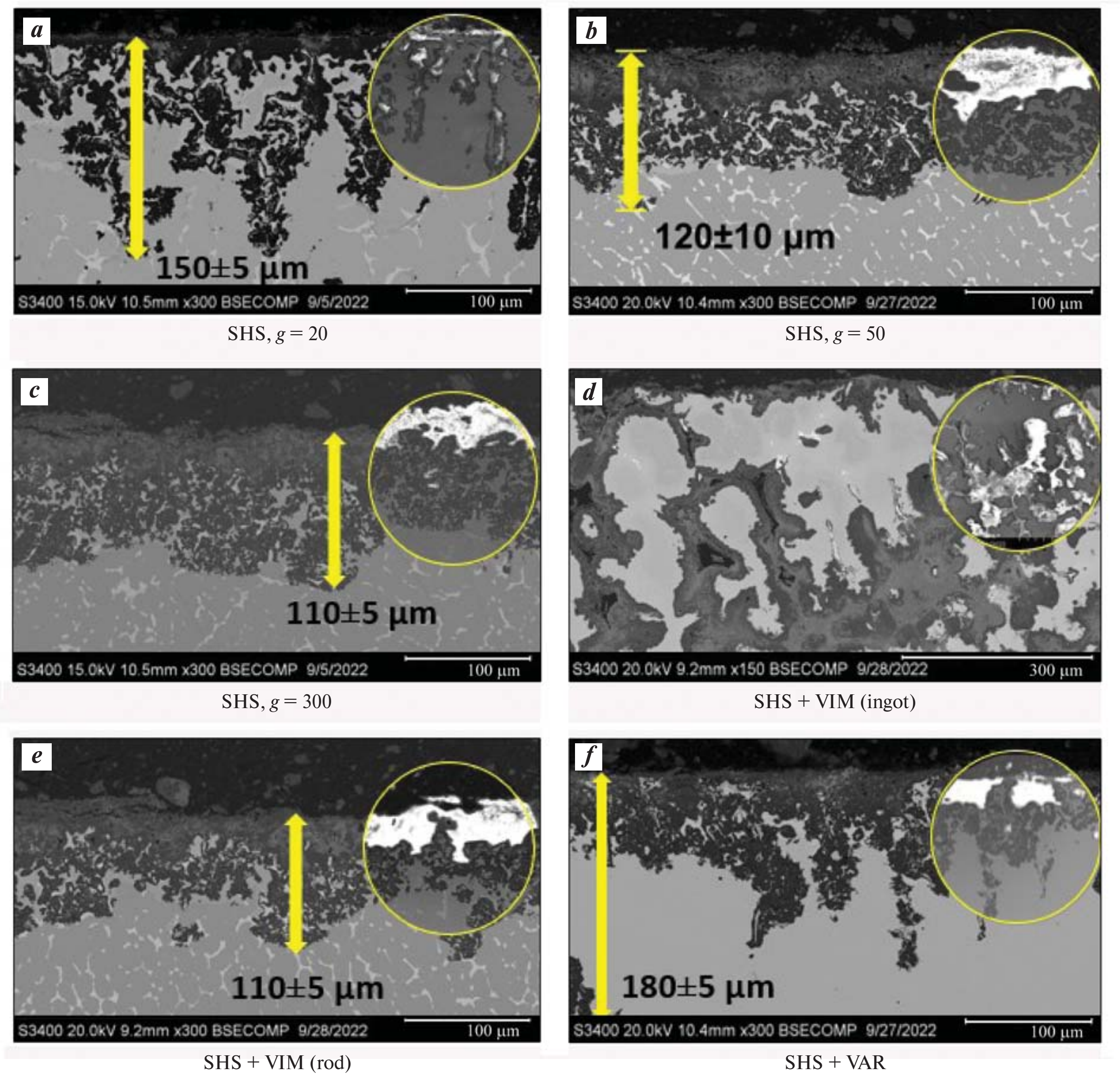

SHS, *g* = 20

SHS, *g* = 50

SHS, *g* = 300

SHS + VIM (ingot)

SHS + VIM (rod)

SHS + VAR

Fig. 7. Microstructure of base–2.5Mo–1.5Re–1.5Ta–0.2Ti alloy samples after annealing at 1150 °C for 30 h

Рис. 7. Микроструктура образцов сплавов base–2,5Mo–1,5Re–1,5Ta–0,2Ti после отжига при температуре 1150 °C в течение 30 ч

SHS sample synthesized at $g = 20$ is distinguished by the wedge-like penetration of aluminum nitrides into the ingot along the grain boundaries, which contributes to an increased oxide layer thickness. The mass gain for the SHS + VIM (rod) sample registers at 45.1 ± 10 g/m^2, likely attributable to the diminution of deleterious gas impurities from $\Sigma_{\text{O,N}} = 0.0191$ wt.% in the SHS sample ($g = 300$) to $\Sigma_{\text{O,N}} = 0.0027$ in the SHS + VIM (rod) sample. The dissolved nitrogen and oxygen content markedly affects both the kinetics and mechanism of oxidation. [18; 19]. However, the impact of dissolved gases on oxidation mechanisms must be evaluated in conjunction with the scale of structural constituents.

The VIM ingot sample, cooled at a different rate and characterized by larger dendritic sizes, displayed distinct oxidation kinetics and mechanism. This sample witnessed an oxidized layer thickness exceeding 250 µm, with oxidation progressing along β-phase interphase boundaries. Its substantial mass gain during oxidation ($\tau = 30$ h; 421 ± 5 g/m^2) is attributed to intense oxidation ($k_p = 5.28 \cdot 10^{-9} \div 1.64 \cdot 10^{-8}$ g^2/cm^4/s), where Cr and Mo form volatile oxides that sublimate without forming additional protective layers, leaving no continuous aluminum oxide layer on the sample's surface.

The SHS + VAR sample also recorded a high mass gain during oxidation ($\tau = 30$ h; 183 ± 5 g/m^2), with no-

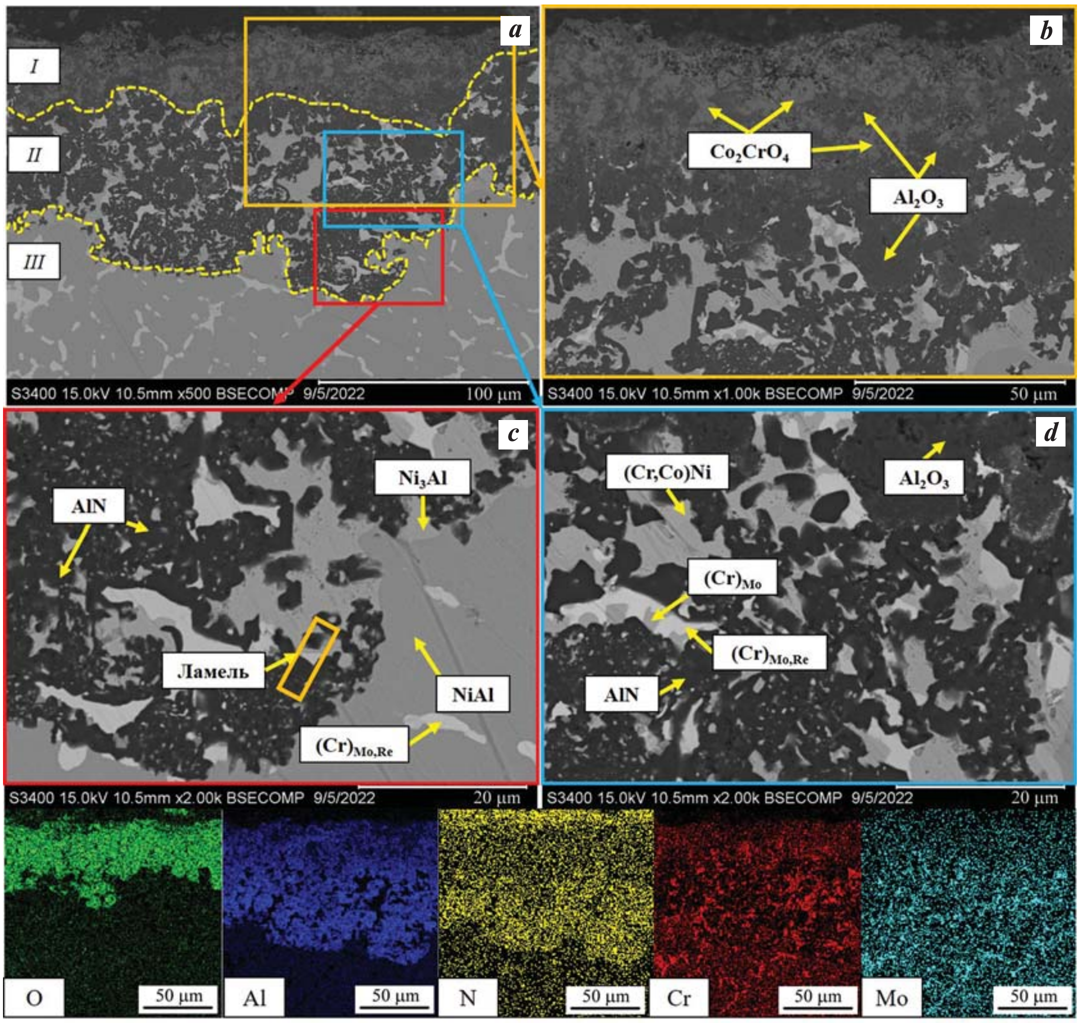

Fig. 8. Surface microstructure of oxidized (***a***) base–2.5Mo–1.5Re–1.5Ta–0.2Ti sample ($g = 50$), selected areas for analysis (***b***–***d***), element distribution maps, lamellae cutting site (***c***)

Рис. 8. Микроструктура поверхности окисленного образца (***a***) состава base–2,5Mo–1,5Re–1,5Ta–0,2Ti ($g = 50$), выделенные области анализа (***b***–***d***), карты распределения элементов и место резки ламели (***c***)

table crack formation after 12 h (Fig. 5) shows a crack formed after 12 h of oxidation. Analysis (Fig. 5 and 7) reveals that structural components' dimensional factors resemble those in other samples, but the oxidation kinetics change with alterations in chemical composition due to the VAR process. This process increases the tungsten content to 0.11 wt.%, while reducing the presence of tantalum and other elements (refer to Table 4).

The examination of the oxidized surface of sample *3* of the base—2.5Mo—1.5Re—1.5Ta—0.2Ti alloy ($g = 50$) is depicted in Fig. 8. This alloy is composed of three distinct layers. The uppermost oxide layer, measuring 40 μm in thickness and comprising Al_2O_3 and Co_2CrO_4 spinel, is notable for its low density and the presence of numerous pores. Beneath this layer lies a thin, continuous sublayer of Al_2O_3 (5—10 μm thick) that acts as a barrier against oxygen infiltration into the ma-

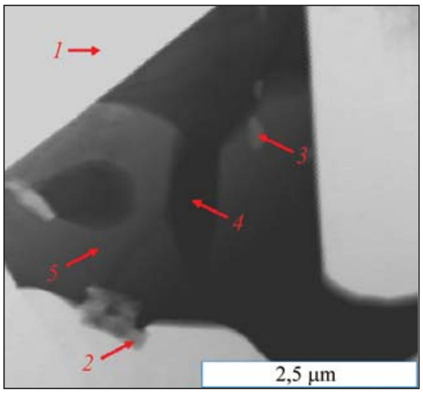

Fig. 9. TEM image and EDS analysis areas of lamella from oxidized layer of base–2.5Mo–1.5Re–1.5Ta–0.2Ti sample ($g = 50$) in the Me–MeO transition layer

Рис. 9. ПЭМ изображение ламели из окисленного слоя образца base–2,5Mo–1,5Re–1,5Ta–0,2Ti ($g = 50$) и области ЭДС в переходном слое Me–MeO

Table 6. **Chemical composition (at.%) of lamella from oxidized layer of base–2.5%Mo–1.5%Re–1.5%Ta–0.2%Ti sample (*g* = 50)**

Таблица 6. Химический состав (ат.%) ламели из окисленного слоя образца base–2,5Mo–1,5Re–1,5Ta–0,2Ti (*g* = 50)

Spectrum	N	Al	Ti	Cr	Co	Ni	Mo	Re
1	38.71	61.29	–	–	–	–	–	–
2	52.83	–	40.24	5.63	0.38	0.93	–	–
3	–	–	21.79	48.61	5.76	18.35	5.49	–
4	–	–	–	49.31	12.33	20.40	10.83	7.13
5	7.28	–	–	54.11	7.36	24.04	7.20	0.00

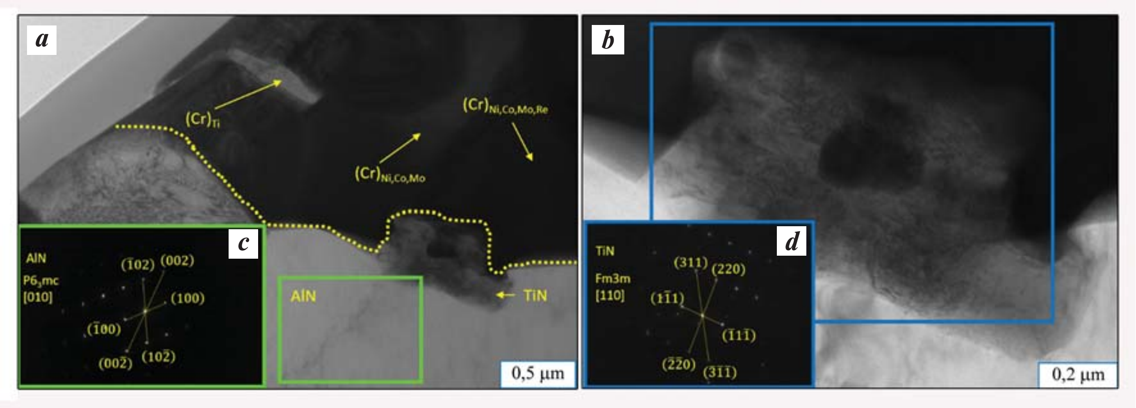

Fig. 10. TEM image of transition layer in base–2.5Mo–1.5Re–1.5Ta–0.2Ti sample (*g* = 50)

a – distribution of structural components; ***b*** – enlarged view of TiN phase; ***c*** – *X*-ray diffraction pattern from AlN grain along zone axis [010]; ***d*** – *X*-ray diffraction pattern from TiN grain along zone axis [110]

Рис. 10. ПЭМ-изображение структурных составляющих переходного слоя образца base–2,5Mo–1,5Re–1,5Ta–0,2Ti (*g* = 50)

a – распределение структурных составляющих в ламели; ***b*** – увеличенная область фазы TiN; ***c*** – электронограмма с зерна AlN вдоль оси зоны [010]; ***d*** – электронограмма с зерна TiN вдоль оси зоны [110]

terial. Adjacent to the substrate, a substantial layer (up to 100 μm thick) predominated by AlN features inclusions of chromium-containing phases such as (Cr,Co)Ni, $(Cr)_{MoRe}$, and $(Cr)_{Mo}$.

TEM studies were conducted to detail the composition of dispersed phases located along the AlN grain boundaries in the intermediate layer near the substrate. A lamella was extracted from the cross-section of the metal-nitride (MeN—Me) transition layer, with its position depicted in Fig. 8, *c*. The structure of this lamella is illustrated in Figs. 9 and 10, with specific analysis sites marked in Fig. 9. These sites were identified using the EDS method (spectra *1*—*5*), and the findings are documented in Table 6. AlN, exhibiting a hexagonal crystal structure (space group P6₃mc) with lattice parameters *a* = 3.078 Å and *c* = 5.004 Å, is identified as the principal phase of the transition layer (Fig. 9, Table 6, spectrum *1*). Nitrogen diffusing along the grain boundaries of the porous oxide layer Al_2O_3 + Co_2CrO_4 into the alloy's depth, and nitrogen impurities in the alloy, react with the aluminum in the matrix to form AlN. This interaction leads to a localized depletion of aluminum in the alloy, resulting in the creation of chromium (Cr)-based solid solutions with a BCC crystal lattice (space group Im3m), containing Ti, Co, Ni, Mo, and Re in concentrations ranging from 5 to 24 at.% (Fig. 9, Table 6, spectra *3*—*5*). Moreover, the oxidized layer contains submicron grains of a titanium-containing phase, likely TiN nitride (spectrum *2*).

At the interface of the solid solution of chromium (Cr) and AlN aluminum nitride, submicron inclusions of the HCC-phase of TiN with a lattice parameter *a* = = 4.207 Å were observed (Fig. 10). The formation of TiN, in reducing the alloy's dissolved nitrogen content (refer to Table 4), also activates the diffusion of aluminum towards the surface. This process facilitates the formation of a dense oxide layer, thereby enhancing the alloy's heat resistance.

Investigating the effects of impurities and non-metallic inclusions on the mechanical properties and oxidation kinetics of the base—2.5Mo—1.5Re—1.5Ta—0.2Ti alloy is crucial for devising the optimal ingot production method to achieve superior alloy characteristics.

Conclusions

1. The investigation elucidated the significant impact of centrifugal acceleration and subsequent metallurgical treatments (VIM) and VAR) on the structural, mechanical, and thermal resistance characteristics of the base—2.5Mo—1.5Re—1.5Ta—0.2Ti alloy.

2. Evaluation of the samples, adhering to GOST 1778-70 and amalgamating all categories of non-metallic inclusions, demonstrated a reduction in the presence of non-metallic inclusions from 5 to 1—2 points with an increase in centrifugal acceleration. The optimal centrifugal acceleration was identified as $g = 50$, beyond which the reduction in inclusion count was not significantly observed. While metallurgical processing (VIM, VAR) did not notably affect the inclusion score, it resulted in the noticeable growth of grain size.

3. Within the β-phase matrix, the presence of globular micron and submicron inclusions of a chromium solid solution was noted. Inclusions $(Cr)_{Ni,Mo,Co}$, $(Cr)_{Mo,Re}$ and $(Cr)_{Re,Mo}$ with a thickness of 2—8 μm are formed in the intergrain space. Additionally, the formation of the Ni(Al,Ti) phase at grain boundaries was observed, contributing to an enhanced resistance to plastic deformation and increased alloy strength.

4. The best combination mechanical properties, including tensile strength (σ_{ucs}), yield strength (σ_{ys}), and residual deformation, were observed in alloys synthesized under overload conditions of $g = 50$ to 300, achieving $\sigma_{ucs} = 1640 \pm 20$ MPa and $\sigma_{ys} = 1518 \pm 10$ MPa. the SHS + VIM samples (ingot) exhibited deteriorated mechanical properties ($\sigma_{ucs} = 1304 \pm 10$ MPa and $\sigma_{ys} = 1126 \pm 10$ MPa), attributed to the enlargement of structural components due to slow cooling rates ($V_{cooled\ 1} = 50$ °C/min).

5. Impurity elements such as Mg, Na, Si, Ca, K, Mn, Cu were identified as incidental, originating from the initial reagents. The total impurity content remained within acceptable limits of 0.15 ± 0.02 %. Notably, an increase in centrifugal acceleration resulted in a decrease in the levels of impurity oxygen and nitrogen.

References

1. Ying Wang, Hong-bo Guo, Hui Peng, Li-quan Peng, Sheng-kai Gong. Diffusion barrier behaviors of (Ru,Ni) Al/NiAl coatings on Ni-based superalloy substrate. *Intermetallics.* 2011;19(2):191—195. https://doi.org/10.1016/j.intermet.2010.08.016
2. Dongjun Wang, Ying Liang, Hanwei Ning, Bao Wang. Effects of Zr and Co on the microstructure and mechanical properties of NiAl-based alloys. *Journal of Alloys and Compounds.* 2021;883:160815. https://doi.org/10.1016/j.jallcom.2021.160815
3. Sui X., Lu J., Wei D., Zhang L., Wang R., Zhao W., Zhang W. Unveiling the influence of TiN on the microstructure and high-temperature oxidation behavior of Ti—Al—Cr composite coating. *Corrosion Science.* 2022;206:110539. https://doi.org/10.1016/j.corsci.2022.110539
4. Shang Z., Shen J., Wang L., Du Y., Xiong Y., Fu H. Investigations on the microstructure and room temperature fracture toughness of directionally solidified NiAl—Cr(Mo) eutectic alloy. *Intermetallics.* 2015;57:25—33. https://doi.org/10.1016/j.intermet.2014.09.012
5. Hu L., Zhang G., Hu W., Gottstein G., Bogner S., Bührig-Polaczek A. Tensile creep of directionally solidified NiAl—9Mo in situ composites. *Acta Materialia.* 2013;61(19):7155—7165. https://doi.org/10.1016/j.actamat.2013.08.017
6. Grabke H.J. Oxidation of NiAl and FeAl. *Intermetallics.* 1999;7(10):1153—1158. https://doi.org/10.1016/S0966-9795(99)00037-0
7. Kovalev A., Wainstein D., Rashkovskiy A. Influence of Al grain boundaries segregations and La-doping on embrittlement of intermetallic NiAl. *Applied Surface Science.* 2015;354:323-327. https://doi.org/10.1016/j.apsusc.2015.06.110
8. Kaplanskii Yu.Yu., Levashov E.A., Korotitskiy A.V., Loginov P.A., Sentyurina Zh.A., Mazalov A.B. Influence of aging and HIP treatment on the structure and properties of NiAl-based turbine blades manufactured by laser powder bed fusion. *Additive Manufacturing.* 2020;31:100999 https://doi.org/10.1016/j.addma.2019.100999
9. Levashov E.A., Mukasyan A.S., Rogachev A.S., Shtansky D.V. Self-propagating high-temperature synthesis of advanced materials and coatings. *International Materials Reviews.* 2017; 62(4): 203—239. https://doi.org/10.1080/09506608.2016.1243291
10. Kurbatkina V.V. Nickel aluminides. In: *Concise encyclopedia of self-propagating high-temperature synthesis.* Elsevier, 2017. P. 212—213. https://doi.org/10.1016/B978-0-12-804173-4.00099-5
11. Sanin V.V., Kaplansky Y.Y., Aheiev M.I., Levashov E.A.,

Petrzhik M.I., Bychkova M.Ya., Samokhin A.V., Fadeev A.A., Sanin V.N. Structure and properties of heat-resistant alloys NiAl—Cr—Co—X (X = La, Mo, Zr, Ta, Re) and fabrication of powders for additive manufacturing. *Materials.* 2021;14(12):3144.
https://doi.org/10.3390/ma14123144

12. Zaitsev A.A., Sentyurina Zh.A., Levashov E.A., Pogozhev Yu.S., Sanin V.N., Loginov P.A., Petrzhik M.I. Structure and properties of NiAl—Cr(Co,Hf) alloys prepared by centrifugal SHS casting. Part 1 — Room temperature investigations. *Materials Science and Engineering: A*. 2017;690:463—472.
https://doi.org/10.1016/j.msea.2016.09.075
13. Klumpes R., Maree C.H.M., Schramm E., de Wit J.H.W. The influence of chromium on the oxidation of β-NiAl at 1000 °C. *Materials and Corrosion.* 1996;47(11):619—624.
https://doi.org/10.1002/maco.19960471105
14. Bo Li, Fei Liu, Cong Li, Yimin Gao, Congmin Fon, Xiaohu Hou. Effect of Cr element on the microstructure and oxidation resistance of novel NiAl-based high temperature lubricating composites. *Corrosion Science.* 2021;188:109554.
https://doi.org/10.1016/j.corsci.2021.109554
15. Gao W., Li Z., Wu Z., Li S., He Y. Oxidation behavior of Ni_3Al and FeAl intermetallics under low oxygen partial pressures. *Intermetallics.* 2002;10(3):263—270.
https://doi.org/10.1016/S0966-9795(01)00132-7
16. Zaitsev A.A., Sentyurina Zh.A., Levashov E.A., Pogozhev Yu.S., Sanin V.N., Sidorenko D.A. Structure and properties of NiAl—Cr(Co,Hf) alloys prepared by centrifugal SHS casting followed by vacuum induction remelting. Part 2 — Evolution of the structure and mechanical behavior at high temperature. *Materials Science and Engineering: A*. 2017;690:473—481.
http://doi.org/10.1016/j.msea.2017.02.089
17. Kaplanskii Yu.Yu., Zaitsev A.A., Levashov E.A., Pogozhev Yu.S., Loginov P.A., Sentyurina Zh.A., Logacheva A.I. The structure and properties of pre-alloyed NiAl—Cr(Co,Hf) spherical powders produced by plasma rotating electrode processing for additive manufacturing. *Journal of Materials Research and Technology.* 2018;7(4):461—468.
https://doi.org/10.1016/j.jmrt.2018.01.003
18. Aheiev M.I., Sanin V.V., Shvindina N.V., Kaplanskii Yu.Yu., Levashov E.A. Oxidation kinetics and mechanism of nickel alloys. *Powder Metallurgy and Functional Coatings.* 2022;(3):4—23.
https://doi.org/10.17073/1997-308X-2022-3-4-23
Агеев М.И., Санин В.В., Швындина Н.В., Капланский Ю.Ю., Левашов Е.А. Кинетика и механизм окисления никелевых сплавов. *Известия вузов. Порошковая металлургия и функциональные покрытия.* 2022;(3):4—23.
19. Sanin V.V., Aheiev M.I., Kaplanskii Yu.Yu., Loginov P.A., Bychkova M.Ya., Levashov E.A. The effect of dopants on structure formation and properties of cast SHS alloys based on nickel monoaluminide. *Materials.* 2023;16(9):3299.
https://doi.org/10.3390/ma16093299
20. Logunov A.V. Heat-resistant nickel alloys for gas turbine blades and discs. Moscow: Gazoturbinnye Tekhnologii, 2017. 854 p. (In Russ.).
Логунов А.В. Жаропрочные никелевые сплавы для лопаток и дисков газовых турбин. М.: Газотурбинные технологии, 2017. 854 с.
21. Zhang W.L., Li S.M., Fu L.B., Li W., Sun J., Wang T.G., Jiang S.M., Gong J., Sun C. Preparation and cyclic oxidation resistance of Hf-doped NiAl coating. *Corrosion Science.* 2022;195:110014.
https://doi.org/10.1016/j.corsci.2021.110014
22. Dingding Zhu, Xinli Wang, Peng Jia, Canying Cai, Jianyu Huang, Guangwen Zhou. One-dimensional γ-Al_2O_3 growth from the oxidation of NiAl. *Corrosion Science.* 2023;216:111069.
https://doi.org/10.1016/j.corsci.2023.111069

Information about the authors

Vitaly V. Sanin – Cand. Sci. (Eng.), Leading Researcher of the Laboratory of Metallurgical Processes of JSC "Giredmet"; Researcher of the Scientific-Educational Center of SHS of MISIS–ISMAN.
https://orcid.org/0000-0002-9983-654X
E-mail: vivsanin@rosatom.ru

Maksym I. Aheiev – Cand. Sci. (Eng.), Junior Researcher, Scientific-Educational Center of SHS of MISIS–ISMAN.
https://orcid.org/0000-0003-2079-8710
E-mail: aheievmi@gmail.com

Pavel A. Loginov – Cand. Sci. (Eng.), Researcher, Scientific-Educational Center of SHS of MISIS–ISMAN.
https://orcid.org/0000-0003-2505-2918
E-mail: pavel.loginov.misis@list.ru

Marina Ya. Bychkova – Cand. Sci. (Eng.), Assistant Prof. of National University of Science and Technology "MISIS" (NUST MISIS), Researcher of Scientific-Educational Center of SHS of MISIS–ISMAN.
https://orcid.org/0000-0002-9233-4707
E-mail: bychkova@shs.misis.ru

Elizaveta S. Shukman – Head of the Analytical Certification Center of JSC "Giredmet".
https://orcid.org/0000-0001-9999-6888
E-mail: ESKoshel@rosatom.ru

Liliya Yu. Mezhevaia – Senior Researcher of the Analytical Certification Center of JSC "Giredmet"; Postgraduate Student of the Department of Certification and Analytical Control, NUST MISIS.
https://orcid.org/0000-0001-9481-3149
E-mail: lymezhevaya@rosatom.ru

Vladimir N. Sanin – Dr. Sci. (Eng.), Chief Researcher, Merzhanov Institute of Structural Macrokinetics and Materials Science of the Russian Academy of Sciences.
https://orcid.org/0000-0001-8402-4605
E-mail: svn@ism.ac.ru

Tamara A. Lobova – Dr. Sci. (Eng.), Prof. of the Department of Powder Metallurgy and Functional Coating of NUST MISIS.
https://orcid.org/0009-0002-1749-0782
E-mail: smazka39@mail.ru

Информация об авторах

Виталий Владимирович Санин – к.т.н., вед. научный сотрудник лаборатории металлургических процессов АО «Гиредмет», науч. сотрудник Научно-учебного центра (НУЦ) СВС МИСИС–ИСМАН.
https://orcid.org/0000-0002-9983-654X
E-mail: sanin@misis.ru

Максим Игоревич Агеев – к.т.н., мл. науч. сотрудник НУЦ СВС МИСИС–ИСМАН.
https://orcid.org/0000-0003-2079-8710
E-mail: aheievmi@gmail.com

Павел Александрович Логинов – к.т.н., науч. сотрудник НУЦ СВС МИСИС–ИСМАН.
https://orcid.org/0000-0003-2505-2918
E-mail: pavel.loginov.misis@list.ru

Марина Яковлевна Бычкова – к.т.н., доцент Национального исследовательского технологического университета «МИСИС» (НИТУ МИСИС), науч. сотрудник НУЦ СВС МИСИС–ИСМАН.
https://orcid.org/0000-0002-9233-4707
E-mail: bychkova@shs.misis.ru

Елизавета Сергеевна Шукман – начальник испытательного аналитико-сертификационного центра АО «Гиредмет».
https://orcid.org/0000-0001-9999-6888
E-mail: ESKoshel@rosatom.ru

Лилия Юрьевна Межевая – ст. науч. сотрудник испытательного аналитико-сертификационного центра АО «Гиредмет», аспирант кафедры сертификации и аналитического контроля НИТУ МИСИС.
https://orcid.org/0000-0001-9481-3149
E-mail: lymezhevaya@rosatom.ru

Владимир Николаевич Санин – д.т.н., гл. науч. сотрудник Института структурной макрокинетики и проблем материаловедения им. А.Г. Мержанова РАН (ИСМАН).
https://orcid.org/0000-0001-8402-4605
E-mail: svn@ism.ac.ru

Тамара Александровна Лобова – д.т.н., профессор кафедры порошковой металлургии и функциональных покрытий НИТУ МИСИС.
https://orcid.org/0009-0002-1749-0782
E-mail: smazka39@mail.ru

Contribution of the authors

V.V. Sanin – determined the research's objective and conceptual framework, wtote the article, executed the synthesis processes, performed additional metallurgical processing, and engaged in the discussion and documentation of the findings.

M.I. Aheiev – defined the work's aim and conceptualization, contributed to writing the manuscript, conducted microstructural examinations, *X*-ray diffraction structural analyses, mechanical testing, and assessments of heat resistance, participated in discussions and the elucidation the results.

Вклад авторов

В.В. Санин – определение цели работы и концепции исследований, написание статьи, проведение синтезов, проведение дополнительных металлургических переделов, обсуждение и описание результатов.

М.И. Агеев – определение цели работы и концепции исследований, написание статьи, проведение микроструктурных исследований, рентгенофазового структурного анализа, механических испытаний, испытаний на жаростойкость, обсуждение и описание результатов.

P.A. Loginov – focused on transmission microscopy investigations, contributed to the discussions, interpretation of the results, and co-authored the article.

M.Ya. Bychkova – participating in the discussion of the research concept and results, describing the results of the *X*-ray diffraction structural analysis and microstructural studies.

E.S. Shukman – undertook the analysis to ascertain the chemical composition of the alloys, described these findings, and participated in the deliberation of the results.

L.Yu. Mezhevaia – carried out the investigation of metallographic sections using optical microscopy, evaluated the nonmetallic inclusions, documented the chemical composition results, and contributed to the discussion of the findings.

V.N. Sanin – engaged in conceptual discussions, undertook synthesis and metallurgical processing tasks, and participated in analyzing and discussing the research outcomes.

T.A. Lobova – defined the research direction and framework, took part in discussions on the findings, and described the outcomes of the mechanical tests.

П.А. Логинов – проведение исследований методом просвечивающей микроскопии, описание результатов и их обсуждение, написание статьи.

М.Я. Бычкова – участие в обсуждении концепции исследований, участие в обсуждении результатов, описание результатов рентгенофазового структурного анализа и микроструктурных исследований.

Е.С. Шукман – проведение исследований по определению химического состава, описание результатов и участие в их обсуждении.

Л.Ю. Межевая – исследование металлографических шлифов методом оптической микроскопии, проведение оценки неметаллических включений, описание результатов определения химического состава, участие в обсуждении результатов.

В.Н. Санин – участие в обсуждении концепции исследований, проведение синтезов и металлургических переделов, обсуждение результатов исследований.

Т.А. Лобова – определение цели работы и концепции исследований, обсуждение результатов исследований, описание результатов механических испытаний.

The article was submitted 29.01.2024, revised 12.02.2024, accepted for publication 14.02.2024

Статья поступила в редакцию 29.01.2024, доработана 12.02.2024, подписана в печать 14.02.2024

PHYSICAL METALLURGY AND HEAT TREATMENT / МЕТАЛЛОВЕДЕНИЕ И ТЕРМИЧЕСКАЯ ОБРАБОТКА

UDC 620.181 : 669
https://doi.org/10.17073/0021-3438-2024-1-42-54

Research article
Научная статья

Effects of quenching temperature on the structure, segregation, and properties of the AM4.5Kd + 0.2 wt.% La alloy after artificial aging

N.A. Slavinskaya, H. Ri, E.H. Ri, A.S. Zhivetev

Pacific National University
136 Tikhookeanskaya Str., Khabarovsk 680035, Russia

✉ Andrei S. Zhivetev (007881@pnu.edu.ru)

Abstract: The identification of structural components in the AM4.5Kd + 0.2 wt.% La alloy, subjected to quenching at different temperatures (535–605 °C) and artificial aging at 155 °C for 4 h, was conducted through electron microscopy and XRD. An increase in the quenching temperature (t_q) from 535 to 605 °C promotes the enlargement of structural components, including the α-solid solution, various aluminides, and eutectics. We observed that the base metal is not homogeneous in its chemical composition, consisting of two types of solid solutions: α_1 and α_2. The Cu and Mn solubility in the α_2-solid solution is higher than in the α_1-solid solution. As the quenching temperature increases to t_q = 605 °C, the copper content in the α_1-solid solution decreases. In contrast, the copper content in the α_2-solid solution follows a curve with two maxima at 545 °C (4.5 at.%) and 585 °C (8.7 at.%). The Mn content in the α_1-solid solution decreases sharply to the 545 °C quenching temperature and remains relatively constant up to t_q = 605 °C (0.2 at.%). The Mn content in the α_2-solid solution follows a curve with its maximum at t_q = 545 °C (4.3 at.% Mn). Subsequent temperature rise results in a sharp drop in Mn content from 1.0 at.% at t_q = 565 °C to 0.3 at.% at 605 °C. Hence, the max solubility of Cu and Mn in the α_2-solid solution occurs at 545 °C. At 585 °C, only an elevated Cu content (~8.7 at.%) was observed. Aluminides of alloying elements with different stoichiometries crystallize at different quenching temperatures, with complex $Al_xTi_yLa_zCu_vCd_w$ and $Al_xCu_yMn_zCd_v$ alloyed aluminides being most commonly found. ncreasing the quenching temperature to 535–545 °C results in higher hardness of the AM4.5Kd + 0.2 wt.% of La alloy, reaching 98–104 HB, with subsequent decrease to 60 HB as the quenching temperature reaches 605 °C. The hardness of the unhardened alloy is 60 HB. The optimal quenching temperature for the AM4.5Kd + 0.2 wt.% of La alloy is in the range of 535–545 °C. This temperature corresponds to the highest hardness of the alloy and the microhardness of the aluminide.

Keywords: AM4.5Kd aluminum alloy, La addition, quenching, aging, phase composition, aluminides, hardness, microhardness.

For citation: Slavinskaya N.A., Ri H., Ri E.H., Zhivetev A.S. The influence of tempering temperature conditions on the formation of the structure, liquation processes and properties of the alloy AM4.5Kd + 0.2 wt.% La after artificial aging. *Izvestiya. Non-Ferrous Metallurgy.* 2024;30(1):42–54. https://doi.org/10.17073/0021-3438-2024-1-42-54

Влияние температурных режимов закалки на формирование структуры, ликвационные процессы и свойства сплава АМ4,5Кд + 0,2 мас.% La после искусственного старения

Н.А. Славинская, Х. Ри, Э.Х. Ри, А.С. Живетьев

Тихоокеанский государственный университет
Россия, 680035, г. Хабаровск, ул. Тихоокеанская, 136

✉ Андрей Сергеевич Живетьев (007881@pnu.edu.ru)

Аннотация: Методами электронно-микроскопического исследования и микрорентгеноспектрального анализа элементов идентифицированы структурные составляющие сплава АМ4,5Кд + 0,2 мас.% La после закалки с различных температур (t = 535÷605 °С) и искусственного старения при t = 155 °С в течение 4 ч. Повышение температуры закалки от 535 до 605 °С способствует укрупнению структурных составляющих – α-твердого раствора, алюминидов различного состава, эвтектики. Установлено, что металлическая основа неоднородна по химическому составу и состоит из двух видов твердого раствора – α_1 и α_2. В α_2-твердом растворе растворяются в большей степени Cu и Mn, по сравнению с α_1-твердым раствором. С увеличением температуры закалки до 605 °С содержание меди в α_1-твердом растворе уменьшается, в то же время в α_2-твердом растворе концентрация меди изменяется по экстремальной зависимости с двумя ее максимумами при температурах 545 °С (4,5 ат.%) и 585 °С (8,7 ат.%). Содержание марганца в α_1-твердом растворе резко снижается до температуры закалки 545 °С, а затем остается без изменения до t = 605 °С (0,2 ат.%). Содержание марганца в α_2-твердом растворе изменяется также по экстремальной зависимости с максимумом концентрации при t = 545 °С (4,3 ат.% Mn). Дальнейшее повышение температуры закалки способствует резкому уменьшению содержания марганца от 1,0 ат.% при t = 565 °С до 0,3 ат.% Mn при температуре закалки 605 °С. Таким образом, максимальная растворимость Cu и Mn в α_2-твердом растворе наблюдается при температуре закалки 545 °С. При температуре закалки 585 °С фиксируется только повышенное содержание меди (~8,7 ат.%). В зависимости от температуры закалки кристаллизуются алюминиды легирующих элементов с различной стехиометрией. Наиболее часто встречаются комплексно-легированные алюминиды титана $Al_xTi_yLa_zCu_vCd_w$ и меди $Al_xCu_yMn_zCd_v$. Увеличение температуры закалки до 535–545 °С способствует росту твердости сплава АМ4,5Кд + 0,2 мас.% La до 98–104 HB с последующим ее снижением (60 HB) до температуры закалки 605 °С. Сплав без термической обработки имел твердость 60 HB. Оптимальный режим закалки сплава АМ4,5Кд + 0,2 мас.% La соответствует температуре 535–545 °С, при которой наблюдаются максимальные твердость сплава и микротвердость интерметаллида.

Ключевые слова: алюминиевый сплав АМ4,5Кд, модифицирование La, закалка, искусственное старение, фазовый состав, алюминиды, твердость, микротвердость.

Для цитирования: Славинская Н.А., Ри Х., Ри Э.Х., Живетьев А.С. Влияние температурных режимов закалки на формирование структуры, ликвационные процессы и свойства сплава АМ4,5Кд + 0,2 мас.% La после искусственного старения. *Известия вузов. Цветная металлургия*. 2024;30(1):42–54.
https://doi.org/10.17073/0021-3438-2024-1-42-54

Introduction

The enhancement of aluminum alloys, both at standard and elevated temperatures, is frequently employed to manufacture dependable and durable components for the aerospace and automotive industries [1]. Their strength characteristics closely resemble those of gray cast iron and carbon steel [2]. However, it is noteworthy that aluminum alloys exhibit lower wear resistance compared to the latter materials [3; 4].

It has been established that Al—Cu alloys exhibit high heat resistance, as exemplified by the AM5 casting alloy (GOST 1583—93) and the deformable alloys 1201, D16, and AK4—1 (GOST 4784—97). Nevertheless, their heat resistance is sustained only up to temperatures of 200—250 °C [2].

A comprehensive literature review indicates that heat treatment (HT) of aluminum alloys is often the sole viable method for achieving the necessary mechanical properties and creating the desired structures in the alloy [5—11]. Previous works, such as those presented in references [5; 8], propose optimal heat treatment procedures aimed at enhancing the mechanical properties [11] of Al—Cu—Mg alloys. Additionally, Korotkova N. et al. [7]

investigated the correlation between the structure of aluminum wire with a 7 % rare earth metal (REM) content and the annealing temperature within the 300—600 °C range.

The impact of heat treatment conditions on the structure and mechanical performance of Al—Mg alloys is systematically assessed in works cited in references [6; 9].

Certain researchers [12—14] employ simulation techniques to model heat treatment processes. Notably, papers [15—17] showcase a notable concordance between the simulated structure, properties, and processes in the Al—Cu—Cd alloy and the corresponding experimental data.

Alloying additives play a crucial role in modifying and controlling the structure and properties of alloys [1; 18—29]. Among the frequently utilized alloying additives, Ti and B are prominent. Research studies [18; 19; 22—24] indicate that these additives alter the morphology of the dendritic α-Al phase, promote the formation of equiaxed grains, and establish new nucleation sites for Ti and B compounds. This leads to a substantial refinement of the alloy structure, resulting in improved mechanical properties. Furthermore, the incorporation of REEs and transition group metals (up to 1 wt.%) enhances the structure of aluminum alloys post-casting and heat treatment. Sahin H. et al. [20] observed that additions of Er and Eu reduce the size of intermetallic phases, while the addition of 0.1 wt.% Sc increases the nanohardness of certain intermetallic compounds [21]. Additionally, the introduction of Ce (up to 0.5 %) diminishes the size of β-Al_5FeSi inclusions from 51 to 21 μm [29]. Andrushevich A. et al [25] remark that the addition of Sr to the AK7h alloy enhances its mechanical properties and influences casting characteristics. This alteration in the solidification pattern disperses pores, positively impacting the tightness of housing parts.

Ri E. et al. [30] conducted a study examining the impacts of metallic lanthanum and cerium additions on the alloy structure, segregation, hardness, and microhardness of the AM4.5Kd (VAL 10) cast alloy. Their findings revealed that lanthanum plays a role in refining the alloy structure, redistributing elements, and augmenting microhardness.

In contrast to aluminum—silicon alloys, the influence of REEs, particularly lanthanum, on the structure, segregation, and properties of the AM4.5Kd cast alloy has not been thoroughly investigated. The components of the AM4.5Kd alloy typically undergo heat treatment involving quenching and aging. The exploration of the synergistic effects of alloying and heat treatment is both theoretically and practically significant.

The objective of this study is to ascertain the impact of quenching temperatures (535, 545, 565, 585, 605 °C) on the structure, segregation, and properties of the AM4.5Kd alloy, which incorporates 0.2 wt.% of lanthanum, following combined heat treatment involving quenching and aging.

Materials and methods

The AM4.5Kd (VAL10) alloy, conforming to GOST 1583-93, was the subject of our investigation. The alloy, weighing 0.7 kg, was melted along with additives in a Graficarbo furnace. The initial AM4.5Kd alloy was loaded into a pre-heated graphite crucible at 450 °C, followed by heating to a temperature of 740 °C. The melting process included a 5-minute holding period to stabilize the temperature within the required range. Subsequently, metallic lanthanum (LaM-1), wrapped in aluminum foil, was introduced. The additional 5-minute holding time ensured a uniform distribution of lanthanum within the alloy. This was succeeded by reheating to 740 °C, another 5-minute holding period, and the casting process. All operations were conducted in an argon environment. Casting was performed using a metal mold with a diameter of 30 mm and a height of 50 mm.

Patel N. et al. [5] proposed the following heat treatment parameters for the AM4.5Kd (VAL 10) cast alloy: T5 heat treatment, involving a temperature range of 545^{+3}_{-5}, with a holding time of 10—14 h, followed by water cooling in the range of 20 to 100 °C. In our study, we employed the following treatment protocol: heating for quenching (to temperatures of 535, 545, 565, 585, 605 °C); holding for 2.5 h, quench hardening in water (at 20 °C), and aging at a temperature of 155 °C for 4.0 h.

The average chemical composition after melting was as following (%): Al: 94.62; Cu: 4.3; Mn: 0.55; Ti: 0.19; La: 0.17; Si: 0.1; Fe: 0.07.

For microstructural analysis, we utilized a FE-SEM Hitachi Su70 (Japan) field emission scanning electron microscope equipped with Thermo Fisher Scientific MagnaRay spectrometers for energy and wave dispersion *X*-ray analysis.

Microhardness measurements (HV) were conducted using the Vickers hardness test method (in accordance with GOST 2999-75 and 9450-76) with a Shimadzu HMV-G microhardness tester (Japan).

Results and discussion

Our investigation focused on examining the impact of quenching temperatures (535, 545, 565, 585, and 605 °C) on the structure, segregation, microhardness of structural components, and overall hardness of the AM4.5Kd alloy with an additional 0.2 wt.% of La. The subsequent aging process at 155 °C was maintained for 4 h.

The SEM analysis of the alloy structure revealed that elevated quenching temperatures contribute to the enlargement of structural components within the α-solid solution and metal aluminides, as depicted in Fig. 1.

At a quenching temperature of $t_q = 565$ °C and above, interfaces of the α-solid solution become evident. Additionally, spherical intermetallic inclusions crystallize within the grains of the α-solid solution.

XRD microanalysis allowed for the identification of structural components that crystallized at different quenching temperatures and subsequent aging.

Let us examine the results for two specific quenching temperatures: 545 °C (Figs. 2, 3, and Table 1) and 605 °C (Fig. 4 and Table 2). At these temperatures, structural

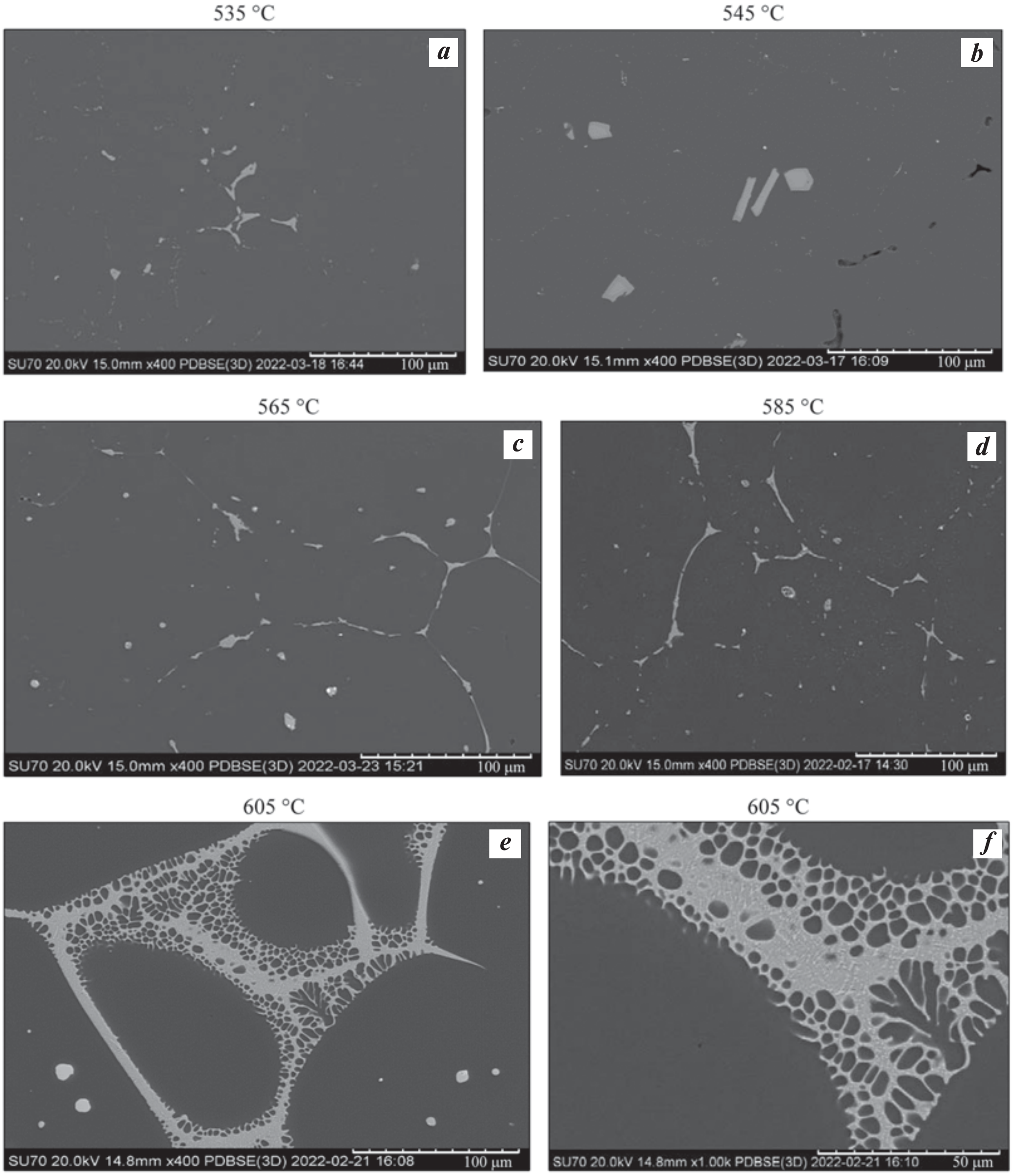

Fig. 1. Microstructure of the AM4.5Kd + 0.2 wt.% of La alloy vs. the quenching temperature (t_q) and after aging at 155 °C

t_q, °C: 535 (***a***), 545 (***b***), 565 (***c***), 585 (***d***), 605 (***e***, ***f***)

Рис. 1. Микроструктура сплава АМ4,5Кд + 0,2 мас.% La в зависимости от температуры закалки ($t_з$) и после искусственного старения при температуре 155 °С

$t_з$, °С: 535 (***a***), 545 (***b***), 565 (***c***), 585 (***d***), 605 (***e***, ***f***)

Table 1. **Composition of the structural components of AM4.5Kd alloy + 0.2 wt.% of La after quenching (545 °C) and subsequent aging (155 °C)**

Таблица 1. Состав структурных составляющих сплава АМ4,5Кд + 0,2 мас.% La после закалки (545 °C) и последующего искусственного старения (155 °C)

Structural components	Elemental analysis points (see Fig. 2)	Content, at.%						
		Al	Ti	Mn	Fe	Cu	Cd	La
α_1 solid solution of Cu, Mn, and Ti in Al	*11–17*	97.45	0.15	0.33	–	2.27	–	–
α_2 solid solution of Cu, Mn, and Fe in Al	*8–10*	89.8	–	4.25	1.22	4.7	0.08	0.46
$Al_{5.45}$(Ti, La, Cd, Cu) alloyed aluminide	*2–6*	84.5	8.52	–	–	0.95	1.63	3.41
		$Al_{84.5}(Ti, La, Cd, Cu)_{15.5} = Al_{5.45}(Ti, La, Cd, Cu)$						
$Al_{5.5}$(Cu, La, Mn, Fe) alloyed aluminide	*1*	84.6	–	1.56	0.33	9.82	–	3.68
		$Al_{84.6}(Cu, La, Mn, Fe)_{15.4} = Al_{5.5}(Cu, La, Mn, Fe)$						

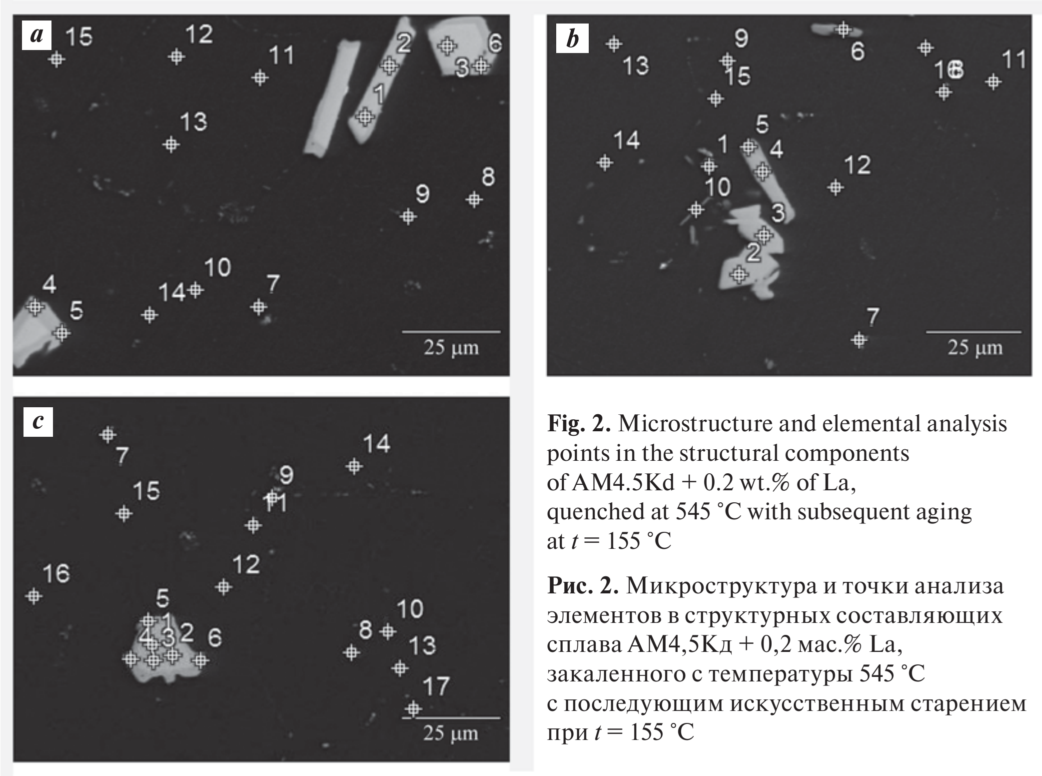

Fig. 2. Microstructure and elemental analysis points in the structural components of AM4.5Kd + 0.2 wt.% of La, quenched at 545 °C with subsequent aging at *t* = 155 °C

Рис. 2. Микроструктура и точки анализа элементов в структурных составляющих сплава АМ4,5Кд + 0,2 мас.% La, закаленного с температуры 545 °C с последующим искусственным старением при *t* = 155 °C

changes occur, leading to the formation of various metal aluminides

In Figs. 2, 3, and Table 1, the results reveal that at t_q = 545 °C, the following structures are formed: α_1 and α_2 solid solutions, as well as $Al_{5.45}$(Ti, La, Cd, Cu) and $Al_{5.5}$(Cu, La, Mn, Fe) aluminides. The crystals of the alloyed aluminide $Al_{5.45}$(Ti, La, Cd, Cu) exhibit a compact morphology resembling either polyhedra or plates, with a width in the range of several microns and a length approximately measuring 25—30 µm.

The presence of these structures is affirmed by the element distribution curves within the structural components of the AM4.5Kd + 0.2 wt.% of La alloy, quenched at 545 °C with subsequent aging. The curves follow the *A—A* line, as illustrated in Fig. 3.

In the structure of the AM4.5Kd + 0.2 wt.% of La alloy, quenched at 605 °C with subsequent aging (Fig. 4 and Table 2), similar crystallized aluminides are observed, differing in their stoichiometry: $Al_{6.0}$(Ti, La, Cu, Cd) and $Al_{3.83}$(Cu, La, Ti, Cd, Mn). Additionally, the $Al_{3.63}$(Cu, La, Mn, Fe) aluminide is crystallized, with its crystals either forming part of the eutectics (Fig. 4, points *5—7*, (*a*), *1—3* (*b*), *9—11* (*c*)) or appearing as light, spherical inclusions (points *1—2* (*c*)).

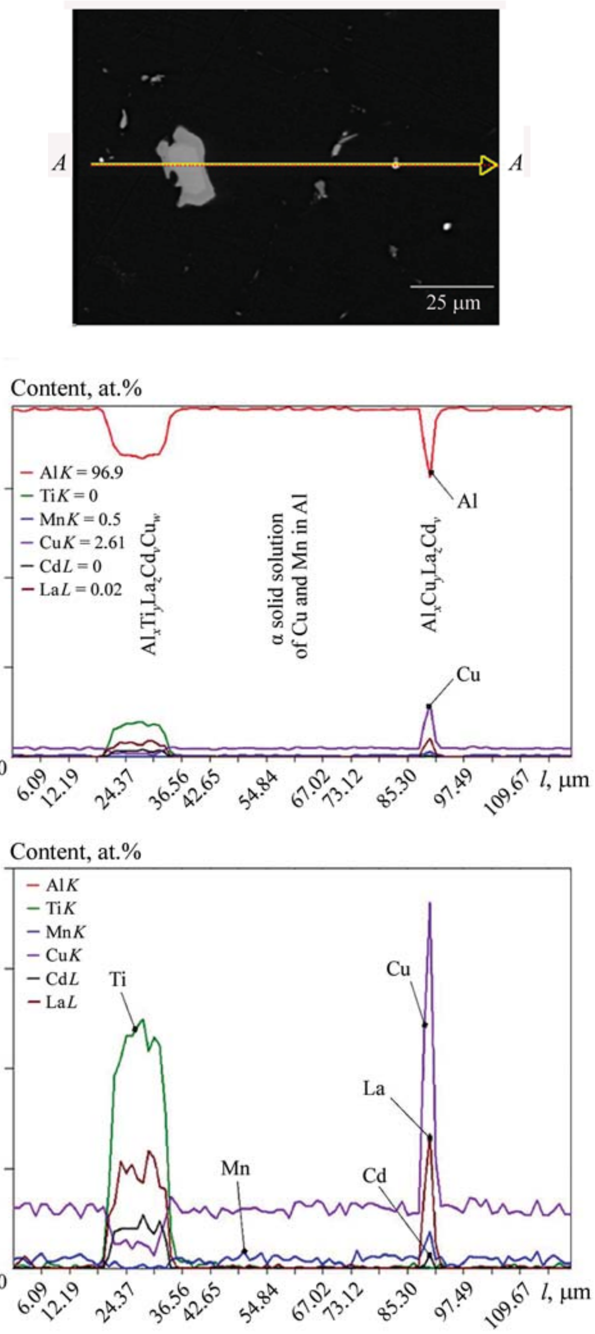

Fig. 3. Element distribution curves in the structural components of the AM4.5Kd + 0.2 wt.% of La alloy quenched at 545 °C with subsequent aging, along the *A*–*A* line

Рис. 3. Кривые распределения элементов в структурных составляющих сплава АМ4,5Кд + 0,2 мас.% La, закаленного с температуры 545 °C с последующим искусственным старением, по направлению профиля *A*–*A*

Table 3 and Fig. 5 reveal that the base metal (α-solid solution) exhibits not-homogeneity in its chemical composition, comprising two types of solid solutions: α_1 and α_2.

As the quenching temperature increases to 605 °C, the copper content in the α_1-solid solution decreases, while the copper content in the α_2-solid solution follows a curve with two maxima at t_q = 545 and 585 °C.

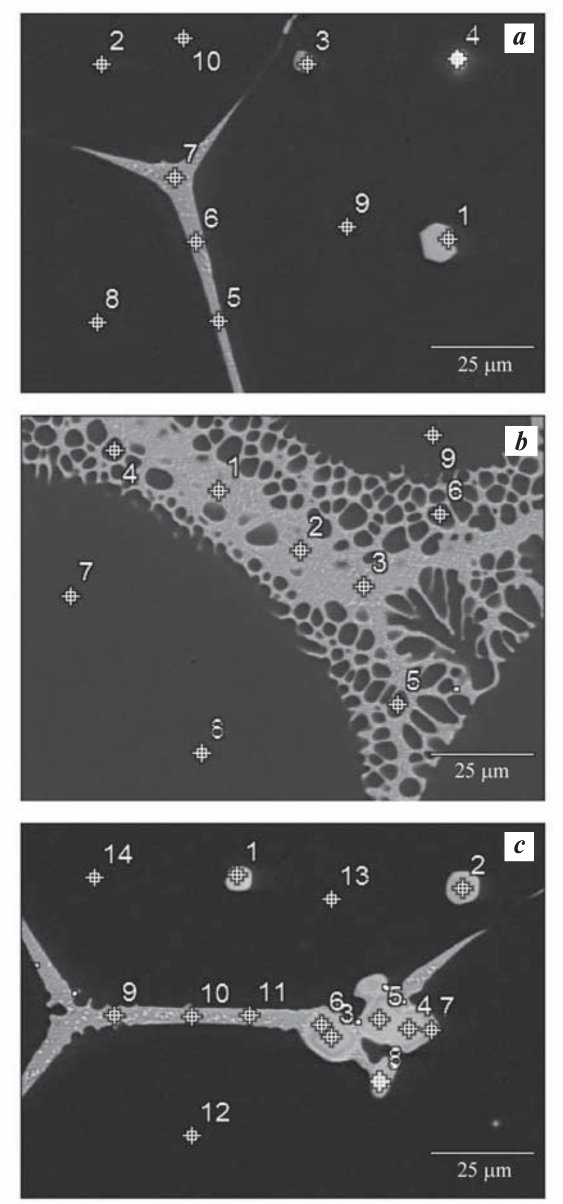

Fig. 4. Microstructure and elemental analysis points in the structural constituents of the AM4.5Kd + 0.2 wt.% of La alloy, quenched at 605 °C with subsequent aging at *t* = 155 °C

Рис. 4. Микроструктура и точки анализа элементов в структурных составляющих сплава АМ4,5Кд + 0,2 мас.% La, закаленного с температуры 605 °C с последующим искусственным старением при *t* = 155 °C

The total copper content in the solid solutions varies similarly. The aluminum content is inversely related to the solubility of copper in the α-solid solution. The content of Al in the α_1-solid solution increases monotonically to t_q = 605 °C (Fig. 5, *a*).

The content of Mn in the α_1-solid solution experiences a rapid decrease until t_q = 545 °C and remains relatively constant up to t_q = 605 °C (Fig. 5, *b*). In contrast, the content of Mn in the α_2-solid solution follows a curve with a maximum at t_q = 545 °C, decreasing thereafter

Table 2. **Composition of the structural components of AM4.5Kd alloy + 0.2 wt.% of La after quenching (605 °C) and subsequent aging (155 °C)**

Таблица 2. Состав структурных составляющих сплава АМ4,5Кд + 0,2 мас.% La после закалки (605 °C) и последующего искусственного старения (155 °C)

Structural components	Elemental analysis points (see Fig. 4)	Content, at.%						
		Al	Ti	Mn	Fe	Cu	Cd	La
α_1 solid solution of Cu, Mn, and Ti in Al	*8–10* (***a***) *7–9* (***b***) *12–14* (***c***)	98.2	0.11	0.44	–	1.27	–	–
α_2 solid solution of Cu, Mn, and Ti in Al	*4–6* (***b***)	95.7	–	0.7	–	3.94	–	–
$Al_{3.63}$(Cu, Cd, Mn, Fe) alloyed aluminide	*5–7* (***a***) *1–3* (***b***) *9–11* (***c***) *1–2* (***c***)	78.4	–	0.32	0.27	20.5	0.5	–
		$Al_{78.4}$(Cu, Cd, Mn, Fe)$_{21.6}$ = $Al_{3.63}$(Cu, Cd, Mn, Fe)						
$Al_{3.83}$(Cu, La, Ti, Cd, Mn) alloyed aluminide	*1–2* (***a***)	79.3	1.23	0.48	–	13.5	0.21	5.32
		$Al_{79.3}$(Cu, La, Ti, Cd, Mn)$_{20.7}$ = $Al_{3.83}$(Cu, La, Ti, Cd, Mn)						
$Al_{6.0}$(Ti, La, Cu, Cd) alloyed aluminide	*3–8* (***c***)	85.7	8.6	–	–	1.27	0.41	3.98
		$Al_{85.7}$(Ti, La, Cu, Cd)$_{14.3}$ = $Al_{6.0}$(Ti, La, Cu, Cd)						

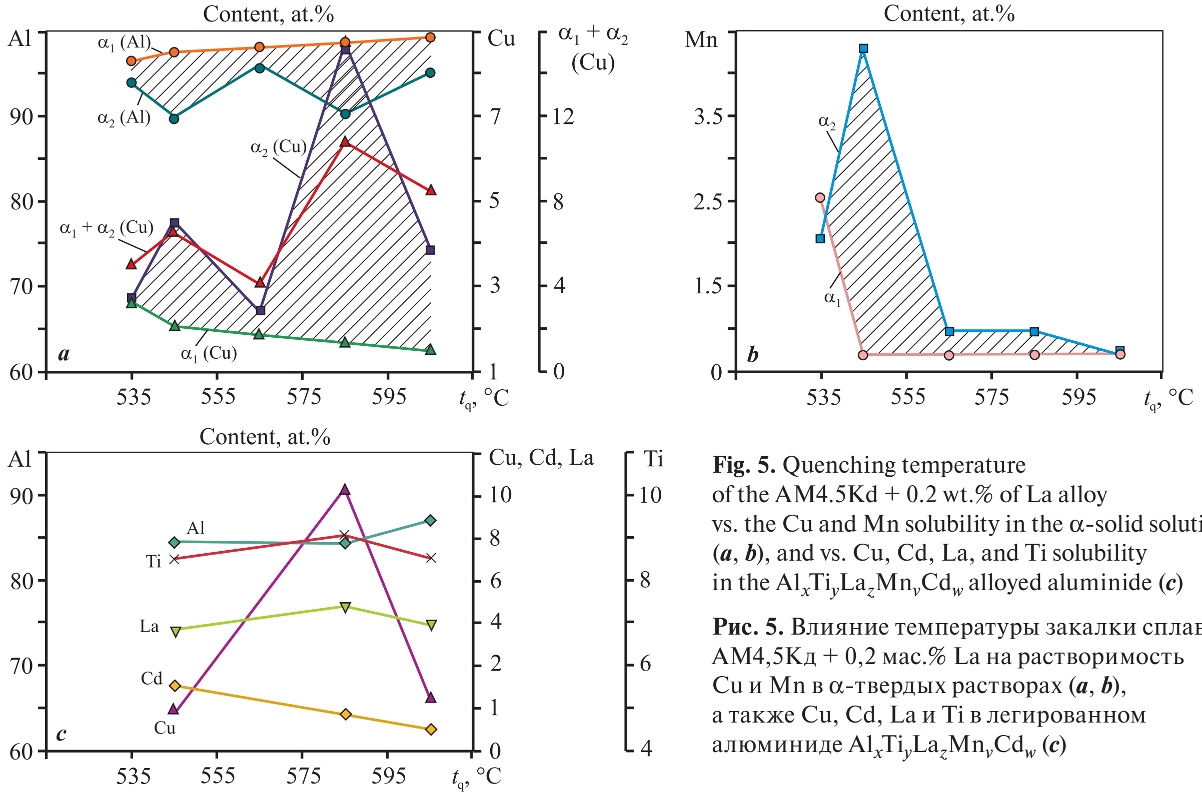

Fig. 5. Quenching temperature of the AM4.5Kd + 0.2 wt.% of La alloy vs. the Cu and Mn solubility in the α-solid solutions (***a***, ***b***), and vs. Cu, Cd, La, and Ti solubility in the $Al_xTi_yLa_zMn_vCd_w$ alloyed aluminide (***c***)

Рис. 5. Влияние температуры закалки сплава АМ4,5Кд + 0,2 мас.% La на растворимость Cu и Mn в α-твердых растворах (***a***, ***b***), а также Cu, Cd, La и Ti в легированном алюминиде $Al_xTi_yLa_zMn_vCd_w$ (***c***)

Table 3. **Elemental composition (at.%) in the structural components of the AM4.5Kd + 0.2 wt.% of La alloy vs. the quenching temperature with subsequent aging**

Таблица 3. Содержание элементов (ат.%) в структурных составляющих сплава АМ4,5Кд + 0,2 мас.% La в зависимости от температуры закалки с последующим старением

t_q, °C	α_1 solid solution	α_2 solid solution	$Al_xCu_yMn_zFe_v$	$Al_xCu_yMn_zLa_vCd_w$	$Al_xTi_yLa_zCu_vCd_w$	$Al_xCu_yLa_zMn_vFe_w$	$Al_xCu_yTi_zMn_v$	$Al_xCu_yMn_zFe_vCd_wLa$	$Al_xCu_yCd_zMn_vFe_w$
535	97.1 Al 0.31 Mn 2.55 Cu $\alpha_1 + \alpha_2 = 5.13$ Cu $\alpha_1 + \alpha_2 = 2.67$ Mn	93.3 Al 2.12 Mn 0.28 Fe 2.58 Cu	74.38 Al 0.1 Mn 24.62 Cu 0 Fe **$Al_{2.9}$(Cu, Mn)**	85.35 Al 1.2 Mn 0.16 Fe 1.54 Cu 1.75 La 0.09 Cd **$Al_{5.83}$(Cu, La, Mn, Fe)**	–	–	–	–	–
545	97.45 Al 0.15 Ti 0.33 Mn 2.07 Cu $\alpha_1 + \alpha_2 = 6.77$ Cu $\alpha_1 + \alpha_2 = 4.58$ Mn	89.4 Al 4.25 Mn 1.22 Fe 4.7 Cu 0.46 La	–	–	84.5 Al 8.52 Ti 0.95 Cu 1.63 Cd 3.41 La **$Al_{5.45}$(Ti, La, Cu, Cd)**	84.6 Al 1.56 Mn 0.33 Fe 9.82 Cu 3.68 La **$Al_{5.5}$(Cu, La, Mn, Fe)**	–	–	–
565	97.65 Al 0.12 Ti 0.25 Mn 1.98 Cu $\alpha_1 + \alpha_2 = 4.27$ Cu $\alpha_1 + \alpha_2 = 1.03$ Mn	96.96 Al 0.78 Mn 2.26 Cu	–	80.9 Al 1.55 Mn 13.44 Cu 0.32 Cd 3.5 La **$Al_{4.24}$(Cu, La, Mn)**	–	81.6 Al 7.9 Mn 1.32 Fe 9.05 Cu 0.15 La **$Al_{4.4}$(Cu, Mn, Fe, La)**	–	–	–
585	97.80 Al 0.365 Mn 1.93 Cu $\alpha_1 + \alpha_2 = 10.77$ Cu $\alpha_1 + \alpha_2 = 1.22$ Mn	90.2 Al 0.85 Mn 0.09 Fe 8.84 Cu	72.5 Al 0.11 Mn 0.22 Fe 27.2 Cu **$Al_{2.64}$(Cu, Fe, Mn)**	–	84.8 Al 9.1 Ti 10.9 Cu 0.73 Cd 4.28 La **$Al_{5.6}$(Ti, Cu, La, Cd)**	–	80.5 Al 9.09 Ti 1.18 Mn 9.22 Cu **$Al_{4.12}$(Cu, Ti, Mn)**	78.3 Al 1.84 Mn 0.26 Fe 15.18 Cu 0.37 Cd 4.03 La **$Al_{3.6}$(Cu, La, Cd, Fe, Mn)**	–
605	98.2 Al 0.11 Ti 0.44 Mn 1.27 Cu $\alpha_1 + \alpha_2 = 5.21$ Cu $\alpha_1 + \alpha_2 = 0.44$ Mn	95.7 Al 0.44 Mn 3.94 Cu	–	–	85.7 Al 8.6 Ti 1.27 Cu 0.41 Cd 3.98 La **$Al_{6.0}$(Ti, La, Cu, Cd)**	–	–	79.3 Al 1.23 Ti 0.48 Mn 13.5 Cu 0.21 Cd 5.32 La 0 Fe **$Al_{3.83}$(Cu, La, Ti, Cd, Mn)**	78.4 Al 0.32 Mn 0.27 Fe 20.5 Cu 0.5 Cd **$Al_{3.63}$(Cu, Cd, Mn, Fe)**

Note. The components are underlined.

until t_q = 605 °C. Consequently, the maximum total solubility of copper and manganese in the α_2-solid solution is reached at 545 °C. At the quenching temperature of 585 °C, only an increased copper content in the α_2-solid solution is observed. As a result, higher microhardness of the α-solid can be anticipated at these quenching temperatures.

Table 3 indicates that segregation increases with the quenching temperature, impacting the stoichiometry of the crystallized metal aluminides. Aluminides with La additions ($Al_xTi_yLa_zCu_vCd_w$) most commonly crystallize at t_q = 545÷605 °C. Notably, $Al_{4.12}$(Cu, Ti, Mn) aluminides, containing 9.09 at. % of Ti and 9.22 at. % of Cu, form at the 585 °C quenching temperature. Additionally, $Al_{3,63}$(Cu, Cd, Mn, Fe) is formed at t_q = 605 °C (refer to Table 3).

For the $Al_xTi_yLa_zMn_vCd_w$ alloyed aluminide, the highest solubility of the additions (Cu, La, Ti) occurs at t_q = 585 °C. In this aluminide, the Cd content decreases, while the Al content increases (Fig. 5, *c*).

Microhardness measurements of the $Al_xTi_yLa_zMn_vCd_w$ aluminides are presented in Fig. 5, *c*.

The AM4.5Kd + 0,2 wt.% La alloy exhibits its maximum hardness (98—104 HB) at quenching temperatures of 535—545 °C. At t_q = 605 °C, the hardness drastically drops to ~60 HB (Fig. 6, *a*). The maximum microhardness of the base metal (α-solid solution) is achieved at t_q = 535÷545 °C, reaching ~150 HV (Fig. 6, *b*).

Fig. 2, 4, and Table 1, 2 illustrate that all the intermetallides, except for the complex $Al_xTi_yLa_zMn_vCd_w$ alloyed aluminide, exhibit a dispersed structure, preventing the measurement of their microhardness.

The microhardness of the $Al_xTi_yLa_zMn_vCd_w$ alloyed aluminide is 760 HV at t_q = 535÷545 °C and it drops to 660 HV at t_q = 605 °C (Fig. 6, *c*).

Consequently, the maximum total hardness of the alloy is observed at 535—545 °C, primarily due to the high microhardness of the α-solid solution with its elevated Cu and Mn content. There appears to be a relationship between the variations in hardness for the AM4.5Kd + + 0.2 wt.% La alloy, the microhardness of the α-solid solution, the complex $Al_xTi_yLa_zMn_vCd_w$ alloyed aluminide, and their respective compositions.

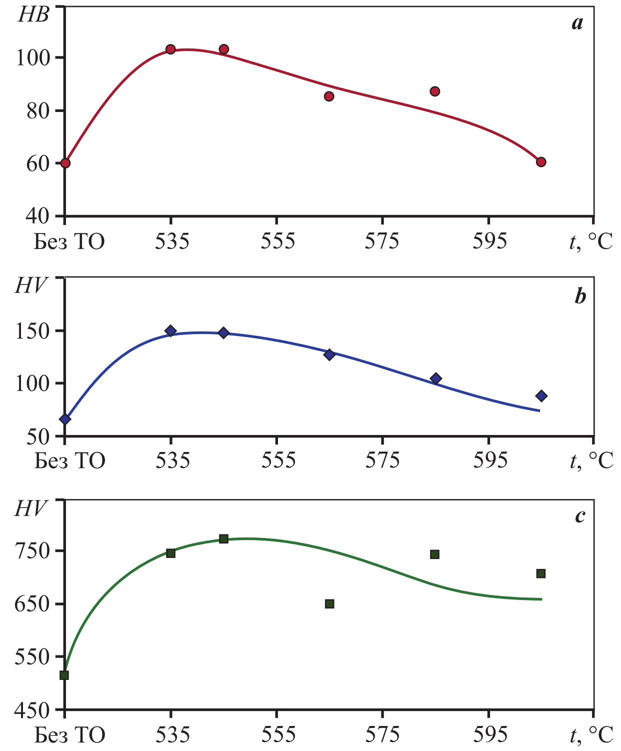

Fig. 6. Quenching temperature vs. the hardness of the AM4.5Kd + 0.2 wt.% of La alloy (***a***), α-solid solution microhardness (***б***), and $Al_xTi_yLa_zMn_vCd_w$ alloyed aluminide microhardness (***в***)

Рис. 6. Влияние температуры закалки на твердость сплава АМ4,5Кд + 0,2 мас.% La (***а***) и микротвердость α-твердого раствора (***б***) и легированного алюминида типа $Al_xTi_yLa_zMn_vCd_w$ (***в***)

Conclusion

1. An increase in the quenching temperature from 535 to 605 °C, followed by aging at 155 °C for 4 h, promotes the enlargement of structural components, including the α-solid solution, metal aluminides, and eutectics.

2. XRD elemental analysis identified the structural components of the AM4.5Kd + 0.2 wt.% of La for various quenching temperatures.

3. The base metal (α-solid solution) exhibits nonhomogeneity in its chemical composition. The contents of Cu and Mn in the α_1-solid solution decrease from 2.6 at.% of Cu and 2.5 at.% of Mn at 535 °C to 1.27 at.% of Cu and 0.44 at.% of Mn at 605 °C. The Cu and Mn solubility in the α_2-solid solution depends on the quenching temperatures. The maximum Cu (4.5 at.%) and Mn (4.25 at.%) contents occur at t_q = 545 °C. The α_2-solid solution has a second peak of Cu content (8.7 at.%) at t_q = 585 °C, and the Mn content at t_q = = 585 °C is 1.0 at.%.

4. Aluminides of alloying elements with different stoichiometries crystallize at different quenching temperatures. Complex $Al_xTi_yLa_zCu_vCd_w$ и $Al_xCu_yMn_zCd_v$ alloyed aluminides are most commonly found in the 545—605 °C quenching temperature range. The highest content of Cu, Ti, and La additions in the $Al_xTi_yLa_zCu_vCd_w$ aluminide occurs at 585 °C, where the Cd content decreases, and that of Al increases at $t_q = 605$ °C.

5. Increasing the quenching temperature to 535—545 °C results in a higher hardness of the AM4.5Kd + + 0.2 wt.% of La alloy, reaching to 98—104 HB, with subsequent decrease to 60 HB as the quenching temperature reaches 605 °C. The hardness of the unhardened alloy is 60 HB.

6. A relationship was identified between the alloy hardness, microhardness of the α-solid solution, microhardness of the complex $Al_xTi_yLa_zCu_vCd_w$ alloyed aluminide, and their compositions.

7. The optimal quenching temperature t for the AM4.5Kd alloy is 535—545 °C. This temperature corresponds to the highest hardness of the alloy and the $Al_xTi_yLa_zMn_vCd_w$ alloyed aluminide.

References

1. Ogorodov D.V., Trapeznikov A.V., Popov D.A., Pentyukhin S.I. Development of foundry aluminum alloys in VIAM (to the 120th anniversary of the birth of I.F. Kolobnev). *Trudy VIAM.* 2017;2(50):105—122. (In Russ.).
   Огородов Д.В., Трапезников А.В., Попов Д.А., Пентюхин С.И. Развитие литейных алюминиевых сплавов в ВИАМ (к 120-летию со дня рождения И.Ф. Колобнева). *Труды ВИАМ*. 2017;2(50):105—112.
2. Belov N.A., Alabin A.N. Promising aluminum alloys with increased heat resistance for reinforcement engineering as a possible alternative to steels and cast iron. *Armaturostroenie.* 2010;2(65):50—54. (In Russ.).
   Белов Н.А., Алабин А.Н. Перспективные алюминиевые сплавы с повышенной жаростойкостью для арматуростроения как возможная альтернатива сталям и чугунам. *Арматуростроение*. 2010;2(65): 50—54.
3. Kvasova F.I., Fridlyander I.N. Industrial aluminum alloys. Moscow: Metallurgiya, 1984. 528 p. (In Russ.).
   Квасова Ф.И., Фридляндер И.Н. Промышленные алюминиевые сплавы. М.: Металлургия, 1984. 528 с.
4. Alieva S.G., Al'tman M.B., Ambartsumyan S.M. Industrial aluminum alloys. Moscow: Metallurgiya, 1984. 527 p. (In Russ.).
   Алиева С.Г., Альтман М.Б., Амбарцумян С.М. Промышленные алюминиевые сплавы. М.: Металлургия, 1984. 527 с.
5. Patel N., Joshi M., Singh A., Pradhan A.K. Effect of solution heat treatment on microstructure and some properties of Al—Cu—Mg alloy. *Transactions of the Indian Institute of Metals.* 2023;76(10):2681—2689.
   https://doi.org/10.1007/s12666-023-02961-x
6. Aryshensky E.V., Aryshensky V.Yu., Drits A.M., Grechnikov F.V., Ragazin A.A. Thermal treatment effect on the mechanical properties of 1570, 1580 and 1590 aluminum alloys. *Vestnik of Samara University. Aerospace and Mechanical Engineering.* 2022;21(4):76—87. (In Russ.).
   https://doi.org/10.18287/2541-7533-2022-21-4-76-87
   Арышенский Е.В., Арышенский В.Ю., Дриц А.М., Гречников Ф.В., Рагазин А.А. Влияние режимов термической обработки на механические свойства алюминиевых сплавов 1570, 1580 и 1590. *Вестник Самарского университета: Аэрокосмическая техника, технологии и машиностроение*. 2022;21(4):76—87.
7. Korotkova N.O., Belov N.A., Timofeev V.N., Motkov M.M., Cherkasov S.O. Influence of heat treatment on the structure and properties of an Al—7% REM conductive aluminum alloy casted in an electromagnetic crystallizer. *Physics of Metals and Metallography.* 2020;121(2): 173—179.
   https://doi.org/10.31857/S0015323020020096
   Короткова Н.О., Белов Н.А., Тимофеев В.Н., Мотков М.М., Черкасов С.О. Влияние режима термической обработки на структуру и свойства проводникового алюминиевого сплава Al—7%РЗМ, полученного литьем в электромагнитном кристаллизаторе. *Физика металлов и металловедение.* 2020;121(2): 200—206.
8. Paitova O.V., Bobruk E.V., Skotnikova M.A. Optimization of the structure and properties of the Al—Cu—Mg system aluminum alloy. *Journal of Instrument Engineering.* 2020;63(5):476—482. (In Russ.).
   https://doi.org/10.17586/0021-3454-2020-63-5-476-482
   Паитова О.В., Бобрук Е.В., Скотникова М.А. Оптимизация структуры и свойств алюминиевого сплава системы Al—Cu—Mg. *Известия высших учебных заведений. Приборостроение*. 2020;63(5):476-482.
9. Zenin M.N., Guryev A.M., Ivanov S.G., Guryev M.A., Chernykh E.V. Influence of high-temperature annealing of aluminum alloys AMg6 and V95 on their structural-phase state and strength proper-ties. *Fundamental'nye Problemy Sovremennogo Materialovedenia (Basic Problems of Material Science (BPMS)).* 2022;19(1):106—114. (In Russ.).
   https://doi.org/10.25712/ASTU.1811-1416.2022.01.012
   Зенин М.Н., Гурьев А.М., Иванов С.Г., Гурьев М.А., Черных Е.В. Влияние высокотемпературного отжига алюминиевых сплавов АМг6 и В95 на их структурно-фазовое состояние и прочностные свойства. *Фундаментальные проблемы современного материаловедения*. 2022:19(1):106—114.
10. Zhou W.B., Teng G.B., Liu C.Y., Qi H.Q., Huang H.F., Chen Y., Jiang H.J. Microstructures and mechanical properties of binary Al—Zn alloys fabricated by casting

and heat treatment. *Journal of Materials Engineering and Performance*. 2017;26:3977—3982.
https://doi.org/10.1007/s11665-017-2852-y

11. Tan E. Change in the wear characteristics of T6 heat-treated 2024, 6063, and 7075 alloys at different quenching temperatures. *Journal of Materials Engineering and Performance*. 2023;32:1—13.
https://doi.org/10.1007/s11665-023-08177-w
12. Anjabin N. Modeling the age-hardening process of aluminum alloys containing the prolate/oblate shape precipitates. *Metals and Materials International*. 2021;27:1620—1630.
https://doi.org/10.1007/s12540-019-00579-7
13. Alexandrov A.A., Butorin D.V., Daneev R.A., Livshits A.V. Error estimation of the heat transfer coefficient determination devices based on mathematical modeling. *Vestnik RGUPS*. 2019;(4):8—16. (In Russ.).
Александров А.А., Буторин Д.В., Данеев Р.А., Лившиц А.В. Система компьютерного моделирования термических остаточных напряжений. *Вестник Ростовского государственного университета путей сообщения*. 2019;(4):8—16.
14. Krivopalov I.V., Baturin A.P., Erisov Ya.A. Application of computer simulation to determine the influence of quenching parameters on the geometry of parts from AK6 aluminium alloy. *Izvestiya Samarskogo Nauchnogo Tsentra Rossiiskoi Akademii Nauk*. 2021:23(6):5—9. (In Russ.).
https://doi.org/10.37313/1990-5378-2021-23-6-5-9
Кривопалов И.В., Батурин А.П., Ерисов Я.А. Применение компьютерного моделирования для определения влияния параметров закалки на геометрию штамповок из алюминиевого сплава АК6. *Известия Самарского научного центра Российской академии наук*. 2021:23(6):5—9.
15. Hu Y., Wang G., Ye M., Wang S., Wang L., Rong Y. A precipitation hardening model for Al—Cu—Cd alloys. *Materials & Design*. 2018;151:123—132.
https://doi.org/10.1016/j.matdes.2018.04.057
16. Hu Y., Wang G., Ji Y., Wang L., Rong Y., Chen L.Q. Study of θ'precipitation behavior in Al—Cu—Cd alloys by phase-field modeling. *Materials Science and Engineering: A*. 2019;746:105—114.
https://doi.org/10.1016/j.msea.2019.01.012
17. Liu X., Wang G., Hu Y., Ji Y., Rong Y., Hu Y., Chen L.Q. Multi-scale simulation of Al—Cu—Cd alloy for yield strength prediction of large components in quenching-aging process. *Materials Science and Engineering: A*. 2021;814:141223.
https://doi.org/10.1016/j.msea.2021.141223
18. Choudhary C., Bar H.N., Arif S. Sahoo K.L., Mandal D. Effect of structural refinement and modification on the mechanical properties of Al—7Si alloy. *Journal of Materials Engineering and Performance*. 2023;1—13.
https://doi.org/10.1007/s11665-023-08313-6
19. Ruan Q., Meng C., Xie Z., Tao Z., Wu J., Peng Y., Tang H., Chen P. Effect of (Ti+V)B_2 on the grain structure of Al—7Si alloy. *Transactions of the Indian Institute of Metals*. 2023;76(10):2765—2771.
https://doi.org/10.1007/s12666-023-02954-w
20. Sahin H., Dispinar D. Effect of rare earth elements erbium and europium addition on microstructure and mechanical properties of A356 (Al—7Si—0.3Mg) alloy. *International Journal of Metalcasting*. 2023;17(4):2612—2621.
https://doi.org/10.1007/s40962-023-01060-3
21. Laponogova P.A., Kolisova M.V., Goncharov A.V., Dzuyba G.S. The application of scandium for the modification of aluminum alloys on the example of 2003 aluminum alloy. In: *Innovative technologies in foundry production*. Moscow: IIU MGOU, 2019. P. 75–78. (In Russ.).
Лапоногова П.А., Колисова М.В., Гончаров А.В., Дзюба Г.С. Применение скандия для модифицирования алюминиевых сплавов на примере ВАЛ10. В сб.: *Инновационные технологии в литейном производстве*. М.: ИИУ МГОУ, 2019. С. 75—78.
22. Amer S.M., Barkov R.Y., Prosviryakov A.S., Pozdniakov A.V. Structure and properties of new heat-resistant cast alloys based on the Al—Cu—Y and Al—Cu—Er systems. *Physics of Metals and Metallography*. 2021;122(9):908-914.
https://doi.org/10.31857/S0015323021090023
Амер С.М. Барков Р.Ю., Просвиряков А.С., Поздняков А.В. Структура и свойства новых литейных жаропрочных сплавов на основе систем Al—Cu—Y и Al—Cu—Er. *Физика металлов и металловедение*. 2021;122(9):977—983.
23. Bazhenov V.E., Baranov I.I., Titov A.Yu., Sannikov A.V., Ozherelkov D.Yu., Lyskovich A.A., Koltygin A.V., Belov V.D. Influence of Ti, Sr and B additions on the fluidity of A356.2 aluminium alloy. *Izvestiya. Non-Ferrous Metallurgy*. 2022;28(4):55—66. (In Russ.).
https://doi.org/10.17073/0022-3438-2021-4-55-66
Баженов В.Е., Баранов И.И., Титов А.Ю., Санников А.В., Ожерелков Д.Ю., Лыскович А.А., Колтыгин А.В., Белов В.Д. Изучение влияния добавок Ti, Sr и B на жидкотекучесть алюминиевого сплава А356.2 (АК7пч). *Известия вузов. Цветная металлургия*. 2022;28(4):55—66.
24. Abramov A.A. Aluminium-titanium-boron alloying composition as an effective grain modifier for cast aluminum alloys. *Metallurgiya Mashinostroeniya*. 2021;(2):2—4. (In Russ.).
Абрамов А.А. Лигатура алюминий—титан—бор — эффективный модификатор зерна литейных алю-

миниевых сплавов. *Металлургия машиностроения*. 2021(2):2—4.

25. Andrushevich A.A., Sadokha M.A. Shrinkage phenomena in silumins when treated with long-acting modifiers. *Litiyo i Metallurgiya (Foundry Production and Metallurgy)*. 2022;(3):30—35. (In Russ.). https://doi.org/10.21122/1683-6065-2022-3-30-35
Андрушевич А.А., Садоха М.А. Усадочные явления в силуминах при обработке модификаторами длительного действия. *Литье и металлургия*. 2022;(3):30—35.
26. Shlyaptseva A.D., Petrov I.A., Ryakhovsky A.P. Complex modification of industrial silumins. *Teoriya i Tekhnologiya Metallurgicheskogo Proizvodstva*. 2021;1(36):4—10. (In Russ.).
Шляпцева А.Д., Петров И.А., Ряховский А.П. Комплексное модифицирование промышленных силуминов. *Теория и технология металлургического производства*. 2021;1(36):4—10.
27. Ri H., Ri E.H., Zernova T.S., Kalaushin M.A., Ri V.E., Ermakov M.A. Modifier: Patent 2521915 (RF). 2012. (In Russ.).
Ри Х., Ри Э.Х., Зернова Т.С., Калаушин М.А., Ри В.Э., Ермаков М.А. Модификатор: Пат. 2521915 (РФ). 2012.
28. Dobatkin V.A., Elagin V.I., Fedorov V.M. Rapidly crystallizing aluminum alloys. Moscow: VILS, 1995. 341 p. (In Russ.).
Добаткин В.А., Елагин В.И., Федоров В.М. Быстрозакристаллизующиеся алюминиевые сплавы. М.: ВИЛС, 1995. 341 с.
29. Xiao-hui Ao, Shu-ming Xing, Bai-shui Yu, Qing-you Han. Effect of Ce addition on microstructures and mechanical properties of A380 aluminum alloy prepared by squeeze-casting. *International Journal of Minerals, Metallurgy and Materials*. 2018;25(5):553—564. https://doi.org/10.1007/s12613-018-1602-y
30. Ri E.H., Prikhodko A.A., Slavinskaya N.A. Structure forming and properties of VAL10 cast alloy modified with cerium and lanthanum. *Metallurgiya Mashinostroeniya*. 2020;(2):24—30. (In Russ.).
Ри Э.Х., Приходько А.А., Славинская Н.А. Структурообразование и свойства литейного сплава ВАЛ 10, модифицированного церием и лантаном. *Металлургия машиностроения*. 2020;(2): 24—30.

Information about the authors

Nadezhda A. Slavinskaya – Postgraduate Student of the Department of foundry production and technologies of metals of the Pacific National University (PNU).
https://orcid.org/0009-0006-6712-4923
E-mail: 2016101722@pnu.edu.ru

Hosen Ri – Dr. Sci. (Eng..), Professor of the Department of foundry production and technology of metals of PNU.
https://orcid.org/0000-0001-7633-8989
E-mail: opirus@list.ru

Ernst H. Ri – Dr. Sci. (Eng.), Head of the Department of foundry production and technologies of metals of PNU.
https://orcid.org/0000-0001-7784-1252
E-mail: 003232@pnu.edu.ru

Andrei S. Zhivetev – Cand. Sci (Eng.), Assistant Professor of the Department of foundry production and technology of metals of PNU.
https://orcid.org/0000-0003-2932-0203
E-mail: 007881@pnu.edu.ru

Информация об авторах

Надежда Александровна Славинская – аспирант кафедры «Литейное производство и технологии металлов» (ЛПиТМ) Тихоокеанского государственного университета (ТОГУ).
https://orcid.org/0009-0006-6712-4923
E-mail: 2016101722@pnu.edu.ru

Хосен Ри – д.т.н., профессор кафедры ЛПиТМ университета ТОГУ.
https://orcid.org/0000-0001-7633-8989
E-mail: opirus@list.ru

Эрнст Хосенович Ри – д.т.н., профессор, заведующий кафедрой «Литейное производство и технологии металлов» ЛПиТМ университета ТОГУ.
https://orcid.org/0000-0001-7784-1252
E-mail: 003232@pnu.edu.ru

Андрей Сергеевич Живетьев – к.т.н., доцент кафедры ЛПиТМ университета ТОГУ.
https://orcid.org/0000-0003-2932-0203
E-mail: 007881@pnu.edu.ru

Contribution of the authors

N.A. Slavinskaya – conducted experiments, performed calculations, processed results, and contributed to paper authoring.

H. Ri – formulated the problem statement, developed the research concept, authored the text, and drew conclusions.

E.H. Ri – conducted calculations, processed results.

A.S. Zhivetev – provided resources for experiments.

Вклад авторов

Н.А. Славинская – подготовка и проведение экспериментов, выполнение расчетов, обработка полученных результатов, подготовка текста статьи.

Х. Ри – формирование основной концепции, постановка цели и задачи исследования, подготовка текста статьи, формулировка выводов.

Э.Х. Ри – проведение расчетов, анализ результатов исследований.

А.С. Живетьев – планирование и проведение экспериментов, ресурсное обеспечение испытаний.

The article was submitted 12.01.2023, revised 09.11.2023, accepted for publication 13.11.2023

Статья поступила в редакцию 12.01.2023, доработана 09.11.2023, подписана в печать 13.11.2023

UDC 621.762
https://doi.org/10.17073/0021-3438-2024-1-55-69

Research article
Научная статья

Mechanical and tribological characteristics of nickel-rich $CoCrCu_xFeNi_2$ high entropy-alloys

A.D. Fedotov, S.K. Mukanov, B.Yu. Romanenko, P.A. Loginov, M.Ya. Bychkova, S.I. Rupasov

National University of Science and Technology "MISIS"
4 Bld. 1 Leninskiy Prosp., Moscow 119049, Russia

✉ Alexander D. Fedotov (sashok12221998@mail.ru)

Abstract: This research explores the potential to enhance the copper solubility limit in high-entropy alloys (HEAs) within the CoCrCuFeNi system by increasing the nickel content twofold and applying additional heat treatment. The $CoCrCu_xFeNi_2$ HEAs were synthesized through mechanical alloying of elemental powders followed by hot pressing. The study investigated the microstructure and phase composition of $CoCrCu_xFeNi_2$ HEAs in relation to varying copper concentrations ($x = 0$; 0.25; 0.5; 0.75; 1.0). The evaluation of the alloy matrix's chemical composition, which is based on the FCC solid solution, enabled the determination of copper solubility. It was found that doubling the nickel content, relative to the equiatomic ratio, facilitated the formation of HEAs with a homogenous FCC structure for copper concentrations up to $x \le 0.75$. Further heat treatment of these HEAs resulted in an enhanced copper solubility of up to 17.5 at.%. The mechanical and tribological properties of $CoCrCu_xFeNi_y$ HEAs were also assessed, revealing significant improvements in tensile strength (ranging from 910 to 1045 MPa) and hardness (285–395 HV) for the $CoCrCu_xFeNi_2$ alloys. Despite the increased copper solubility limit, the heat treatment process caused a decline in mechanical properties by 35–50 %, attributed to grain size enlargement to 5.5 μm. The $CoCrCu_{0.75}FeNi_2$ and $CoCrCuFeNi_2$ alloys exhibited the lowest wear rates when tested against Al_2O_3 counterbody, with wear rates of $1{,}58\cdot10^{-5}$ and $1{,}48\cdot10^{-5}$ mm^3/(N·m), respectively.

Keywords: powder metallurgy, high-entropy alloys, mechanical properties, wear resistance, heat treatment, transmission electron microscopy, scanning electron microscopy.

Acknowledgments: The work was carried out with the financial support of the Russian Science Foundation (project No. 22-79-10144).
The authors express their gratitude to Dr. M.I. Petrzhik for assistance in studies of mechanical properties (hardness and elastic modulus).

For citation: Fedotov A.D., Mukanov S.K., Romanenko B.Yu., Loginov P.A., Bychkova M.Ya., Rupasov S.I. Mechanical and tribological characteristics of nickel-rich $CoCrCu_xFeNi_2$ high entropy-alloys. *Izvestiya. Non-Ferrous Metallurgy*. 2024;30(1):55–69.
https://doi.org/10.17073/0021-3438-2024-1-55-69

Механические и трибологические свойства высокоэнтропийных сплавов $CoCrCu_xFeNi_2$ с высоким содержанием никеля

А.Д. Федотов, С.К. Муканов, Б.Ю. Романенко, П.А. Логинов, М.Я. Бычкова, С.И. Рупасов

Национальный исследовательский технологический университет «МИСИС»
Россия, 119049, г. Москва, Ленинский пр-т, 4, стр. 1

✉ Александр Дмитриевич Федотов (sashok12221998@mail.ru)

Аннотация: Работа посвящена изучению возможности повышения предела растворимости меди в высокоэнтропийных сплавах (ВЭС) системы CoCrCuFeNi путем двукратного увеличения концентрации никеля и проведения дополнительной термической обработки. ВЭС $CoCrCu_xFeNi_2$ изготовлены механическим легированием элементных порошковых смесей и их последующим горячим прессованием. Исследованы микроструктура и фазовый состав ВЭС $CoCrCu_xFeNi_2$ в зависимости от концентрации Cu (x = 0; 0,25; 0,5; 0,75; 1,0). Анализ химического состава матрицы сплава на основе ГЦК твердого раствора позволил определить растворимость меди. Показано, что двукратное (относительно эквиатомного) содержание никеля способствовало получению ВЭС с однофазной ГЦК-структурой при $x \leq 0,75$. Последующая термическая обработка ВЭС привела к увеличению растворимости меди до 17,5 ат.%. Проведены испытания механических и трибологических свойств ВЭС $CoCrCu_xFeNi_y$. В сплавах $CoCrCu_xFeNi_2$ достигнут высокий уровень прочности при растяжении (от 910 до 1045 МПа) и твердости (285–395 HV). Несмотря на повышение предела растворимости меди, термическая обработка привела к понижению механических свойств на 35–50 % из-за увеличения размера зерен до 5,5 мкм. Минимальным приведенным износом при трении в паре с контртелом из Al_2O_3 обладают сплавы $CoCrCu_{0,75}FeNi_2$ и $CoCrCuFeNi_2$ ($1,58 \cdot 10^{-5}$ и $1,48 \cdot 10^{-5}$ мм^3/(Н·м) соответственно).

Ключевые слова: порошковая металлургия, высокоэнтропийные сплавы, механические свойства, износостойкость, термическая обработка, просвечивающая электронная микроскопия, растровая электронная микроскопия.

Благодарности: Работа выполнена при финансовой поддержке Российского научного фонда (проект № 22-79-10144).

Авторы выражают благодарность д.т.н. М.И. Петржику за помощь в исследовании механических свойств (твердость и модуль упругости).

Для цитирования: Федотов А.Д., Муканов С.К., Романенко Б.Ю., Логинов П.А., Бычкова М.Я. , Рупасов С.И. Механические и трибологические свойства высокоэнтропийных сплавов $CoCrCu_xFeNi_2$ с высоким содержанием никеля. *Известия вузов. Цветная металлургия.* 2024;30(1):55–69. https://doi.org/10.17073/0021-3438-2024-1-55-69

Introduction

Over the past decade, high-entropy alloys (HEAs) based on the Co—Cr—Cu—Fe—Ni system have gained significant attention across various engineering disciplines [1—5] due to their exceptional mechanical properties at both ambient and elevated temperatures, coupled with remarkable thermal stability. These attributes render them ideal for critical applications such as combustion chambers and heat exchangers [6]. Their high corrosion resistance has led to their widespread adoption in the shipbuilding industry [7]. These alloys have been effectively utilized in coatings to enhance the corrosion resistance of magnesium alloy products [8]. Among their diverse uses, one of the most notable is in friction pair materials, attributed to their superior wear resistance at both room [9—11] and elevated temperatures [12; 13]. Collectively, the attributes of high wear resistance, ease of manufacturing, and low consolidation temperature when utilizing powder metallurgy methods render HEAs promising candidates as binders in diamond cutting tools [14; 15].

Extensive research has focused on the interplay between the mechanical properties and phase composition of CoCrCuFeNi high-entropy alloys (HEAs). These alloys can manifest as either a single-phase entity, comprising a substitutional solid solution with an FCC lattice structure, or a two-phase combination of FCC structures, contingent upon the concentration of copper [16]. Exceeding the solubility limit of copper results in a HEA structure characterized by a matrix FCC solid solution interspersed with copper-based interlayers also exhibiting an FCC structure [17—19]. Contemporary theories suggest that the inclusion of a copper phase diminishes the mechanical properties of CoCrCuFeNi HEAs and increases susceptibility to brittle fracture [20—24]. Alloys maintaining an equiatomic composition of cobalt, chromium, iron, and nickel can incorporate up to 9 at.% Cu while preserving a single-phase structure [18]. Therefore, broadening the copper concentration range that allows $CoCrCu_xFeNi$ HEAs to remain single-phase is a crucial objective, as achieving this would enable the development of HEAs with enhanced physical and mechanical characteristics, including improved strength, hardness, and wear resistance.

To augment the solubility of copper within the solid FCC solution, one strategy involves increasing the nickel content, which is uniquely characterized by its unlimited mutual solubility with copper within this family of HEAs, as evidenced by prior findings [25; 26]. Another approach is through heat treatment (HT), which stabilizes the structurally unstable state of HEAs typical at elevated temperatures, thereby enhancing the solubility of copper in the CoCrFeNi matrix.

This research aims to explore the potential of augmenting copper solubility in Co—Cr—Cu—Fe—Ni HEAs by increasing the nickel concentration and employing a supplementary quenching process. It entails a comparative analysis of the mechanical and tribological properties of equiatomic CoCrCuFeNi HEAs and the modified HEA with a doubled nickel content relative to the equiatomic ratio, designated as $CoCrCuFeNi_2$, which were obtained through quenching.

1. Materials and methods

The initial materials utilized in this study included carbonyl iron powder of grade VK-3 (Sintez-CIP LLC, Dzerzhinsk, Russia) with an average particle size of 9 μm and an impurity content of ≤0.3 wt.%, carbonyl nickel powder of grade PNK-UT3 (Kola MMC, Monchegorsk, Russia) with a particle size of 10 μm and impurity content of ≤0.06 wt.%, reduced cobalt powder of grade PK-1u (Hanrui Cobalt Co. LTD, China), with a particle size of 1.2 μm and impurity content of ≤0.03 wt.%, electrolytic chromium powder of grade PM-ERKh (AO Polema, Tula, Russia) with a particle size of 80 μm and impurity content of 0.05 wt.%, and electrolytic copper powder of grade PMS-1 (AO Uralelectromed, V. Pyshma, Russia) with a particle size of 24 μm and impurity content of 0.12 wt.%.

The base alloy for this study was $CoCrFeNi_2$, to which copper was added in varying mole fractions (0.25, 0.50, 0.75, and 1.0) relative to Co, Cr, and Fe. Powder mixtures were prepared using a planetary ball mill (PBM) "Activator-2sl" (Chemical Engineering Plant LTD, w.v. Dorogino, Novosibirsk region), under conditions optimized in prior research: a jar rotation speed of 694 rpm, a centrifugal factor of 90 *g*, for a duration of 30 min, and a ball to powder weight ratio of 15 : 1. To achieve finer particle sizes, the mixtures were further treated with 10 wt.% isopropyl alcohol in the same milling conditions for an additional 5 min, facilitating uniform distribution and mutual dissolution of Co, Cr, Cu, Fe, and Ni [17].

Cylindrical compact samples, 50 mm in diameter and 5 mm in height, were produced by hot pressing (HP) the $CoCrCu_xFeNi_2$ powder mixtures using a DSP-515 SA machine (Dr. Fritsch, Germany). The HP was conducted in a vacuum at a maximum temperature of 1100 °C, under a compaction pressure of 35 MPa, with an isobaric hold time of 3 min. After HP, the samples underwent additional HT in a protective hydrogen atmosphere at 1000 °C for 1.5 h.

Flat samples for tensile tests measuring 50 mm in total length with the working part dimensions of 20×5×2 mm, were fabricated from the compact samples using the electrical discharge cutting method.

The hardness of the hot-pressed samples was assessed using the Vickers method with an HVS-50 digital hardness tester (Time Group Inc., China) under a 10 kgf load. Hardness and elastic modulus measurements were also performed at the Testing Laboratory of Functional Surfaces (National scientific and educational center MISIS-ISMAN, Moscow, Russia) using a "Nano-Hardness Tester" (CSM Instruments, Switzerland). A Berkovich indenter (diamond triangular pyramid) was employed, applying an 8 mN load, with a loading speed of 0.36 mN/s, and a hold time at maximum load of 5 s.

Tensile tests were conducted on an "Instron 5966" universal testing machine (Instron, USA), with the ultimate tensile strength determined using the Bluehill software (Instron, USA).

The tribological behavior of the samples was evaluated using a "Tribometer" automated friction machine (CSM Instruments, Switzerland), employing a reciprocating motion based on the "Ball-on-Disc" configuration. The testing conditions included a track length of 6 mm, an applied load of 2 N, a maximum speed of 5 cm/s, and a sintered aluminum oxide (Al_2O_3) ball with a 3 mm diameter as the counterbody. The tests were run for 4000 cycles (covering 48 m) in air.

The microstructural analysis of both powdered and compacted materials was examined through scanning electron microscopy (SEM) using an S-3400N microscope (Hitachi, Japan), equipped with a "NORAN System 7 *X*-ray" energy-dispersive spectrometer (Thermo Scientific, USA). Further analysis of the materials' fine structure was conducted using a JEM 2100 transmission electron microscope (JEOL, Japan). Sample preparation for these analyses involved ion etching with a PIPS II system (Gatan, USA).

X-ray diffraction (XRD) analysis was performed using a "D2 Phaser" diffractometer (Bruker, USA) with CoK_α radiation, employing the Bragg—Brentano geometry over a 2θ range of 30 to 130°. Phase identification was facilitated by the Diffrac. EVA software (Bruker, USA). To refine the process for generating single-phase powders, XRD patterns of mixtures post 5, 10, 15, and 30 min of milling were analyzed, and the microstructure of their transversal cross-sections was examined.

2. Results and discussion

2.1. Fabrication of $CoCrCu_xFeNi_2$ alloy powders

To investigate phase formation processes during mechanical alloying (MA) of a Co—Cr—Cu—Fe—Ni powder mixture and to determine the optimal conditions for generating single-phase powders, XRD patterns of the mixtures after 5, 10, 15, and 30 min of treatment were examined, alongside analyses of their transversal cross-section microstructures.

Analysis after 5-minute treatment in the PBM revealed the presence of all phases corresponding to the starting powders (see Fig. 1 and Table 1), with the phase weight content closely aligning with the theoretical calculations based on the mixture composition. As the treatment duration increased, a broadening of the diffraction peaks was observed, indicative of significant deformation within the crystallite lattices. Concurrently, a reduction in the peak intensities for Co, Cu, and Fe was noted.

The XRD pattern from the powder mixture after 15 min of PBM treatment, showed asymmetry in the Ni peaks from the (311) planes. This asymmetry suggests the formation of a new phase with an FCC lattice type, exhibiting lattice parameters slightly different from those of Ni (0.3570 and 0. 3525 nm, respectively).

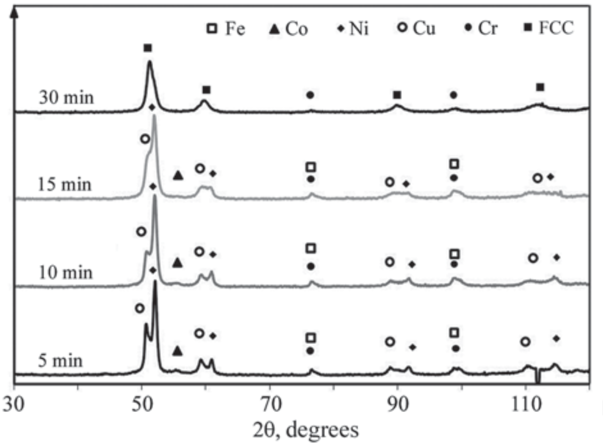

Fig. 1. XRD patterns of $CoCrCuFeNi_2$ alloy powders after PBM treatment

Рис. 1. Рентгенограммы порошковых смесей $CoCrCuFeNi_2$ после обработки в ПЦМ

Phase composition (wt.%) of Co–Cr–Cu–Fe–2Ni powder mixtures after mechanical alloying (MA) at various milling durations (τ_{MA})

Фазовый состав (мас.%) порошковых смесей Co–Cr–Cu–Fe–2Ni после механического легирования с различной продолжительностью ($\tau_{МЛ}$)

Phase (Pearson symbol)	τ_{MA}, min			
	5	10	15	30
Co (hP2/1)	12	8	6	–
Cr (cI2/1)	14	14	12	5
Cu (cF4/1)	16	12	10	–
Fe (cI2/1)	22	19	13	–
Ni (cF4/1)	36	47	47	–
FCC (cF4/1)	–	–	12	95

Following a 30-min treatment in the PBM, the powder predominantly consisted of an FCC solid solution with a minor presence of undissolved chromium (about 5 %). The residual chromium is not detrimental to the production of HEAs, as it is expected to dissolve into the matrix during the consolidation process through diffusion.

SEM studies on the structural evolution of the powder mixtures over different processing times revealed (Fig. 2) that due to the plastic nature of the components, structure formation during MA occurs via a mechanism typical for "ductile—ductile" systems. Under the impact of the grinding media, particles deform, creating new surfaces uncontaminated with oxygen, which form strong van der Waals bonds.

In the process of PBM, the initial metal particles tend to form large agglomerates (Fig. 2, *a*). These agglomerates exhibit a layered structure comprising distinguishable layers of Co, Cr, Cu, Fe, and Ni. The thickness of these metal layers varies with the particle size used in the process, typically ranging from 3—5 μm for Fe, Co, and Ni, to 20—30 μm for Cr and Cu (Fig. 2, *e*). As the milling process progresses, there is a notable gradual homogenization of the composite granules' structure (Fig. 2, *b*, *c*). expressed in a decrease in the thickness of the layers of metal components and their more chaotic arrangement. After $\tau_{MA} = 30$ min, the resulting powders exhibit a homogeneous microstructure, with Cr present as submicron-thick interlayers (Fig. 2, *d*).

The fine structure of $CoCrCuFeNi_2$ alloy powders after 30-minute treatment in the PBM was examined using transmission electron microscopy (TEM). As shown in Fig. 3, the powders form complex-shaped agglomerates with a nanocrystalline structure exhibiting crystallite sizes ranging between 20—25 nm. Electron diffraction analysis of these particles identified diffraction rings consistent with the FCC phase. To further evaluate the alloy elemental homogeneity, EDS mapping was performed. The uniform intensity of characteristic *X*-ray emissions from Co, Cr, Cu, Fe, and Ni across the mapped area of the MA powder indicates a uniform distribution of these elements.

2.2. Analysis of CoCrCuxFeNi2 HEAs after HP and HP + HT

The consolidation of mechanically alloyed powder mixtures was achieved using the HP method, with some of the HP alloy samples undergoing additional treatments of annealing and hardening, referred to as HP + HT. The objective was to examine the copper solubility within the $CoCrCu_xFeNi_2$ HEA matrix, which

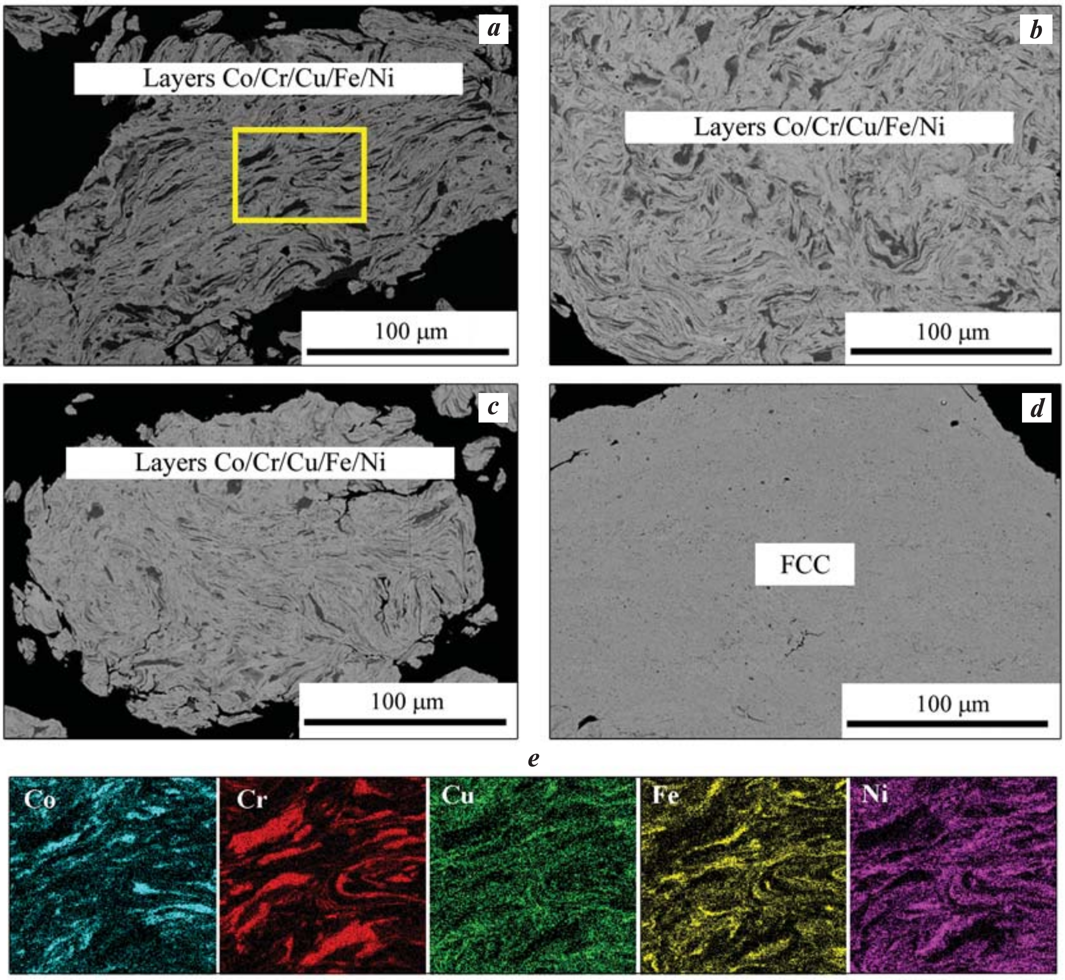

Fig. 2. Microstructures of $CoCrCuFeNi_2$ powder mixtures after PBM treatment at varied durations (***a***–***d***) and elemental distribution maps (***e***) derived from a particle treated for 5 min, corresponding to the region indicated in image ***a***
τ_{MA}, min: ***a*** – 5, ***b*** – 10, ***c*** – 15, ***d*** – 20

Рис. 2. Микроструктуры порошковых смесей $CoCrCuFeNi_2$ после обработки в ПЦМ с различной продолжительностью (***a***–***d***) и карты распределения элементов (***e***), снятые с частицы после 5 мин обработки, из выделенной на фото ***a*** области
$\tau_{МЛ}$, мин: ***a*** – 5, ***b*** – 10, ***c*** – 15, ***d*** – 20

involved analyzing the phase composition, microstructure, and the chemical composition of the different phases present.

XRD patterns presented in Fig. 4 showcase the structural outcomes for $CoCrCu_xFeNi_2$ HEAs after HP and HP + HT treatments. The primary structure identified in all HP-treated $CoCrCu_xFeNi_2$ HEA samples is an FCC solid solution that incorporates all alloy components, characterized by a cF4/1 structural type and a lattice parameter of 0.3577 nm. Previous studies indicated [17] that in $CoCrCu_xFeNi$ alloys, the formation of a secondary copper-based phase occurs at $x \geq 0.5$. In $CoCrCu_xFeNi_2$ alloys with an elevated nickel content, traces of this copper phase become apparent only at $x \geq 0.75$. The detection of this copper phase in $CoCrCu_{0,75}FeNi_2$ and $CoCrCuFeNi_2$ HP alloys was confirmed by low-intensity peaks on the lower angle (2θ) side of the XRD patterns (Fig. 4, inset).

Applying HT for HP samples of all $CoCrCu_xFeNi_2$ HEAs effectively prevents the emergence of the copper (Cu) phase across the board. Notably, even in the alloy with the highest copper content examined, $CoCrCuFeNi_2$, the anticipated peaks for the (Cu) phase were absent, illustrating that HT successfully maintains the $CoCrCuFeNi_2$ HEAs in a single-phase state at elevated temperatures (Fig. 4).

The microstructural characteristics of the compacted samples were explored using the SEM me-

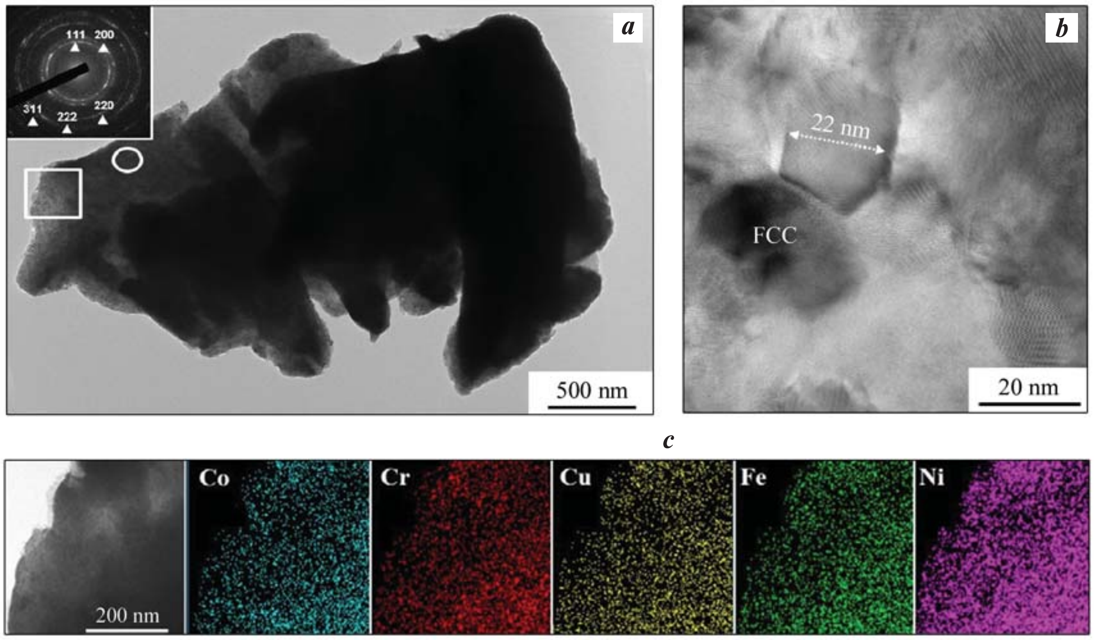

Fig. 3. Visualization of a CoCrCuFeNi$_2$ powder particle after 30 minutes PBM treatment (***a***); area within the white circle indicating the grain microstructure examination zone (***b***); white rectangle delineating the region analyzed via EDS (***c***)

Рис. 3. Изображение частицы порошка CoCrCuFeNi$_2$ после обработки в ПЦМ в течение 30 мин (***a***); область (белая окружность на рис. ***a***), в которой изучена зеренная микроструктура (***b***) и область (белый прямоугольник на рис. ***a***), в которой проводился ЭДС-анализ (***c***)

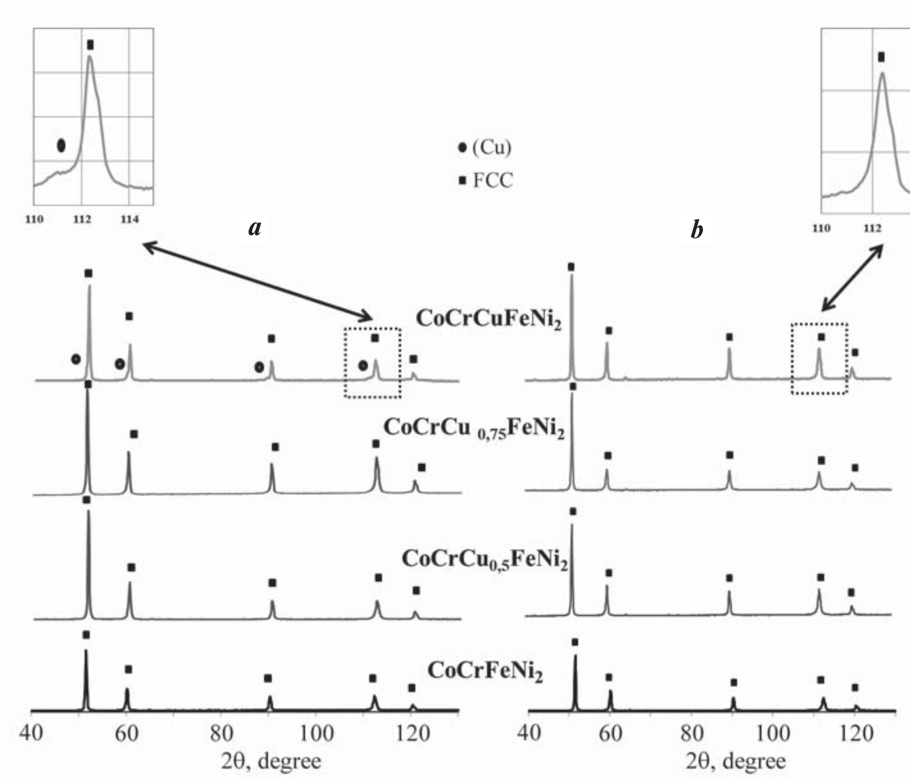

Fig. 4. XRD patterns of CoCrCu$_x$FeNi$_2$ HEAs after HP (***a***) and HP + HT (***b***)

Рис. 4. Рентгенограммы ВЭС CoCrCu$_x$FeNi$_2$ после ГП (***a***) и ГП + ТО (***b***) thod (Fig. 5). It was determined that the matrix of all HP $CoCrCu_xFeNi_2$ HEA samples comprises a FCC solid solution phase. This phase uniformly incorporates submicron Cr_2O_3 oxide particles, which are not detectable by XRD due to their minimal concentration. The (Cu) phase grains only become visible at copper concentrations $x \geq 0.75$ (Fig. 5, *e*). In the $CoCrCuFeNi_2$ alloy, the (Cu) constitutes about 10 % of the material and manifests as polygonal grains located along the grain boundaries of the FCC matrix (Fig. 5, *g*).

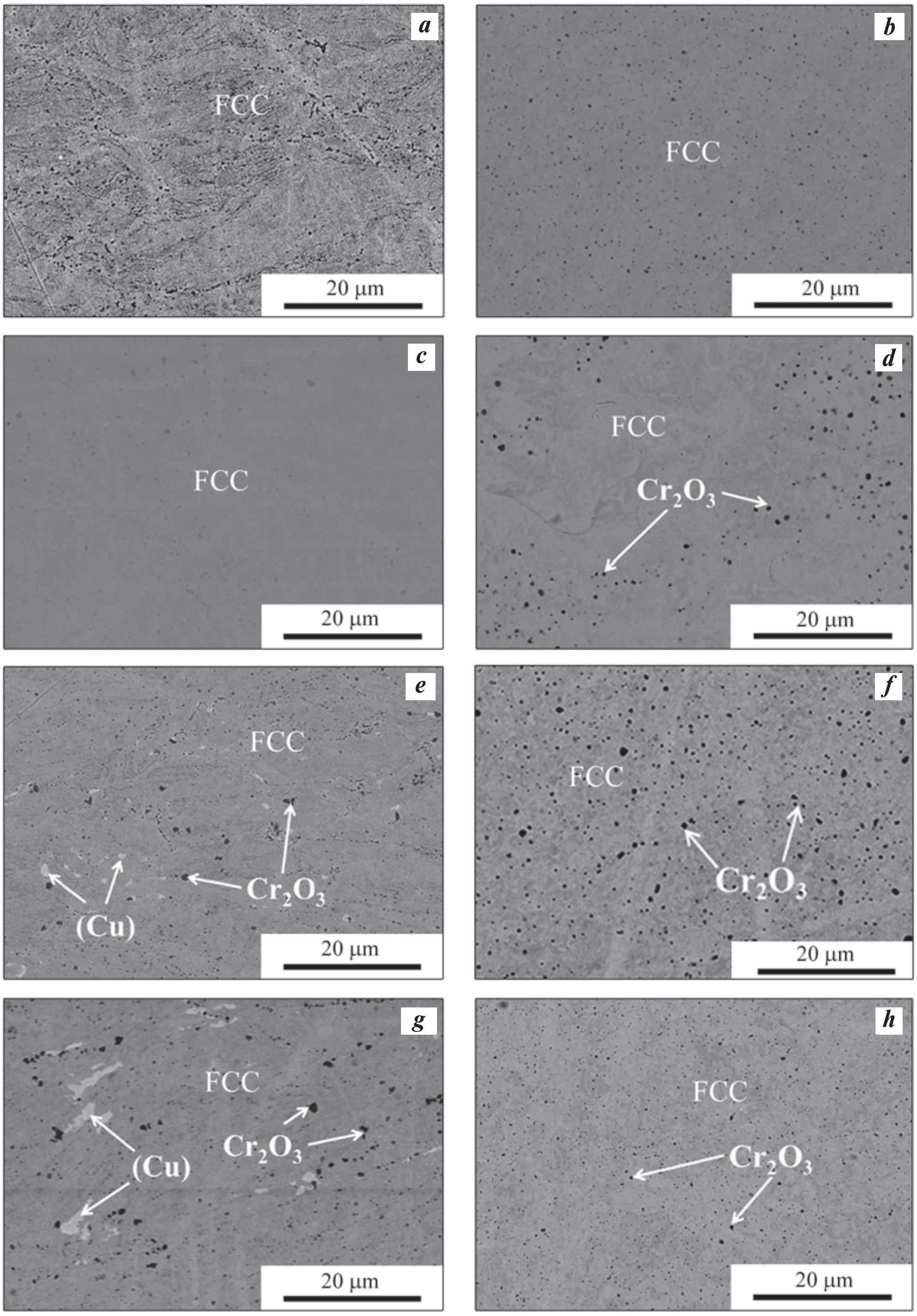

Рис. 5. Микроструктура ВЭС $CoCrCu_xFeNi_2$ после ГП (***a***, ***c***, ***e***, ***g***) и ГП + ТО (***b***, ***d***, ***f***, ***h***)
a, ***b*** – $CoCrFeNi_2$; ***c***, ***d*** – $CoCrCu_{0,5}FeNi_2$; ***e***, ***f*** – $CoCrCu_{0,75}FeNi_2$; ***g***, ***h*** – $CoCrCuFeNi_2$

Fig. 5. Microstructures of $CoCrCu_xFeNi_2$ HEAs after HP (***a***, ***c***, ***e***, ***g***) and HP + HT (***b***, ***d***, ***f***, ***h***)
a, ***b*** – $CoCrFeNi_2$; ***c***, ***d*** – $CoCrCu_{0.5}FeNi_2$; ***e***, ***f*** – $CoCrCu_{0.75}FeNi_2$; ***g***, ***h*** – $CoCrCuFeNi_2$

The HEAs subjected to HP + HT display a uniform microstructure, with the alloy matrix comprising solely of a FCC solid solution across all concentrations of Cu (Fig. 5, *b*, *d*, *f*, *h*).

TEM was employed to delve into the structural nuances of the $CoCrCuFeNi_2$ alloys afted HP and after HP + HT, with Fig. 6 presenting images at a uniform magnification to highlight the structural differences between these treatment stages. The HP-treated $CoCrCuFeNi_2$ alloy showcases an ultrafine-grained structure, evident from the bright-field image through the varied contrast across different regions, indicative of diverse crystallite orientations, and a ring-type diffraction pattern signaling a polycrystalline structure. The

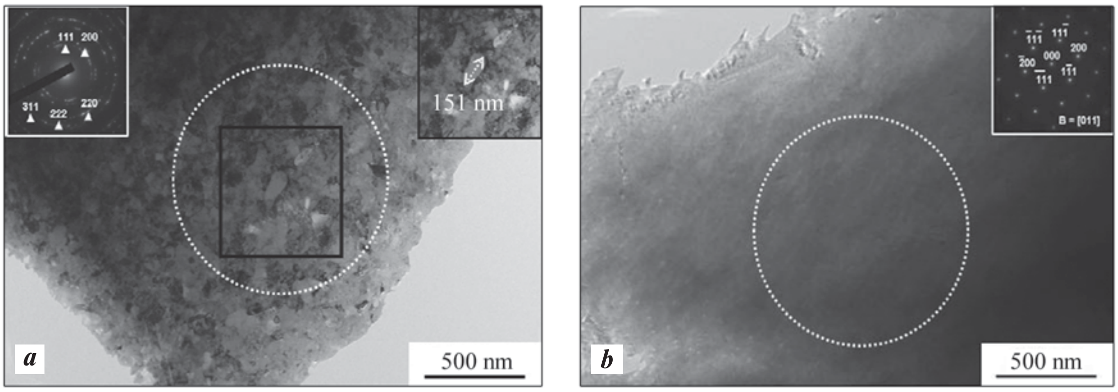

Fig. 6. Microstructure and electron diffraction pattern of $CoCrCuFeNi_2$ alloy samples after HP (***a***) and HP + HT (***b***)

Рис. 6. Микроструктура и электронная дифракция образцов сплава $CoCrCuFeNi_2$ после ГП (***a***) и ГП + ТО (***b***)

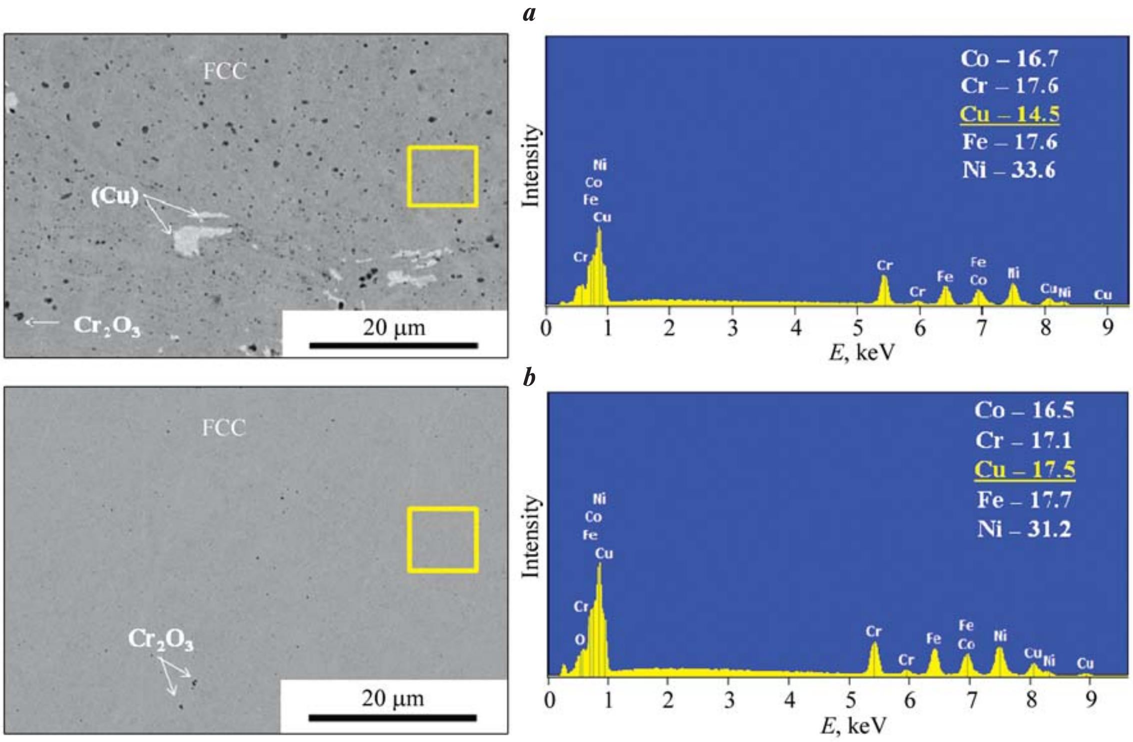

Fig. 7. Microstructures of $CoCrCuFeNi_2$ HEA after HP (***a***) and after HP + HT (***b***), including characteristic *X*-ray spectra from designated areas

Element concentrations presented in at.%

Рис. 7. Микроструктуры ВЭС $CoCrCuFeNi_2$ после ГП (***a***) и ГП + ТО (***b***) со спектрами характеристического рентгеновского излучения, снятыми с выделенных областей

Концентрации элементов указаны в ат.%

average grain size for the HP-treated $CoCrCuFeNi_2$ alloy is 150 nm (Fig. 6, *a*).

The application of HT to the $CoCrCuFeNi_2$ alloy induces a substantial increase in the grain size, a consequence of significant recrystallization activity. This is visualized in Fig. 6, *b* which displays a grain of the FCC phase nearly aligned with the [011] zone axis. Notably, within this grain, there are neither discernible grain boundaries nor inclusions of the (Cu) phase. This observation is in alignment with the findings from both XRD and SEM analyses. After undergoing the combined HP + HT process, the average grain size in the $CoCrCuFeNi_2$ alloy is recorded to be 5.5 μm.

The Co—Cr—Cu—Fe—Ni powder mixtures were subjected to high-energy mechanical treatment using PBM, resulting in a non-equilibrium phase composition, as outlined in Table 1. This process led to the formation of a supersaturated FCC solid solution, notably with copper among other components. Analysis of the chemical composition of the FCC phase after HP, which encouraged the formation of a thermodynamically stable structure through activated diffusion processes, allowed for the examination of copper solubility within the alloy matrix. The EDS analysis, conducted at 10 different points, yielded the average elemental concentrations in the FCC phase. Additionally, it provided visuals of a characteristic microstructure alongside EDS spectra, depicted in Fig. 7, *a*. The findings indicated that the solubility of copper in the FCC phase reached 14.5 at.%, which is 5.5 at.% higher than that in the equiatomic CoCrCuFeNi HEA [17].

Subsequent HT further augmented the solubility of copper in the matrix, achieving a concentration up to 17.5 at.% (Fig. 7, *b*).

2.3. Investigation of the mechanical characteristics of $CoCrCu_xFeNi_2$ HEAs

Figure 8 showcases the relationship between the hardness and tensile ultimate strength of $CoCrCu_xFeNi_2$ HEAs and the fraction of Cu present within them. The established trends from the test results reveal that the hardness of the HP samples increases linearly with the copper content, reaching a peak hardness of 395 HV for the $CoCrCuFeNi_2$ alloy. The hardness of HEAs after HP + HT is considerably less, ranging from 188 to 240 HV.

The indentation measurements (see Fig. 8, *c*) indicate that a rise in Cu content results in a reduction of hardness. This softening effect is likely due to the inclusion of the softer (Cu) phase. The process of heat treatment prompts grain growth, which in turn contributes to the deterioration of mechanical properties. However, it is important to note that the hardness variance in the HP + HT samples, relative to Cu concentration, falls within acceptable error margins, suggesting that the phase composition of these HEAs remains unchanged post-treatment.

In terms of tensile strength, the $CoCrCu_xFeNi_2$ HEAs produced via the HP method exhibit impressive values ranging from 910 to 1045 MPa (Fig. 8, *b*). These figures not only align with those of equiatomic $CoCrCu_xFeNi$ alloys obtained by powder metallurgy techniques [17] but also surpass the tensile strength of other similar alloys in the same system [27—30]. After HP + HT, the HEAs experience a 35—50 % reduction in tensile strength when compared to the HP-only alloys. This decline is attributed to the grain growth observed during the annealing phase of the heat treatment process (illustrated in Fig. 6) during the annealing process.

2.4. Study of wear resistance of $CoCrCu_xFeNi_2$ HEAs

Figure 9 illustrates the relationship between the friction coefficient and the number of cycles, including both 2D and 3D profiles of wear track. Data for comparison are also provided for alloys with a single-molar content of Ni as detailed in reference [17]. Despite variations in the Ni content and the application of HT, the friction coefficient remains relatively unchanged, falling within the range of 0.6 to 0.7. The fluctuations observed are likely due to the accumulation of wear debris between the surfaces in contact during tribological testing.

According to the data displayed in Fig. 10, a histogram delineates the reduced wear rate of $CoCrCu_xFeNi_2$ HEAs in relation to varying Cu concentrations.

For $CoCrCu_xFeNi_2$ HEAs obtained via the HP method, there is a discernible trend showing a decrease in reduced wear as the Cu content increases. This suggests a direct correlation between the hardness of the HEAs and their wear resistance. Specifically, the $CoCrCu_{0.75}FeNi_2$ and $CoCrCuFeNi_2$ alloys, which have the highest amounts of copper dissolved in the FCC matrix, exhibit the lowest wear rates under the conditions tested ($1.58\cdot10^{-5}$ and $1.48\cdot10^{-5}$ $mm^3/(N\cdot m)$, respectively).

The wear resistance of $CoCrCu_xFeNi_2$ HEAs processed through the HP+HT method is comparable or even superior to that of HP-only alloys at lower Cu concentrations. For Cu contents between 0.75 and 1.0 molar fractions, the wear resistance of the HP + HT alloys decreases by 2.5 to 3.0 times.

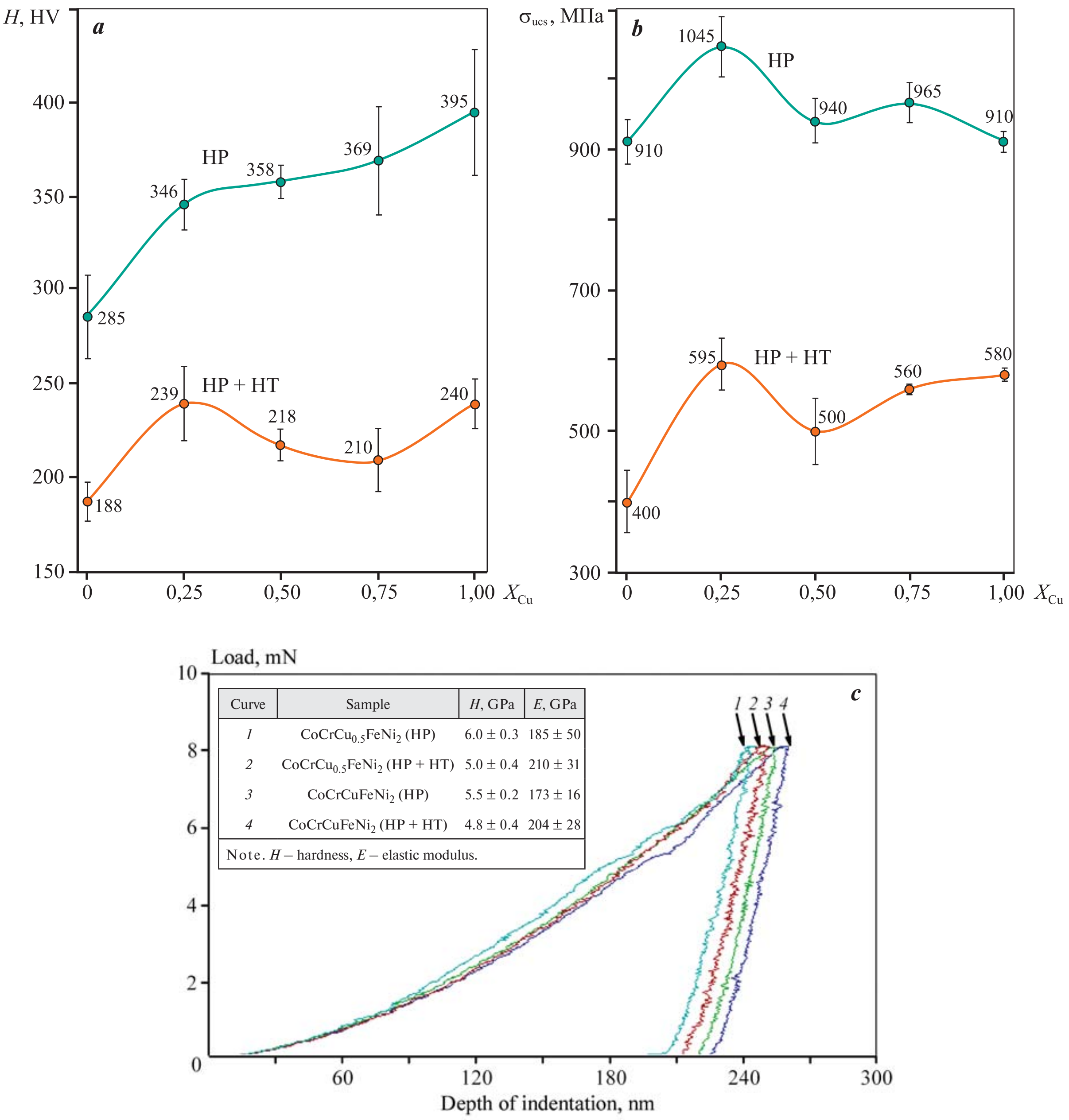

Curve	Sample	H, GPa	E, GPa
1	$CoCrCu_{0.5}FeNi_2$ (HP)	6.0 ± 0.3	185 ± 50
2	$CoCrCu_{0.5}FeNi_2$ (HP + HT)	5.0 ± 0.4	210 ± 31
3	$CoCrCuFeNi_2$ (HP)	5.5 ± 0.2	173 ± 16
4	$CoCrCuFeNi_2$ (HP + HT)	4.8 ± 0.4	204 ± 28

Note. H – hardness, E – elastic modulus.

Fig. 8. Hardness (***a***), tensile strength (***b***) and measuring indentation (***c***) of $CoCrCu_xFeNi_2$ HEA

Рис. 8. Зависимости твердости (***a***) и предела прочности при растяжении (***b***) от концентрации меди в ВЭС $CoCrCu_xFeNi_2$ и результаты измерительного индентирования (***c***)

This lack of a clear trend can be attributed to the grain growth during the annealing phase of HT, which counteracts the beneficial effect of increased Cu concentration in the FCC matrix. This finding indicates that further research is necessary to optimize HT conditions for certain alloys.

The wear mechanism of HEAs was analyzed by examining wear tracks after testing (Fig. 11). Grooves marked by white arrows point in the direction of sliding of the Al_2O_3 counterbody, while dark gray regions identified by EDS consist of Ni and Fe oxides. These local oxidized areas are a result of frictional heating during the sliding process [31]. This oxidative wear mechanism, characterized by the presence of cracks perpendicular to the sliding direction, is common in HEAs with an FCC structure during dry friction with Al_2O_3 or Si_3N_4 balls [33]. The oxidation process initiates wear, leading to the detachment of oxidized fragments along the cracks (insets in Fig. 11, *a*), which con-

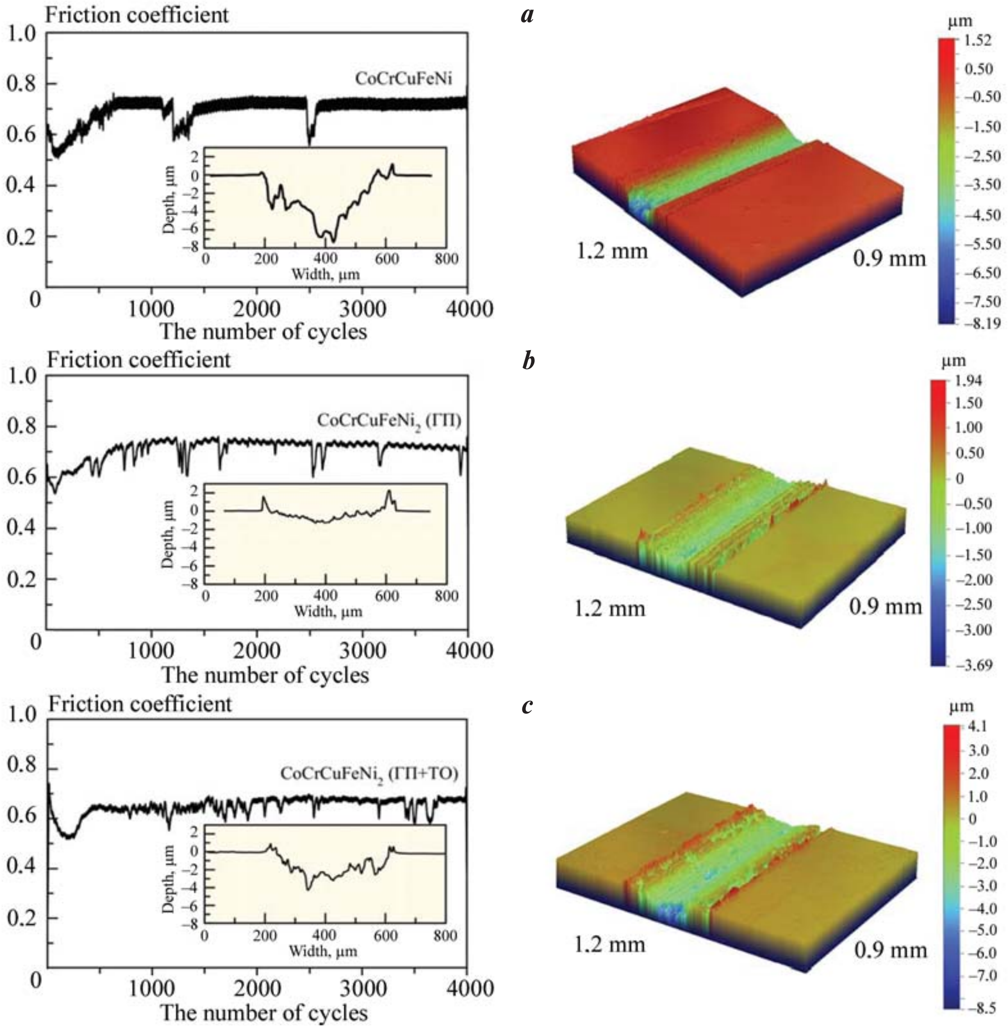

Fig. 9. Friction coefficient over cycle number with 3D and 2D representations of wear tracks in $CoCrCuFeNi_y$ HEAs
a – CoCrCuFeNi [17]; ***b*** – $CoCrCuFeNi_2$ (HP); ***c*** – $CoCrCuFeNi_2$ (HP + HT)

Рис. 9. Зависимость коэффициента трения от количества циклов и 3D- и 2D-изображения дорожек износа ВЭС $CoCrCuFeNi_y$
a – CoCrCuFeNi [17]; ***b*** – $CoCrCuFeNi_2$ (ГП); ***c*** – $CoCrCuFeNi_2$ (ГП + ТО)

tributes to the fluctuation of the friction coefficient (Fig. 9). Additionally, the solid wear debris causes micro-cutting of the sample, as evidenced by the grooves in the worn areas.

The study concludes that while the concentration of Cu in the HEAs and subsequent HT do not alter the wear mechanism, the hardness of the HEAs remains the key factor determining their wear resistance.

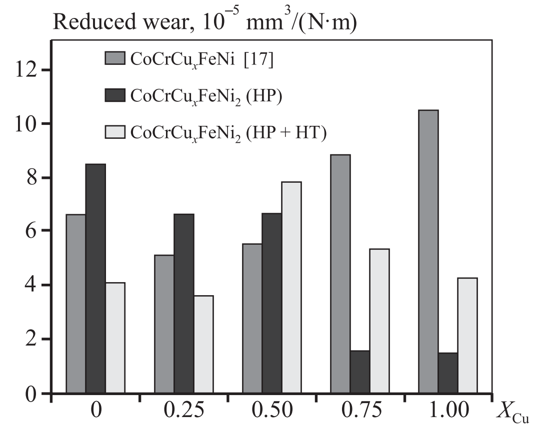

Fig. 10. Relationship between copper content and reduced wear rate in $CoCrCu_xFeNi_y$ HEAs

Рис. 10. Зависимость приведенного износа от содержания меди в ВЭС $CoCrCu_xFeNi_y$

Conclusions

1. Compact samples of $CoCrCu_xFeNi_2$ HEAs were produced using MA and HP methods, resulting in either a single-phase FCC or a two-phase FCC + (Cu) structure.

2. It has been demonstrated that the solubility limit

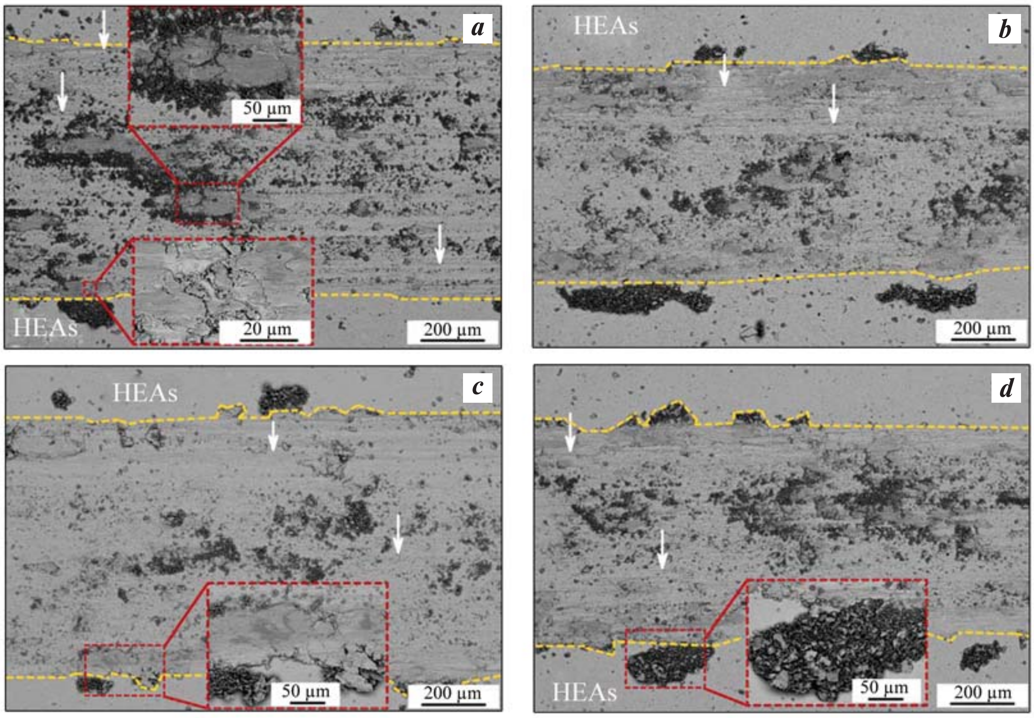

Fig. 11. SEM images of wear tracks on $CoCrCu_xFeNi_y$ HEAs
a – $CoCrCu_{0.5}FeNi_2$ (HP); ***б*** – $CoCrCu_{0.5}FeNi_2$ (HP + HT); ***в*** – $CoCrCuFeNi_2$ (HP); ***г*** – $CoCrCuFeNi_2$ (HP + HT)

Рис. 11. РЭМ-изображения дорожек износа ВЭС $CoCrCu_xFeNi_y$
а – $CoCrCu_{0,5}FeNi_2$ (ГП); ***б*** – $CoCrCu_{0,5}FeNi_2$ (ГП + ТО); ***в*** – $CoCrCuFeNi_2$ (ГП); ***г*** – $CoCrCuFeNi_2$ (ГП + ТО)

of Cu in the FCC solid solution can be increased from 9.0 at.% to 14.5 at.% by doubling the mole fraction of Ni in the $CoCrCu_xFeNi$ HEAs. This solubility is further enhanced to 17.5 at.% with the application of heat treatment, which includes annealing and quenching processes.

3. $CoCrCu_xFeNi_2$ HEAs obtained through the HP method exhibited high mechanical properties, with hardness values ranging between 285—395 HV and tensile strengths spanning 910 to 1045 MPa. However, heat treatment was found to reduce these mechanical properties, which is attributed to grain growth during isothermal annealing.

4. HEAs with a Cu content of 0.75—1.0 molar fractions, specifically those processed by HP, demonstrated high wear resistance ($1.48 \cdot 10^{-5}$ $mm^3/(N \cdot m)$) in friction tests with an Al2O3. The wear mechanism of the $CoCrCu_xFeNi_2$ HEAs involves oxidative processes combined with abrasive action.

References

1. Sanin V.N., Ikornikov D.M., Golosova O.A., Andreev D.E., Yukhvid V.I. Centrifugal metallothermic SHS of cast Co—Cr—Fe—Ni—Mn—(X) alloys. *Russian Journal of Non-Ferrous Metals*. 2020;61(4):436—445. https://doi.org/10.3103/S1067821220040070
2. Sanin V.N., Ikornikov D.M., Golosova O.A., Andreev D.E., Yukhvid V.I. Centrifugal SHS metallurgy of cast Co—Cr—Fe—Ni—Mn high-entropy alloys strengthened by precipitates based on Mo and Nb borides and silicides. *Physical Mesomechanics*. 2021;24: 692—700. https://doi.org/10.1134/S1029959921060072
3. Panina E.S., Yurchenko N.Y., Tozhibaev A.A., Mishunin M.V., Zherebtsov S.V., Stepanov N.D. A study of the structure and mechanical properties of Nb—Mo—Co—X (X = Hf, Zr, Ti) refractory high-entropy alloys. *Physical Mesomechanics*. 2023;26:666—677. https://doi.org/10.1134/S1029959923060061
4. Gromov V.E., Shlyarova Yu.A., Konovalov S.V., Vorob'ev S.V., Peregudov O.A. Application of high-entropy alloys. *Izvestiya. Ferrous Metallurgy*. 2021;64(10): 747—754. (In Russ.). https://doi.org/10.17073/0368-0797-2021-10-747-754
Громов В.Е., Шляпова Ю.А., Коновалов С.В., Воробьев С.В., Перегудов О.А. Применение высокоэнтропийных сплавов. *Известия высших учеб-*

ных заведений. Черная металлургия. 2021;64(10):747—754.
https://doi.org/10.17073/0368-0797-2021-10-747-754

5. Jiaojiao Yia, Lin Yang, Mingqin Xu, Lu Wang. Investigation of a novel CoCrCuNiTi high entropy alloy on microstructure and mechanical properties. *Russian Journal of Non-Ferrous Metals*. 2021;62:197—205.
https://doi.org/10.3103/S1067821221020073
6. Rao K.R., Alshgari R.A., Bahajjaj A.A.A., Chakraborty S., Sinha S.K. Effects of nano scale Y_2O_3 additions on microstructural stability and mechanical properties of equiatomic CoCrCuFeNi based high entropy alloys. *Materials Chemistry and Physics*. 2023;296:127325.
https://doi.org/10.1016/j.matchemphys.2023.127325
7. Kuptsov K.A., Antonyuk M.N., Sheveyko A.N., Bondarev A.V., Ignatov S.G., Slukin P.V., Dwivedi P., Fraile A., Polcar T., Shtansky D.V.. High-entropy Fe—Cr—Ni—Co—(Cu) coatings produced by vacuum electro-spark deposition for marine and coastal applications. *Surface and Coatings Technology*. 2023;453:129136.
https://doi.org/10.1016/j.surfcoat.2022.129136
8. Huang K., Chen L., Lin X., Huang H., Tang S., Du F. Wear and corrosion resistance of $Al_{0.5}$CoCrCuFeNi high-entropy alloy coating deposited on AZ91D magnesium alloy by laser cladding. *Entropy*. 2018;20(12):915.
https://doi.org/10.3390/e20120915
9. Changqing Shu, Zhengjun Yao, Xiaolin Li, Wenbo Du, Xuewei Tao, Hemei Yang. Microstructure and wear mechanism of CoCrCuFeNiVx high entropy alloy by sintering and electron beam remelting. *Physica B: Condensed Matter*. 2022;638:413834.
https://doi.org/10.1016/j.physb.2022.413834
10. Kamalakannan R., DineshKumar K., NarenRaj K. The sliding wear behavior of CrCuFeNi alloyed with various combinations of cobalt. *Materials Today: Proceedings*. 2022;50(5):1814—1817.
https://doi.org/10.1016/j.matpr.2021.09.211
11. Verma A., Chauhan L., Kumar T.S., Singh Prashant Kumar, Dommeti Satya Gowtam, Thangaraju Shanmugasundaram. Laser cladding of CoCrCuFeNi and CoCrFeNi high-entropy alloys on DMR 249A steel: Corrosion, wear and antibacterial behaviour. *The Journal of the Minerals, Metals and Materials Society (TMS)*. 2023;75(7):2701—2713.
https://doi.org/10.1007/s11837-023-05861-z
12. Verma A., Tarate P., Abhyankar A.C., Mohape M.R., Gowtam D.S., Deshmukh V.P., Shanmugasundaram T. High temperature wear in CoCrFeNiCu$_x$ high entropy alloys: The role of Cu. *Scripta Materialia*. 2019;171:28—31.
https://doi.org/10.1016/j.scriptamat.2018.10.007
13. Yubin Huang, Yongle Hu, Mingjun Zhang, Cong Mao, Yonggang Tong, Jian Zhang, Kangwei Li, Kaiming Wang. On the enhanced wear resistance of laser-clad CoCrCuFeNiTi$_x$ high-entropy alloy coatings at elevated temperature. *Tribology International*. 2022;174:107767.
https://doi.org/10.1016/j.triboint.2022.107767
14. Yang Gao, Haibo Xiao, Bin Liu, Yong Liu. Enhanced drilling performance of impregnated diamond bits by introducing a novel HEA binder phase. *International Journal of Refractory Metals and Hard Materials*. 2024;118:106449.
https://doi.org/10.1016/j.ijrmhm.2023.106449
15. Loginov P.A., Fedotov A.D., Mukanov S.K., Manakova O.S., Zaitsev A.A., Akhmetov A.S., Rupasov S.I., Levashov E.A. Manufacturing of metal—diamond composites with high-strength CoCrCu$_x$FeNi high-entropy alloy used as a binder. *Materials*. 2023;16(3):1285
https://doi.org/10.3390/ma16031285
16. Takeshi Nagase, Philip D. Rack, Joo Hyon Noh, Takeshi Egami. In-situ TEM observation of structural changes in nano-crystalline CoCrCuFeNi multicomponent high-entropy alloy (HEA) under fast electron irradiation by high voltage electron microscopy (HVEM). *Intermetallics*. 2015;59:32—42.
https://doi.org/10.1016/j.intermet.2014.12.007
17. Mukanov S.K., Loginov P.A., Fedotov A.D., Bychkova M.Ya., Antonyuk M.N., Levashov E.A. The effect of copper on the microstructure, wear and corrosion resistance of CoCrCuFeNi high-entropy alloys manufactured by powder metallurgy. *Materials*. 2023;16(3):1178.
https://doi.org/10.3390/ma16031178
18. Shkodich N.F., Kovalev I.D., Kuskov K.V., Kovalev D.Yu., Vergunova Yu.S., Scheck Yu.B., Vadchenko S.G., Politano O., Baras F., Rogachev A.S. Fast mechanical synthesis, structure evolution, and thermal stability of nanostructured CoCrFeNiCu high entropy alloy. *Journal of Alloys and Compounds*. 2022;893:161839.
https://doi.org/10.1016/j.jallcom.2021.161839
19. Moghaddam A.O., Samodurova M.N., Pashkeev K., Doubenskaia M., Sova A., Trofimov E.A. A novel intermediate temperature self-lubricating CoCrCu$_{1-x}$FeNi$_x$ high entropy alloy fabricated by direct laser cladding. *Tribology International*. 2021;156:106857.
https://doi.org/10.1016/j.triboint.2021.106857
20. Peng Jian, Li Zi-yong, Ji Xin-bo, Sun Yan-le, Fu Li-ming, Shan Ai-dang. Decomposition kinetics of carbon-doped FeCoCrNiMn high-entropy alloy at intermediate temperature. *Transactions of Nonferrous Metals Society of China*. 2020;30(7):1884—1894.
https://doi.org/10.1016/S1003-6326(20)65347-X
21. Dabrowa J., Cieslak G., Stygar M., Mroczka K., Berent K., Kulik T., Danielewski M. Influence of Cu content on high temperature oxidation behavior of AlCoCrCu$_x$FeNi

high entropy alloys (x = 0; 0.5; 1). *Intermetallics*. 2017; 84:52—61. https://doi.org/10.1016/j.intermet.2016.12.015

22. Li Cheng, Xue Yun-fei, Hua Mu-tian, Cao Tang-qing, Ma Li-li, Wang Lu. Microstructure and mechanical properties of $Al_xSi_{0.2}CrFeCoNiCu_{1-x}$ high-entropy alloys. *Materials and Design*. 2016;90:601—609. https://doi.org/10.1016/j.matdes.2015.11.013
23. Lin C.M., Tsai H.L. Equilibrium phase of high-entropy $FeCoNiCrCu_{0.5}$ alloy at elevated temperature. *Journal of Alloys and Compounds*. 2010;489(1):30—35. https://doi.org/10.1016/j.jallcom.2009.09.041
24. Lin C.M., Tsai H.-L. Effect of annealing treatment on microstructure and properties of high-entropy $FeCoNiCrCu_{0.5}$ alloy. *Materials Chemistry and Physics*. 2011;128(1-2):50—56. https://doi.org/10.1016/j.matchemphys.2011.02.022
25. Fangyan Liu, Qiang Song, Ruirun Chen, Canming Wang, Jiawei Sun. Effect of Co, Ni, Cu content on phase composition, microstructure and corrosion resistance of $Co_{1-x}CrFeNi_{1+x}Cu_y$ series high-entropy alloys. *Vacuum*. 2013;210:111830. https://doi.org/10.1016/j.vacuum.2023.111830
26. Zhu Z.G., Ma K.H., Wang Q., Shek C.H. Compositional dependence of phase formation and mechanical properties in three CoCrFeNi—(Mn/Al/Cu) high entropy alloys. *Intermetallics*. 2016;79:1—11. https://doi.org/10.1016/j.intermet.2016.09.003
27. Qiang Hu, Hai-ling Wang, Li-hua Qian, Liang-cai Zeng, Qiang Wang, Xin-wang Liu. Effects of Cu additions on microstructure and mechanical properties of as-cast $CrFeCoNiCu_x$ high-entropy alloy. *Transactions of Nonferrous Metals Society of China*. 2023;33(6):1803—1813. https://doi.org/10.1016/S1003-6326(23)66223-5
28. Du C., Hu L., Pan Q., Chen K., Zhou P., Wang G. Effect of Cu on the strengthening and embrittling of an FeCoNiCr—xCu HEA. *Materials Science and Engineering: A*. 2023;832:142413. https://doi.org/10.1016/j.msea.2021.142413
29. Fiocchi Jacopo, Casati Riccardo, Tuissi Ausonio, Biffi Carlo Alberto. Laser beam welding of CoCuFeMnNi high entropy alloy: Processing, microstructure, and mechanical properties. *Advanced Engineering Materials*. 2022;24(10):202200523. https://doi.org/10.1002/adem.202200523
30. Seung Min Oh, Sun Ig Hong. Microstructural stability and mechanical properties of equiatomic CoCrCuFeNi, CrCuFeMnNi, CoCrCuFeMn alloys. *Materials Chemistry and Physics*. 2018;210:120—125. https://doi.org/10.1016/j.matchemphys.2017.09.010
31. Fei Liang, Ao Meng, Yixing Sun, Zhaoshuo Chen, Zhouwen Jiang, Yaping Zhang, Yong Zhang, Yuntian Zhu, Xiang Chen. A novel wear-resistant Ni-based superalloy via high Cr-induced subsurface nanotwins and heterogeneous composite glaze layer at elevated temperatures. *Tribology International*. 2023;183:108383. https://doi.org/10.1016/j.triboint.2023.108383
32. Zhuo Cheng, Lu Yang, Zhikun Huang, Tian Wan, Mingyu Zhu, Fuzeng Ren. Achieving low wear in a μ-phase reinforced high-entropy alloy and associated subsurface microstructure evolution. *Wear*. 2021;474-475:203755. https://doi.org/10.1016/j.wear.2021.203755
33. Qiang Wang, Qiang Hu, Hailing Wang, Liangcai Zeng. Investigations on the microstructures and tribological behaviors of as-cast $CrFeCoNiCu_x$ high entropy alloys. *Intermetallics*. 2023;157:107886. https://doi.org/10.1016/j.intermet.2023.107886

Information about the authors

Alexander D. Fedotov – Postgraduate Student, Scientific Project Engineer, Department of Powder Metallurgy and Functional Coatings (PM&FC), National University of Science and Technology “MISIS” (NUST MISIS).
https://orcid.org/0009-0009-9208-1453
E-mail: sashok12221998@mail.ru

Samat K. Mukanov – Cand. Sci. (Eng.), Research Assistant, Laboratory “In situ diagnostics of structural transformations” of Scientific-Educational Center of SHS of MISIS–ISMAN.
https://orcid.org/0000-0001-6719-6237
E-mail: sam-mukanov@mail.ru

Информация об авторах

Александр Дмитриевич Федотов – аспирант, инженер научного проекта, кафедра порошковой металлургии и функциональных покрытий (ПМиФП), Национальный исследовательский технологический университет «МИСИС» (НИТУ МИСИС).
https://orcid.org/0009-0009-9208-1453
E-mail: sashok12221998@mail.ru

Самат Куандыкович Муканов – к.т.н., мл. науч. сотрудник, лаборатория «In situ диагностика структурных превращений» Научно-учебного центра (НУЦ) СВС МИСИС–ИСМАН.
https://orcid.org/0000-0001-6719-6237
E-mail: sam-mukanov@mail.ru

Bogdan Yu. Romanenko – Graduate Student, Training Master, Department of PM&FC, NUST MISIS.
https://orcid.org/0009-0003-7470-5185
E-mail: a.v.d.romanenko@gmail.com

Pavel A. Loginov – Cand. Sci. (Eng.), Assistant Prof. of NUST MISIS; Senior Researcher at the Laboratory “In situ diagnostics of structural transformations” of Scientific-Educational Center of SHS of MISIS–ISMAN.
https://orcid.org/0000-0003-2505-2918
E-mail: loginov.pa@misis.ru

Marina Ya. Bychkova – Cand. Sci. (Eng.), Assistant Prof. of NUST MISIS; Researcher Researcher at the Laboratory “In situ diagnostics of structural transformations” of Scientific-Educational Center of SHS of MISIS–ISMAN.
https://orcid.org/0000-0002-9233-4707
E-mail: bychkova@shs.misis.ru

Sergey I. Rupasov – Leading Expert of the scientific project, Department of PM&FC, NUST MISIS.
https://orcid.org/0000-0003-0948-688X
E-mail: rupasov@misis.ru

Богдан Юрьевич Романенко – магистр, учебный мастер, кафедра ПМиФП, НИТУ МИСИС.
https://orcid.org/0009-0003-7470-5185
E-mail: a.v.d.romanenko@gmail.com

Павел Александрович Логинов – к.т.н., доцент НИТУ МИСИС, ст. науч. сотрудник лаборатории «In situ диагностика структурных превращений» НУЦ СВС МИСИС–ИСМАН.
https://orcid.org/0000-0003-2505-2918
E-mail: loginov.pa@misis.ru

Марина Яковлевна Бычкова – к.т.н., доцент НИТУ МИСИС, науч. сотрудник НУЦ СВС МИСИС–ИСМАН.
https://orcid.org/0000-0002-9233-4707
E-mail: bychkova@shs.misis.ru

Сергей Иванович Рупасов – вед. эксперт научного проекта, кафедра ПМиФП, НИТУ МИСИС.
https://orcid.org/0000-0003-0948-688X
E-mail: rupasov@misis.ru

Contribution of the authors

A.D. Fedotov – planned the experiment, processed the experimental data, wrote the manuscript.

S.K. Mukanov – carried out tribological tests, participated in the discussion of the results.

B.Yu. Romanenko – prepared powder mixtures, processed the obtained results.

P.A. Loginov – formulated the general concept of the study, set the research goals, performed transmission electron microscopy experiments, and engaged in result discussions.

M.Ya. Bychkova – analyzed the experimental data and contributed to manuscript preparation.

S.I. Rupasov – executed sample compaction and performed mechanical testing (tension, bending).

Вклад авторов

А.Д. Федотов – планирование экспериментов, обработка экспериментальных данных, написание статьи.

С.К. Муканов – проведение трибологических испытаний, участие в обсуждении результатов.

Б.Ю. Романенко – приготовление порошковых смесей, обработка полученных результатов.

П.А. Логинов – разработка общей концепции статьи, определение цели работы, проведение экспериментов по просвечивающей электронной микроскопии, участие в обсуждении результатов.

М.Я. Бычкова – анализ экспериментальных данных, подготовка текста.

С.И. Рупасов – компактирование образцов, проведение механических испытаний (растяжение, изгиб).

The article was submitted 29.01.2024, accepted for publication 02.02.2024

Статья поступила в редакцию 29.01.2024, подписана в печать 02.02.2024

PHYSICAL METALLURGY AND HEAT TREATMENT / МЕТАЛЛОВЕДЕНИЕ И ТЕРМИЧЕСКАЯ ОБРАБОТКА

UDC 669.1 : 620.1
https://doi.org/10.17073/0021-3438-2024-1-70-80

Research article
Научная статья

Structure and mechanical properties of PR-03N18K9M5TYu steel grade fabricated by selective laser melting and post-processing

A.O. Kayasova, F.A. Baskov, T.A. Lobova, E.A. Levashov

National University of Science and Technology "MISIS"
4 Bld. 1 Leninskiy Prosp., Moscow 119049, Russia

✉ Anastasiya O. Kayasova (NKayasova@gmail.com)

Abstract: We fabricate samples of PR-03N18K9M5TYu steel (equivalent to ChS4) using selective laser melting (SLM) in a nitrogen atmosphere. Our research focused on the influence of hot isostatic pressing (HIP) combined with heat treatment (HT), specifically hardening and aging, on the steel's structure and its physical and mechanical properties (σ_{ucs}, σ_{ys}, δ, ψ). Through tensile testing, we evaluated the impact of post-processing treatments (HIP followed by HT) on the material's strength. We also assessed how different post-processing protocols affected residual porosity. Our findings indicate that samples exhibiting the highest strength and plastic properties correspond to those with the least structural defects and minimal residual porosity. In-depth microstructural analysis revealed that the optimal structure—a fine-grained, homogeneous configuration—is achieved via the combined application of SLM, HIP, and subsequent HT. The improvement in mechanical properties can be primarily attributed to the dispersed hardening effect, which is a consequence of the precipitation of the superfluous Ni_3Ti phase. Fractographic examination revealed that the post-processing leads to a ductile and dimple fracture, occurring through mechanisms of shearing and detachment, giving rise to mixed-type fractures. The samples that displayed superior mechanical properties were characterized by a homogenous ductile intergranular fracture surface with clear evidence of plastic deformation. We measured the hardness (H), modulus of elasticity (E), and elastic recovery via indentation methods. The post-processing treatments notably enhanced material hardness and elastic modulus, with an increase from $H = 4.6$ GPa and $E = 194$ GPa in the sample post-HIP to $H = 8.5$ GPa and $E = 256$ GPa following HIP coupled with hardening and aging.

Keywords: selective laser melting, maraging steel, hot isostatic pressing, heat treatment, microstructure, mechanical properties.

Acknowledgments: The work was carried out with financial support from the Ministry of Science and Higher Education of the Russian Federation within the framework of a state assignment (project No. 0718-2020-0034).

For citation: Kayasova A.O., Baskov F.A., Lobova T.A., Levashov E.A. Structure and mechanical properties of PR-03N18K9M5TYu steel grade fabricated by selective laser melting and post-processing. *Izvestiya. Non-Ferrous Metallurgy.* 2024;30(1):70–80.
https://doi.org/10.17073/0021-3438-2024-1-70-80

Особенности структуры и механические свойства стали ПР-03Н18К9М5ТЮ, полученной методом селективного лазерного сплавления в сочетании с постобработкой

А.О. Каясова, Ф.А. Басков, Т.А. Лобова, Е.А. Левашов

Национальный исследовательский технологический университет «МИСИС»
Россия, 119049, г. Москва, Ленинский пр-т, 4, стр. 1

✉ Анастасия Олеговна Каясова (NKayasova@gmail.com)

Аннотация: Методом селективного лазерного сплавления (СЛС) в среде азота был получен материал из стали марки ПР-03Н18К9М5ТЮ (аналог ЧС4). Изучено влияние горячего изостатического прессования (ГИП) и термообработки (ТО) – закалки (З) и старения (С) – на структуру и физико-механические свойства ($\sigma_в$, $\sigma_{0,2}$, δ, ψ) СЛС-материала. Для анализа влияния постобработки (ГИП + ТО) на прочностные характеристики проведены испытания на разрыв. Проанализировано изменение остаточной пористости в результате различных режимов постобработки. Установлено повышение прочностных и пластических характеристик материала с наименьшей концентрацией структурных дефектов и минимальной остаточной пористостью. Исследованы микроструктура и изменения, происходящие в материале под влиянием различных технологических режимов термообработки. Мелкозернистая однородная структура, полученная при сочетании СЛС с ГИП и ТО, обеспечивает оптимальные показатели прочностных и пластических свойств материала. Прирост механических свойств обусловлен дисперсным упрочнением в результате выделения избыточной фазы Ni_3Ti. Фрактографический анализ образцов показал, что в результате постобработки разрушение материала происходит по вязко-ямочному механизму путем среза и отрыва с образованием изломов смешанного типа. Изломы образцов, с наилучшими показателями механических свойств, характеризуются однородной поверхностью вязкого внутрезеренного разрушения с выраженными признаками пластической деформации Методом измерительного индентирования определены твердость (H), модуль упругости (E) и степень упругого восстановления. Значения твердости и модуля упругости возрастают от $H = 4{,}6$ ГПа и $E = 194$ ГПа для образца в состоянии ГИП до $H = 8{,}5$ ГПа, $E = 256$ ГПа для образца после ГИП + З + С.

Ключевые слова: селективное лазерное сплавление, мартенситно-стареющая сталь, горячее изостатическое прессование, термическая обработка, микроструктура, механические свойства.

Благодарность: Работа выполнена при финансовой поддержке Министерства науки и высшего образования Российской Федерации в рамках государственного задания (проект № 0718-2020-0034).

Для цитирования: Каясова А.О., Басков Ф.А., Лобова Т.А., Левашов Е.А. Особенности структуры и механические свойства стали ПР-03Н18К9М5ТЮ, полученной методом селективного лазерного сплавления в сочетании с постобработкой. *Известия вузов. Цветная металлургия.* 2024;30(1):70–80. https://doi.org/10.17073/0021-3438-2024-1-70-80

Introduction

Powder maraging steels are distinguished by their high strength and minimal carbon content. The mechanical properties of these steels are enhanced through alloying with elements that substitute for carbon, such as nickel, molybdenum, and cobalt. The notable strength of maraging steels originates from the precipitation of strengthening intermetallic phases. A critical advantage of maraging steels over other steel grades is their resistance to brittle fracture [1—4].

In comparison to other steel grades, maraging steels exhibit superior processability. They demonstrate exceptional hardenability, weldability, ductility, and resistance to cracking upon cooling. The heat treatment (HT) process for maraging steels is straightforward, involving hardening followed by aging, without the occurrence of warping during heat treatment or decarburization after hardening, which could lead to a loss of strength and increased wear. Consequently, maraging steels are highly suitable for machining.

The outstanding performance of maraging steels enables their use in the production of mission-critical components that demand high strength, ductility, and fracture toughness.

Maraging steel powder is characterized by low reflectivity and excellent weldability, making it well-suited for selective laser melting (SLM) [5; 6]. The SLM process enables the creation of products with complex geometries in a single operation, a task that poses challenges for traditional manufacturing techniques.

However, the SLM process may result in incomplete fusion of powder particles, potentially leading to structural defects, residual porosity, and microcracks. These imperfections can diminish the mechanical properties and overall performance of the products. Therefore, the post-processing of SLM products, including hot isostatic pressing followed by heat treatment, is crucial [7—11].

Researchers [12] fabricated SLM samples of $FeCo_{15}Cr_{14}Ni_4Mo_3$ maraging steel and analyzed the material's structure and mechanical properties before and after aging. Under optimized conditions, the SLM steel displayed a tensile strength of 1484 ± 6 MPa and a yield strength of 1376 ± 4 MPa.

Another study [13] focused on maraging steel with a high molybdenum content (15 %), aging the material at 530 °C to initiate dispersion hardening. The steel retained its martensitic structure through the aging process, which also induced a solid solution transformation and the precipitation of nanosized, dispersed Fe_2Mo particles. Consequently, the steel demonstrated exceptional mechanical properties, with a tensile strength of 1978 ± 38 MPa and a relative elongation of 7.36 %.

The strength of this category of steels can be enhanced through heat treatment at temperatures ranging from 480 to 500 °C over several hours. The presence of alloying elements during the aging process facilitates the segregation of hardening phases such as Ni_3Mo, Ni_3Ti,

Ni_3Al, and within the martensite phase. These phases obstruct the Orowan mechanism [14]. In SLM structures, the layer-by-layer fusion of the powder subjects the steel to cyclic reheating, leading to dispersive hardening [15]. Research has demonstrated that HT significantly improves the steel's mechanical properties. By fine-tuning the HT parameters, the desired properties can be achieved. For example, Tan C. et al. [16] explored the impact of aging at $t = 490$ °C for $\tau = 6$ h and hardening after holding at $t = 840$ °C ($\tau = 1$ h) on the microstructure and mechanical properties of the 18N300 grade steel. Compared to samples aged post-SLM, those subjected to hardening followed by aging exhibited increased strength and hardness, albeit with a reduction in elongation at break.

This study aims to examine the influence of post-processing treatments, specifically hot isostatic pressing (HIP) and heat treatment, on the structural, physical, and mechanical properties (σ_{ucs}, σ_{ys}, δ, ψ) of the SLM-fabicated materials made from PR-03N18K9M5TYu steel (equivalent to ChS4).

Materials and methods

The samples were fabricated by SLM using PR-03N18K9M5TYu steel powder (Polema, Tula, Russia). The powder's chemical composition is as follows (wt.%):

Fe	base metal	C	0.02
Mo	5.02	Al	0.15
N	18.2	O	0.017
Ti	0.99	N	0.003
Co	8.99		

The powder particle ranged in size from 10 to 63 µm, with size distribution metrics d_{10} = 18.6 µm, d_{50} = 43.2 µm, and d_{90} = 72.9 µm. The bulk density of the powder was 4.378 g/cm^3. he particles were irregularly shaped, some with attached satellites, and up to 65 µm in size. The powder's microstructure featured fine dendrites, notably without any closed gas micropores. (Fig. 1, *c*).

A "Concept Laser M2" (Germany) machine operating in a nitrogen atmosphere, was utilized for the SLM process. Samples were aligned at 0, 45, and 90 degrees relative to the build platform. SLM parameters included a layer thickness of 30 µm, laser power of 180 W, and scanning speed of 600 mm/s. Internal defects and porosity of the samples were examined using computed tomography with an XTH450 LC *X*-ray scanner (Japan).

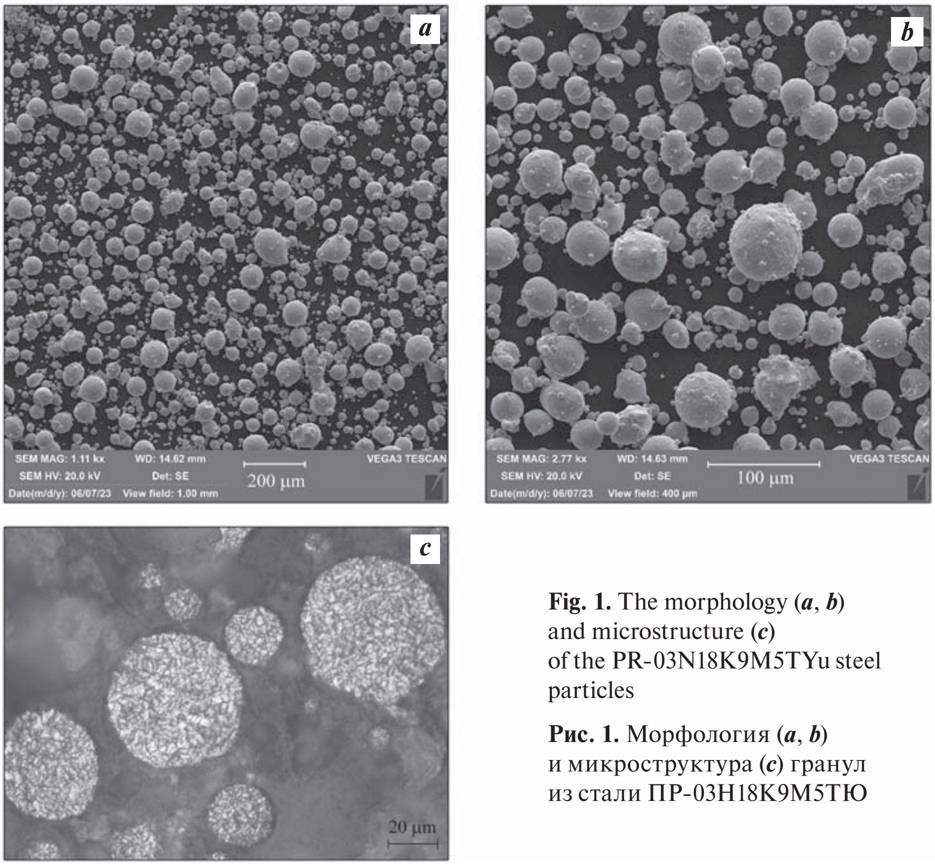

Fig. 1. The morphology (***a***, ***b***) and microstructure (***c***) of the PR-03N18K9M5TYu steel particles

Рис. 1. Морфология (***a***, ***b***) и микроструктура (***c***) гранул из стали ПР-03Н18К9М5ТЮ

The SLM samples underwent HIP using an ABRA HIRP 10/26-200-2000 gasostat (Sweden) in four different modes (HIP1 to HIP4), each with increasing temperature ranges from 920 to 1140 °C, maintained for 2 h at constant pressure. Air quenching followed by aging was performed in an argon-filled electric furnace, with conditions referenced from previous studies [7; 14].

Mechanical properties were assessed by preparing cylindrical tensile test specimens according to GOST 1497-84, type IV, No. 8 standards. A “Shimadzu 100kN” (Japan) tensile test system measured the offset yield strength (σ_{ys}), yield strength (σ_{ucs}), relative elongation (δ), and relative contraction (ψ).

Hardness, elastic modulus, and elastic recovery were determined via indentation using a “Nano-Hardness Tester” (CSM Instruments, Switzerland), applying a 20 mN load to a Berkovich tip, and employing the Oliver—Farr method for plotting loading/unloading curves. Structural investigation employed both scanning electron microscopy (SEM) and transmission electron microscopy (TEM) using an S-3400 (Hitachi, Japan) and a JEM-2100 (JEOL, Japan), respectively, with TEM samples prepared via mechanical thinning and ion beam etching on a PIPS II precision ion polishing system (Gatan, USA). *X*-ray diffraction (XRD) analysis utilized a “Phaser D2” XRD diffractometer (Bruker, USA) with a CuK_α radiation, and energy dispersive spectroscopy was performed with a “NORAN *X*-ray System 7” (Thermo-Fisher Scientific, USA) on the S-3400N electron microscope.

Results and discussion

The SLM process successfully fabricated samples from PR-03N18K9M5TYu steel powder on the build table, as depicted on Fig. 2. *X*-ray tomography analysis revealed no internal defects, such as discontinuities or cracks, within the samples (Fig. 3).

To ascertain the impact of HIP on these samples, tensile tests and porosity analyses were conducted. The initial SLM samples exhibited a porosity level of 0.6 %. Their mechanical properties were measured as follows: an offset yield strength (σ_{ys}) of 1098 MPa, a yield strength (σ_{ucs}) of 1323 MPa, a relative elongation (δ) of 12.6 %, and a relative contraction (ψ) of 42.7 %.

The application of hot isostatic pressing significantly reduced the residual porosity levels to 0.37 % in HIP1 mode, 0.2 % in HIP2, 0.1 % in HIP3, and 0.46 % in HIP4. The combined treatment of HIP with HT (H + A) markedly enhanced the mechanical properties, with increases in σ_{ys} and σ_{ucs}:

— HIP1 + H + A: by 25 % (1335 MPa) and 18 % (1534 MPa), respectively

— HIP2 + H + A: by 26 % (1389 MPa) and 20 % (1590 MPa), respectively

— HIP3 + H + A: by 46 % (1603 MPa) and 35 % (1790 MPa), respectively

— HIP4 + H + A: by 30 % (1430 MPa) and 24 % (1630 MPa), respectively.

These post-processing steps effectively eliminated structural defects and reduced residual porosity, which, in turn, improved the material’s strength and plastic

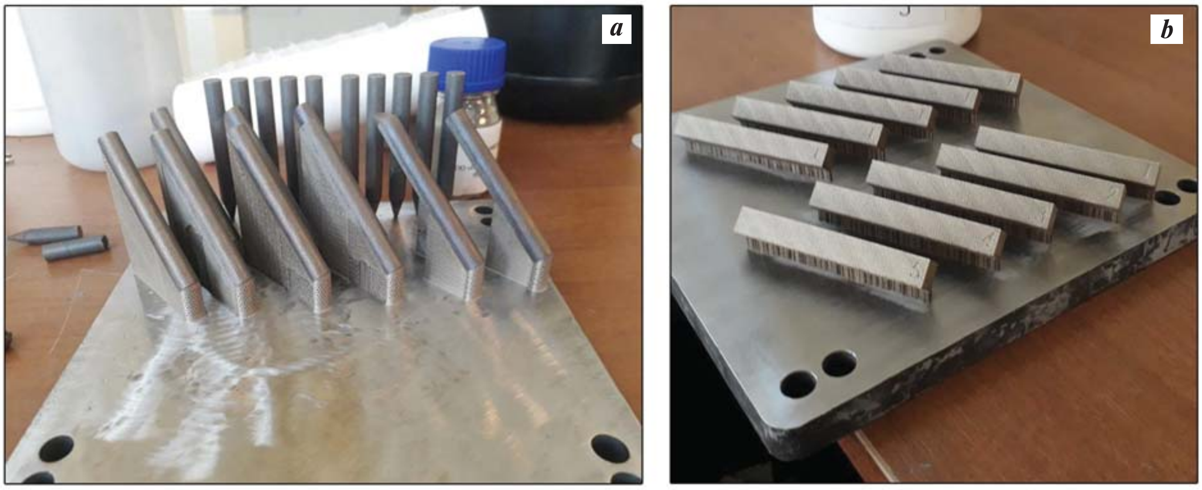

Fig. 2. The SLM samples fabricated from the PR-03N18K9M5TYu steel grade on the build table
a – 45° and 90°; ***b*** – 0°

Рис. 2. Расположение СЛС-образцов из стали ПР-03Н18К9М5ТЮ на платформе построения
a – положение 45° и 90°; ***b*** – положение 0°

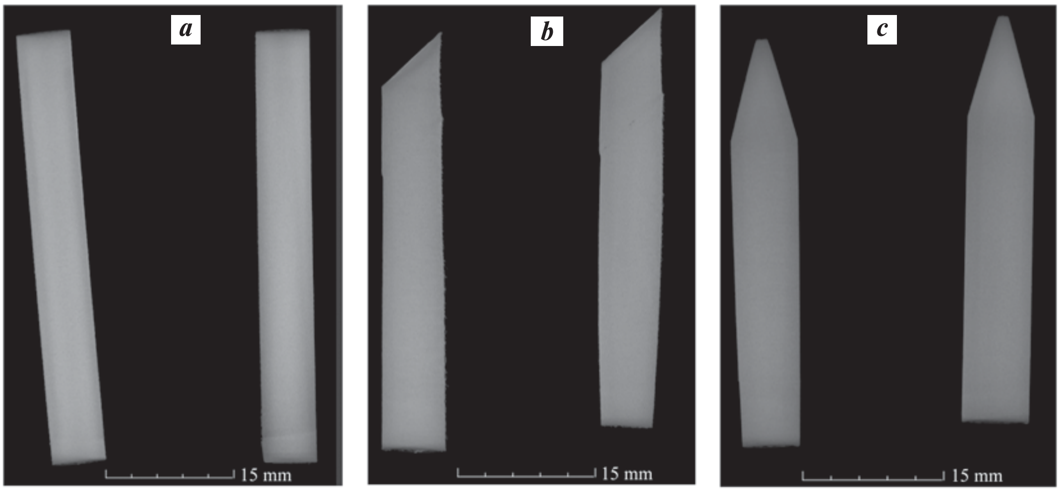

Fig. 3. CT image of the SLM samples
a – 0°; ***b*** – 45°; ***c*** – 90°

Рис. 3. Компьютерная томография СЛС-образцов из стали ПР-03Н18К9М5ТЮ
a – 0°; ***b*** – 45°; ***c*** – 90°

properties. The optimal results in terms of strength and ductility were obtained through the combination of HIP, followed by hardening and aging treatments.

Fig. 4 illustrates the uniaxial strain curves for the samples oriented at 0°, 45°, and 90°, subjected to various post-processing treatments. These curves indicate that the samples possess high strength and plasticity, with a consistent region of plastic deformation. The most favorable outcomes in both plastic and strength properties were achieved with the HIP3 + H + A treatment.

The influence of heat treatment on the material's properties was further confirmed through nanoindentation tests. As shown in Fig. 5 and table, there was a significant increase the hardness (H) and elastic modulus (E) from $H = 4.6$ GPa and $E = 195$ GPa for the sample after HIP, to $H = 8.5$ GPa, $E = 256$ GPa for the sample treated with HIP + H + A.

Fig. 6 depicts the fracture surfaces and the mechanisms of faluer observed in the samples. The prevalent mode of failure is ductile, characterized by dimpling through shearing and detachment, leading to the formation of mixed-type fractures. Some fracture surfaces exhibit pores with diameters up 50 μm.

The fracture morphology of the sample treated with HIP1 + H + A displays heterogeneity, with regions indicative of both brittle and ductile fractures, alongside the presence of micropores. The ductile fracture zones are distinguished by an extensive microrelief, featuring pits and ridges, indicative of significant plastic deformation. Conversely, the sample subjected to HIP3 + H + A presents a uniformly ductile intergranular fracture surface, with pronounced plastic deformation evidence. The microrelief in this case consists of equiaxed pits, ranging from 5 to 10 μm in size, and notably lacks any signs of brittle fracture.

Microstructure analysis reveals that the samples processed through SLM + HIP + HT exhibit a high degree of structural homogeneity (Fig. 7). The absence of the subgrain structure, typically observed in SLM samples, suggests that grain recrystallization has been completed during post-processing. This structural change enhances mechanical properties through dispersed hardening, resulting from the precipitation of excess Ni_3Ti phase (Fig. 7, *e*), consistent with findings from various studies [7; 17—25].

Conclusions

1. The application of hot isostatic pressing combined with hardening and aging markedly enhances the strength and ductility of SLM-fabricated PR-03N18K9M5TYu steel components. This post-processing approach not only facilitates a sixfold decrease in porosity but also promotes the recrystallization of subgrain structures and induces dispersion hardening.

2. Adjustments in HIP parameters result in a substantial increase in the offset yield strength and tensile strength, specifically between 25 to 46 % and 18 to 35 %, respectively. The combined treatment involving HIP3, followed by hardening and aging, is distinguished by its

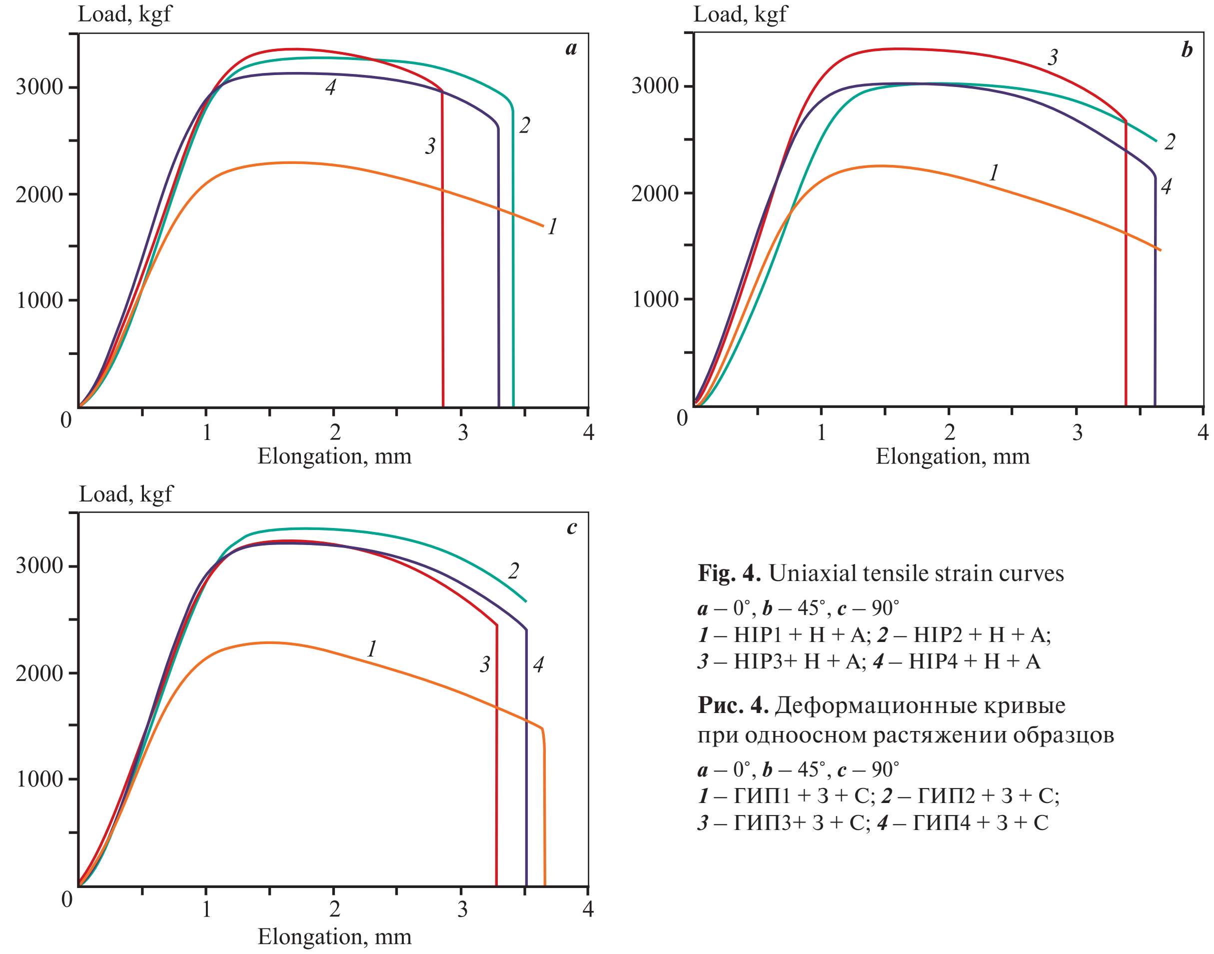

Fig. 4. Uniaxial tensile strain curves

a – 0°, ***b*** – 45°, ***c*** – 90°
1 – HIP1 + H + A; ***2*** – HIP2 + H + A;
3 – HIP3+ H + A; ***4*** – HIP4 + H + A

Рис. 4. Деформационные кривые
при одноосном растяжении образцов

a – 0°, ***b*** – 45°, ***c*** – 90°
1 – ГИП1 + З + С; ***2*** – ГИП2 + З + С;
3 – ГИП3+ З + С; ***4*** – ГИП4 + З + С

Hardness (*H*), modulus of elasticity (*E*), and indent depth (h_p)

Значения твердости (H), модуля упругости (E)
и глубины отпечатка (h_p)

Sample post-processing	*H*, GPa	*E*, GPa	h_p, nm
HIP1	5.1	209	340
HIP2	4.8	203	342
HIP3	4.6	195	357
HIP4	4.7	196	350
HIP1 + H + A	8.0	240	245
HIP3 + H + A	8.5	256	256

capacity to deliver the highest mechanical performance metric: σ_{ys} = 1603 MPa, σ_{ucs} = 1790 MPa, H = 8 GPa, E = 243 GPa. The fracture mode is primarily ductile with dimple rupture, occurring through mechanisms of shearing and detachment, thus leading to the formation of mixed-type fractures.

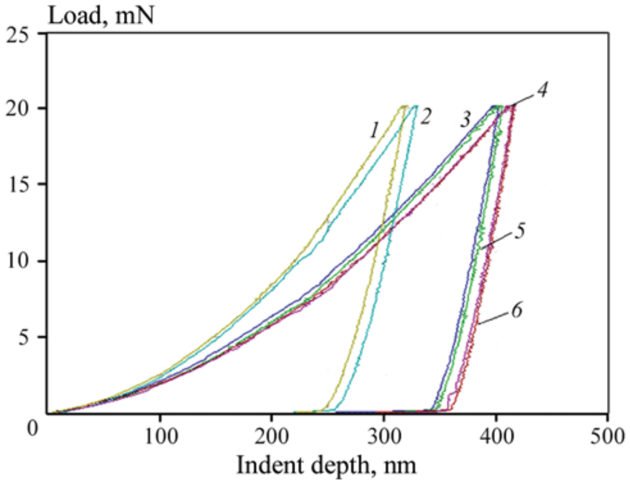

Fig. 5. Loading/unloading curves of samples subjected to various post-processing treatments

1 – HIP1 + H + A; ***2*** – HIP3 + H + A; ***3*** – HIP1; ***4*** – HIP4;
5 – HIP2; ***6*** – HIP3

Рис. 5. Кривые «нагружение – снятие нагрузки» для образцов в различных состояниях

1 – ГИП1 + З + С; ***2*** – ГИП3 + З + С; ***3*** – ГИП1; ***4*** – ГИП4;
5 – ГИП2; ***6*** – ГИП3

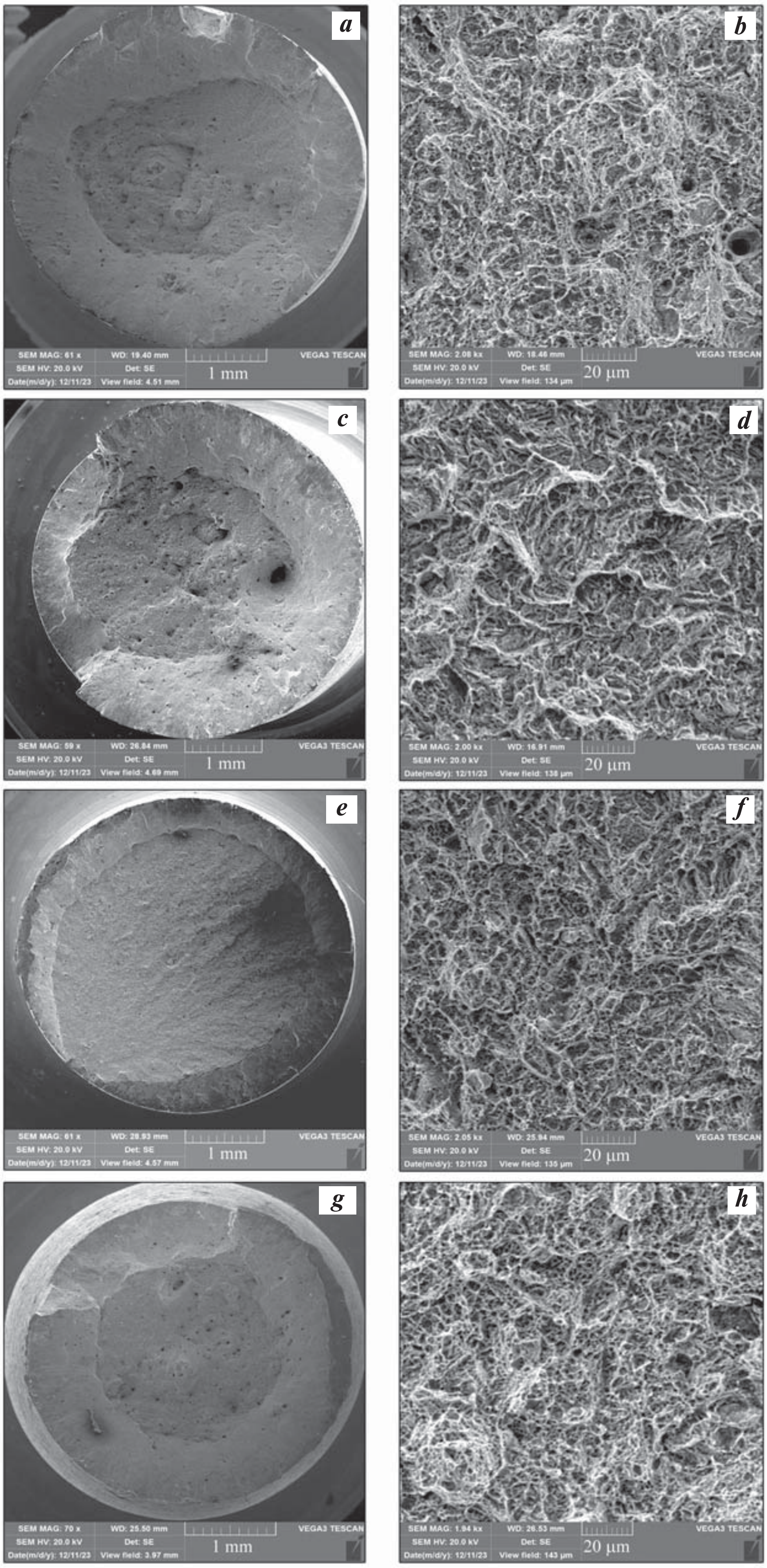

Fig. 6. Samples after HIP1 + H + A (***a***, ***b***), HIP2 + H + A (***c***, ***d***), HIP3 + H + A (***e***, ***f***), HIP4 + H + A (***g***, ***h***)
a, c, e, g – fracture images; ***b, d, f, h*** – fracture surface reliefs

Рис. 6. Образцы в состояниях ГИП1 + З + С (***a***, ***b***), ГИП2 + З + С (***c***, ***d***), ГИП3 + З + С (***e***, ***f***), ГИП4 + З + С (***g***, ***h***)
a, c, e, g – внешний вид излома образца; ***b, d, f, h*** – рельеф поверхности излома

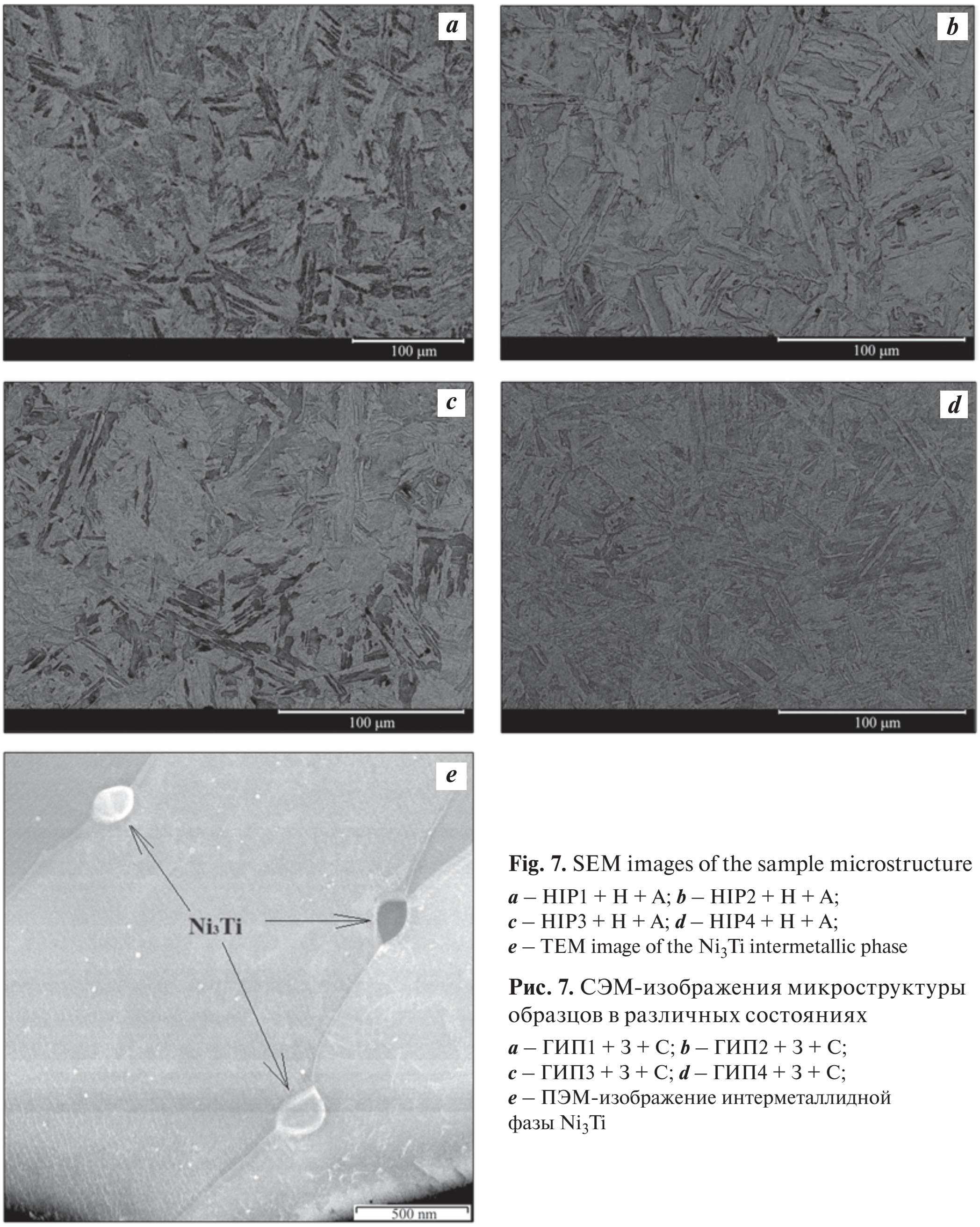

Fig. 7. SEM images of the sample microstructure

a – HIP1 + H + A; ***b*** – HIP2 + H + A;
c – HIP3 + H + A; ***d*** – HIP4 + H + A;
e – TEM image of the Ni_3Ti intermetallic phase

Рис. 7. СЭМ-изображения микроструктуры образцов в различных состояниях

a – ГИП1 + З + С; ***b*** – ГИП2 + З + С;
c – ГИП3 + З + С; ***d*** – ГИП4 + З + С;
e – ПЭМ-изображение интерметаллидной фазы Ni_3Ti

References

1. Ullah R., Akmal J.S. Anisotropy of additively manufactured 18Ni300 maraging steel: threads and surface characteristics. *Procedia CIRP*. 2020;93:68—78. https://doi.org/10.1016/j.procir.2020.04.059
2. Kucerova L., Zetkova I., Jenicek S., Burdova K. Hybrid parts produced by deposition of 18Ni300 maraging steel via selective laser melting on forged and heat treated advanced high strength steel. *Additive Manufacturing*. 2020;32:100—111. https://doi.org/10.1016/j.addma.2020.101108
3. Yuchao Bai, Cuiling Zhao, Jiayi Zhang, Hao Wang. Abnormal thermal expansion behaviour and phase transition of laser powder bed fusion maraging steel with different thermal histories during continuous heating. *Additive Manufacturing*. 2022;53:102712. https://doi.org/10.1016/j.jsis.2019.01.003
4. Dinghui Liu, Jie Su, Ao Wang, Zhuoyue Yang, Jiaoxi Yang, Zhen Wang, Yali Ding, Geng Liu. Tailoring the microstructure and mechanical properties of FeCrNiCoMo maraging stainless steel after laser melting deposition. *Materials Science and Engineering: A*. 2022;840:142931. https://doi.org/10.1016/j.jsis.2019.01.003

5. Vishwakarma J., Chattopadhyay K., Santhi Srinivas N.C. Effect of build orientation on microstructure and tensile behaviour of selectively laser melted M300 maraging steel. *Materials Science and Engineering: A*. 2020; 798:140130.
https://doi.org/10.1016/j.msea.2020.140130
6. Souza A.F., Al-Rubaie K.S., Marques S., Zluhan B., Santos E.C. Effect of laser speed, layer thickness, and part position on the mechanical properties of maraging 300 parts manufactured by selective laser melting. *Materials Science and Engineering: A*. 2019;767:138425.
https://doi.org/10.1016/j.msea.2019.138425
7. Kayasova A.O., Levashov E.A. Features of the impact of hot isostatic pressing and heat treatment on the structure and properties of maraging steel obtained by selective laser melting method. *Powder Metallurgy and Functional Coatings*. 2022;16(4):84—92. (In Russ.).
http://doi.org/10.17073/1997-308X-2022-4-84-92
Каясова А.О., Левашов Е.А. Особенности влияния горячего изостатического прессования и термообработки на структуру и свойства мартенситно-стареющей стали, полученной методом селективного лазерного сплавления. *Известия вузов. Порошковая металлургия и функциональные покрытия*. 2022;16(4):84—92.
http://doi.org/10.17073/1997-308X-2022-4-84-92
8. Kaplanscky Yu.Yu., Levashov E.A., Korotitskiy A.V., Loginov P.A., Sentyurina Zh.A., Mazalov A.B. Influence of aging and HIP treatment on the structure and properties of NiAl-based turbine blades manufactured by laser powder bed fusion. *Additive Manufacturing*. 2020;31:100999.
https://doi.org/10.1016/j.addma.2019.100999
9. Sentyurina Zh.A., Baskov F.A., Loginov P.A., Kaplanskii Yu.Yu. Mishukov A.V. Logachev I.A., Bychkova M.Ya., Levashov E.A. Logacheva A.I. The effect of hot isostatic pressing and heat treatment on the microstructure and properties of EP741NP nickel alloy manufactured by laser powder bed fusion. *Additive Manufacturing*. 2021.37:101629.
https://doi.org/10.1016/j.addma.2020.101629
10. Kaplanskii Yu.Yu., Sentyurina Zh.A., Loginov P.A., Levashov E.A., Korotitskiy A.V., Travyanov A.Ya., Petrovskii P.V. Microstructure and mechanical properties of the (Fe, Ni)Al-based alloy produced by SLM and HIP of spherical composite powder. *Materials Science and Engineering: A*. 2019;743:567—580.
https://doi.org/10.1016/j.msea.2018.11.104
11. Baskov F.A., Sentyurina Zh.A., Kaplanskii Yu.Yu., Logachev I.A., Semerich A.S., Levashov E.A. The influence of post heat treatments on the evolution of microstructure and mechanical properties of EP741NP nickel alloy produced by laser powder bed fusion. *Materials Science and Engineering: A*. 2021;817:141340.
https://doi.org/10.1016/j.msea.2021.141340
12. Conde F.F., Escobar J.D., Oliveira J.P., Jardini A.L., Bose Filho W.W., Avila J.A. Austenite reversion kinetics and stability during tempering of an additively manufactured maraging 300 steel. *Additive Manufacturing*. 2019;29:100804.
https://doi.org/10.1016/j.addma.2019.100804
13. Xu T.Z., Zhang S., Du Y., Wu C.L., Zhang C.H., Sun X.Y., Chen H.T., Chen J. Development and characterization of a novel maraging steel fabricated by laser additive manufacturing. *Materials Science and Engineering: A*. 2024;891:145975.
https://doi.org/10.1016/j.msea.2023.145975
14. Mouritz A.P. 11 — Steels for aircraft structures. In: *Introduction to aerospace material*. Woodhead Publishing, 2012. P. 232—250.
https://doi.org/https://doi.org/10.1533/9780857095152.232
15. Kürnsteiner P., Wilms M.B., Weisheit A., Barriobero-Vila P., Jägle E.A., Raabe D. Massive nanoprecipitation in an Fe—19Ni—*x*Al maraging steel triggered by the intrinsic heat treatment during laser metal deposition. *Acta Materialia*. 2017;129:52—60.
https://doi.org/10.1016/j.actamat.2017.02.069
16. Tan C., Zhou K., Ma W., Zhang P., Liu M., Kuang T. Microstructural evolution, nanoprecipitation behavior and mechanical properties of selective laser melted high-performance grade 300 maraging steel. *Materials & Design*. 2017;134:23—34.
https://doi.org/10.1016/j.matdes.2017.08.026
17. Karolczuk Aleksander, Kurek Andrzej, Böhm Michał, Derda Szymon, Prażmowski Mariusz, Kluger Krzysztof, Żak Krzysztof, Pejkowski Łukasz, Seyda Jan. Heterogeneous effect of aging temperature on the fatigue life of additively manufactured thin-walled 18Ni300 maraging steel tubular specimen. *Materials & Design*. 2024;237:112561.
https://doi.org/10.1016/j.matdes.2023.112561
18. Jonghyun Jeong, Gun Woo No, Hyo Ju Bae, Sang Kyu Yoo, In-Chul Choi, Hyoung Seop Kim, Jae Bok Seol, Jung Gi Kim. Mechanical properties of lamellar-structured 18Ni300 maraging steel manufactured via directed energy deposition. *Materials Science and Engineering: A*. 2024;892:146031.
https://doi.org/10.1016/j.msea.2023.146031
19. Sha W., Guo Z., Wilson E.A. Modeling the evolution of microstructure during the processing of maraging steels, *JOM*. 2004; 56:62—66.
https://doi.org/10.1007/s11837-004-0037-2
20. Moshka O., Pinkas M., Brosh E., Ezersky V., Meshi L. Addressing the issue of precipitates in maraging steels —

unambiguous answer. *Materials Science and Engineering: A*. 2015;638:232—239
https://doi.org/10.1016/j.msea.2015.04.067

21. Zhonghui Cheng, Shengzhi Sun, Xi Du, Qing Tang, Jinguang Shi, Xiaofeng Liu, Qiu Jianrong. Microstructural evolution of a FeCo15Cr14Ni4Mo3 maraging steel with high ductility prepared by selective laser melting. *Materials Today Communications*. 2022;31:103243.
https://doi.org/10.1016/j.mtcomm.2022.103243
22. Lulu Guo, Lina Zhang, Joel Andersson, Olanrewaju Ojo. Additive manufacturing of 18 % nickel maraging steels: Defect, structure and mechanical properties: A review. *Journal of Materials Science & Technology*. 2022;120:227—252.
https://doi.org/10.1016/j.jmst.2021.10.056
23. Yuchao Bai, Di Wang, Yongqiang Yang, Hao Wang. Effect of heat treatment on the microstructure and mechanical properties of maraging steel by selective laser melting. *Materials Science and Engineering: A*. 2019;760: 105—117.
https://doi.org/10.1016/j.msea.2019.05.115
24. Vishwakarma Jaydeep, Chattopadhyay K., Santhi Srinivas N.C. Effect of build orientation on microstructure and tensile behaviour of selectively laser melted M300 maraging steel. *Materials Science and Engineering: A*. 2020;798:140130.
https://doi.org/10.1016/j.msea.2020.140130
25. Habassi Faiçal, Houria Manel, Barka Noureddine, Jahazi Mohammad. Influence of post-treatment on microstructure and mechanical properties of additively manufactured C300 maraging steel. *Materials Characterization*. 2023;202:112980.
https://doi.org/10.1016/j.matchar.2023.112980

Information about the authors

Anastasiya O. Kayasova – Postgraduate Student, Department of Powder Metallurgy and Functional Coating (PM&FC), National University of Science and Technology “MISIS” (NUST MISIS).
https://orcid.org/0009-0009-2144-0332
E-mail: NKayasova@gmail.com

Fedor A. Baskov – Cand. Sci. (Eng.), Researcher, Laboratory “In situ diagnostics of structural transformations”, Scientific-Educational Center of SHS of MISIS–ISMAN, NUST MISIS.
https://orcid.org/0000-0001-6238-4378
E-mail: baskov_fa@mail.ru

Tamara A. Lobova – Dr. Sci. (Eng.), Prof. of the Department of PM&FC, NUST MISIS.
https://orcid.org/0009-0002-1749-0782
E-mail: smazka39@mail.ru

Evgeny A. Levashov – Dr. Sci. (Eng.), Prof., Acad. of the Russian Academy of Natural Science, Head of the Department of PM&FC of NUST MISIS, Head of the Scientific-Educational Center of SHS of MISIS–ISMAN.
https://orcid.org/0000-0002-0623-0013
E-mail: levashov@shs.misis.ru

Информация об авторах

Анастасия Олеговна Каясова – аспирант кафедры «Порошковая металлургия и функциональные покрытия» (ПМиФП) Национального исследовательского технологического университета «МИСИС» (НИТУ МИСИС).
https://orcid.org/0009-0009-2144-0332
E-mail: NKayasova@gmail.com

Федор Алексеевич Басков – к.т.н., науч. сотрудник лаборатории «In situ диагностика структурных превращений» Научно-учебного центра (НУЦ) СВС МИСиС–ИСМАН, НИТУ МИСИС.
https://orcid.org/0000-0001-6238-4378
E-mail: baskov_fa@mail.ru

Тамара Александровна Лобова – д.т.н., профессор кафедры ПМиФП, НИТУ МИСИС.
https://orcid.org/0009-0002-1749-0782
E-mail: smazka39@mail.ru

Евгений Александрович Левашов – д.т.н., проф., акад. РАЕН, заведующий кафедрой ПМиФП НИТУ МИСИС, директор НУЦ СВС МИСИС–ИСМАН.
https://orcid.org/0000-0002-0623-0013
E-mail: levashov@shs.misis.ru

Contribution of the authors

A.O. Kayasova – formulated the problem statement, created SLM samples and prepared the samples for additional analysis, performed heat treatment, and authored the manuscripte.

F.A. Baskov – provided guidance on the optimal conditions for HIP, performed the HIP process, and contributed to discussions.

T.A. Lobova – assisted with the SEM studies, analysis of the results, and participated in discussions.

E.A. Levashov – provided general supervision of the study and writing the paper, engaged in discussions.

Вклад авторов

А.О. Каясова – определение цели работы, изготовление СЛС-образцов, подготовка образцов для дальнейших исследований, проведение термической обработки, написание статьи.

Ф.А. Басков – консультирование при выборе параметров ГИП, проведение ГИП, участие в обсуждении результатов.

Т.А. Лобова – помощь при СЭМ-исследованиях, помощь с анализом полученных результатов, участие в обсуждении результатов.

Е.А. Левашов – общее руководство работой, помощь в написании статьи, участие в обсуждении результатов.

The article was submitted 1.01.2024, revised 13.02.2024, accepted for publication 19.02.2024

Статья поступила в редакцию 31.01.2024, доработана 13.02.2024, подписана в печать 19.02.2024

PHYSICAL METALLURGY AND HEAT TREATMENT / МЕТАЛЛОВЕДЕНИЕ И ТЕРМИЧЕСКАЯ ОБРАБОТКА

UDC 620.186; 620.172
https://doi.org/10.17073/0021-3438-2024-1-81-92

Research article
Научная статья

Impact of ECAP at 300 °C on the microstructure and mechanical properties of the quenched Zr–2.5%Nb alloy

D.V. Gunderov[1,2], **A.G. Stotskiy**[1], **S.D. Gunderova**[1,2], **V.R. Aubakirova**[1], **A.Yu. Demin**[1]

[1] **Ufa University of Science and Technology**
32 Zaki Validi Str., Ufa, Republic of Bashkortostan 450076, Russia

[2] **Institute of Molecule and Crystal Physics of the Ufa Federal Research Centre of the RAS**
71 Oktyabrya Prosp., Ufa, Republic of Bashkortostan 450054, Russia

✉ Andrey G. Stotskiy (stockii_andrei@mail.ru)

Abstract: We investigated the microstructure of the Zr–2.5%Nb zirconium alloy after subjecting it to equal-channel angular pressing (ECAP) and found that ECAP at 300 °C increases the strength by 1.4–1.8 times. Notably, unlike other studies, our alloy did not show complete dissolution of niobium particles, which may be due to the reduced diffusion rates at the lower deformation temperature of 300 °C. Pre-treatment involving quenching before severe plastic deformation was also studied, which developed a lamellar structure introducing additional boundaries that facilitated grain refinement during subsequent ECAP. The strength of the alloy was further enhanced by solid-solution hardening, achieved through the complete dissolution of the Nb particles into the matrix post-quenching. This process resulted in a 2.3-fold increase in yield strength after quenching plus ECAP compared to the initial coarse-grained state.

Keywords: microstructure, quenching, equal channel angular pressing, strength, Nb particles, Zr–2.5%Nb zirconium alloy.

Acknowledgments: This work was carried out with financial support from the Russian Science Foundation under Project № 20-79-10189-П, https://rscf.ru/en/project/23-79-50039/
Mechanical tests and microstructure study were carried out in the Center for collective use «Nanotech» of Ufa University of Science and Technology.

For citation: Gunderov D.V., Stotskiy A.G., Gunderova S.D., Aubakirova V.R., Demin A.Yu. Impact of ECAP at 300 °C on the microstructure and mechanical properties of the quenched Zr-2.5%Nb alloy. *Izvestiya. Non-Ferrous Metallurgy.* 2024;30(1):81–92.
https://doi.org/10.17073/0021-3438-2024-1-81-92

Влияние РКУП при температуре 300 °С на структуру и свойства закаленного сплава Zr–2,5%Nb

Д.В. Гундеров[1,2], **А.Г. Стоцкий**[1], **С.Д. Гундерова**[1,2], **В.Р. Аубакирова**[1], **А.Ю. Демин**[1]

[1] **Уфимский университет науки и технологий**
Россия, 450076, Респ. Башкортостан, г. Уфа, ул. Заки Валиди, 32

[2] **Институт физики молекул и кристаллов Уфимского федерального исследовательского центра РАН**
Россия, 450054, Респ. Башкортостан, г. Уфа, пр-т Октября, 71

✉ Андрей Геннадиевич Стоцкий (stockii_andrei@mail.ru)

Аннотация: Исследована эволюция структуры циркониевого сплава Zr–2,5%Nb при деформации методом равноканального углового прессования (РКУП). Показано, что РКУП при температуре 300 °С приводит к повышению прочностных характеристик в 1,4–1,8 раза. Вместе с тем отмечено, что, по сравнению с другими исследованиями, в данном сплаве не происходит полного растворения частиц ниобия, что может быть вызвано замедлением процессов диффузии с понижением температуры деформации до 300 °С. Проведено исследование по предварительной подготовке структуры перед интенсивной пластической деформацией в виде закалки, что позволило сформировать пластинчатую структуру с дополнительными границами. Это способствует измельчению зерна при последующей деформации РКУП. Дополнительно повысить прочность сплава позволяет твердорастворное упрочнение – полное растворение частиц Nb в матрице сплава после закалки. Результатом является повышение в 2,3 раза предела текучести сплава после закалки и РКУП по сравнению с крупнозернистым состоянием.

Ключевые слова: микроструктура, закалка, равноканальное угловое прессование, прочностные характеристики, частицы Nb, циркониевый сплав Zr–2,5%Nb.

Благодарности: Исследование выполнено за счет гранта Российского научного фонда № 20-79-10189-П, https://rscf.ru/project/23-79-50039/

Механические испытания и исследования микроструктуры проводились в ЦКП «Нанотех» Уфимского университета науки и технологий.

Для цитирования: Гундеров Д.В., Стоцкий А.Г., Гундерова С.Д., Аубакирова В.Р., Демин А.Ю. Влияние РКУП при температуре 300 °С на структуру и свойства закаленного сплава Zr–2,5%Nb. *Известия вузов. Цветная металлургия.* 2024;30(1):81–92.
https://doi.org/10.17073/0021-3438-2024-1-81-92

Introduction

Zirconium and its alloys are widely used in such critical applications as nuclear power and medicine. Like titanium, this metal is highly bioinert to the human body [1—4]. Additionally, it is important to note the lower modulus of elasticity of zirconium compared to titanium. This characteristic is crucial for osteoimplants that integrate with human bone, influencing implant acceptance and preventing bone tissue necrosis. Such necrosis may be caused by excessive stress concentration resulting from a significant mismatch between the elastic moduli of the artificial implant and the bone tissue [5; 6]. Stronger materials enable the creation of implants with smaller cross-sections, leading to less traumatic surgery. Therefore, a Zr-based bioinert material that possesses a low modulus of elasticity but higher strength than Zr alloys after conventional treatments is desirable.

Well-known severe plastic deformation (SPD) enhances mechanical properties by grain refining to a nanostructured state [7]. SPD increases strength without altering the chemical composition, thereby preserving biocompatibility, unlike alloying [8; 9]. SPD processes such as equal channel angular pressing (ECAP), multi-axial forging, and rotary swaging enable the production of bulk workpieces/semi-finished products for further processing.

The Zr—2.5%Nb alloy is a renowned zirconium alloy utilized in nuclear power facilities and medical implants. The components of the alloy, zirconium and niobium, are biocompatible. There have been studies [10—13] focused on enhancing the strength of the Zr—2.5%Nb alloy through ECAP.

Typically, the initial coarse-grained structure of the Zr—2.5%Nb alloy consists of a zirconium α-phase and fine niobium particles, present both at the grain boundaries and within the Zr grains. The Zr—2.5%Nb alloy was investigated before and after undergoing ECAP [13]. The initial alloy was obtained through cold rolling followed by annealing at 530 °C for 1 h. It exhibited a two-phase structure: α-phase Zr and some high-temperature β-phase Zr, with Nb dissolved in it. The initial microstructure featured a partially polygonized structure with 100—300 nm grains, a partially recrystallized structure with 1—5 μm grains, and some β-Nb particles sized 5—15 nm.

The ECAP was carried out in four passes at 430 °C [13]. After ECAP, the Zr—2.5%Nb alloy transitioned to a single-phase structure of niobium solid solution in α-zirconium, with the initial β-phase of zirconium transforming into the α-phase. Studies [10, 13] indicated that, after ECAP deformation at 400 °C, the niobium particles dissolved while the grains refined, leading to a single-phase, ultrafine structure. ECAP effectively refines grains to ultrafine sizes, forming a subgrain/grain structure. After ECAP at 430 °C, equiaxed grains (subgrains) sized between 50 and 200 nm were observed. Initially, the alloy displayed a yield strength of about 380 MPa, a tensile strength of 570 MPa, and a relative elongation at break (δ) of 26 %. Following ECAP (n = 4, t = 430 °C), yield strength increased by 1.6 times to 620 MPa, and tensile strength to 770 MPa, although δ decreased to 9 %.

Another study [11] performed a more complex ECAP process with temperature reduction between passes. The Zr—2.5%Nb alloy underwent recrystallization annealing at 580 °C for 6 hours before ECAP, leading to a grain size of 1—2 μm. Subsequently, the metal was processed through isothermal ECAP with a stepwise temperature reduction. Two ECAP modes were applied: 1) two passes at 425 °C followed by two passes at 400 °C and then two passes at 350 °C; 2) two passes each at 450 °C, 425 °C, and 400 °C respectively. The average grain/subgrain size after ECAP Mode *1* was 185 nm. Increasing the final ECAP temperature from 350 to 400 °C (Mode *2*) resulted in a predominantly equiaxed structure, with the average grain size growing to 250 nm [11]. XRD analysis revealed α-Zr as the primary phase in the initial alloy with minor amounts of β-Nb and β-Zr. After ECAP Modes *1* and *2*, the samples contained only the α-Zr phase, likely due to phase decomposition and particle dissolution in the matrix. The grain refinement and increased dislocation density after ECAP led to a 420 % increase in microstrain. The Zr—2.5%Nb alloy remained a single-phase (α-Zr) material when heated to temperatures between 23 and 490 °C. The second β-Nb phase only formed after annealing at 570 °C [11].

The tensile strength and yield strength of the initial alloy were 420 and 230 MPa, respectively [9], significantly lower than the σ_{ucs} = 570 MPa and σ_{ys} = = 380 MPa of the initial Zr—2.5%Nb alloy as reported in [10; 13]. Mode *1* ECAP with a final temperature of 350 °C, significantly increased tensile strength and yield strength to 820 and 700 MPa, respectively, with δ = 10 % (compared to δ = 27 % for the initial alloy). Mode *2* ECAP, at a final temperature of 400 °C, resulted in tensile strength and yield strength of σ_{ucs} = = 650 MPa and σ_{ys} = 470 MPa, respectively, with δ = 14 % [11]. The analysis of structure thermostability and mechanical properties showed no changes below 350 °C. Annealing the ultrafine-grained Zr—2.5%Nb at 450 °C led to a 15 % decrease in strength due to grain growth, while δ increased to 15—16 %.

Our literature review indicates that ECAP with temperature reduction remains insufficiently explored. Investigating this process for its potential in enhancing strength, refining grains, and achieving structural fragmentation to ultrafine and/or nanoscale levels presents an interesting and significant opportunity. Additionally, it is worth considering quenching as another method to improve microstructure in low-alloy metals by dissolving secondary phases into the base metal.

Additionally, research [14] on high-pressure torsion (HPT) in the Zr—2.5%Nb alloy found a significant increase in microhardness (almost double) compared to the material in its coarse-grained state. This suggests that the Zr—2.5%Nb alloy has the capacity for further grain refinement and enhancement of mechanical properties through ECAP conducted at lower temperatures than those in other studies. Previous research also indicated that quenching the Zr—2.5%Nb zirconium alloy at 890 °C from the β-phase significantly improves its mechanical properties. The aim of this study is to examine the microstructure and mechanical properties of the Zr—2.5%Nb zirconium alloy subjected to ECAP at 300 °C, considering both its coarse-grained state and post-quenching.

1. Materials and methods

We studied the low-alloyed E125 (Zr—2.5%Nb) zirconium alloy. It is a well-known Russian-made biocompatible metal. Its chemical composition is as follow, wt.%: Zr as the base metal; Nb: 2.46; O: 0.032; Fe: 0.001; C: 0.002; and N: 0.0016.

The initial material was the Zr—2.5%Nb alloy after recrystallization annealing at 600 °C for 3 h (hereinafter referred to as the CG state), and after quenching from the β-phase at 890 °C. We used ECAP tooling with 15 mm diameter channels spaced at 120°. The CG state Zr—2.5%Nb alloy underwent ECAP at 300 °C with 1, 4, and 8 passes. The quenched Zr—2.5%Nb alloy, which initially exhibited higher strength and lower plasticity, was subjected to ECAP at 300 °C with fewer passes: $n = 2$ and 4.

X-ray diffraction (XRD) analysis was performed using an “Ultima IV” diffractometer (Rigaku, Japan) with CuK_α radiation (40 kV, 30 mA).

The metal structure was examined using a JEM 2100 transmission electron microscope (TEM) (Jeol, Japan). The foil samples for transmission electron microscopy (TEM) were 3 mm diameter disks cut from a plate pre-thinned to 100 μm. The disk was electropolished on a “Tenupol-5” machine (Struers, Denmark) using an electrolyte composed of 15 % perchloric acid and 85 % glacial acetic acid. The electropolishing voltage ranged from 22 to 25 V, with a temperature of 15—20 °C. Semi-automatic electropolishing was used until a through-hole appeared.

Flat samples for mechanical tests, measuring 1.1×0,5×4 mm, were cut from Zr—2.5%Nb billets prepared in various ECAP modes. The mechanical properties were determined by tensile tests at room temperature with a strain rate of $1{\cdot}10^{-3}$ s^{-1}, performed on an INSTRON 5982 universal testing machine (Instron, USA).

2. Results and discussion

2.1. Microstructure

The Zr—2.5Nb zirconium alloy after recrystallization displays a coarse-grained structure with Zr grain sizes of a few micrometers and some niobium particles. These particles are found both at the Zr grain boundaries and inside the grains, with the average size of the Nb particles being 52 ± 2 nm (Fig. 1, *a*).

After ECAP with 1, 4, and 8 passes, significant changes in the microstructure are observed, as showed in the Fig. 1, *b*—*d*. A single ECAP pass begins the process of structural refinement and dislocation accumulation, but results in a very heterogeneous structure. The TEM figures reveal areas of refinement (evidenced by small angles between reflexes and identical reciprocal lattices), fragments up to 1 μm with no visible substructure, and individual grains that are weakly deformed (Fig. 1, *b*). The diffraction images of the subgrain structure also show a misorientation of no more than 10° (Fig. 1, *b*). With four passes ($n = 4$), the structure becomes finer and more homogeneous, including fragmented areas that contain subgrains/grains with an average size of approximately 280 nm (Fig. 2). The presence of niobium particles, indicated with arrows in the figures, and their diffractions showing the reciprocal lattice of niobium are also noted (Fig. 1, *c*). As the number of ECAP passes increases to eight, the microstructure exhibits grains oriented at larger angles and niobium particles. The average size of the grains/subgrains is approximately 260 nm. The evolution of the average grain and subgrain sizes is showed in Fig. 2. The ECAP process also affects the Nb particles, with the smallest particles, a few tens of nanometer in size, dissolving. The particle size decreases only slightly as the number of ECAP passes increases from four to eight (Fig. 2).

The microstructure of the Zr—2.5Nb alloy after quenching exhibits α-Zr oriented lamellae of varying widths, a consequence of the β → α phase transformation during martensitic quenching, which leads to the formation of α-Zr martensitic lamellae. It is re-

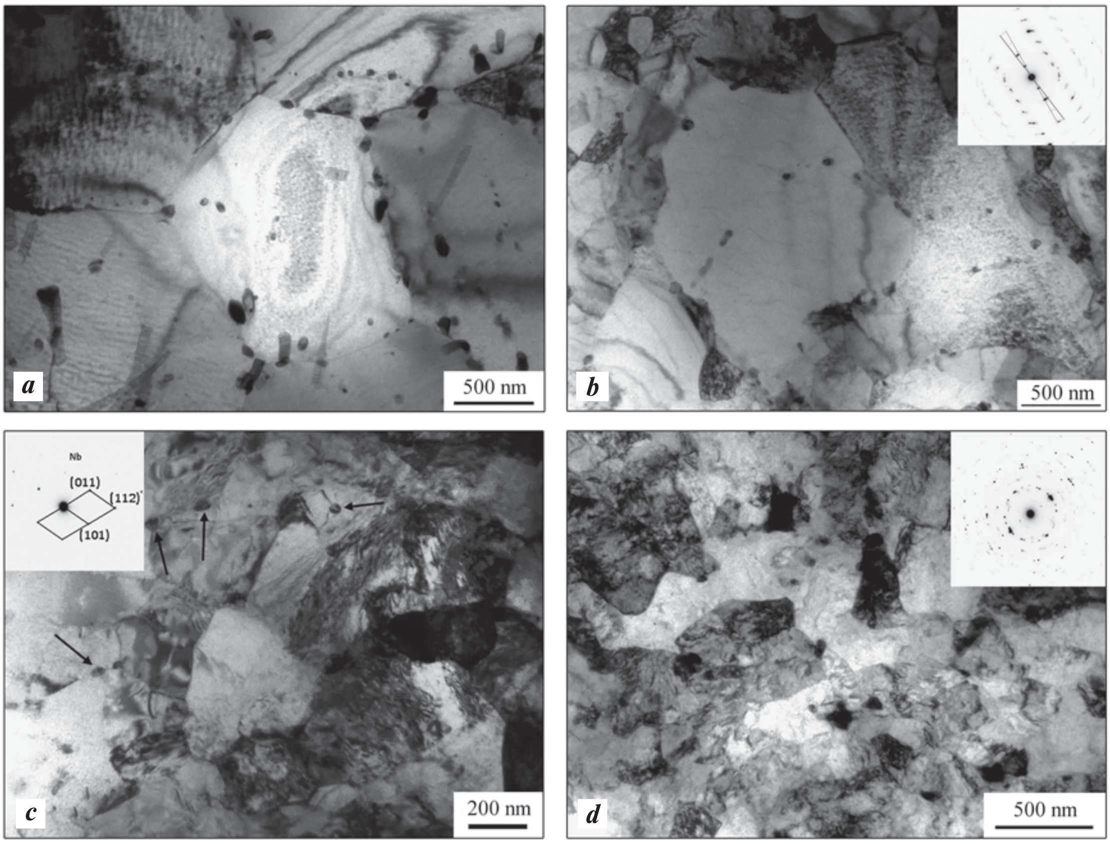

Fig. 1. Microstructure of the Zr–2.5Nb alloy in the CG state (***a***) and after ECAP (***b***–***d***)
Number of passes: ***b*** – 1, ***c*** – 4, ***d*** – 8

Рис. 1. Микроструктура сплава Zr–2,5Nb в КЗ-состоянии (***a***) и после РКУП (***b***–***d***)
Число проходов: ***b*** – 1, ***c*** – 4, ***d*** – 8

cognized that at high cooling rates (such as in water), a duplex structure develops in the Zr—2.5Nb alloy, comprising lamellar α-grains formed after the β → α phase transformation within the original β-grains [15]. After quenching, the Nb particles are completely dissolved, and the niobium atoms forms a solid solution (Fig. 3, *a*, *b*). Following ECAP with 2 and 4 passes, the lamellae are refined, resulting in the formation of equiaxed grains. With four passes ($n = 4$), lamellae fragmentation becomes more significant compared to two passes ($n = 2$), leading to a structure consisited of ultrafine grains averaging approximately 190 nm in size (Fig. 3, *d*).

XRD analysis reveals that the initial structure of the alloy is predominately the Zr α-phase. While Nikulin S. et al. [11] and Kishore R. et al. [16] suggested the possible presence of the β-Zr phase, the lack of characteristic peaks for the β-phase or their superposition on the Zr α-phase peaks precludes definitive identification of this phase. The XRD analysis also detects a minor amount of the β-Nb phase within the α-Zr matrix, but the (011) peak corresponding to β-Nb is very weak, making it challenging to accurately estimate the volume fraction of this phase from the XRD data (Fig. 4), with its content evidently under 5 %.

XRD results confirm that the primary phase after quenching is α-Zr, as it remains after ECAP in any mode. The potential peaks of the β-Nb and β-Zr phases are either too weak to be discerned or indicate that the alloy is in a single phase. Table 1 details the XRD findings, including *a* and *c*, which are the interplanar distances for the (101) peak of the α-phase, Δ*c* representing the difference in the "*c*" lattice parameters of the α-phase for the initial alloy and the alloy after treatment, coherent scattering regions (CSR), and micro-distortion.

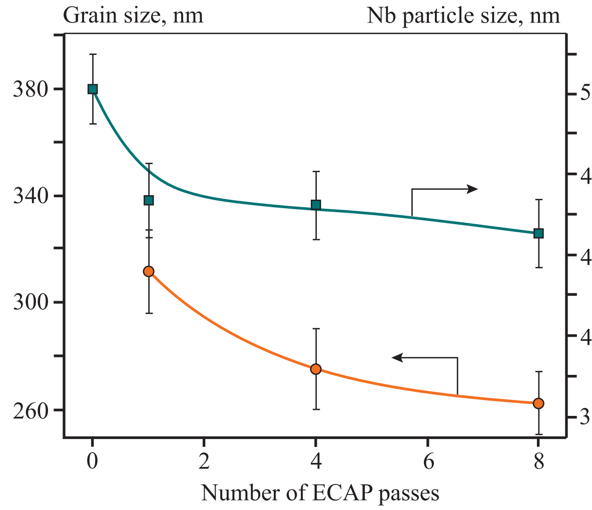

Fig. 2. Variations in the average grain/subgrain and Nb particle size in the Zr–2.5Nb alloy after ECAP

Рис. 2. Изменение среднего размера зерен/субзерен и частиц Nb в сплаве Zr–2,5Nb при деформации методом РКУП

We found that after ECAP with 4 and 8 passes, the lattice parameter c of the Zr—2.5Nb alloy decreases in comparison to the initial alloy. This reduction can be explained by the dissolution of Nb nanoparticles during ECAP, which is also confirmed by TEM. The dissolution of Nb, which has a smaller atomic radius, into the Zr lattice leads to a reduction in the lattice

Tabl. 1. **XRD of the Zr–2.5Nb alloy**

Таблица 1. Результаты РСА сплава Zr–2,5Nb

XRD parameters State	*a*, Å	*c*, Å	Δ*c*, Å	CSR, nm	Microdistortions ε, %
CG (after annealing at 600 °C)	3.2352	5.1605	–	640	0.0007
Quenching ($t = 890$ °C)	3.2231	5.1358	0.0247	780	0.0018
CG + ECAP ($t = 300$ °C, $n = 4$)	3.2318	5.1500	0.0105	527	0.0019
CG + ECAP ($t = 300$ °C, $n = 8$)	3.2302	5.1497	0.0108	475	0.0017
Quenching + ECAP ($t = 300$ °C, $n = 2$)	3.2274	5.1436	0.0168	398	0.0023
Quenching + ECAP ($t = 300$ °C, $n = 4$)	3.2331	5.1526	0.0079	313	0.0026

parameters. After quenching, the "*c*" lattice parameter of the α-phase decreases most significantly due to the complete dissolution of Nb into the Zr lattice. Following quenching and ECAP ($n = 2$, $n = 4$), the parameter "*c*" increases relative to the quenched-only state, approaching the value for the initial alloy. This could be due to the decomposition of the solid solution and possible precipitation of Nb nanoparticles, which may

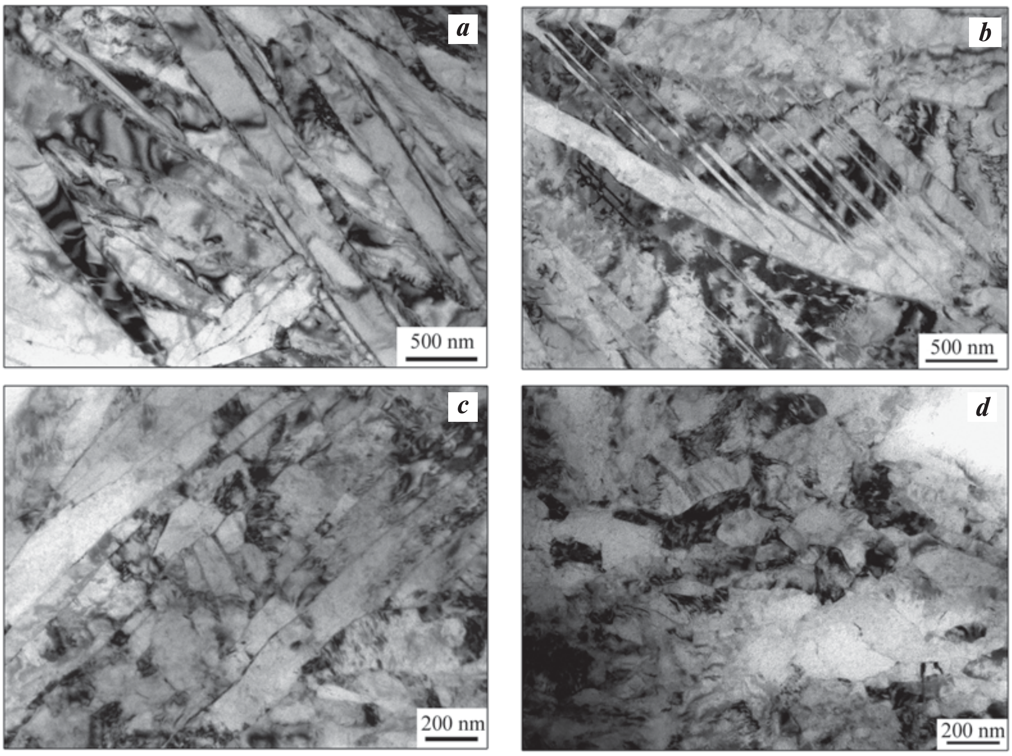

Рис. 3. Микроструктура сплава Zr–2,5Nb после закалки (***a***, ***b***) и после дополнительной РКУП-деформации в 2 прохода (***c***) и 4 прохода (***d***)

Fig. 3. Microstructure of the Zr–2.5Nb alloy after quenching (***a***, ***b***) and following further ECAP in 2 passes (***c***) and 4 passes (***d***)

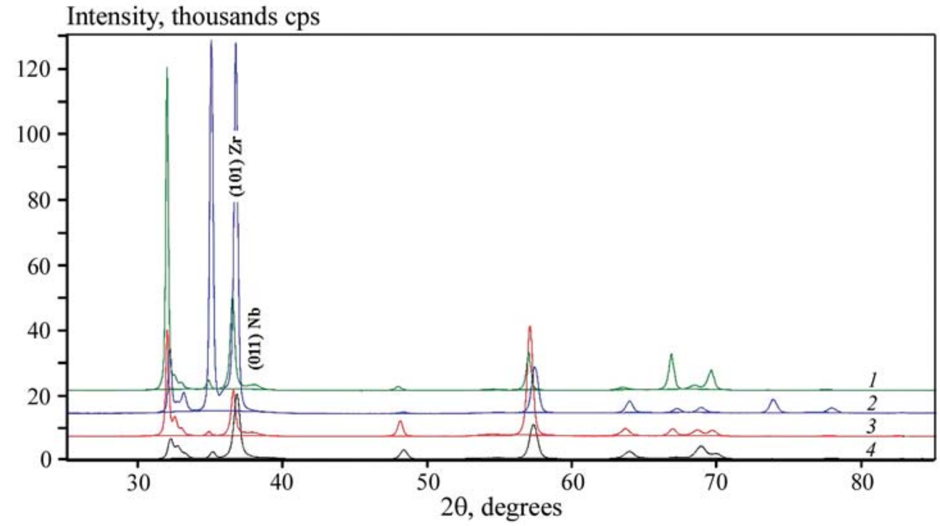

Fig. 4. XRD patterns of the Zr–2.5Nb alloy in various treated states

1 – CG; ***2*** – quenching; ***3*** – CG + ECAP ($n = 4$); ***4*** – quenching + ECAP ($n = 4$)

Рис. 4. Дифрактограммы сплава Zr–2,5Nb в различных состояниях

1 – КЗ; ***2*** – закалка; ***3*** – КЗ + РКУП ($n = 4$); ***4*** – закалка + РКУП ($n = 4$)

be undetectable by TEM because of their small size. As proposed by Straumal B. et al. [17], severe plastic deformation may form a metastable "solid solution—nanoparticles" state with the concentration of the solid solution and the quantity of intermetallic phase dissipation particles being dependent on the equilibrium between the metastable dissolution and phase dissipation processes for the specified SPD, rather than on the initial structure of the alloy [17—19].

With ECAP at $n = 4$ and 8 passes, there is an increase in micro-distortions as a result of grain refinement. However, an increase in the number of ECAP passes from 4 to 8 does not lead to further growth in micro-distortions. Four passes seem sufficient to reach an equilibrium between dislocation formation and relaxation processes under the given SPD conditions [19—21]. Additional passes do not generate extra dislocations; instead, the new dislocations created by further deformation are redistributed to the grain boundaries, causing increased grain misalignment, as indicated by TEM.

After quenching, micro-distortions increase compared to the initial annealed state, likely due to the higher quenching stresses and the formation of a fine lamellar structure. ECAP following quenching leads to further growth in micro-distortions, more so than in the quenched and ECAP-plus-annealing alloys, which is attributed to the grain refinement and higher dislocation density achieved by ECAP. The ECAP of the quenched alloy results in a higher dislocation density and the formation of a more refined structure.

For the commercial alloy, after hot rolling and annealing, the ratio of the XRD peaks corresponding to the Zr α-phase significantly deviates from the nominal value, attributed to the pronounced texturing of the commercial bar. After quenching, the peak ratio for the Zr α-phase shifts, indicating that rapid cooling in water tends to weaken the texture in Zr alloys [22]. It appears that ECAP on the quenched alloy further diminishes and blurs the texture. After quenching + + ECAP ($n = 2$) and quenching + ECAP ($n = 4$), the (101) peak of the α-phase emerges as the most intense, aligning with the expected behavior for a texture-free α-phase of Zr.

2.2. Tensile tests

Fig. 5, *a* presents the engineering stress vs. strain curves for the initial alloy and the alloys subjected to ECAP. For comparison, Fig. 5, *b* displays these curves after quenching and subsequent ECAP. Table 2 lists the results of the tensile tests.

Deforming the initial Zr—2.5Nb alloy results in significant hardening. ECAP in 4 and 8 passes increases the strength by 140 to 180 %. After ECAP ($n =$ $= 4$, $n = 8$), the ultimate strength rises from 500 to 720 MPa. However, the ductility and uniform elongation decrease from 21.4 to 8.6 % and from 12.0 to 1.3 %, respectively, which is typical for metals after SPD. It is noteworthy that there is no significant increase in strength when the number of ECAP passes increases from 4 to 8. ECAP with $n = 4$ at 300 °C leads to substantial refinement of the structure. Further deformation achieves an equilibrium between refinement and relaxation in the nanostructure [8; 20; 21], hence no further notable refinement of the structure or increase in strength is observed. This is also supported by the micro-distortions detected by XRD. Post-ECAP, the tensile strength and yield strength in the cross section are slightly higher than in the longitudinal direction, a phenomenon also observed in other metals and alloys [9], attributable to the formation of an ECAP-specific texture [9].

Quenching the Zr—2.5Nb alloy significantly increases its strength due to the formation of a lamellar structure, the complete dissolution of Nb particles, and consequently, solid-solution hardening. After quenching at 890 °C, the alloy exhibits improved strength (comparable to that after the initial state + ECAP in 8 passes): 635 MPa yield strength and 718 MPa tensile strength. Plasticity post-quenching drops to 19 %, and the uniform elongation decreases from 12.0 to 3.6 %, typical for hardening through quenching and the formation of a fine lamellar structure. Applying ECAP with $n = 4$ to the quenched alloy increases the yield strength and tensile strength by 120% to $\sigma_{ys} = 772 \pm 11$ MPa and $\sigma_{ucs} = 864 \pm 8$ MPa (longitudinal), with plasticity decreasing from 18.8 to 11.7 %, and uniform elongation to 1.7 %. The strength of 864 ± 8 MPa is slightly higher than that reported [11] after a complex ECAP treatment involving 6 passes with temperature reduction to 350 °C. For ECAP of the quenched alloy, the tensile strength and yield strength in the cross section are slightly higher than in the longitudinal section. So tensile strength and yield strength in the cross section after ECAP of the quenched alloy with $n = 4$ reaching 935 and 846 MPa, respectively. These are the highest values for the current study and for ECAP of the Zr—2.5Nb alloy reported in the literature.

3. Discussion

The structure of the Zr—2.5Nb zirconium alloy in its coarse-grained state consists of equiaxed Zr grains

Tabl. 2. **Results of tensile tests for the Zr–2.5Nb alloy**

Таблица 2. Результаты механических испытаний сплава Zr–2,5Nb

State	Engineering yield stress σ_{ys}, MPa	Tensile strength σ_{ucs}, MPa	Percent elongation to fracture δ, %	Relative uniform elongation δ_{uni},%
CG	335 ± 9	500 ± 8	21.4 ± 0.5	12.0 ± 0.8
CG + ECAP (*n* = 4), longitudinal section	601 ± 18	720 ± 6	11.6 ± 1.5	2.1 ± 0.2
CG + ECAP (*n* = 4), cross section	638 ± 14	732 ± 8	8.8 ± 0.3	1.3 ± 0.1
CG + ECAP (*n* = 8), longitudinal section	622 ± 12	724 ± 9	10.4 ± 0.8	1.5 ± 0.5
CG + ECAP (*n* = 8), cross section	658 ± 12	786 ± 5	8.6 ± 0.7	1.4 ±0.2
Quenching (*t* = 890 °C, τ = 30 min)	635 ± 20	718 ± 10	18.8 ± 0.5	3.6 ± 0.5
Quenching + ECAP (*n* = 2), longitudinal section	750 ± 5	817 ± 16	12.8 ± 0.7	1.5 ± 0.2
Quenching + ECAP (*n* = 2), cross section	784 ± 20	849 ± 11	10.2 ± 0.6	1.1 ± 0.1
Quenching + ECAP (*n* = 4), longitudinal section	772 ± 11	864 ± 8	11.7 ± 0.5	1.7 ± 0.2
Quenching + ECAP (*n* = 4), cross section	846 ± 20	935 ± 15	9.0 ± 0.6	1.2 ± 0.1

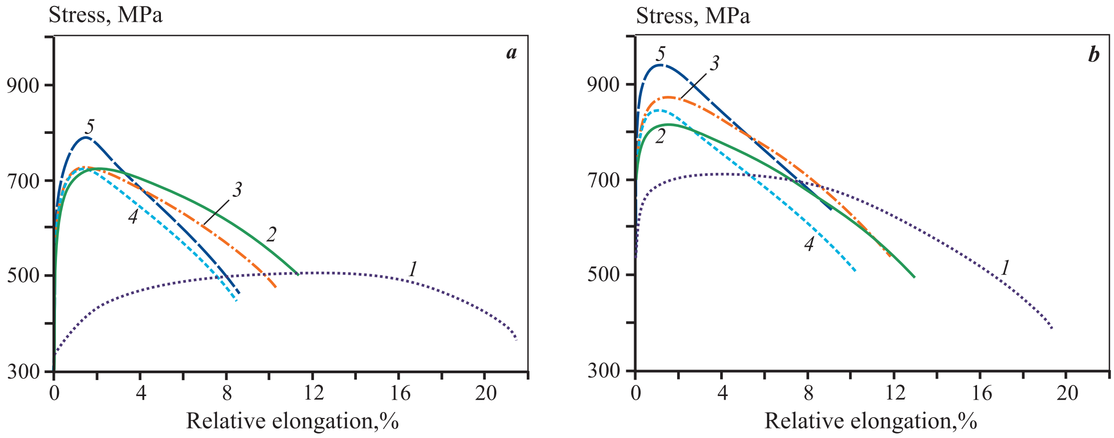

Fig. 5. Mechanical properties of the Zr–2.5Nb alloy in its CG state and after ECAP (***a***), as well as after quenching + ECAP (***b***)

a: ***1*** – CG; ***2*** – CG + ECAP (*n* = 4), longitudinal section; ***3*** – CG + ECAP (*n* = 8), longitudinal section;
4 – CG + ECAP (*n* = 4), cross section; ***5*** – CG + ECAP (*n* = 8), cross section
b: ***1*** – quenching; ***2*** – quenching + ECAP (*n* = 2), longitudinal section; ***3*** – quenching + ECAP (*n* = 4), longitudinal section;
4 – quenching + ECAP (*n* = 2), cross section; ***5*** – quenching + ECAP (*n* = 4), cross section

Рис. 5. Механические свойства сплава Zr–2,5Nb в КЗ-состоянии и после РКУП (***a***), а также после закалки и РКУП (***b***)

a: ***1*** – КЗ; ***2*** – КЗ + РКУП (*n* = 4), продольное сечение; ***3*** – КЗ + РКУП (*n* = 8), продольное сечение;
4 – КЗ + РКУП (*n* = 4), поперечное сечение; ***5*** – КЗ + РКУП (*n* = 8), поперечное сечение
b: ***1*** – закалка; ***2*** – закалка + РКУП (*n* = 2), продольное сечение; ***3*** – закалка + РКУП (*n* = 4), продольное сечение;
4 – закалка + РКУП (*n* = 2), поперечное сечение; ***5*** – закалка + РКУП (*n* = 4), поперечное сечение

several micrometers in size and Nb particles, which are often distributed non-uniformly within the grain body and at the grain boundaries. ECAP at 300 °C leads to grain refinement, reducing the grain size to approximately 260 nm. The Nb particles are also refined and partially dissolved due to strain-induced "dissolution" during SPD. Previous studies of ECAP at 400 °C reported complete dissolution of the Nb particles after SPD. It may be attributed to the higher temperature of deformation. ECAP at 300 °C results in incomplete dissolution (as seen in Fig. 1). Potential mechanisms for the dissolution of Nb particles include the active sliding of dislocations through the particles, the formation of vacancies under deformation, and more intense diffusion at an elevated temperature, which all contribute to the transition of Nb atoms into the zirconium lattice, resulting in the partial dissolution of the Nb particles [9].

Reducing the ECAP temperature to 300 °C, compared to 400 °C as studied in [10; 13]), improves structural refinement, and the remaining particles may harden the matrix via the Orowan mechanism. At 300 °C, the yield strength surpasses the values achieved in the above-mentioned studies [10; 13].

Pre-queching of the Zr—2.5Nb alloy dissolves the Nb particles in into the matrix, forms a thin-lamellar structure, and significantly increases strength. Subsequent ECAP of the quenched alloy causes fragmentation of the lamellae and results in the formation of an ultrafine structure with nearly equiaxed grains of ~190 nm in average size. ECAP on the quenched alloy contributes to greater strength growth. Quenching and subsequent ECAP with $n = 4$ results in the highest strength, surpassing that of the initial alloy after ECAP with eight passes.

It is recognized that ECAP deformation for most metals and alloys refines the structure to a grain size of 200 to 300 nm. Typically, to further enhance strength, materials undergo additional ECAP with temperature reduction or other deformation processes, such as drawing, although these approaches can make challenges due to the low ductility of SPD-hardened materials. Nonetheless, specific heat treatments, like quenching or aging, can prepare the initial structure for ECAP by forming additional boundaries that aid grain refinement during ECAP. For the Zr—2.5Nb zirconium alloy, quenching leads to solid-solution hardening due to the dissolution of Nb atoms into the matrix and the creation of numerous martensitic thin-lamellar boundaries in the structure. The greater strength observed after quenching plus four-pass ECAP can be attributed to an increase in solid-solution hardening and a more substantial refinement of the initial thin-lamellar structure. It is also possible that ECAP of the quenched alloy results in a partial decay of the solid solution with potential presepitation of the hardening Nb nanoparticles (which may not be detectable by TEM). However, the dissolution of the solid solution is evidenced by the lattice parameter measured by XRD.

Conclusions

The microstructural and mechanical properties analysis of the Zr—2.5%Nb zirconium alloy subjected to ECAP at 300 °C in both its initial coarse-grained state and after quenching revealed several key findings:

1. ECAP led to the refinement of the initial alloy structure, creating boundaries oriented at large angles and forming grains with a size of ~260 nm. However, ECAP at 300 °C did not completely dissolve the Nb particles, which might be attributed to reduced diffusion during strain-induced dissolution, as opposed to what has been noted in other studies at higher temperatures.

2. The strength of the initial alloy increased by 1.4—1.8 times after ECAP with 4 and 8 passes. Conversely, the ductility decreased from 21.4 to 8.6 %, and the uniform elongation decreased from 12.0 to 1.3 %, typical for metals after severe plastic deformation.

3. Pre-treatment via quenching before ECAP developed a thin-lamellar structure, thus creating more boundaries that enhanced grain refinement during ECAP. Quenching also resulted in solid-solution hardening due to the complete dissolution of the Nb particles into the matrix.

4. Mechanical testing indicated that the yield strength of the alloy, once quenched and then subjected to ECAP, was by 2.3 times higher than that of the initial coarse-grained alloy. The ultimate strength in both longitudinal and cross-sectional directions increased to 864 and 935 MPa, respectively. Pre-quenching followed by 4-pass ECAP yielded higher strength than that achieved by 8-pass ECAP without pre-treatment.

References

1. Chopra D., Gulati K., Ivanovski S. Towards clinical translation: optimized fabrication of controlled nanostructures on implant-relevant curved zirconium surfaces. *Nanomaterials*. 2021;11(4):868. https://doi.org/10.3390/nano11040868
2. Lee D.B.N., Roberts M., Bluchel C.G., Odell R.A.

Zirconium: biomedical and nephrological applications. *ASAIO Journal*. 2010;56:550—556. https://doi.org/10.1097/MAT.0b013e3181e73f20

3. Rosalbino F., Macciò D., Giannoni P., Quarto R., Saccone A. Study of the in vitro corrosion behavior and biocompatibility of Zr—2,5Nb and Zr—1.5Nb—1Ta (at.%) crystalline alloys. *Journal of Materials Science: Materials in Medicine*. 2011;22:1293—1302. https://doi.org/10.1007/s10856-011-4301-z
4. Golovin K.I. Clinico-experimental substantiation of orthopedic treatment with the use of intraosseous zirconium screw implants: Cand. Med. Sci. (PhD in Medicine). Moscow: Moscow State University of Medicine and Dentistry, 2002. (In Russ.).
   Головин К.И. Клинико-экспериментальное обоснование ортопедического лечения с применением внутрикостных винтовых имплантатов из циркония: Автореф. дис. канд. мед. наук. М.: Московский государственный медико-стоматологический университет, 2002.
5. AlFarraj A.A., Sukumaran A., Al Amri M.D., Van Oirschot A.B., Jansen J.A. A comparative study of the bone contact to zirconium and titanium implants after 8 weeks of implantation in rabbit femoral condyles. *Odontology*. 2018;106:37—44. https://doi.org/10.1007/s10266-017-0296-3
6. He X., Reichl F.-X., Milz S., Michalke B., Wu X., Sprecher C.M., Yang Y., Gahlert M., Röhling S., Kniha H., Hickel R., Högg C. Titanium and zirconium release from titanium- and zirconia implants in mini pig maxillae and their toxicity in vitro. *Dental Materials*. 2020;36: 402—412. https://doi.org/10.1016/j.dental.2020.01.013
7. Valiev R.Z., Zhilyaev A.P., Langdon T.G. Bulk nanostructured materials: fundamentals and applications. 1st ed. Wiley, 2013.
8. Zhilyaev A.P., Valiev R.Z., Langdon T.G. Ultrafine-grained metallic materials and coatings. *Advanced Engineering Materials*. 2020;22(10):2001012. https://doi.org/10.1002/adem.202001012
9. Valiev R.Z., Parfenov E.V., Raab G.I., Semenova I.P., Dluhoš L. Bulk nanostructured metals for advanced medical implants and devices. In: *IOP Conference Series: Materials Science and Engineering. 5th International Conference Recent Trends in Structural Materials* (14—16 November 2018). 2018;461:012089. https://doi.org/10.1088/1757-899X/461/1/012089
10. Terent'ev V.F., Dobatkin S.V., Nikulin S.A., Kopylov V.I., Prosvirin D.V., Rogachev S.O., Bannykh I.O. Effect of equal-channel angular pressing on the fatigue strength of titanium and a zirconium alloy. *Russian Metallurgy (Metally)*. 2011;201:981—988. https://doi.org/10.1134/S0036029511100119
11. Nikulin S.A., Rozhnov A.B., Rogachev S.O., Khatkevich V.M., Turchenko V.A., Khotulev E.S. Investigation of structure, phase composition, and mechanical properties of Zr—2,5% Nb alloy after ECAP. *Materials Letters*. 2016;169:223—226. https://doi.org/10.1016/j.matlet.2016.01.148
12. Nikulin S.A., Rogachev S.O., Rozhnov A.B., Gorshenkov M.V., Kopylov V.I., Dobatkin S.V. Resistance of alloy Zr—2,5%Nb with ultrafine-grain structure to stress corrosion cracking. *Metal Science and Heat Treatment*. 2012;54:407—413. https://doi.org/10.1007/s11041-012-9522-3
13. Kukareko V.A., Kopylov V.I., Kononov A.G., Rogachev S.O., Nikulin S.A., Dobatkin S.V. Structural transformations during heating of a Zr—2,5%Nb alloy subjected to equal-channel angular pressing. *Russian Metallurgy (Metally)*. 2010;2010:642—647. https://doi.org/10.1134/S0036029510070116
14. Gunderov D., Stotskiy A., Lebedev Y., Mukaeva V. Influence of HPT and accumulative high—pressure torsion on the structure and Hv of a zirconium alloy. *Metals*. 2021;11(4):573. https://doi.org/10.3390/met11040573
15. Chai L., Xia J., Zhi Y., Chen K., Wang T., Song B., Guo N. Strengthening or weakening texture intensity of Zr alloy by modifying cooling rates from α + β region. *Materials Chemistry Physics*. 2018;213:414—421.
16. Kishore R., Singh R.N., Dey G.K., Sinha T.K. Age hardening of cold-worked Zr—2,5wt%Nb pressure tube alloy. *Journal of Nuclear Materials*. 1992;187:70—73. https://doi.org/10.1016/0022-3115(92)90320-K
17. Straumal B.B., Zavorotnev Yu.D., Davdyan G.S. High-pressure torsion and phase transformations in metal alloys. *Physics and High Pressure Technology*. 2022;32(4):5—29. (In Russ.).
   Страумал Б.Б., Заворотнев Ю.Д., Давдян Г.С. Кручение под высоким давлением и фазовые превращения в металлических сплавах. *Физика и техника высоких давлений*. 2022;32(4):5—29.
18. Glaser A.M., Sundeev R.V., Shalimova A.V., Metlov L.S. Physics of severe plastic deformation. *Physics—Uspekhi*. 2023;66(1):32—58. https://doi.org/10.3367/UFNr.2021.07.039024

Глезер А.М., Сундеев Р.В., Шалимова А.В., Метлов Л.С. Физика больших пластических деформаций. *Успехи физических наук*. 2023;193(1):33—62. https://doi.org/10.3367/UFNr.2021.07.039024

19. Gunderov D.V. Some regularities of amorphization and nanocrystallization at intensive plastic deformation of crystalline and amorphous multicomponent alloys. *Investigated in Russia (Electronic journal)*. 2006;151:1404—1413. (In Russ.).
Гундеров Д.В. Некоторые закономерности аморфизации и нанокристаллизации при интенсивной пластической деформации кристаллических и аморфных многокомпонентных сплавов. *Исследовано в России (электронный журнал)*. 2006;151:1404—1413.

20. Razumov I.K., Yermakov A.E., Gornostyrev Y.N., Straumal B.B. Nonequilibrium phase transformations in alloys under severe plastic deformation. *Physics—Uspekhi*. 2020;63:733—757. https://doi.org/10.3367/UFNe.2019.10.038671
Разумов И.К., Ермаков А.Е., Горностырев Ю.Н., Страумал Б.Б. Неравновесные фазовые превращения в сплавах при интенсивной пластической деформации. *Успехи физических наук*. 2020;190:785—810. https://doi.org/10.3367/UFNe.2019.10.038671

21. Teitel I., Metlov L.S., Gunderov D.V., Korznikov A.V. On the nature of structural and phase transformations induced by severe plastic deformations in solids. *Physics of Metals and Metallurgy*. 2012;113(12):1—8. (In Russ.).
Тейтель И., Метлов Л.С., Гундеров Д.В., Корзников А.В. О природе индуцируемых интенсивными пластическими деформациями структурных и фазовых превращениях в твердых телах. *Физика металлов и металловедение*. 2012;113(12):1—8.

22. Chai L., Xia J., Zhi Y., Chen K., Wang T., Song B., Guo N. Strengthening or weakening texture intensity of Zr alloy by modifying cooling rates from α + β region. *Materials Chemistry and Physics*. 2018;213:414—421. https://doi.org/10.1016/j.matchemphys.2018.04.044

Information about the authors

Dmitry V. Gunderov – Dr. Sci. (Phys.-Math.), Head Researcher of the Institute of Physics of Molecules and Crystals, Chief Researcher of the Ufa University of Science and Technology.
https://orcid.org/0000-0001-5925-4513
E-mail: dimagun@mail.ru

Andrey G. Stotskiy – Junior Researcher, Ufa University of Science and Technology.
https://orcid.org/0000-0002-2667-1115
E-mail: stockii_andrei@mail.ru

Sofia D. Gunderova – Undergraduate Student of the Ufa University of Science and Technology, Research Laboratory Assistant of the Institute of Physics of Molecules and Crystals.
https://orcid.org/0009-0005-7986-8156
E-mail: gynderova@mail.ru

Veta R. Aubakirova – Cand. Sci. (Eng.), Senior Researcher, Ufa University of Science and Technology.
https://orcid.org/0000-0002-8483-6408
E-mail: veta_mr@mail.ru

Alexey Yu. Demin – Dr. Sci. (Eng.), Associate Prof., Head of the Department of Electronic Engineering, Ufa University of Science and Technology.
https://orcid.org/0000-0002-6668-3356
E-mail: deminal77@yandex.ru

Информация об авторах

Дмитрий Валерьевич Гундеров – д.ф.-м.н., вед. науч. сотрудник Института физики молекул и кристаллов (ИФМК) УФИЦ РАН, гл. науч. сотрудник Уфимского университета науки и технологий (УУНиТ).
https://orcid.org/0000-0001-5925-4513
E-mail: dimagun@mail.ru

Андрей Геннадиевич Стоцкий – мл. науч. сотрудник УУНиТ.
https://orcid.org/0000-0002-2667-1115
E-mail: stockii_andrei@mail.ru

Софья Дмитриевна Гундерова – студент бакалавриата УУНиТ, лаборант-исследователь ИФМК УФИЦ РАН.
https://orcid.org/0009-0005-7986-8156
E-mail: gynderova@mail.ru

Вета Робертовна Аубакирова – к.т.н., ст. науч. сотрудник УУНиТ.
https://orcid.org/0000-0002-8483-6408
E-mail: veta_mr@mail.ru

Алексей Юрьевич Демин – д.т.н., доцент, заведующий кафедрой электронной инженерии УУНиТ.
https://orcid.org/0000-0002-6668-3356
E-mail: deminal77@yandex.ru

Contribution of the authors

D.V. Gunderov – defined the problem statement and study concept, authored the paper.

A.G. Stotskiy – conducted studies on microstructure and mechanical properties, contributed to paper authoring and discussions.

S.D. Gunderova – performed XRD analysis, participated in discussions.

V.R. Aubakirova – contributed to paper authoring and discussions.

A.Yu. Demin – authored the paper, analyzed the results.

Вклад авторов

Д.В. Гундеров – определение цели работы и ее концепции, участие в написании статьи.

А.Г. Стоцкий – исследование микроструктуры и механических свойств, участие в написании статьи и в обсуждении результатов.

С.Д. Гундерова – проведение рентгенофазового анализа, участие в обсуждении результатов.

В.Р. Аубакирова – участие в написании статьи и обсуждении результатов.

А.Ю. Демин – участие в написании статьи, анализ результатов.

The article was submitted 11.12.2023, revised 26.01.2024, accepted for publication 07.02.2024

Статья поступила в редакцию 11.12.2023, доработана 26.01.2024, подписана в печать 07.02.2024